Stability of electrical distribution grids in the presence of renewable energies

Arshpreet Singh

To cite this version:

Arshpreet Singh. Stability of electrical distribution grids in the presence of renewable energies. Electric power. Université Grenoble Alpes [2020-..], 2023. English. NNT : 2023GRALT066 . tel-04446002

HAL Id: tel-04446002
https://theses.hal.science/tel-04446002
Submitted on 8 Feb 2024

THÈSE

Pour obtenir le grade de

DOCTEUR DE L'UNIVERSITÉ GRENOBLE ALPES

École doctorale : EEATS - Electronique, Electrotechnique, Automatique, Traitement du Signal (EEATS)
Spécialité : Génie électrique
Unité de recherche : Laboratoire de Génie Electrique

Stabilité des réseaux électriques de distribution en présence de productions d'énergie renouvelable

Stability of electrical distribution grids in the presence of renewable energies

Présentée par :

Arshpreet SINGH

Direction de thèse :

Nouredine HADJSAID PROFESSEUR, G-INP	Directeur de thèse
Vincent DEBUSSCHERE MAITRE DE CONFERENCES, Université Grenoble Alpes	Co-directeur de thèse

Rapporteurs :

Johan DRIESEN
PROFESSEUR, KU Leuven Energy Ville
Josep POU
PROFESSEUR, Nanyang Technological University

Thèse soutenue publiquement le **20 octobre 2023**, devant le jury composé de :

Nouredine HADJSAID PROFESSEUR, Université Grenoble Alpes	Directeur de thèse
Johan DRIESEN PROFESSEUR, KU Leuven Energy Ville	Rapporteur
Josep POU PROFESSEUR, Nanyang Technological University	Rapporteur
Yvon BESANGER-MOLERES PROFESSEUR, Université Grenoble Alpes	Examinateur

Invités :

Marie-Cécile ALVAREZ-HERAULT
Maitresse de conférences, Grenoble INP, Présidente de la chaire Enedis SmartGrids
Xavier LEGRAND
Docteur, Enedis

To my family

Abstract / Résumé

Abstract — Aiming to reach carbon neutrality by 2050, France is committed to integrating more renewable energy into the grid. In the meantime, Enedis, the French distribution system operator, expects up to ten times more wind and solar power connected to the distribution grid. This perspective is raising concerns about the stable operation of future distribution networks, especially with respect to interactions between inverter-based resources. Hence, this thesis provided a study of slow-interaction converter-driven stability in medium-voltage distribution grids with inverter-based resources, assessing the impact of both grid-following and grid-forming operation modes. Our main objective was to develop a methodology for distribution-system operators to analyze and prevent these instabilities, for which we employ electromagnetic transient models and small-signal stability analysis. After investigating the nature of these instabilities and identifying key control parameters, a solution was provided in the form of an optimization problem to determine the ranges of these parameters. A heuristic method was also proposed as a computationally-efficient alternative to solve this optimization.

Keywords: Converter-driven stability, distribution grid, small-signal stability, grid-following, grid-forming

Résumé — Pour parvenir à la neutralité carbone en 2050, la France s'est engagée à intégrer davantage d'énergies renouvelables. Entre-temps, Enedis, le gestionnaire du réseau de distribution, prévoit jusqu'à dix fois plus d'énergie éolienne et solaire raccordée à son réseau. Cette perspective soulève des inquiétudes quant à la stabilité des futurs réseaux, en particulier en ce qui concerne les interactions entre les onduleurs. Ainsi, cette thèse propose une étude de la stabilité liée aux convertisseurs à interactions lentes au sein des réseaux de distribution HTA, tout en évaluant l'impact des réglages *grid-following* et *grid-forming*. L'objectif est de concevoir une méthodologie destinée aux gestionnaires de réseaux de distribution pour l'analyse et la prévention de ces instabilités, à l'aide de modèles transitoires électromagnétiques et de l'analyse de stabilité petits-signaux. Suite à l'étude des causes de ces instabilités et à l'identification des paramètres-clés, une problème d'optimisation a été formulée pour déterminer les plages de ces paramètres. Une méthode heuristique a également été proposée pour apporter une solution plus efficace sur le plan des calculs.

Mots clés : Stabilité liée aux convertisseurs, réseau électrique de distribution, stabilité petits-signaux, grid-following, grid-forming

Acknowledgements

Thank you to the jury members for their kindness in accepting our invitation, their valuable remarks, and their precious time.

This thesis would not have been possible without the funding provided by the *Fondation Grenoble-INP* and *Enedis*, so let me express my deep gratitude. A special thanks to Mr. Bernard Ugnon-Coussioz, director of the foundation, who was eager to support me during the scariest days of the pandemic, support without which I would not have been able to commit to my research endeavors.

Thank you to Mrs. Marie-Cécile Alvarez-Hérault, directress of the *Chaire Enedis Smart Grids*, who took the risk of proposing me this PhD program (it paid off, thankfully!), and Mr. Nouredine Hadjsaid, director of the *G2ELab*, for all his expertise, leadership, and wisdom. Thank you as well to Mr. Yvon Bésanger, president of the jury, but also director of my first internship in the lab, back in 2018, for first introducing me to the world of research.

Thank you to Mr. Vincent Debusscherre, director of my work-related mental-health program, so to say. It was a great honor to have you as a supervisor, I would not have been able to persevere if not for the calmness of your presence. Thank you for both your technical and human support. A special thanks to Mr. Rémy Rigo-Mariani, director of my final chapter, for his thorough revisions, his technical advice, and also for his inspiring words about this beautiful country.

Thank you as well to my friends and colleagues, directors of my happiness, for the joy, the jokes, the conversations. For the food, the recipes, and the book recommendations.

Thank you, of course, to my family, my parents, my siblings, the directors of my life. For the inexhaustible sacrifices, for the unflagging support, for the unconditional love. Thank you.

Thank you to my *fiancée*, directress of my future. For everything. My wife-to-be, my wife-to-be-soon, thank you for your patience, thank you for your love.

Contents

List of Figures

List of Tables

List of Acronyms

AC	Alternative Current
ADN	Active Distribution Network
AGC	Automatic Generation Control
BC	Boundary Configuration
BESS	Battery Energy Storage System
CDS	Converter-Driven Stability
CIG	Converter-Interfaced Generation
CIGRE	*Conseil International des Grands Réseaux Électriques*, i.e., International Council on Large Electric Systems
CSC	Converter-Side Control
DBC	Droop-Based Control
DC	Direct Current
DFIG	Double-Fed Induction Generator, a.k.a, Type-3 Wind Turbine
DG	Distributed Generation/Distributed Generator
DPS	Double-Parameter Sensitivity
DSO	Distribution System Operator
dVOC	Dispatchable Voltage Oscillator Control
EAC	Equal-Area Criterion
EC	Extreme Configuration
EMT	Electromagnetic Transient
EPR	Evolutionary Power Reactor
EU	European Union
FACTS	Flexible AC Transmission System
FFR	Fast-Frequency Response

FICDS	Fast-Interaction Converter-Driven Stability
GA	Genetic Algorithm
GFL	Grid-Following (Inverter)
GFM	Grid-Forming (Inverter)
HV	High Voltage
HVDC	High Voltage Direct Current
IBM	Impedance-Based Method
IBR	Inverter-Based Resource
IPM	Interior-Point Method
IEEE	Institute of Electrical and Electronics Engineers
IPCC	Intergovernmental Panel on Climate Change
LFO	Low-Frequency Oscillations
LV	Low Voltage
MC	Matching Control
MG	Micro-Grid
MPPT	Maximum Power Point Tracking
MPS	Multi-Parameter Sensitivity
MSC	Machine-Side Control
MV	Medium Voltage
MVDG	Medium Voltage Distribution Grid
NAM	Norton-Admittance-Matrix
ODE	Ordinary Differential Equation
OLTC	On-load Tap Changing Transformers
PCC	Point of Common Coupling
PE	Power Electronic
PES	Power and Energy Society

PF	Participation Factor
PI	Proportional-Integral (Control)
PLL	Phase-Locked Loop
PMSG	Permanent Magnet Synchronous Generator, a.k.a, Type-4 Wind Turbine
POI	Point of Interconnection
PSC	Power-Synchronization Control
PSL	Power-Synchronization Loop, same as PSC
PSO	Particle Swarm Optimization
PSS	Power Systems Stabilizer
pu	Per-Unit
PV	Photovoltaic/Solar Photovoltaic
PWM	Pulse-Width Modulation
QSS	Quasi Steady-State
RCP	Representative Concentration Pathways
RMS	Root-Mean-Square
RTE	*Réseau de Transport d'Électricité*
SCR	Short-circuit Ratio
SG	Synchronous Generator
SICDS	Slow-Interaction Converter-Driven Stability
SMIB	Single-Machine Infinite Bus
SMR	Small Modular Reactor
SNBC	*Stratégie National Bas-Carbone*, i.e., National Low-Carbon Strategy
SPS	Single-Parameter Sensitivity
SQP	Sequential Quadratic Programming
SSAT	State-Space Association Technique
SSC	Short-circuit Power, usually measured in MVA

SSO	Subsynchronous Oscillations
SSSA	Small Signal Stability Analysis
SSVI	Steady-State Virtual Impedance
TDS	Time-Domain Simulation
THD	Total Harmonic Distortion
TSO	Transmission System Operator
TVI	Threshold Virtual Impedance
TVR	Threshold Virtual Resistor
UNIFI	Universal Interoperability for Grid-Forming Inverters
UPS	Uninterrupted Power Supply
VI	Virtual Impedance
VSC	Voltage Source Converter
VSM	Virtual Synchronous Machine
WPP	Wind Power Plant

General Introduction

Distribution grids are a portion of electric power systems situated between a transmission grid, which transports the power supplied by centralized power plants, and the electrical installations of final consumers. Their purpose is to ensure a continuous supply of electricity, meeting certain standards of quality, security, and cost. Motivated by environmental imperatives, they have also taken the task of providing infrastructure for the integration of distributed generation, allowing for renewable energy sources (RES) to increase their share in the energy mix.

Most of these RES are connected to the grid via power-electronic devices, constituting inverter-based resources (IBR), and a growing presence of such IBRs will inevitably lead to a considerable shift in power system dynamics, given that their behavior is vastly different from that of synchronous generators, primary drivers of traditional power system dynamics. Most notably, this could result in a reduction in system inertia, lower contribution to short-circuit currents from producers, as well as potential interactions between IBR controllers and other elements in the system. These interactions are leading to stability issues that do not fit into the traditional categories of power system stability, i.e., rotor angle, voltage, and frequency stability. In order to better assess them, researchers have suggested a new category denominated "converter-driven stability" (CDS), further subdivided into slow and fast-interaction CDS, depending on their frequency range. In particular, due to their wide-scale impact and complex origins, slow-interaction converter-driven stability (SICDS), generally comprising CDS phenomena below 50 Hz, is becoming a concern for distribution system operators (DSO).

Recent developments in research related to SICDS have been motivated by real-life events, mostly associated with large wind power plants connected to weak transmission grids. With high levels of distribution-level IBR expected to be integrated in future years, where some of them might be connected to weak nodes in the network, DSOs are questioning if such issues may also take place in the distribution grid. Moreover, because the root cause for such instabilities is often related to the IBR operation mode, namely that of a grid-following inverter (GFL), a general solution proposed in the literature is to promote a shift towards a grid-forming (GFM) operation, better adapted for weak grids and low-inertia systems. A wide-scale application of such inverters in distribution grids, however, still awaits further studies, particularly with respect to possible SICDS issues.

This thesis aims to provide therefore a study of stability issues in distribution grids with high penetration of RES. More specifically, we intend to provide a study of slow-interaction converter-driven stability in medium-voltage (MV) distribution grids, describing the ways in which IBRs may interact with each other. Our final goal is to provide a methodology for DSOs to analyze and prevent such instabilities.

Organization of the thesis

Chapter 1 is an extended introduction with three sections. It begins with an overview of the French distribution grid, discussing its perspectives and the expectations of the DSO. We then introduce some major concepts in power system stability, focusing on SICDS and explaining the main method used in this thesis: small signal stability analysis. The chapter ends with a discussion on IBR operation modes, i.e., grid-following and grid-forming inverters.

Chapter 2 provides some preliminaries for the modeling and stability analysis of an MV distribution grid with IBRs. Here we examine some static features of MV networks, such as short-circuit ratio (SCR) and R/X ratio, and their implications on stability. The goal is to explain some common instabilities related to static parameters, such as PLL instability for GFLs connected to weak grids and high-droop instability for GFMs connected to strong grids, and to explore some particularities of MV networks (e.g., an R/X ratio close to unity).

Chapter 3 presents the modeling of an MV distribution grid with IBRs. It starts with a list of our main hypotheses, followed by a description of the chosen network (CIGRE Benchmark MV Distribution Network) and the physical model of an IBR. Both GFL and GFM controllers are then explained in detail. All differential equations required for the small signal stability analysis are outlined, as well as some comments on sizing, tuning, and parameterization. Finally, we provide details on linearization and state-space association, assembling all the information required for the stability assessment.

Finally, **Chapter 4** is dedicated to the small signal stability analysis. We first assess a 1-IBR system, characterizing the major modes and performing sensitivity analyses to assess the impact of some key parameters. This is followed by an assessment of a 2-IBR system, where the interactions between IBRs are examined in detail. Conclusions are then generalized in case studies with more IBRs, accompanied by time-domain simulations. At the end of the chapter, we propose a methodology to improve the stability of the system by determining the bounds of some key parameters and assessing extreme configurations.

Building upon this methodology, **Chapter 5** presents an optimization problem to achieve a maximum parameter surface while still ensuring small signal stability. This allows for the DSO to impose parameter bounds within which all producers may tune their IBRs according to their own needs, without leading to insufficiently-damped configurations, i.e., a compromise between system-level stability and device-level objectives. As an approximate solution to this optimization problem, we propose a heuristic method based on some concepts described in the previous chapter. This method is then compared to other metaheuristic optimization algorithms, proving to be more computationally efficient.

Main contributions

This thesis has a total of ten major contributions, listed below.

1. Context and preliminaries

- C-1 State-of-the-art on converter-driven stability, a recently-defined category of power system stability, with an overview of major real-life events. Special attention is given to slow-interaction converter-driven stability (SICDS), the main subject of this thesis, for which we present and compare the leading assessment methods.
- C-2 Comparison between grid-following (GFL) and grid-forming (GFM) inverters in the context of interconnected medium-voltage distribution grids (MVDG).

2. Static analysis of Inverter-Based Resources

- C-3 A study of the impact of static grid parameters on the stability of Inverter-Based Resources (IBR), especially the R/X ratio, a particularity of MVDGs.
- C-4 Proposition of a new tuning method for steady-state virtual impedances, a tool to adapt GFMs for MVDG applications.

3. Modeling of IBRs connected to the distribution grid

- C-5 Proposition of generic EMT models for GFL and GFM inverters based on leading trends in the literature.

4. Small-signal stability of a distribution grid with IBRs

- C-6 Detailed analysis of SICDS issues related to GFL and GFM controllers, with an emphasis on inter-IBR interactions.
- C-7 Identification of key parameters with the highest impact on SICDS.
- C-8 Proposition of a DSO-oriented methodology to improve the stability of boundary configurations using small signal stability analysis (SSSA).

5. Parameter bounds for SICDS: an optimization-based method

- C-9 Formulation of an optimization problem to conciliate device-level and system-level objectives in an MVDG with IBRs.
- C-10 Proposition of an innovative, computationally efficient heuristic method to determine parameter bounds for SICDS.

List of publications

The work presented in this dissertation has led to the following publications.

Journal publication:

- *Arshpreet Singh*, Vincent Debusschere, Nouredine Hadjsaid, Xavier Legrand, and Benoit Bouzigon, “Slow-interaction Converter-driven Stability in the Distribution Grid: Small-Signal Stability Analysis with Grid-Following and Grid-Forming Inverters,” IEEE Transactions on Power Systems.

Conference proceedings:

- *Arshpreet Singh*, Vincent Debusschere, and Nouredine Hadjsaid, “Slow-interaction Converter-driven Stability in the Distribution Grid: Small Signal Stability Analysis using RMS Models,” 2022 IEEE Power & Energy Society General Meeting (PESGM), 17 - 21 July 2022, Denver, USA.
- Phuong Huynh Minh, *Arshpreet Singh*, Vincent Debusschere, Nouredine Hadjsaid, Marie-Cécile Alvarez-Hérault, Xavier Legrand, and Benoit Bouzigon, “Converter-Driven Stability In A Distribution Grid With High Penetration Of Inverter-Based Generation,” CIRED 2023 - The 27th International Conference and Exhibition on Electricity Distribution, 12 - 15 June 2023, Rome, Italy.

Presentations:

- *Arshpreet Singh*, “Stabilité des réseaux électriques de distribution en présence de productions d’énergie renouvelables,” 3e Journée scientifique de la Chaire d’Excellence Industrielle SmartGrids, 6 May 2022, Grenoble, France.
- *Arshpreet Singh*, “Stabilité des réseaux électriques de distribution en présence de productions d’énergie renouvelables,” 4e Journée scientifique de la Chaire d’Excellence Industrielle SmartGrids, 31 March 2023, Grenoble, France.

CHAPTER 1

Context and Preliminaries

Contents

Electric power systems are infrastructures deployed for producing, transporting, and consuming electricity. Electric power *grids*, or networks, are electric power systems comprised of three-phase AC networks operating at standardized voltage and frequency levels [1]. For the purpose of this thesis, we are interested in the transport of electricity, which is done in two stages: transmission and distribution. While the transmission grid connects large centralized power plants to the main load centers, operating at high voltages, the distribution grid is responsible for delivering smaller amounts of power from substations to final consumers, operating at medium and low voltages. Although this constitutes the major objective of distribution grids worldwide, their specific structure, characteristics, and operation guidelines are not necessarily the same.

1.1 Power distribution grid in France

The power grid in France is operated at the nominal frequency of 50 Hz and nominal RMS line-to-line voltage levels U_n described in Table 1.1. Distribution grids, in particular, are operated primarily at 20 kV in Medium Voltage (MV) and 400 V in Low Voltage (LV), following European standards. Essentially defined by their frontiers, distribution grids are limited by a substation upstream, including the HV/MV transformer, but not the HV bus, and by the downstream terminals of circuit breakers and disconnectors (for LV clients) or supply terminals (for MV clients) [2]. A basic representation of the French power grid is given in Figure 1.1.

A *Distribution System Operator* (DSO) has the role of "distributing electricity", which includes the development of network infrastructure, operation, maintenance, metering, power flow management, and provision of non-discriminatory access for users. DSOs should also ensure that the electricity being provided is in accordance with the standards of quality and security, and is distributed in a cost-effective and environmental-friendly manner. Unlike the Transmission System Operator (TSO), the DSO in France does not own the grid infrastructure (except for substations) but rather operates it via concession from territorial authorities, i.e., *collectivités territoriales*. While there is only one TSO in France, namely RTE (*Réseau de transport d'électricité*), there are 158 DSOs, although Enedis is in charge of around 95 % of the distribution grid, the other 5 % being operated by local DSOs. Unless otherwise stated, all data presented in the remainder of this dissertation refer to the portion of the French distribution grid operated by Enedis[1].

	Denomination (English)	Denomination (French)	Voltage levels	Usual values
Transmission grid	High Voltage (HV)	Haute Tension B (HTB)	$U_n > 50\,\text{kV}$	63, 90, 225 and 400 kV
Distribution grid	Medium Voltage (MV)	Haute Tension A (HTA)	$1\,\text{kV} < U_n \leq 50\,\text{kV}$	15 and 20 kV
	Low Voltage (LV)	Basse Tension (BT)	$50\,\text{V} < U_n \leq 1\,\text{kV}$	400 V (three-phase) 230 V (single-phase)

Table 1.1: Voltage levels in the French power grid

1.1.1 Overview

1.1.1.1 Structure

Distribution grids in France present a radial tree-like structure, i.e., there is only one path from each node to the substation. For MV networks in urban areas, the most common architecture is a "source-to-source secured feeder structure" [3], which is a loopable but radially-operated

---

[1] Most of the data is publicly available at Enedis' open-source platform: https://data.enedis.fr/

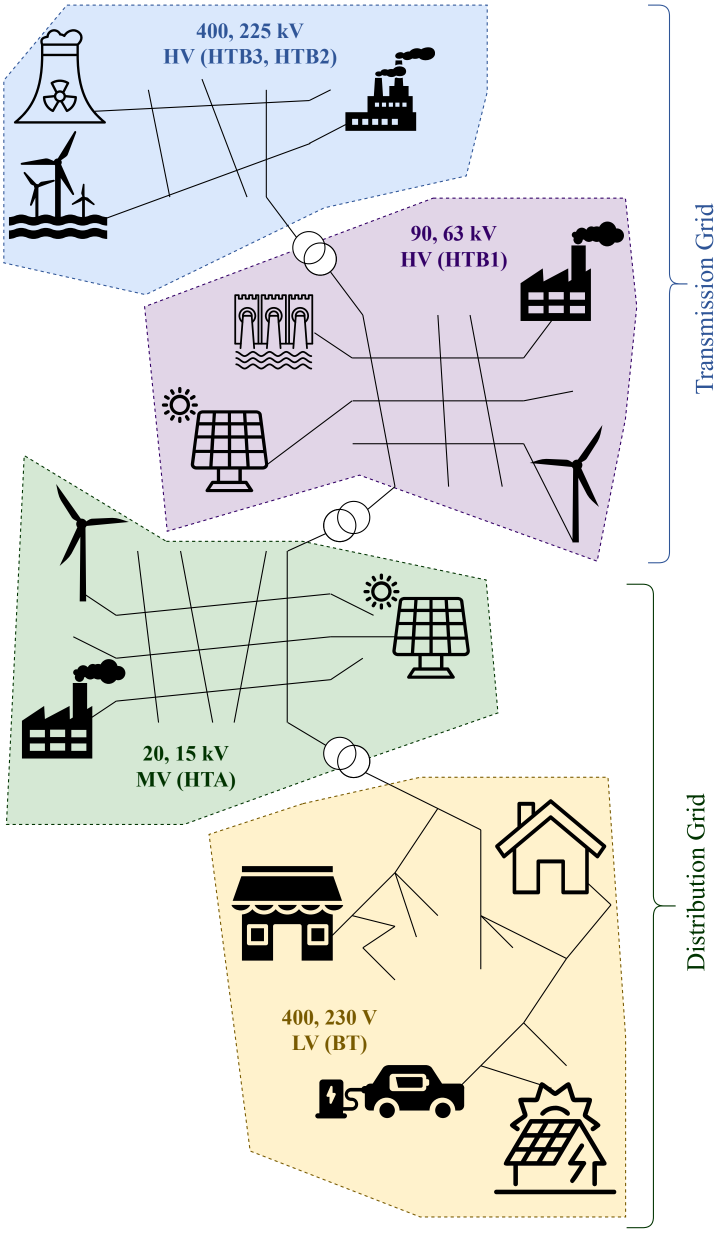

Figure 1.1: Representation of the French power grid

structure, where each MV feeder can be “secured” by a different substation if needed. In rural areas, a simple tree structure is the most common, although a main feeder interconnecting different trees may be employed when the load density is high. LV networks, on the other hand, are almost always simple trees, with certain exceptions, again, when the load density is high. MV feeders generally present a backup transformer in order to ensure the “N-1” principle [2], while LV networks can only be resupplied using emergency generation units or temporary restructuring. In terms of their loading, it is worth noting that MV networks are mostly balanced, while LV networks are rather unbalanced.

As of 2022, the total length of the French MV distribution grid was 664,447 km, from which 52 % were underground cables and 48 % overhead lines. In the LV grid, the total length was 737,032 km, of which 49 % were underground cables and 51 % overhead lines [4]. In general, due to the need for resilience against extreme climate events, there is a push toward more underground cables whenever they are economically justified.

This work is particularly focused on MV distribution grids, and an example of such a network in France is presented in Figure 1.2. We observe two substations (pink circles), located in Voiron and Moirans[2], from which there are several feeders supplying urban zones via underground cables (Figure 1.2a) and rural zones via overhead lines (Figure 1.2b). Figure 1.2a also illustrates the “source-to-source secured feeder structure”, since both substations are interconnected, even if they are operated radially.

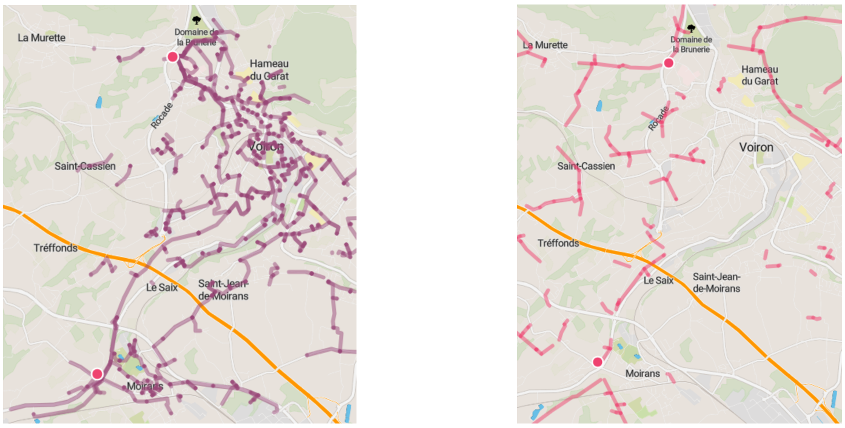

(a) Underground cables (b) Overhead lines

Figure 1.2: MV distribution grid around the city of Voiron. Pink circles designate substations.

---

[2] Municipalities located about 25 km away from Grenoble, in the department of Isère. Images in Figure 1.2 were obtained from Enedis’ open-source platform.

1.1.1.2 Clients

In 2022, the French distribution grid presented a total consumption of 332.5 TWh, from which 32.1 % was due to MV clients, even if they are only 0.2 % of the consumption sites served by Enedis, namely 94,449 clients among a total of around 37.5 million. If consumption has been declining progressively (−3.8 % from 2021 to 2022), distributed generation (DG), i.e., distribution-grid-connected production has been following the opposite trend (+6.2 % in the same period), going from under 40 TWh in 2015 to 65 TWh in 2022. Solar Photovoltaic (PV) generation alone has increased by 26.4 % in 2022, representing about 25 % of the distribution energy mix, whereas Wind Power Plants (WPP) are about 50 %. In terms of installed capacity, PV and WPP have reached a total of 14 GW and 17.3 GW in 2022, respectively, within an aggregated capacity of 37.7 GW connected to the Enedis network [4].

1.1.1.3 Voltage regulation

Since this work is focused on MV distribution grid dynamics, which is mostly related to voltage regulation mechanisms, it is worth providing a short overview of the subject. The goal of such mechanisms is to keep all the voltages in an MV feeder, or rather the 10-min average of their line-to-line RMS values, under a 5 % range around the setpoint voltage U_s. This is a voltage level defined in the connection contract for each client, having to be under a 5 % range around the nominal voltage U_n (typically 20 kV) [5].

Originally conceived to transport electricity in a unidirectional manner – from substations to consumers – MV feeders usually suffer from ever-increasing voltage drops along their length. In order to avoid an undervoltage situation, substations are equipped with on-load tap changing transformers (OLTC), capable of automatically adjusting their transformation ratios in order to regulate the voltages downstream in the feeder. Moreover, if the feeder is chronically overloaded, its upstream node may be reinforced using capacitor banks, dynamic devices capable of providing reactive power support for voltage regulation. Finally, if a specific LV branch requires a voltage adjustment, an offline modification of its MV/LV transformation ratio is also possible: distribution posts offer a choice among three predefined ratios. Any other solution would require a costly network reinforcement, which serves as a last resort [5].

These dynamics are, of course, strongly impacted by the integration of DGs. On the one hand, DGs may revert the power flow in an MV feeder, possibly leading to unreliable voltage regulation in a network that was not designed for bidirectional flows. On the other hand, in theory, they may also provide flexible reactive power support in order to mitigate local undervoltages. Reality is more complicated, however, given that MV-connected DGs are usually located far from the major load centers and their reactive power provision is mostly unavailable when consumption is high, hence they are not only incapable of mitigating local undervoltages, but may cause overvoltages of their own. This is why the French DSO has imposed a volt-var regulation mechanism for MV-connected DGs [6], by which they should inject or absorb reactive power whenever voltages are out of the acceptable range.

Nevertheless, voltage regulation dynamics are usually in a timescale of several seconds up to several minutes, which is considerably slower than our timescale of interest[3]. Throughout this dissertation, we assume therefore that voltage references given to DGs have been properly assigned, whereas we intend to investigate the stability issues that may appear when DGs try to impose such references in their points of interconnection.

1.1.2 Perspectives

This thesis is part of a larger context of transformation in the French distribution grid in response to the climate goals adopted by the government. A short overview and some key figures are presented in this section, linking the national goals to this transformation and providing the main motivations for our research.

1.1.2.1 French climate goals

In 2015, the European Union (EU) and its member states signed and ratified the Paris Agreement, committing to net zero greenhouse gas emissions by 2050, a goal that was written into French legislation in 2019[4]. Published for the first time in 2015 as part of the Energy Transition for Green Growth Act and revised every five years, the National Low-Carbon Strategy (SNBC: *Stratégie National Bas-Carbone*) provides a roadmap for achieving this net-zero objective, committing the country to a 40 % reduction of emissions in 2030 relative to 1990, going from around 550 to 330 Mt CO_2e (megatonnes of carbon dioxide equivalent) [7]. This number may be further reduced if France is to comply with the goal presented by the EU in the 2021 United Nations Climate Change Conference (COP 26), engaging in a 55 % decrease in emissions by 2030, i.e., “Fit for 55”. In any case, the SNBC defines a final goal of 80 Mt CO_2e for carbon neutrality in 2050, hence a drastic 80 % drop in emissions when compared to 2022, as seen in Figure 1.3.

1.1.2.2 RTE’s energy pathways for 2050

In a document from 2021, RTE published a wide-range study about the pathways to reach net zero in 2050 and their impact on the power system [9], applying the principles defined in the SNBC. According to [9], the main challenge is to transition away from fossil fuels, which still

---

[3] Namely a range between 10 ms and 1 s, as will be further explored in Section 1.2.4

[4] *Loi Energie-Climat*, available at `https://www.ecologie.gouv.fr/loi-energie-climat`

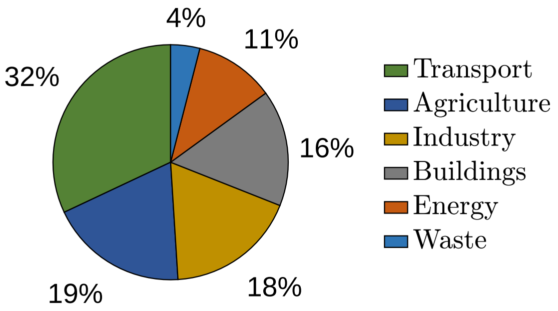

Figure 1.3: French greenhouse gas emissions in 2022, for a total of about 404 Mt CO_2e. [8]

represent around 60 % of the primary energy used in France, i.e., 930 TWh a year, in a total of about 1600 TWh. These 930 TWh are expected to represent the total energy consumption by 2050, translating into a reduction of 40 %, for which the SNBC relies primarily on energy efficiency measures. Electricity consumption, however, is expected to increase from 430 to 645 TWh, representing 55 % of the primary energy by 2050. This electrification drive implies a considerable change in energy supply, for which the SNBC relies primarily on decarbonized electricity (RES or nuclear) and biomass.

In order to achieve this, RTE provides a number of pathways for both consumption and production. Considering a baseline consumption of 645 TWh, additional scenarios range from 555 TWh, counting on lifestyle-based energy sufficiency (*sobriété énergétique*), and 752 TWh in the case of massive reindustrialization, while other factors may be taken into account, such as the pace of electrification and the use of green hydrogen. Similarly, several production pathways are possible, depending on the share and mix of RES production, as well as the strategy for the deployment of nuclear power plants: the "M" scenarios consider that France will not invest in new nuclear reactors[5], confining its investment strategy to RES, whereas the "N" scenarios consider investments in both nuclear and RES. Starting from the generation mix as it is today (see Figure 1.4), there are six reference pathways (see Figure 1.5).

Pathway M0 indicates a 100 % RES mix in 2050, which would require a deliberate decommissioning of nuclear plants. Pathways M1 and M23 provide an 87 % RES mix based on small distributed and large centralized plants, respectively. N1 and N2 differ in the pace of new nuclear development (a pair of new reactors every five and three years, respectively, starting from 2035), while N03 considers a maximum prolongation of current nuclear plants in addition to new developments of both evolutionary power reactors (EPR) and small modular reactors (SMR).

---

[5] Some common assumptions were also considered in all of these scenarios, namely 22 GW of hydro, up to 3 GW of marine energies, and 2 GW of bio-energies.

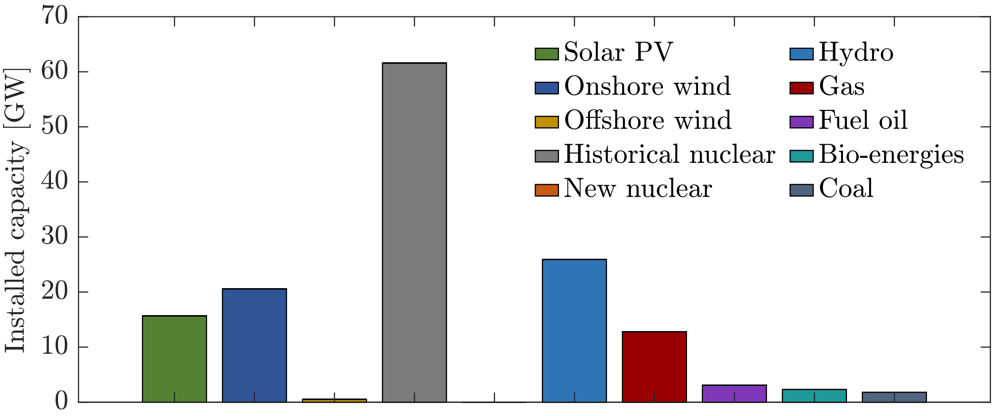

Figure 1.4: French production mix in 2022. This year, France produced 445 TWh of electricity, from a total installed capacity of around 144 GW [10].

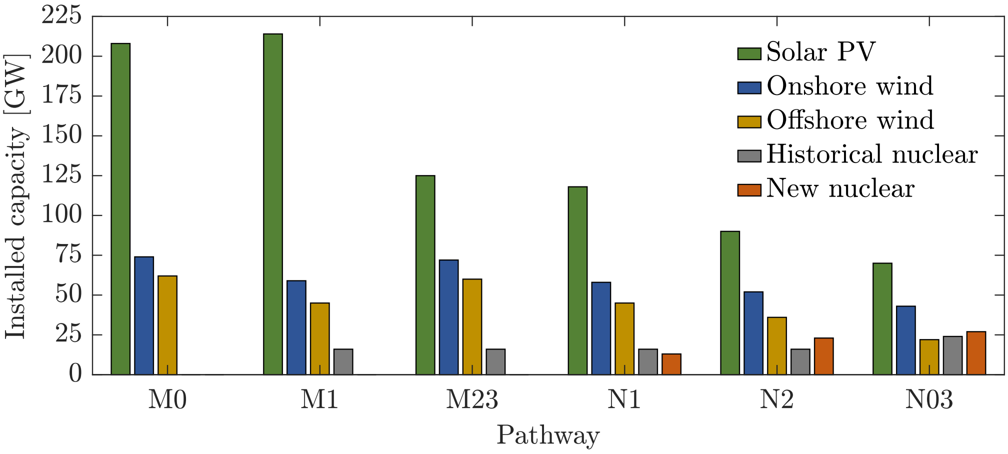

Figure 1.5: RTE's production pathways for 2050 [9].

1.1.2.3 Enedis' perspectives for the distribution grid in 2050

Regardless of the pathway adopted to meet national climate goals, DSOs should be able to anticipate the major changes in the distribution grid in order to define necessary investments. Also in 2021, in light of the SNBC, and considering the role played by the distribution grid in the energy transition (it hosts 87 % of wind and solar capacity in France today), Enedis published a report with the perspectives for the distribution grid in 2050 [11], where four major scenarios are taken into account: stagnation, continuity, transition, and disruption. Unlike RTE's "Energy pathways for 2050", this report did not intend to provide a pathway for carbon neutrality, rather comparing prospective scenarios where the climate objectives are either met or not, with the goal of assessing the most stringent scenarios from the DSO's point of view. Hypothesizing on future economic growth and ecological transition, Enedis also considered a plethora of local information in its assessment, such as demographics, housing, economic activity, meteorology, etc. For our purposes, the most important information is the expected level of RES integration, shown in Figure 1.6, which could be as high as 275 GW, an order of magnitude higher than the 27 GW of distributed generation today[6]. A brief description of the four aforementioned scenarios is given below:

- **Stagnation**: This scenario considers a long economic stagnation (0 % average annual growth in GDP), primarily due to climate-related crises (IPCC's RCP 8.5[7]). Consequently, decarbonization efforts are sluggish (38 GW of wind, 36 GW of ground-mounted PV, and 12 GW of rooftop PV), while consumption is stabilized at a low-efficiency level (building insulation, residential heating, industrial energy performance), with little progress in electrification (33 % EVs, i.e., electric vehicles) and economically-enforced energy sufficiency, mostly due to the low purchasing power of consumers. From the production point-of-view, this scenario is similar to RTE's N03, with new nuclear plants playing an important role.
- **Continuity**: Here, with stable economic growth (1.3 %), there is no deceleration in the efforts for RES integration (same as the previous scenario), energy efficiency, and electrification (81 % EVs), which leads to a better climate scenario (IPCC's RCP 4.5). Centralized RES and nuclear plants play a major role, while consumers are able to provide significant flexibility. From the production point-of-view, this scenario is also similar to RTE's N03, although the overall climate-related measures are better applied.

---

[6] As of July 2023. Distribution-level generation mix is publicly available at `https://data.enedis.fr/pages/parc-raccorde/`. Because of their relatively low values, hydro, bio-energy, co-generation, and storage have been ignored in our assessment.

[7] In its Assessment Reports, the Intergovernmental Panel on Climate Change (IPCC) proposes a number of Representative Concentration Pathways (RCP), i.e., trajectories of greenhouse gas concentration. RCP 4.5 is a scenario in which emissions peak in 2040, leading to a global temperature increase of 2 to 3°C. RCP 8.5 is generally considered a "worst-case scenario", with ever-increasing emissions leading to a temperature rise of 5°C or more.

- **Transition**: Stable economic growth (1.3 %) leads to massive integration of RES (43 GW of wind, 90 GW of ground-mounted PV, and 47 GW of rooftop PV), considerably surpassing the share of centralized nuclear plants. In addition to energy efficiency and electrification (81 % EVs), consumers adopt energy-sufficiency measures of their own accord, once again leading to a better climate scenario (IPCC's RCP 4.5). With respect to RTE's pathways, this scenario is similar to M23, with a high RES share connected via large centralized power plants, specially MV-connected ground-mounted PV.
- **Disruption**: Finally, this extreme scenario is designed to provide an exaggeratedly severe situation for the distribution grid. Considerable economic growth (1.7 %), as well as demographic (a population of 73 million instead of the 71 million considered in all other scenarios), leads to massive growth in consumption, while the production relies on a 100 % RES mix (43 GW of wind, 116 GW of ground-mounted PV, and 116 GW of rooftop PV), mostly connected to the distribution grid, while the climate conditions have deteriorated (IPCC's RCP 8.5). Here, we are close to RTE's M0 pathway, but adopting the structure from M1, where the distribution grid is particularly affected due to the massive integration of small rooftop PV. This scenario assembles all major challenges for the DSO: high risk of climate-related crises, high levels of distribution-connected RES, high levels of electrification coupled with low energy efficiency, and low flexibility from the demand side.

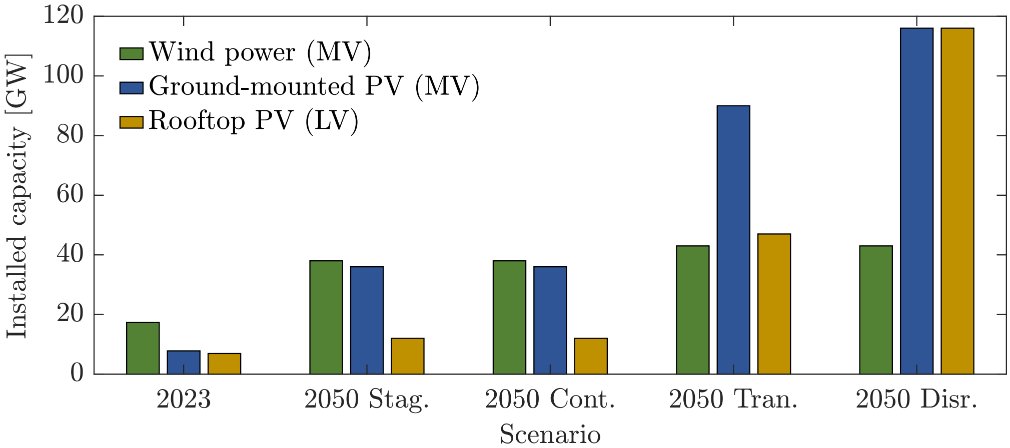

Figure 1.6: Enedis' perspectives for the distribution-level generation mix in 2050 [11].

Even in the least stringent prediction from the DSO's point of view, RES integration is expected to be massive throughout the next 30 years, going from 32 to 86 GW; in particular, ground-mounted PV may go from 7.8 to 36 GW, increasing 4.6 times. In the extremest case, this number could be as high as 116 GW, almost 15 times the current value.

Hence, all predictions lead to a considerable impact on the MV network, where large (10-12 MW) RES plants could be connected in the near future. This naturally leads to questions regarding the operation of such MV distribution grids, especially with respect to stability. This thesis is aimed at providing some answers to these questions and tools to go further. As a starting point, the next section will introduce the main concepts related to power system stability, notably the recent classification proposed by IEEE Power and Energy Society (PES), as well as a literature review on recent developments, real-life instances of instabilities related to RES integration, and the methodology we will use to study these issues.

1.2 Power system stability

As defined by the joint task force set up by the CIGRE Study Committee 38 and the IEEE Power System Dynamic Performance Committee in 2004 [12], power system stability is "the ability of an electric power system, for a given initial operating condition, to regain a state of operating equilibrium after being subjected to a physical disturbance, with most system variables bounded so that practically the entire system remains intact".

An initial operating condition designates the voltages throughout the power system, in amplitude, phase angle, and frequency, as well as the initial value of all the internal state variables in each element connected to the network. In steady-state, the frequency is common to the entire power system, and the local voltages can be obtained from the nominal active and reactive powers through load-flow analysis. There are situations in which the load flow is unsolvable, implying that the system is unable to provide the power demanded by the loads, and thus there is no valid operating condition. But most of the time, the main question in stability studies is whether the system, starting from a valid operation point, is able to regain an acceptable operating condition after a disturbance, either small, such as a slight variation in load, or large, such as a short-circuit. In essence, power system stability is an equilibrium between opposing forces [12]. A brief mathematical overview may help elucidate these definitions.

1.2.1 Mathematical definition

A power system is generally a nonlinear dynamic system, which can be described through a set of n ordinary differential equations (ODE) in the form

$$\dot{\boldsymbol{x}} = \boldsymbol{f}(\boldsymbol{x}) \tag{1.1}$$

where $\boldsymbol{x}$ is the *state vector* and $\boldsymbol{f}$ is a *nonlinear vector function.* We are taking (1.1) to be an *autonomous* system, i.e., $\boldsymbol{f}$ does not depend on time t. A solution $\boldsymbol{x}(t)$ is called a *trajectory,* whereas its initial value $\boldsymbol{x}(0)$ is an *initial condition.* If $\boldsymbol{x}(0)$ is such that $\boldsymbol{x}(t) = \boldsymbol{x}(0)$ for all

$t \geq 0$, then $\boldsymbol{x}(0)$ is an *equilibrium point*, hereby noted as $\boldsymbol{x_0}$. Applying (1.1) to $\boldsymbol{x_0}$, we get the following algebraic system:

$$\dot{\boldsymbol{x_0}} = \boldsymbol{0} \Rightarrow \boldsymbol{f}(\boldsymbol{x_0}) = \boldsymbol{0} \tag{1.2}$$

An equilibrium point $\boldsymbol{x_0}$ is **stable** if, for any $R > 0$, there exists $r > 0$, such that if $||\boldsymbol{x}(0) - \boldsymbol{x_0}|| < r$, then $||\boldsymbol{x}(t) - \boldsymbol{x_0}|| < R$ for all $t \geq 0$ [13]. This a generic definition for *Lyapunov stability*, which essentially means that an equilibrium point is stable if, starting close enough to $\boldsymbol{x_0}$ (within a sphere of radius r), it remains in a bounded region around $\boldsymbol{x_0}$ (sphere of radius R). This definition could be extended to the stability of *motion* if we considered a reference trajectory $\boldsymbol{x_\alpha}(t)$ instead of $\boldsymbol{x_0}$ [14]. Although power systems are in constant motion, it is a common practice to assess their stability with respect to a steady-state operating condition [12], thus when pondering about the stability of a power *system*, we are asking if the *equilibrium point*, i.e., the operating condition, is stable. More precisely, we want to know if this operating condition will remain stable in the event of certain *specific* disturbances.

Moreover, an equilibrium point $\boldsymbol{x_0}$ is **asymptotically stable** if, in addition to being stable, there exists some $r > 0$ such that $||\boldsymbol{x}(0) - \boldsymbol{x_0}|| < r$ implies $\boldsymbol{x}(t) \to \boldsymbol{x_0}$ when $t \to \infty$. In other words, there is a region around the equilibrium point $\boldsymbol{x_0}$ within which every initial condition $\boldsymbol{x}(0)$ will lead to trajectories $\boldsymbol{x}(t)$ that converge to the equilibrium $\boldsymbol{x_0}$, as shown in Figure 1.7. The region defined by the largest possible radius r is called the *region of attraction* of $\boldsymbol{x_0}$, designating the region within which all initial conditions will follow trajectories leading to $\boldsymbol{x_0}$. It is worth noting that a system that is stable but not asymptotically stable[8] will converge to a final state vector whose derivative is not equal to zero, hence it will remain in motion, characterizing a *limit cycle*.

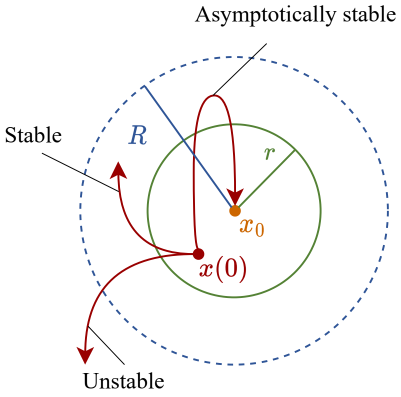

Figure 1.7: Concepts of stability for an equilibrium point $\boldsymbol{x_0}$ [13], [14].

---

[8] Some authors call this a *marginally stable* system.

If the region defined by r is finite, a stable system is said to have finite stability. If this region is small, a stable system is considered to have **local stability** around the equilibrium point $\boldsymbol{x_0}$, in which case we may approximate the nonlinear system by its linearization around $\boldsymbol{x_0}$. If the final region is infinite, i.e., $r \to \infty$, a stable system is said to have **global stability**, which implies that any initial condition would lead to a stable response. In this thesis, we are mostly interested in local stability, which will be further explored in Section 1.2.5, where we use *Lyapunov's first method* (or *Lyapnuov linearization*) as our stability criterion. In power system studies, local stability may be referred to as "stability under small disturbances", "stability in the small", or "small-signal stability", among others.

Global stability, on the other hand, may be assessed by explicitly solving the nonlinear differential equations, mostly via numerical methods, or by applying *Lyapunov's second method* (also called *direct method*). An equilibrium point is stable if there is a positive definite[9] function $V(\boldsymbol{x})$ whose derivative $\dot{V}(\boldsymbol{x}) = \nabla \boldsymbol{V}(\boldsymbol{x}) \cdot \boldsymbol{f}(\boldsymbol{x})$ along any state trajectory is negative semi-definite[10]. For global stability, $V(\boldsymbol{x})$ should also be radially unbounded, i.e., $V(\boldsymbol{x}) \to \infty$ when $||\boldsymbol{x}|| \to \infty$. The direct method is related to the concept of energy in a physical system: defined as a positive scalar, the energy of a system, if continuously dissipated, should lead the system to an equilibrium point. This is why $V(\boldsymbol{x})$ is often called an "energy-like" function [13]. Once again, the literature on power systems presents different denominations for global stability (or finite stability with a sufficiently large region of attraction), particularly "stability under large disturbances", "stability in the large", "large-signal stability", or, in certain cases, "transient stability".

In general, large disturbances – short-circuit, loss of a generator or a large load, loss of a line – modify the dynamic equations of the system, leading to a different equilibrium point; the question is whether the new equilibrium point is capable of attracting the trajectories of this post-event initial condition, which is probably far from the equilibrium. In other words, power systems (or their equilibrium points) should present a large enough region of attraction in order to deal with a number of severe disturbances. Further discussion on global stability is out of the scope of this dissertation.

1.2.2 Classification

Because the causes of instability are diverse, it is practical to subdivide stability studies into different categories, even if the phenomenon of power system stability is just one. There are three "classical" categories defined by an IEEE task force in 2004 [12]: rotor angle, voltage, and frequency stability, as indicated in Figure 1.8.

---

[9] $V(\boldsymbol{x})$ is positive definite in a domain $\mathcal{D}$ if $V(\mathbf{0}) = 0$ and $V(\mathbf{0}) > 0$, $\forall \boldsymbol{x} \in \mathcal{D}$ with $x \neq 0$.

[10] $\dot{V}(\boldsymbol{x})$ is negative semi-definite in a domain $\mathcal{D}$ if $\dot{V}(\boldsymbol{x}) \leq 0$, $\forall \boldsymbol{x} \in \mathcal{D}$. This criterion defines $V(\boldsymbol{x})$ as a *Lyapunov function.*

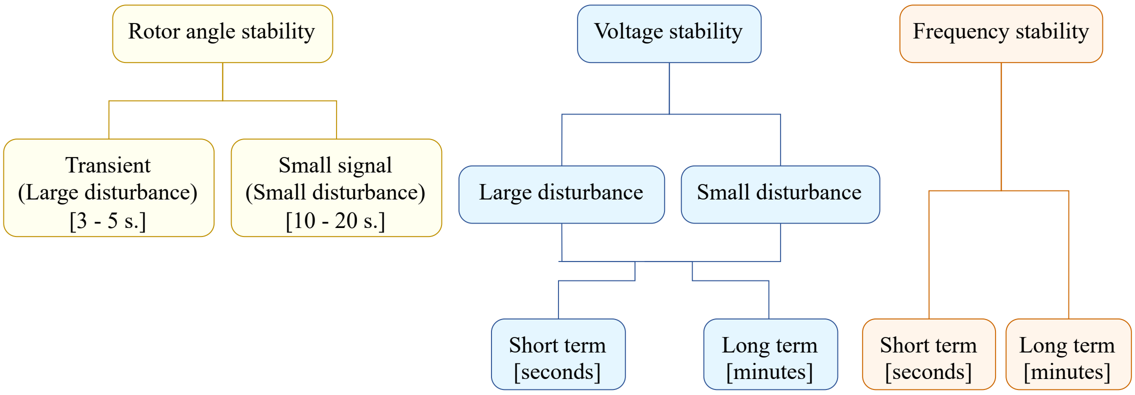

Figure 1.8: Traditional classification of power system stability [12].

From the point of view of dynamics, traditional power systems are dominated by synchronous generators (SG). Their working principle is the interaction between rotor and stator: a direct current excites the rotor, which is driven by a prime mover (turbine), generating a rotating magnetic field that induces three-phase AC voltages in the windings of the stator. The frequency of these voltages is thus related to the rotor speed. When a load is connected, three-phase AC currents start flowing from the SG, inducing a rotating magnetic field in the stator. Both the rotor and the stator fields will tend to align themselves, generating an electromagnetic torque (or power). In order to keep feeding the load, the prime mover has to keep feeding this electromagnetic torque by providing mechanical power. In steady-state, both powers are the same and both fields rotate at the same speed, with an angular difference between them that is proportional to the power delivered by the machine. Also in steady-state, when *multiple* SGs are interconnected, they share a common frequency, hence the magnetic fields of their stators (and consequently rotors) revolve at the same speed. The angular difference between the respective rotors of the SGs is indicative of the power flow between them.

Nevertheless, a slight disturbance – change in load, for instance – is enough to provoke a mismatch between these rotating fields, causing the machines to accelerate or decelerate. When one generator is rotating faster than the other, their relative angular difference will transfer the load from the slower machine to the faster one, leading it to slow down (while accelerating the slower machine). This interaction between SGs characterizes a phenomenon called **rotor angle stability**, which is essentially the ability of SGs to remain synchronized. Rotor angle instability may occur as an aperiodic drift in rotor angle, which happens when the temporary acceleration/deceleration of an SG is followed by an insufficient increase/decrease in load, namely a lack of *synchronizing torque*. Or, if the acceleration/deceleration due to the transfers of load between SGs presents an increasing amplitude, leading them to oscillate their way into instability due to the lack of *damping torque*. Rotor angle stability is subdivided into *small signal stability* and *transient stability*, related to the response of SGs following a small and large disturbance, respectively. These phenomena take place in a time scale of a few seconds up to tens of seconds, namely that of *electromechanical* dynamics, since the devices related to them (automatic voltage regulator, excitation system, turbine governor) operate in such a time frame.

Even if all SGs are well synchronized, the loads in certain buses in the power system may demand more power than what the system can deliver. In such cases, the voltages in such buses may decrease below an acceptable level, activating some automatic devices (OLTCs, for instance) in order to raise them. These actions may increase the load demand even further, which yields an even more accentuated drop in voltage, characterizing a situation of voltage instability. Hence, **voltage stability** is the ability of a power system to maintain steady voltages at all the buses in the system after being subjected to a disturbance [12]. Voltage instability may lead to cascading failures in the system, resulting in a blackout or abnormally low voltages in a large part of the system, constituting a *voltage collapse*. Although load restoration is mostly related to reactive power, with voltage instability ensuing an inability of the system to provide this reactive power [1], requirements in active power also play an important role [15]. Once again, it is useful to distinguish between *small* and *large-disturbance* voltage stability, the former being related to incremental changes in load, for instance, and the latter being related to faults and contingencies. It is also interesting to discern between *short-term* and *long-term voltage stability*. In this case, “short term” corresponds to a few seconds, which is the same time scale usually considered for rotor angle stability studies. Long-term voltage stability involves the dynamics of slow-acting devices (OLTCs, thermostats, current limiters), which could go up to several minutes.

Finally, **frequency stability** is the ability of a power system to maintain a steady frequency after disturbances. Whenever there is a discrepancy between generation and load in a power system, there are frequency excursions with respect to its nominal value. If an event causes a significant increase in load, generators will first decelerate (inertial response) for a few seconds, which leads to a drop in frequency in the network. To contain this descent, some generators will activate their spinning reserve, increasing their power outputs in order to match the load. After 10 to 20 seconds, this frequency will stabilize at a steady value, but not at the nominal one. An Automatic Generation Control (AGC) is thus activated for frequency restoration, taking up to 10 minutes to bring the frequency back to 50 Hz (in Europe). Frequency instability takes place when such mechanisms fail to contain and restore the frequency, which is most common after system splitting, i.e., when previously interconnected networks separate into islands, which then have to sustain their own frequencies.

1.2.3 Impact of inverter-based resources on power system stability

The aforementioned definitions and classification are from 2004, and much has changed since then with respect to power system dynamics, especially due to the integration of inverter-based resources (IBR)[11]. This is why a new classification was proposed by the IEEE PES Power System Dynamic Performance Committee in [16] (summarized in [17]), published in 2020, where the impact of IBRs on power system stability is examined in detail.

IBRs, in addition to flexible AC transmission systems (FACTS), high-voltage direct current (HVDC) lines, and power-electronic (PE) loads, have been causing power system dynamics to depend more and more on fast-acting PE devices, which has serious implications in terms of modeling. Restricting the analysis to electromechanical phenomena (100s of milliseconds to several minutes) has allowed for the use of quasi-steady-state (QSS) models, also called root-mean-square (RMS) models, which enabled some convenient simplifications, such as neglecting stator transients and network dynamics. Including *electromagnetic* phenomena (100s of microseconds to 100s of milliseconds) in the studies, however, requires the use of electromagnetic transient (EMT) models, which usually entail more complex models and computationally demanding simulations. It is worth noting that IBR dynamics are not *restricted* to electromagnetic phenomena, as shown in Figure 1.9: external control loops are usually close to the time-scale of electromechanical dynamics (they may lead to interactions with rotor angle dynamics, for instance), while switching events may be in the scale of a few microseconds (categorized as wave phenomena).

Furthermore, because of the inherent differences between the dynamic behavior of IBRs and SGs, IBR-rich power systems are going through three major shifts: reduction in total inertia, lower contribution to short-circuit currents from producers, and increasing interactions between IBR controllers [17]. IBRs allow for four-quadrant control, hence they can provide independent active and reactive power (if there is enough current coming from the source), in a time scale considerably faster than SGs. They can thus participate in frequency and voltage control, offering flexibility to the grid and contributing to its stability. However, they are unable of providing an inertial response following a generation-load mismatch, since they do not have a large rotational mass storing kinetic energy, possibly leading to large frequency excursions that could trigger protection devices. Although capable of riding through voltage and frequency disturbances, they are also unable of injecting large short-circuit currents (restricted to 1.5 pu, in general, for most IBRs), since their internal components, especially switches, cannot withhold such currents. Finally, their dynamics are largely dependent on their controllers, which act in a larger frequency bandwidth when compared to SGs and are less standardized, accentuating the possibility of undesired interactions.

A growing presence of IBRs has a significant impact on the classic categories of power system stability, shown in Figure 1.8. With respect to rotor angle stability, a low-inertia system will lead to larger and faster rotor swings, which is detrimental to the synchronization of

---

[11] Some authors prefer to use the term "Converter-Interfaced Generation" (CIG), such as in [16], but we have adopted the most commonly-used expression. "Inverter-based resource" is also defined in IEEE Std 2800-2022, although only for transmission networks. We will employ this definition for both transmission and distribution-level inverter-based resources.

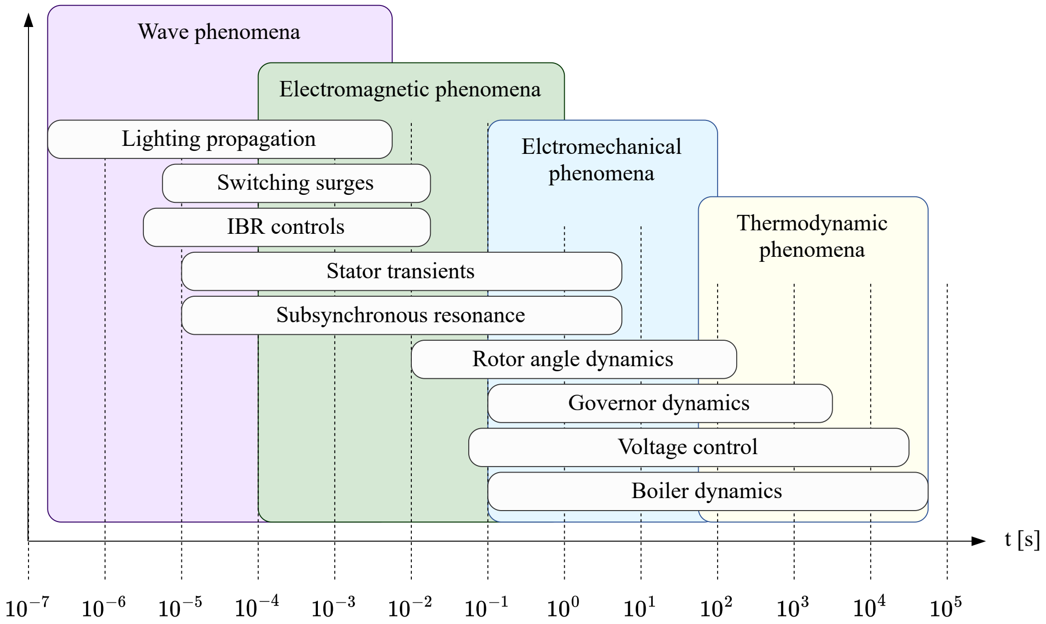

Figure 1.9: Time scales for power system dynamics [17].

SGs following large disturbances. Depending on their controllers, IBRs may also participate in small signal rotor angle stability, either indirectly, by displacing important SGs (such as those with power system stabilizers) and impacting the damping torque of neighboring SGs (a phenomenon already observed for FACTS), or directly, by emulating the behavior of SGs, including undesirable tendencies, e.g., power oscillations. There are also some interesting implications regarding voltage instability. For instance, a large presence of IBRs may increase the risk of overvoltage instability (a rare situation in traditional power systems) [16], since IBRs connected to weakly loaded circuits (a common situation in PV-intensive networks during peak production hours) may temporarily lead to overvoltages, especially in the absence of reactive power regulation. Moreover, the assessment method for voltage stability in bulk power systems is more complex due to the now “active” nature of distribution networks with DGs [18], previously represented as aggregated loads. Finally, frequency stability is also affected by IBRs. Despite their lack of inertia and all of its consequences, IBRs can deliver a much faster primary response than SGs, offering a fast-frequency response (FFR) service in the same time scale as SG inertial response, although voltage and frequency interactions may lead to negative consequences in systems with heterogeneous inertia [19]. In fact, the assumption of a “common frequency” may not hold in low-inertia power systems, given that, unlike SGs, there is no physical relation between the frequency and the active power injected by an IBR [20], although this relation could be imposed by controllers [21]; frequency dynamics may be significantly more complicated in low-inertia power systems, with researchers suggesting innovative interpretations for the concept of frequency itself [22].

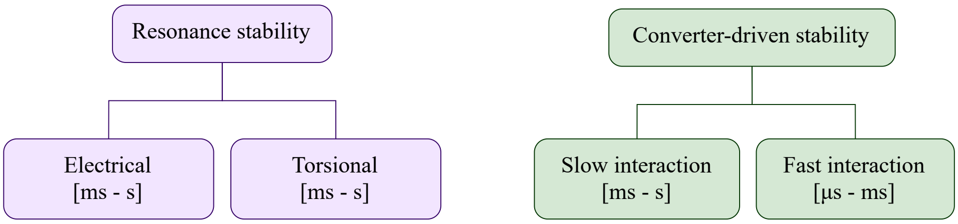

Figure 1.10: New categories of power system stability [16].

Nevertheless, stability events related to high IBR integration cannot be entirely compartmentalized according to the classical definitions, not just because there are new events that would not exist in the absence of IBRs (now categorized as "converter-driven stability"), but also because the extended time scale for power system stability studies calls for the inclusion of certain phenomena that already existed in traditional power systems but whose time scale was considered too fast in [12]. This is the case for **resonance stability**, as shown in Figure 1.10. In power systems with IBRs, resonance, an oscillatory exchange of energy, may occur as an electromechanical resonance (between series compensation capacitors and torsional modes in the turbine-generator shaft of SGs) or an entirely electrical one (between series compensation capacitors and the electrical characteristics of SGs). Electrical resonance has been particularly associated with Type-3 (Double-Fed Induction Generators, i.e., DFIG) wind turbines, leading to undamped subsynchronous oscillations in some real-life events [23].

This thesis, however, is focused on **converter-driven stability** (CDS), defined as "system-wide stability problems due to dynamic interactions between the control systems of power electronic-based systems with other components of the power system" [17]. This category may be subdivided according to the frequency bandwidth of these interactions, which may be slow, i.e., below 50 Hz [24], or fast (up to several kilohertz), also called "harmonic stability" [25]. Regarding fast-interaction converter-driven stability (FICDS), although these issues may take system-level proportions, their origin is usually a local resonance involving the output LCL filter of IBRs and their inner current control loops, being mitigated by the addition of active damping mechanisms [25]–[27]. Slow-interaction converter-driven stability (SICDS), on the other hand, may stem from dynamic interactions between distant IBRs. While FICDS issues may be solved through careful sizing of passive components and proper tuning of specific control loops during interconnection studies, SICDS issues may take place even when IBRs are well-tuned from the producer's viewpoint. From a DSO's perspective, FICDS issues should be solved at a device level, but SICDS may require system-level actions, such as standardized guidelines for IBRs. Therefore, in the context of medium-voltage (MV) distribution networks, where relatively large IBRs can be connected to the grid, having a considerable impact on local dynamics, the question of slow-interaction converter-driven stability, in particular, is raising concerns. The next subsection is dedicated to SICDS, which will be the specific category of power system stability we will address in the remainder of this dissertation.

1.2.4 Slow-interaction converter-driven stability

Going back to the definition proposed by [17], SICDS involves *system-wide* instabilities due to *slow* dynamic interactions between IBR controllers and *slow-response* components of the power system. Such components could be any dynamic device in the electromechanical time scale, such as SGs, or even in the slower portions of the electromagnetic time scale (see Figure 1.9). An interesting case would be the interaction between two IBR controllers, which will be discussed in detail in this dissertation. Although there is no clear frequency range for SICDS ([17] mentions phenomena "typically" under 10 Hz, also called "low-frequency oscillations"), authors have been settling for interactions below the fundamental frequency (50 or 60 Hz) [24], hence including both low-frequency oscillations (LFO), under 10 Hz, and subsynchronous oscillations (SSO) [28], between 10 and 50-60 Hz. It is worth noting that the same control, depending on its tuning, could cause oscillations in the LFO and SSO range: in [29], for instance, authors demonstrate how the gains of the phase-locked loop (PLL) have a determinant role in both LFO (4 Hz) and SSO (30 Hz) for a wind plant connected to a weak network. In [30], PLL-related oscillations are attributed to their inherent asymmetries: most PLLs use a synchronous reference frame aligned to the d-axis voltage v_d at the point of interconnection (POI) [21], which means they control the q-axis voltage v_q to zero; if, under a weak grid condition, there is an oscillation in v_q but not in v_d, with a frequency f_x, the same voltages in a stationary reference frame will present side-band oscillations around the fundamental frequency ($50 \pm f_x$), e.g., 12 Hz and 88 Hz [31], hence both low and high-frequency oscillations.

A clear implication of such a wide range of frequencies is that SICDS studies cannot rely entirely on RMS models, commonly employed in power system stability studies, given that they are inaccurate in representing wide-band phenomena away from the fundamental frequency [32], [33]. At the cost of computational efficiency and genericity, EMT models are more accurate in representing such dynamics. Even if there has been progress in reproducing certain SICDS events using RMS models [34], [35], we will adopt EMT modeling throughout this dissertation.

SICDS is usually a result of inadequate converter control and/or unfavorable grid conditions [24]. A typical example of SICDS is the aforementioned "PLL instability", which happens when a grid-following inverter fails to synchronize to a weak POI. Conceptually, this happens because the inverter requires a steady voltage to serve as a reference for synchronization (mechanism of a PLL), but its own current injection has an impact on this voltage, particularly when the POI is weak, i.e., has a low short-circuit ratio; if the inverter reacts too fast, this voltage may become too irregular for it to synchronize. PLL instability may be solved by decreasing the bandwidth of the PLL, which slows down the inverter, constituting a "converter control" solution, but its root cause is a weak POI, hence an "unfavorable grid condition". For this specific issue, a common solution proposed in the literature is to replace grid-following inverters with grid-forming inverters, which usually synchronize through a power-based mechanism [36], not requiring a PLL. However, these inverters may also be susceptible to instabilities, this time under strong grids [30], given that they act as voltage sources attempting to control a voltage already “imposed” by a strong grid.

The bottom line is that, although SICDS is strongly dependent on local conditions and converter controls, which means it may usually be solved by improving grid conditions or retuning the controllers, there is no “ideal” condition, i.e., different IBR controls may “prefer” different POI conditions and there is no universal rule-of-thumb to adjust the controllers, since the optimal tuning of a given IBR may depend on the dynamics of other IBRs. If such issues appear more frequently in distribution grids, DSOs will have to impose certain dynamic constraints on the most critical IBRs, while keeping some flexibility in light of the evolving grid conditions. Our objective is to provide a methodology to assist DSOs in this quest.

1.2.4.1 Real-life events

It is worth noting that concerns about SICDS are not purely theoretical. Multiple real-life SICDS events have been reported in the literature, although they might have been called by different names. The first largely-reported case of converter-related instability involving wind power plants (WPP) occurred in 2009 [37], in Texas, United States, where the controller of a Type-3 WPP interacted with a series compensated transmission line, constituting a case of electrical resonance instability, namely a sub-synchronous resonance (SSR). Similar incidents took place in Northern China [38], [39], which authors referred to as “sub-synchronous interactions” (SSI) [40] and “sub-synchronous control interactions” SSCI [41]. However, recurrent incidents in Xinjiang, China, in 2014, revealed sub-synchronous oscillations (at around 30 Hz) in Type-4 WPPs connected to weak POIs in a transmission grid without series compensation [42]; although the author also called this event an SSI, the root cause was later attributed to the inadequate PLL tuning for a weak grid condition [28], [43], constituting a classic case of SICDS. In the same grid from Texas, low-frequency voltage oscillations (at approximately 4 Hz), which the authors in [44] considered as a form of “voltage instability”, were reported in 2012; they were compared to the Xinjiang incident in [29], where the authors demonstrated the coexistence of low-frequency and sub-synchronous oscillations in WPPs connected to weak grids.

Interestingly, in 2015, a 20-Hz oscillation was detected in a distribution grid in Canada after the energizing of a shunt capacitor at a substation feeding three 10-MVA solar plants [45]; this situation is particularly relevant for our purposes. Furthermore, in a paper published in 2021, authors in [46] refer to this type of phenomenon as “control stability”, mentioning similar weak-grid-related oscillations in Australia. PLL-related incidents have also been reported for large PV plants (1.2 GW) in California, United States, although they were due to measurement errors leading to unintended tripping rather than a weak grid situation [47]. For an extended list of real-life CDS events, including SICDS, and their underlying mechanisms, please refer to [48]–[50]. Published in 2023, [50] presents a survey of real-life SSO events, which the authors classify as "series capacitor SSO" and "weak grid SSO". A timeline of such events is reproduced in Figure 1.11.

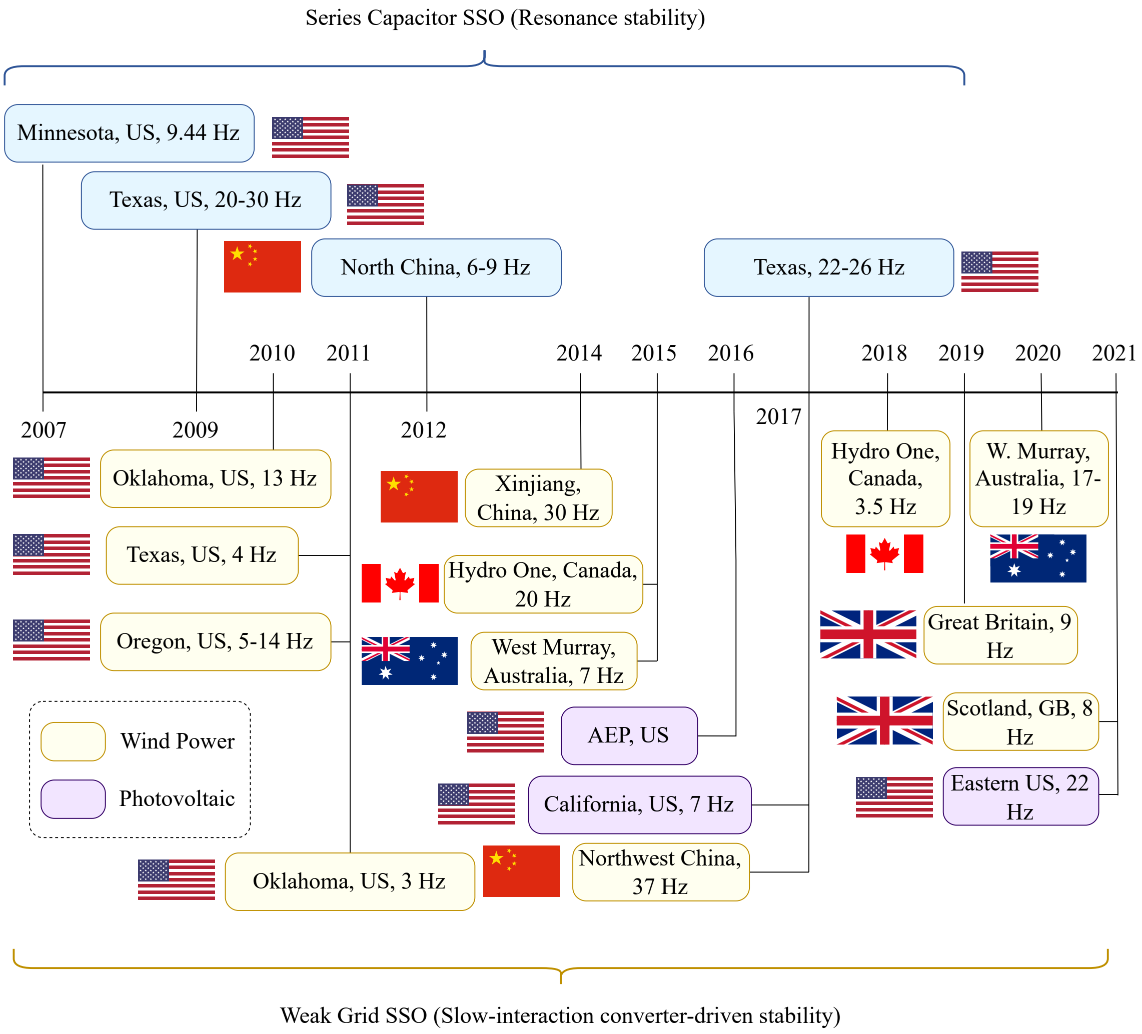

Figure 1.11: Timeline of real-life sub-synchronous oscillation (SSO) events [50].

Most real-life SICDS issues are thus related to large WPPs connected to weak transmission grids [28], [29], [43], [51]–[53], caused primarily by inadequate tuning of controllers, particularly PLLs. For our purposes, considering the perspectives presented in Section 1.1.2, especially the large-scale integration of MV-connected PV plants, two questions are essential, namely the possibility of these transmission-grid events being reproduced in MV distribution grids in the case of very high integration of IBRs, as well as the possibility of SICDS events related to large PV plants instead of WPPs.

1.2.4.2 Assessment methods

SICDS, as a category of CDS, is mostly concerned with the effects of power-electronic devices on power system stability. When searching for assessment methods, we may thus resort to prevailing methods in power electronics, as described in [54], where the author suggests two methodologies for small disturbances (eigenvalue method and impedance-based) and two for large disturbances (time-domain simulations and analytical method). This categorization bears resemblance to the standard methodology in power system stability analysis [1], except for the presence of impedance-based methods and some terminology issues, e.g., “eigenvalue method” is usually interchangeable with “small signal stability analysis” in power systems. An overview of such methods is given in Figure 1.12.

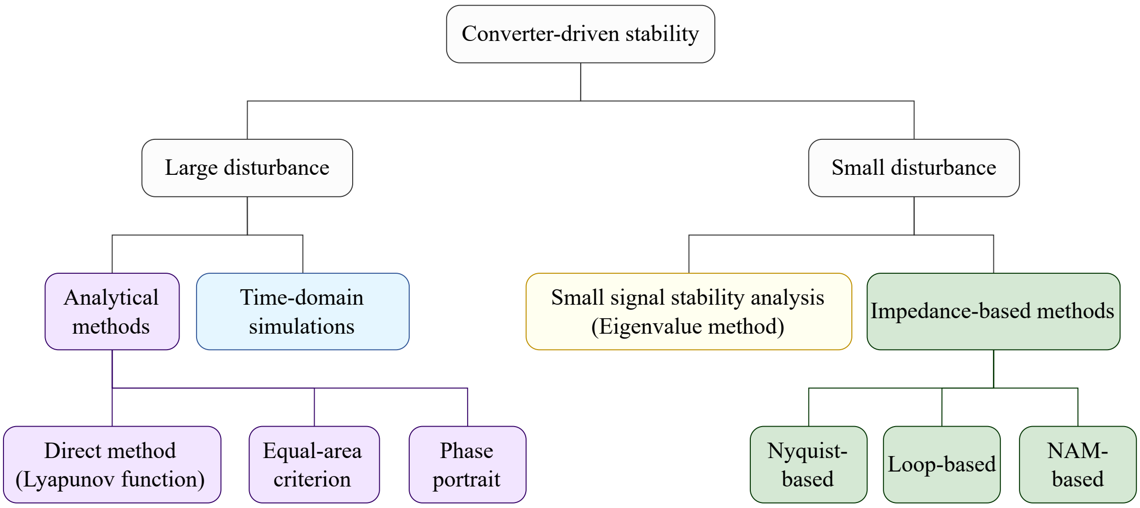

Figure 1.12: Methods to assess converter-driven stability problems

Dividing CDS into small and large disturbances is just as useful as for other stability categories, due to the distinction between local and global stability introduced in Section 1.2.1. In [30], authors present different methods to assess each of these subcategories. For large disturbances, for instance, we may adapt well-known power-system methods, such as the equal-area criterion (EAC) [1]. Although usually employed in transient rotor angle stability studies, the mathematical parallels between the second-order equation of a PLL and the SG swing equation allow for this method to be adapted for CDS [55]. Moreover, other analytical Lyapunov-based methods could be employed for PLL stability analysis, such as the Popov method [56]. More generally, [54] cites techniques such as Takagi-Sugeno, Brayton-Moser’s mixed potential, and Optimal Lyapunov function generation. Finally, [30] also suggests the possibility of resorting to a phase portrait, although this is only practical for simplified systems, with few state variables. In general, due to the simplifications required in most analytical methods, time-domain simulations remain crucial for large-disturbance stability analysis.

When it comes to small disturbances, however, power systems and power-electronic (PE) approaches may be quite distinct. In power systems, the standard method is called "**small-signal stability analysis**" (SSSA), which is an examination of the local stability of an equilibrium point $\boldsymbol{x_0}$. A small disturbance implies that the initial conditions are confined within a small region around $\boldsymbol{x_0}$, hence we can approximate the original nonlinear system by its linearization around $\boldsymbol{x_0}$. This leads to a state-space representation, where the *eigenvalues*[12] of the state matrix can provide information about the local stability of $\boldsymbol{x_0}$: a system is stable if all eigenvalues have negative real parts. **Impedance-based methods** (IBM) [58], [59], on the other hand, are prevalent amongst power electronic engineers, since they are designed to evaluate the stability of a converter at its POI. In terms of physical interpretation, IBMs are indicative of the passivity behavior of the system [30], pointing out if the controllers are causing a destabilizing negative resistance effect [60]. In an IBM, a system containing a PE converter connected to a grid is divided into source and load subsystems, each of which is defined by a transfer function relating the voltage and the current, i.e., an impedance [61], as shown in Figure 1.13.

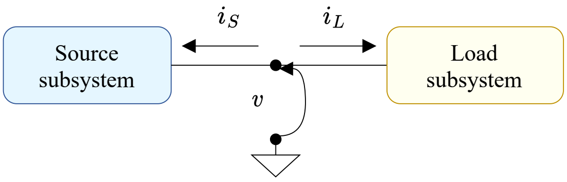

Figure 1.13: Subsystems for impedance-based methods [61]

The open-loop transfer function of this system is a ratio between the source impedance and load impedance:

$$T(s) = \frac{Z_S(s)}{Z_L(s)} \tag{1.3}$$

where

$$Z_S(s) = \frac{\Delta V(s)}{\Delta I_S(s)} \qquad\qquad Z_L(s) = \frac{\Delta V(s)}{\Delta I_L(s)}$$

Here, $\Delta V(s)$, $\Delta I_S(s)$, and $\Delta I_L(s)$ are the linearized variables v, i_S, and i_L (as in Figure 1.13), respectively, represented in the Laplace domain. By applying the Nyquist stability criterion to this ratio $T(s)$, we can evaluate the stability of the closed-loop system: a system is stable if the Nyquist plot of its open-loop transfer function does not encircle the point (-1,0) [54]. Authors in [24] suggest further sub-categories, clustering IBMs into Nyquist-based, loop-based, and Norton-admittance-matrix-based (NAM) methods.

If the full representation of the system is available, it is possible to compute $T(s)$ from the state space, establishing an equivalence between SSSA and IBM [61]. The main advantage of

---

[12] This is why this approach is also named "eigenvalue method" [54] or "eigenvalue analysis" [57].

IBM, however, is that it does not require such full representation, allowing for the stability analysis of "black-box" models (based on field measurements). IBM is also more suitable for converter design-oriented analysis and to study interaction effects between two subsystems [54], as well as in certain situations where SSSA may require too many states, such as for FICDS studies [24]. On the other hand, SSSA allows for the explicit identification of oscillation modes and the states that contribute the most to it [54], which is essential for understanding interactions. SSSA is better suited for the analysis of complex systems where the location of the source of instability is unknown [61] and generally provides a better understanding of the underlying physics involved in a SICDS issue, even if it inevitably requires detailed modeling. In light of these advantages, as well as the maturity of this method, we adopt SSSA as our tool for SICDS assessment.

1.2.5 Small signal stability analysis

Small signal stability analysis is a traditional method in the field of power system stability. This section presents some essential concepts and definitions used throughout this dissertation but is not a complete overview of the subject. For additional properties and equations, please refer to specialized textbooks, such as [1], [57], [62].

Revisiting the definitions given in Section 1.2.1, we know that a power system is a nonlinear dynamic system, which can be described through a set of n ordinary differential equations in the form of (1.1). However, due to the multiple algebraic relations that exist in a power system, it is useful to think of it as a *differential-algebraic* system, which can be described by a set of non-linear differential equations $\boldsymbol{f}$, output equations $\boldsymbol{g}$, and algebraic equations $\boldsymbol{h}$:

$$\dot{\boldsymbol{x}} = \boldsymbol{f}(\boldsymbol{x}, \boldsymbol{u}, \boldsymbol{z}) \tag{1.4}$$

$$\boldsymbol{y} = \boldsymbol{g}(\boldsymbol{x}, \boldsymbol{u}, \boldsymbol{z}) \tag{1.5}$$

$$\boldsymbol{0} = \boldsymbol{h}(\boldsymbol{x}, \boldsymbol{u}, \boldsymbol{z}) \tag{1.6}$$

where $\boldsymbol{x}$, $\boldsymbol{u}$, $\boldsymbol{z}$, and $\boldsymbol{y}$ are the *state*, *input*, *algebraic*, and *output vectors*, respectively.

Each variable x_i in vector $\boldsymbol{x}$, for $i \in [1, n]$, is a *state variable.* They represent the *state* of the system, i.e., the minimum amount of information in a given instant of time that is capable of depicting the system's behavior in the future. The choice of state variables is not unique, any set of n state variables can represent the system, provided they are linearly independent. The total number of state variables n is called the *order* of the system, and the n-dimensional Euclidean space in which the system is represented is called a *state space.* Whenever there is an input and/or an initial condition other than the equilibrium point, the system will be in *motion*, meaning that its state will change with time. This will cause the state variables to follow a trajectory in state space, namely a *state trajectory*. An equilibrium point $\boldsymbol{x_0}$, as defined in (1.7), represents a point in the state trajectory with zero velocity, where all state variables remain constant:

$$\dot{\boldsymbol{x}} = \boldsymbol{f}(\boldsymbol{x_0}, \boldsymbol{u_0}, \boldsymbol{z_0}) = \boldsymbol{0} \tag{1.7}$$

1.2.5.1 Linearization

As mentioned in Section 1.2.1, SSSA is a method to assess *local stability* around the equilibrium point $\boldsymbol{x_0}$, in which case we may approximate the nonlinear system by its linearization around $\boldsymbol{x_0}$. Hence, we may rewrite (1.4)-(1.6) as

$$\dot{\boldsymbol{\Delta x}} = \boldsymbol{A}\,\boldsymbol{\Delta x} + \boldsymbol{B}\,\boldsymbol{\Delta u} \tag{1.8}$$

$$\boldsymbol{\Delta y} = \boldsymbol{C}\,\boldsymbol{\Delta x} + \boldsymbol{D}\,\boldsymbol{\Delta u} \tag{1.9}$$

where

$$\boldsymbol{\Delta x} = \boldsymbol{x} - \boldsymbol{x_0}, \quad \boldsymbol{\Delta u} = \boldsymbol{u} - \boldsymbol{u_0}, \quad \boldsymbol{\Delta y} = \boldsymbol{y} - \boldsymbol{y_0} \tag{1.10}$$

In order to linearize this differential-algebraic system, we may employ a set of Jacobian matrices evaluated at the equilibrium point $\boldsymbol{x_0}$, denoted by the subscript “0”,

$$\boldsymbol{J_{fx}} = \left.\frac{\partial \boldsymbol{f}}{\partial \boldsymbol{x}}\right|_0 \qquad \boldsymbol{J_{fu}} = \left.\frac{\partial \boldsymbol{f}}{\partial \boldsymbol{u}}\right|_0 \qquad \boldsymbol{J_{fz}} = \left.\frac{\partial \boldsymbol{f}}{\partial \boldsymbol{z}}\right|_0 \tag{1.11}$$

$$\boldsymbol{J_{gx}} = \left.\frac{\partial \boldsymbol{g}}{\partial \boldsymbol{x}}\right|_0 \qquad \boldsymbol{J_{gu}} = \left.\frac{\partial \boldsymbol{g}}{\partial \boldsymbol{u}}\right|_0 \qquad \boldsymbol{J_{gz}} = \left.\frac{\partial \boldsymbol{g}}{\partial \boldsymbol{z}}\right|_0 \tag{1.12}$$

$$\boldsymbol{J_{hx}} = \left.\frac{\partial \boldsymbol{h}}{\partial \boldsymbol{x}}\right|_0 \qquad \boldsymbol{J_{hu}} = \left.\frac{\partial \boldsymbol{h}}{\partial \boldsymbol{u}}\right|_0 \qquad \boldsymbol{J_{hz}} = \left.\frac{\partial \boldsymbol{h}}{\partial \boldsymbol{z}}\right|_0 \tag{1.13}$$

by considering the following relations:

$$\boldsymbol{A} = \boldsymbol{J_{fx}} - \boldsymbol{J_{fz}}\,\boldsymbol{J_{gz}}^{-1}\,\boldsymbol{J_{gx}} \tag{1.14}$$

$$\boldsymbol{B} = \boldsymbol{J_{fu}} - \boldsymbol{J_{fz}}\,\boldsymbol{J_{gz}}^{-1}\,\boldsymbol{J_{gu}} \tag{1.15}$$

$$\boldsymbol{C} = \boldsymbol{J_{hx}} - \boldsymbol{J_{hz}}\,\boldsymbol{J_{gz}}^{-1}\,\boldsymbol{J_{gx}} \tag{1.16}$$

$$\boldsymbol{D} = \boldsymbol{J_{hu}} - \boldsymbol{J_{hz}}\,\boldsymbol{J_{gz}}^{-1}\,\boldsymbol{J_{gu}} \tag{1.17}$$

1.2.5.2 Lyapunov’s first method

The small-signal stability of a nonlinear system is given by the eigenvalues λ_i of $\boldsymbol{A}$, particularly their real part $\Re(\lambda_i)$:

1. If $\Re(\lambda_i) < 0, \forall i \in [1, n]$, the original system is *asymptotically stable.*
2. If at least one eigenvalue λ_i presents $\Re(\lambda_i) > 0$, the original system is *unstable.*
3. If there are eigenvalues with $\Re(\lambda_i) = 0$, it is not possible to draw conclusions about the small-signal stability of the original system using its first approximation (linearization). In this case, the equilibrium point $\boldsymbol{x_0}$ is called *degenerate* or *non-hyperbolic* [57].

Equilibrium points for which at least one eigenvalue has zero real part, i.e., $\Re(\lambda_i) = 0$, are called *bifurcations.* A zero eigenvalue $\lambda_k = 0$ indicates a *saddle-node bifurcation*[13], while a complex conjugate pair $\lambda_{h,k} = \pm j\,\omega$ indicates a *Hopf bifurcation.* It is worth mentioning that most cases of saddle-node bifurcations in power systems are due to certain modeling techniques, rather than a stability issue in itself [57]. If the Jacobian J_{gz} from (1.11) is singular, for instance, it will lead to a $\lambda_a = 0$. As explained in [1], [57], using a fictitious synchronous reference for the rotating frame (dq-frame) of each element in the system will lead to such singularity. Since we have employed this approach, zero eigenvalues are mostly ignored in this dissertation.

1.2.5.3 Eigenproperties of state matrix $\boldsymbol{A}$

An **eigenvalue** λ of matrix $\boldsymbol{A}$, sized $n \times n$, is a scalar that satisfies the following relation, for $\boldsymbol{\phi}$, sized $n \times 1$, other than the zero vector $\mathbf{0}$:

$$\boldsymbol{A}\,\boldsymbol{\phi} = \lambda\,\boldsymbol{\phi} \tag{1.18}$$

A complete set of n eigenvalues $\boldsymbol{\lambda} = \{\lambda_1, \lambda_2, \ldots, \lambda_n\}$ is the solution for the *characteristic equation*, obtained via the following determinant, where $\boldsymbol{I_n}$ is an identity matrix of size $n \times n$:

$$\det(\boldsymbol{A} - \lambda\,\boldsymbol{I_n}) = \mathbf{0} \tag{1.19}$$

Each eigenvalue λ_i is associated to a **right eigenvector** $\boldsymbol{\phi_i}$, sized $n \times 1$, and a **left eigenvector** $\boldsymbol{\psi_i}$, sized $1 \times n$, by the following equations:

$$\boldsymbol{A}\,\boldsymbol{\phi_i} = \lambda_i\,\boldsymbol{\phi_i} \qquad \boldsymbol{\psi_i}\,\boldsymbol{A} = \lambda_i\,\boldsymbol{\psi_i} \qquad \forall i \in [1, n] \tag{1.20}$$

For different eigenvalues, the associated right and left eigenvectors are orthogonal, i.e., $\boldsymbol{\psi_j}\,\boldsymbol{\phi_i} = 0$ for $i \neq j$. Moreover, eigenvectors are not unique, since (1.20) could be multiplied by a scalar k on both sides. It is thus a common practice to normalize the eigenvectors, choosing an appropriate scalar: $\boldsymbol{\psi_i}\,\boldsymbol{\phi_i} = 1$.

---

[13] For saddle-node bifurcations, $\det(\boldsymbol{A}) = 0$.

Taking (1.8) in the absence of external forces ($\boldsymbol{\Delta u} = \mathbf{0}$), we can assess the free motion of the system: $\dot{\boldsymbol{\Delta x}} = \boldsymbol{A}\,\boldsymbol{\Delta x}$. Since this is a first-order differential equation, its solution may be derived analytically, yielding, for each state Δx_i,

$$\Delta x_i(t) = \sum_{j=1}^{n} \phi_{ij}\, c_j\, e^{\lambda_j\, t} \tag{1.21}$$

where c_j is a scalar product representing the magnitude of the excitation of the j^{th} mode due to the initial conditions $\boldsymbol{\Delta x}(0)$:

$$c_j = \boldsymbol{\psi_j} \cdot \boldsymbol{\Delta x}(0) \tag{1.22}$$

Therefore the free motion of each state $\Delta x_i(t)$ is a linear combination of its n **modes**. Eigenvalues determine the time characteristic $e^{\lambda_j\, t}$, while eigenvectors and initial conditions determine the excitation of each mode $\phi_{ij}\, c_j$.

For a given eigenvalue λ_k, if $\Im(\lambda_k) = 0$, i.e., zero imaginary part, it corresponds to a *non-oscillatory* mode, leading to either a decay, if $\Re(\lambda_k) < 0$, or an aperiodic instability, if $\Re(\lambda_k) > 0$. Otherwise, if $\Im(\lambda_k) \neq 0$, eigenvalues may appear as a complex conjugate pair $\lambda_{h,k} = \sigma \pm j\,\omega$, corresponding to an *oscillatory* mode.

For the complex conjugate pair of eigenvalues in the form

$$\lambda_{h,k} = \sigma \pm j\,\omega \tag{1.23}$$

the resulting time characteristic will be a damped sinusoid with the following **damped frequency**, in Hz:

$$f = \frac{\omega}{2\,\pi} \tag{1.24}$$

and with a **damping ratio** of

$$\zeta = \frac{-\sigma}{\sqrt{\sigma^2 + \omega^2}} \tag{1.25}$$

The damping ratio ζ represents the rate of decay of the oscillation amplitude, while the oscillation time constant is $1/|\sigma|$. The amplitude decays to $1/e$, i.e., 37 % of its initial value in $1/|\sigma|$ seconds, or $1/(2\,\pi\,\zeta)$ cycles. A negative ζ indicates an unstable mode, as does a positive σ, both could be used as stability criteria. In power systems, the minimum acceptable ζ is generally between 3-5 % [14], [57].

A significant advantage of SSSA is the possibility to locate the origin of a given instability. This is done via **participation factors** (PF), which are computed from both right and left eigenvectors. A PF is defined as:

$$p_{ij} = \frac{\phi_{ij}\,\psi_{ji}}{\boldsymbol{\psi_j}\,\boldsymbol{\phi_j}}[14] \tag{1.26}$$

---

[14] The expression is just $p_{ij} = \phi_{ij}\,\psi_{ji}$ if $\boldsymbol{\phi_j}$ and $\boldsymbol{\psi_j}$ are normalized, i.e., $\boldsymbol{\psi_j}\,\boldsymbol{\phi_j} = 1$.

or, in the case of complex eigenvalues,

$$p_{ij} = \frac{|\phi_{ij}|\,|\psi_{ji}|}{\sum_{k=1}^{n} |\psi_{jk}|\,|\phi_{kj}|} \tag{1.27}$$

Here, p_{ij} is the relative participation of the i^{th} state variable in the j^{th} mode, and vice-versa. The sum of all the PFs associated with a single mode λ_i, i.e., $\sum_{j=1}^{n} p_{ij}$, or a single state variable x_j, i.e., $\sum_{i=1}^{n} p_{ij}$, is equal to one. To clarify, ϕ_{ij} is the i^{th} entry of the right eigenvector $\boldsymbol{\phi_j}$, and ψ_{ji} is also the i^{th} entry of the left eigenvector $\boldsymbol{\psi_j}$[15]. In practice, we may use PFs to establish which states are the most participative in a given unstable or insufficiently-damped mode, locating the *cause* of such instability and defining where to act for its resolution.

In traditional SG-dominated power systems, SSSA measures the ability of the system to maintain synchronism when subjected to small disturbances [1]. In practice, SSSA has been mostly used for detecting insufficient damping of power oscillations, which are mitigated through power systems stabilizers (PSS) but has also found applications in voltage stability and subsynchronous resonance analysis. In recent years, applications of SSSA have been extended to PE-dominated systems [63], being adapted into frequency-domain and impedance-based methods, and being employed in model order reduction techniques [64]. For our purposes, SSSA serves as an instrument for assessing interactions between IBRs; we may employ classical tools, such as eigen-sensitivity (the way eigenvalues evolve in response to variations of a chosen parameter) and PFs, to detect the modes by which IBRs interact with each other and the key parameters that could be tuned for mitigating oscillations and instabilities.

1.3 IBR operation mode

As defined in Section 1.2.4, SICDS is intimately related to the behavior of IBR controllers, it is thus crucial to understand their control strategies. In fact, structurally identical inverters may differ considerably with respect to their control strategies, two of which are predominant [21]: grid-following (GFL) and grid-forming (GFM). These strategies, also called “operation modes” [63] are briefly described in this section, although their detailed modeling will be done in a later chapter. The goal here is to explain some fundamental concepts and understand the major differences between GFL and GFM.

1.3.1 Grid-following inverter

Grid-following inverters (GFL), also called grid-feeding, are power converters controlled as current sources [21]. They represent most of the IBRs used for the integration of RES in

---

[15] Remember that the right eigenvector $\boldsymbol{\phi_j}$ is a *column* vector, while the left eigenvector $\boldsymbol{\psi_j}$ is a *row* vector.

power systems today. A basic diagram is provided in Figure 1.14. GFLs receive commands in terms of active and reactive power (P_f^* and Q_f^*), as well as measurements of voltage and current at the POI. Their objective is to simply inject P_f^* and Q_f^*, which, if POI voltage $\overline{V_f}$ is held constant by the grid, can be done by injecting a current $\overline{I_f}^*$:

$$\overline{I_f}^* = \frac{P_f^* - j\,Q_f^*}{V_f \angle -\delta_f} = \frac{I_d^* + j\,I_q^*}{1 \angle -\delta_f} \tag{1.28}$$

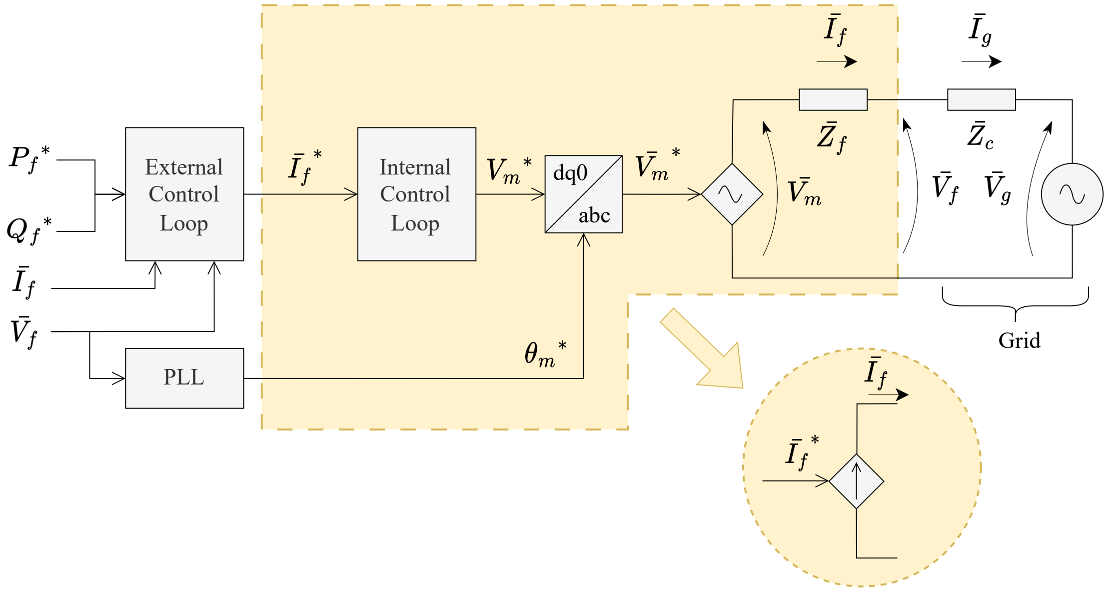

Figure 1.14: GFL inverter diagram

For most purposes, GFL is a very effective operation mode. First of all, most producers are interested in injecting as much power as possible, so as to best use their primary resource. Since most countries have opted for incentive schemes such as feed-in tariffs to increase RES penetration, it is in the best economic interest of producers to inject maximum power, using control schemes such as maximum power point tracking (MPPT). Battery energy storage systems (BESS) are still expensive, hence most RES connected to the grid do not rely on storage, which is yet one more reason for them to opt for MPPT. Grid following inverters are primarily designed for MPPT.

A similar logic can be applied to reactive power. System operators, including Enedis [6], usually require RES producers to provide reactive power for voltage support. GFLs do not control the POI voltage directly, but they can provide reactive power according to a volt-var scheme since these are usually much slower than the control loops within the inverter. Because P and Q are controlled independently – through I_d and I_q, active and reactive components of the injected current – GFLs are able to inject an adequate P while providing a specific Q for voltage support. This satisfies the requirements for most prevailing SG-dominated power systems.

Another major advantage of GFLs concerns their DC side, namely the possibility of controlling the DC voltage through the inverter rather than the source. A diagram is provided in Figure 1.15. RES may be either a power source alone (single-stage conversion) or a power source coupled with a DC/DC converter (two-stage conversion).

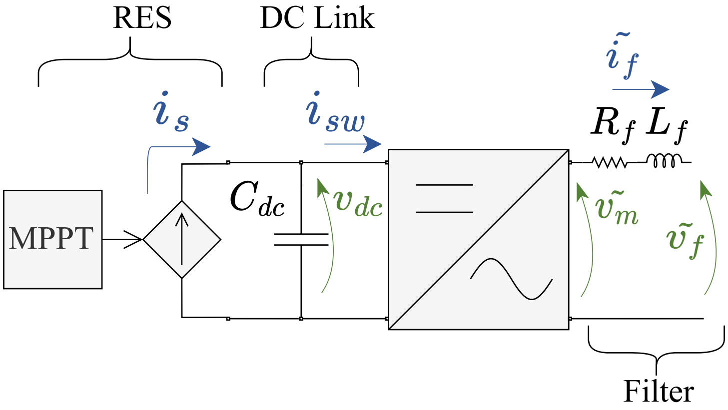

Figure 1.15: Diagram for the DC side of an IBR connected to the grid

DC side dynamics can be described by (1.29),

$$C_{dc}\,\frac{d\,v_{dc}}{dt} = i_s - i_{sw} \tag{1.29}$$

which can be rewritten as

$$\frac{C_{dc}}{2}\,\frac{d\,(v_{dc}^2)}{dt} = P_{DC} - P_{AC} \tag{1.30}$$

where

$$P_{DC} = i_s\,v_{dc}, \quad P_{AC} = i_{sw}\,v_{dc}$$

P_{AC} is the power injected to the AC side through the switches, which are considered lossless in our studies. From (1.30), we can see how the difference between generated power P_{DC} and injected power P_{AC} leads to changes in DC voltage v_{dc}. For safety purposes, v_{dc} must be kept under a certain range; this can be done by controlling the power source, via i_s or P_{DC}, or else by controlling the injected power, via i_{sw} or P_{AC}.

For IBRs connected to large networks rather than isolated loads, there are significant advantages in adopting the second method. First of all, sources can take some time to respond, which would lead to large capacitance requirements in order to keep v_{dc} under control. Also, while P_{AC} can be both increased and decreased without restrictions, P_{DC} can only be curtailed; increasing it would depend on resource availability, which is highly uncertain for intermittent

RES without BESS. GFL inverters can inject maximum power by controlling v_{dc} using the active component of the injected current ${I_d}^*$, which is equivalent to using i_{sw} or P_{AC}. In other words, GFLs can "perform grid forming on the DC side".

Hence, GFL inverters provide MPPT, in addition to independent P and Q injection, while keeping v_{dc} under control without imposing restrictions on the source or requiring an oversized energy buffer. This explains their predominance in modern power systems. Nevertheless, there are major shortcomings related to GFLs, both static and dynamic.

In the absence of voltage control, from a load-flow point of view, GFL inverters are PQ buses in steady-state. For weak grids, power transfer limitations can lead PQ buses to voltage instability when attempting to inject their rated powers, just as constant-power loads [1]. This phenomenon is classically assessed via Q-V sensitivity plots. Another static issue related to GFLs is their P-I sensitivity. Since GFLs are operated as current sources, whenever an increase in power is required, they increase their current output; under weak grids, however, an increase in current can lead to a decrease in active power injection i.e. negative P-I sensitivity [43], [51], which causes instability. These problems usually entail convergence issues in load-flow algorithms, and only take place under extreme circumstances; the major static issue related to GFLs is their inability to keep POI voltage under an appropriate range when operating in weak grids.

When considering dynamic limitations, the discussion is quite vast. As mentioned previously, in traditional power systems whenever there is a discrepancy between generation and load, there is a frequency deviation. Synchronous generators have an inertial response at first, following the swing equation [1], where their rotating masses prevent abrupt frequency variations; later on, the primary response is activated in order to restrain the frequency, which is then brought back to the nominal value. IBRs, on the other hand, have a very limited inertial response, since the energy buffer is mostly concentrated in the DC-link capacitor, which is orders of magnitude smaller than the kinetic energy provided by the rotating mass of a SG. Their response, given that v_{dc} is managed properly, is actually dictated by controllers. While grid-forming inverters can be controlled so as to emulate SGs – using droop-based methods, for instance – grid-following inverters, on the other hand, are unable to do so. If there is a rise in frequency, they will keep on injecting P and Q while synchronizing to the rising frequency; they will not counteract it in order to provide support for the grid.

This reliance on an external reference in order to synchronize is the most relevant shortcoming of GFLs. In essence, this is what leads them to "follow" the grid rather than to "form" it: they cannot impose their own frequency, they have to *follow* the frequency of their reference. Hence, relying exclusively on GFLs in a future power system where the dynamics are dictated by IBRs rather than SGs is virtually impossible[16]. Today, this issue is usually expressed in the form of PLL instability, which is the origin of many of the events mentioned in Section 1.2.4.1. All aforementioned shortcomings of GFL inverters will be further explored in this dissertation.

1.3.2 Grid-forming inverter

Grid-forming inverters (GFM) are power converters controlled as voltage sources [21], [66], [67]. Originally conceived for Micro-Grids (MG) and Uninterrupted Power Supplies (UPS), they are now at the forefront of IBR integration into modern power systems. Unlike GFL inverters, GFMs are expected to set up the voltage and frequency in a grid, i.e., "form the grid"; this means their control scheme usually does not include a PLL, although there are exceptions [68]. In any case, GFMs do not require an external stable voltage for synchronization, they are able to emulate a SG in its ability to synchronize through the active power. A simple diagram of a GFM is presented in Figure 1.16.

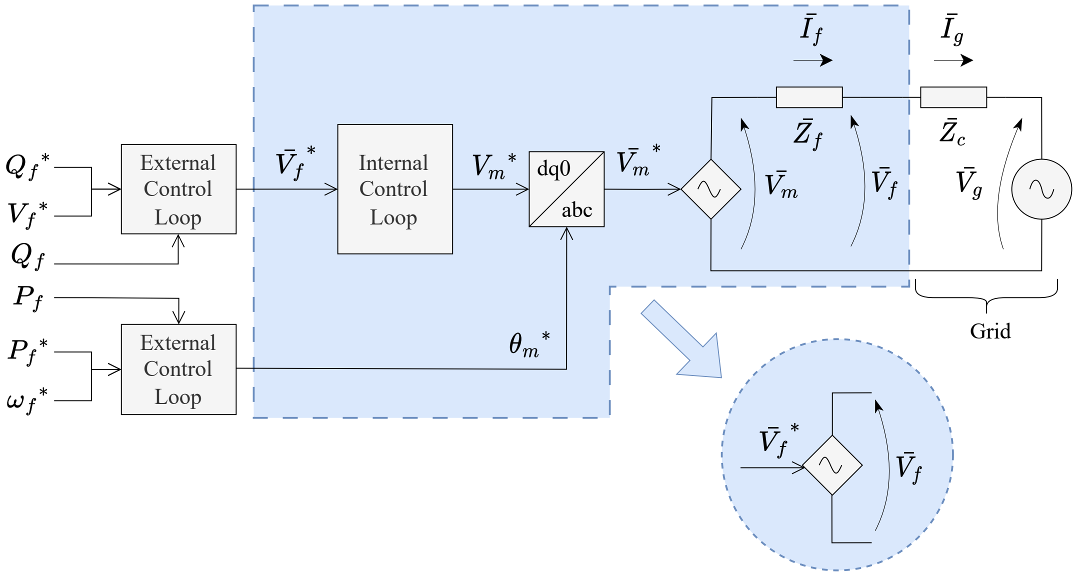

Figure 1.16: GFM inverter diagram

For interconnected grids, GFMs can also be characterized by a set of capabilities [65]. These include the ability to operate with or without SGs or other IBRs, robust fault ride-

---

[16] This statement is commonly found in the literature, but there are nuances. In [65], for instance, the authors argue that a power system entirely composed of current sources may still present stable solutions, as per Kirchhoff's law, although it would require IBRs to quickly change their current output in response to load variations. They argue that most GFL-related instabilities are due to improper tuning rather than their current-source behavior. This would justify a service-based definition of grid-forming inverters (GFM) rather than a structure-based definition, i.e., GFMs could technically still be current sources or PLL-based, as long as they are able to provide a number of essential "grid-forming services".

through, as well as a positive contribution towards load/generation balancing, voltage control, power quality, and system stability margin. Due to their MG legacy, GFMs have also been expected to present black-start capabilities, which is an onerous task for certain RES, such as WPPs. GFM capabilities are still a matter of debate, however. A recent consortium funded by the US Department of Energy – Universal Interoperability for Grid-Forming Inverters (UNIFI) – synthesized the basic requirements for GFMs by unifying information provided in multiple reports, publishing a first version of these specifications in [67], summarized in Table 1.2.

Operating conditions	Requirement	Description
Normal (V and f within normal ranges)	Autonomous grid support	Voltage and frequency support based on local measurements
	Dispatchable power	Based on operator command or local objective
	Damping of oscillations	Positive resistance against resonances
	P and Q power-sharing	Share the burden with other generators after disturbances
	Weak-grid operation	Remain stable under weak grids and improve system strength[a]
	Voltage balancing	Not prevent the flow of negative-sequence current for small V unbalance
Abnormal (V and f outside normal ranges)	Ride-through behavior	Provide fault current (within IBR limits) and post-disturbance support
	Asymmetrical faults	Maintain balanced voltage, thus inject unbalanced current
	Response to abnormal frequency	Regulate P in response to f excursions for stability
	Response to phase jumps and voltage sags	Inject/absorb P and Q in response to V excursions (phase and magnitude)
	Intentional islanding	Provide support for stable V and f in island
Additional services	Black-start	Some GFMs may provide system restoration service
	Regulate harmonics	Output harmonic distortion should comply with grid requirements
	Communications with system operator	Cybersecurity compliance when communication is required
	Secondary V and f control	Some GFMs should be able to receive signals for secondary control
	IBR short-term rated current (ISRC)	This current should be disclosed (magnitude and duration)
	Constraints due to input source	Specificities should be disclosed for studies, e.g., DC-side limitations

Table 1.2: Universal performance requirements for GFMs [67]

---

[a] In [67], an improvement in system strength denotes a reduction in voltage sensitivity to current injection from the IBR, as well as a reduction in the rate-of-change-of-frequency (ROCOF).

As discussed in Section 1.3.1, GFL inverters present several drawbacks, in particular their inability to hold voltage levels under an adequate range, as well as their susceptibility to stability issues when operating in weak grids, e.g., PLL instability. GFMs, on the other hand, are capable of keeping stiff voltages even during transients [69], and are capable of operating under weak grid conditions, since their synchronization does not require an external reference.

There are a few shortcomings related to GFMs, though. Unlike GFLs, which act as PQ buses in steady-state, GFMs act as PV buses, and cannot, therefore, provide perfectly decoupled active and reactive power injection. With respect to transient P-Q coupling in large transmission networks, some control strategies apply low-pass filters in order to eliminate this interaction [70], but in grids with a non-negligible R/X ratio, this issue still takes place in steady-state. One possible solution is to apply a virtual impedance in order to reduce the R/X ratio effectively perceived by GFM controllers [21], which will be discussed later in this dissertation. It is worth noting, however, that P-Q coupling may not be a problem after all; if an inverter is capable of holding POI voltage while controlling its injection of active power, there may not be any need for reactive power, which is primarily used for voltage support.

When comparing GFMs to GFLs in terms of synchronization, there is a certain duality between both methods – power-synchronization control (PSC) and PLL – which has been recently explored in literature [71]. This framework is helpful in explaining why there have been reports on GFM instability under strong grids [24], [30], [72], in contrast to the classic PLL instability. While GFLs using a PLL have to "follow the voltage" in order to synchronize, GFMs using a PSC have to "follow the current". In fact, GFMs will follow the power injected at the POI, which translates into following the injected current, since the POI voltage is controlled by the inverter. Hence, because the voltage is more volatile in weak grids, GFLs may experience synchronization instability; in strong grids, on the other hand, the injected power, and consequently the current, are more volatile, which poses a synchronization challenge to GFMs instead.

Another issue with GFM inverters is their inability to perform converter-side control for DC voltage v_{dc}, at least for most droop-based control methods; in such cases, most examples available in the literature assume a DC voltage source. This assumption may not always hold true, and GFM AC-side requirements may lead to instabilities and oscillations on the DC side, especially for wind turbines [73]. Going back to Figure 1.15 and considering (1.30), we note that v_{dc} may experience strong deviations when there is a power imbalance between the source (DC side) and the POI (AC side). While GFLs allow for strict v_{dc} control using the converter, GFMs with PSC cannot do the same; since the power to be injected is determined by the controller in order to achieve synchronization, the source has to be responsible for v_{dc} control, which may not be possible, either due to resource availability or machine-side dynamics. This issue may be solved through advanced control techniques, such as "matching control" [74] and dual-port GFM control [75], although they have not yet been validated in large-scale experimental setups. Another solution is to oversize the DC-link capacitor to provide an instantaneous energy buffer; some demonstrators have resorted to 10 MW-s ultra-capacitors for this purpose [76].

Transient phenomena in power systems usually demand high instantaneous currents. While SGs have a powerful short-circuit current contribution, IBRs do not have such capability, as mentioned in Section 1.2.3, since their PE switches cannot handle significant overcurrents. Thus, in order to protect the equipment, IBR controllers must apply an effective current limitation method. Once again, GFLs have an advantage: since they are controlled as current sources, a simple saturation in current references can enable this feature. GFMs, on the other hand, may require more complex current limitation algorithms, such as a Threshold Virtual Impedance (TVI) [77]. Current reference saturation is still possible for GFMs if they employ a cascaded two-level control, with an outer loop for voltage and an inner loop for current control [78]. It is worth noting that such control architecture may require a bandwidth of tens of kHz for the inner loop, which may not be practical for transmission-level IBRs [70]. For distribution applications, however, given the smaller size of the IBRs, they may still be viable.

As a final note, while there is a variety of methods to control GFLs, they mostly rely on the same principles and may be reproduced using standardized models [34], with tuning methods available in power electronic textbooks [79]. GFMs, on the other hand, present a wide range of control strategies. These include droop-based methods, which originated almost 30 years ago for parallel operation of UPS [80] and have been applied in MGs [81], as well as further developments, such as the PSC [36]. When adding a low-pass filter to the droop control, a GFM is able to emulate an inertial response; this has been called "Virtual Synchronous Machine" (VSM) [82], which is also a category of major control methods for GFM. More recently, alternative methods have gained notoriety in the literature, especially with respect to future low-inertia power systems. These include "Matching Control" [74] and "Dispatchable Virtual Oscillator Control (dVOC)" [83], among others [84]. This list is not exhaustive, of course. More detailed comparisons between GFM control methods are also available in the literature [85].

Taking all these advantages and drawbacks into account, there are many reasons to keep GFLs in a bulk power system. As mentioned in Section 1.3.1, they are perfectly adapted for MPPT, they provide adequate P-Q decoupling and fast synchronization, while also allowing for converter-side DC voltage control. However, their success relies primarily on a strong power system, with sufficient inertia and high SCR POIs, which is made possible by the still predominant presence of SGs. A future power grid, dominated by IBRs, will not provide such features. In such case, a stable operation can only be assured by GFMs [46]. In fact, further penetration of GFLs is only possible if there are enough GFMs providing these "strengthening" services in the first place. With policymakers redirecting their attention to the definition of "grid-forming requirements" and the research community advancing their technical feasibility, a large-scale presence of GFMs in the power grid is possibly just a matter of time.

In light of the inevitable and indispensable presence of GFMs in a future power grid, including MV distribution networks, it is crucial to assess their impact on small-signal stability, as will be done in this dissertation.

1.4 Chapter summary

It is worth recalling that France intends to reach carbon neutrality by 2050, for which an accelerated integration of RES is a key factor. Enedis, the major French DSO, expects up to 10 times more distribution-grid-connected wind and solar power by 2050. In particular, the total installed capacity of MV-connected PV plants could increase by up to 15 times. This perspective is raising concerns about the stable operation of future IBR-rich MV distribution grids, especially in light of recent instances of IBR-related instability in transmission grids. Some important questions are thus raised, for instance: could these real-life events also take place in MV distribution grids? More generally, which are the situations that could instigate converter-driven instabilities? What actions can the DSO take to prevent them? This dissertation is a quest for such answers, but because the questions are too broad, we should first delineate our scope, as indicated in Figure 1.17.

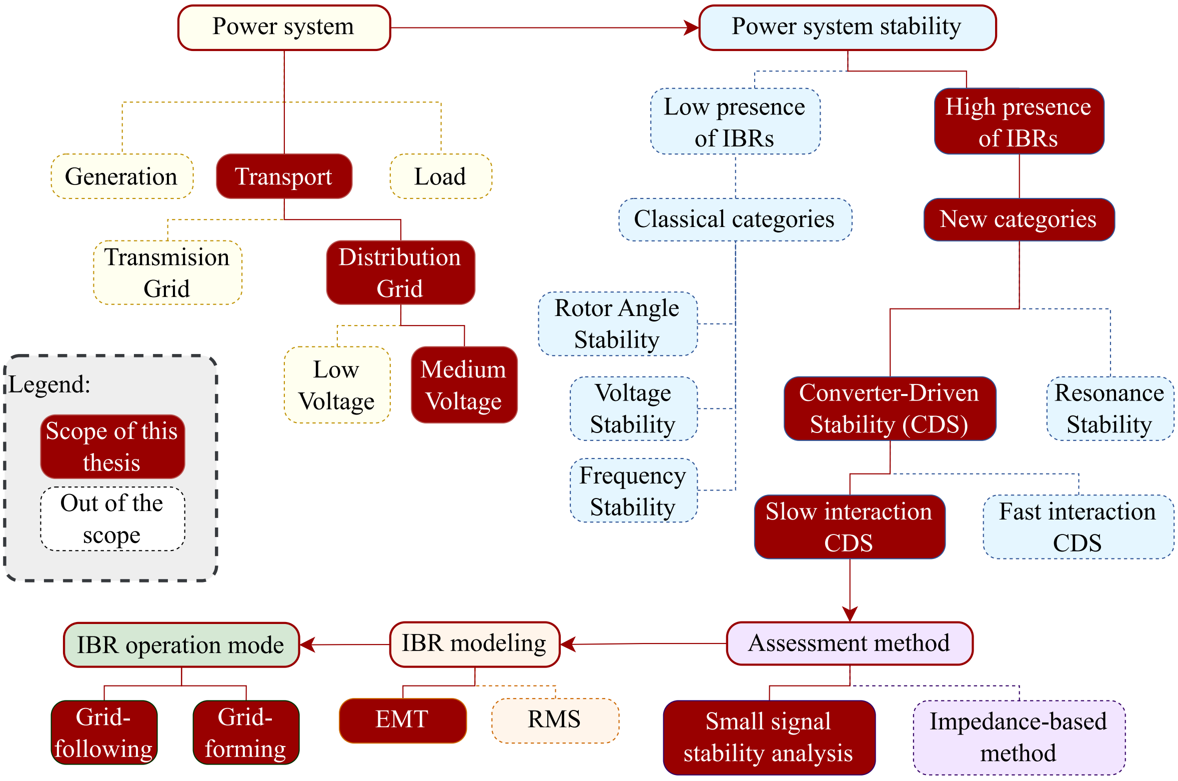

Figure 1.17: The scope of this thesis

We begin by restricting our analysis to MV distribution grids (**MVDG**) with **high penetration of IBRs**. Within the categories of power system stability, we are interested in slow-interaction converter-driven stability (**SICDS**), given their system-wide implications and real-life instances in recent years. In order to assess it, we will apply the method of small-signal stability analysis (**SSSA**) due to the powerful tools associated with it, e.g. participation factors, which can provide insights into the physics behind SICDS issues. SSSA, however, requires accurate modeling of the system, for which we have opted for **EMT models**, given that IBR controls usually act on multiple time scales, demanding such representation. Finally, since IBR controllers are at the root of the matter, it is important to distinguish between their two major operation modes: grid-following (**GFL**) and grid-forming (**GFM**), both of which will be analyzed in detail. This thesis also aims at evaluating the possible role of GFMs in MVDGs, and which actions the DSO could take in order to better integrate them.

Chapter 2

Static Analysis of Inverter-Based Resources

Contents

Before presenting the dynamic modeling and subsequent stability analysis of an MV distribution grid with IBRs, it is useful to examine some static aspects of these systems. This is important either because some static parameters are particularly relevant for stability, such as the short-circuit ratio (SCR), or because they are a distinctive feature of an MV distribution grid (MVDG), such as the R/X ratio. Static analysis is also pertinent for distinguishing the behavior of GFL and GFM inverters, which will be helpful in later chapters. Hence, we start by defining SCR and R/X ratio, evaluating their impact, and determining their ranges in MVDGs, proceeding into a deeper analysis of GFL-related static issues, such as the maintenance of steady-state voltage levels, and V-Q and P-I sensitivities, as well as GFM-related issues, such as P-Q coupling and steady-state virtual impedance.

2.1 Transfer of power between voltage sources

In steady-state, IBRs connected to any power grid may be depicted, in its simplest form, as two voltage sources with an impedance in between. This means the power grid at the point of interconnection (POI) is represented by a *Thévenin* equivalent, as in Figure 2.1.

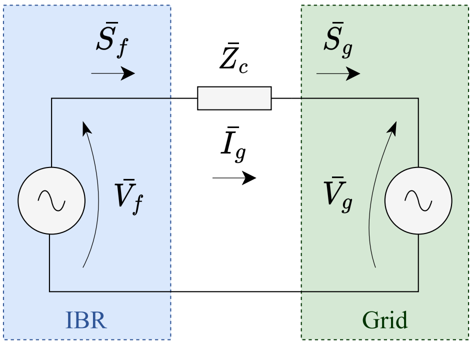

Figure 2.1: Power exchange between voltage sources

Both voltage sources will exchange power according to the following expressions:

$$\begin{aligned}
P_f &= \Re(\overline{S}_f) = \frac{R_c}{R_c^2 + X_c^2}\left(V_f^2 - V_f\,V_g\,\cos\delta_f\right) + \frac{X_c}{R_c^2 + X_c^2}\,V_f\,V_g\,\sin\delta_f \\
Q_f &= \Im(\overline{S}_f) = \frac{X_c}{R_c^2 + X_c^2}\left(V_f^2 - V_f\,V_g\,\cos\delta_f\right) - \frac{R_c}{R_c^2 + X_c^2}\,V_f\,V_g\,\sin\delta_f \\
P_g &= \Re(\overline{S}_g) = \frac{R_c}{R_c^2 + X_c^2}\left(V_g\,V_f\,\cos\delta_f - V_g^2\right) + \frac{X_c}{R_c^2 + X_c^2}\,V_g\,V_f\,\sin\delta_f \\
Q_g &= \Im(\overline{S}_g) = \frac{X_c}{R_c^2 + X_c^2}\left(V_g\,V_f\,\cos\delta_f - V_g^2\right) - \frac{R_c}{R_c^2 + X_c^2}\,V_g\,V_f\,\sin\delta_f
\end{aligned} \tag{2.1}$$

where

$$\overline{V}_f = V_f \,\underline{/\delta_f}, \qquad \overline{V}_g = V_g \,\underline{/0}, \qquad \overline{Z}_c = R_c + j\,X_c, \qquad \overline{I}_g = \frac{\overline{V}_f - \overline{V}_g}{\overline{Z}_c},$$

$$\overline{S}_f = \overline{V}_f\,\overline{I}_g^* = \overline{V}_f\left(\frac{\overline{V}_f^* - \overline{V}_g^*}{\overline{Z}_c^*}\right), \qquad \overline{S}_g = \overline{V}_g\,\overline{I}_g^* = \overline{V}_g\left(\frac{\overline{V}_g^* - \overline{V}_f^*}{\overline{Z}_c^*}\right)$$

In order to compute a *Thévenin* impedance $\overline{Z_c}$ at the POI, it is a common practice to use a metric called *Short-Circuit Ratio* (SCR), which is a standard measurement of the strength of a given node in a power system. According to [1], SCR is a relation between the Short-Circuit Power (SSC) at the POI, usually expressed in MVA, and the rated power of the device (P_n) in MW. For a rated power equal to 1 pu, SCR can be expressed in terms of the per-unit impedance $\overline{Z_c}$, as in (2.2).

$$\overline{\text{SCR}} = \frac{\text{SSC}_{[\text{MVA}]}}{P_{n[\text{MW}]}} = \frac{1}{\overline{Z}_{c[\text{pu}]}} \tag{2.2}$$

A complex representation of SCR corresponds to the admittance seen by a device connected to the POI and is recommended to be written in its polar form, in order to take damping effects into account [86]. In practice, however, SCR is usually considered to be only the absolute value of this admittance, as in (2.3). This is the notation adopted in this dissertation.

$$\text{SCR} = |\overline{\text{SCR}}| = \frac{1}{|Z_c|} = \frac{1}{\sqrt{R_c^2 + X_c^2}} \tag{2.3}$$

For transmission grids, R_c is much lower than X_c, which reduces P_f and Q_f from (2.1) to

$$\begin{aligned} P_f &\approx \frac{V_f\,V_g\,\sin\delta_f}{X_c} \approx \frac{V_f\,V_g}{X_c}\,\delta_f \\ Q_f &\approx \frac{V_f\,(V_f - V_g\,\cos\delta_f)}{X_c} \approx \frac{V_f\,(V_f - V_g)}{X_c} \end{aligned} \tag{2.4}$$

This famous "P-δ" relation may not be true for MVDGs, however, since R_c and X_c are of the same order. It would be convenient, therefore, to express active and reactive powers as a function of the R/X ratio of $\overline{Z_c}$, which we will note as σ_c, computed as:

$$\sigma_c = \frac{R_c}{X_c} \tag{2.5}$$

Substituting (2.3) and (2.5) in (2.1), we rewrite both injected and delivered powers (P_f and P_g, respectively) as a function of SCR and σ_c:

$$\begin{aligned} P_f &= \frac{\text{SCR}}{\sqrt{1+\sigma_c^2}}\Big(\sigma_c\,V_f\,(V_f - V_g\,\cos\delta_f) + V_f\,V_g\,\sin\delta_f\Big) \\ Q_f &= \frac{\text{SCR}}{\sqrt{1+\sigma_c^2}}\Big(V_f\,(V_f - V_g\,\cos\delta_f) - \sigma_c\,V_f\,V_g\,\sin\delta_f\Big) \\ P_g &= \frac{\text{SCR}}{\sqrt{1+\sigma_c^2}}\Big(\sigma_c\,V_g\,(V_f\,\cos\delta_f - V_g) + V_g\,V_f\,\sin\delta_f\Big) \\ Q_g &= \frac{\text{SCR}}{\sqrt{1+\sigma_c^2}}\Big(V_g\,(V_f\,\cos\delta_f - V_g) - \sigma_c\,V_g\,V_f\,\sin\delta_f\Big) \end{aligned} \tag{2.6}$$

There is a number of reasons to justify using the set of equations (2.6) instead of (2.1). Since the R/X ratio σ_c is one of the major differences between medium-voltage distribution and high-voltage transmission networks, it is useful to explicitly assess its impact on the power injected by an IBR. Also, since most CDS issues are reported for weak grids (See Section 1.2.4), it is interesting to rewrite these equations as a function of SCR. Weak grids, or weak POIs, are usually defined as the nodes in a power system for which SCR is below 3. If SCR is even lower, i.e. below 2, the grid is considered to be "very weak" [86].

Of course, quantifying the "strength" of a POI is complicated, especially in grids where IBRs are considerably affecting the dynamics [87]. For large WPPs connected to remote locations via long HV lines, a typical weak-grid scenario, IBRs operated in GFL mode are susceptible to PLL instability, which happens when the phase-locked loop (PLL) fails to synchronize the inverter to the grid frequency. A PLL requires an external voltage to provide a frequency reference, thus the voltage must be relatively stabilized for the PLL to be accurate. This frequency reference is then used by the IBR to inject a current into the grid. In strong grids, the POI voltage is not usually sensitive to the current injected by the IBR. In weak grids, however, this voltage may deviate considerably, which would lead to an unstable closed loop with the PLL. In this case, a good metric for evaluating the "weakness" of the grid is voltage-current sensitivity, e.g. how much the IBR current impacts the POI voltage. This is a complex impedance in the Laplace domain, which can be used for local stability assessment [58]. Nevertheless, real-life instances of PLL instability have also been successfully studied using SCR [42], which suggests that, at least for most contemporary power systems, dominated by SGs, a low SCR is correlated to high V-I sensitivity.

SCR is indeed a legacy metric from a power system largely dominated by synchronous generators (SGs). With more and more IBRs being integrated, the power system is shifting from a high-inertia to a low-inertia dynamic system [20], motivating researchers to evaluate other ways of assessing "weakness". In our case, nonetheless, namely interconnected MV networks, SCR serves the purpose. An IBR connected to the French MV network is still expected to see a strong grid at its POI, unless the feeder is considerably long, exceeding 20 km from the HV/MV substation [88]. As for now, the dynamics of the power grid upstream from an HV/MV substation in continental Europe are still largely dominated by SGs.

2.1.1 Impact of R/X ratio on the power delivered by an IBR

In large transmission networks, $\sigma_c \approx 0$ in (2.1) leads to a nearly linear $P-\delta$ and $Q-V$ relation for strong grids, i.e., small δ_f, as in (2.4). This is convenient for IBRs inasmuch as P and Q can be almost perfectly decoupled, allowing the use of certain droop-based control methods to synchronize the IBR with the grid, such as the "power synchronization loop" (PSL) [36], one of the major GFM control methods.

Figure 2.2 for $\sigma_c = 0.01$ is an illustration of (2.4), and is a familiar image in power system stability studies, usually employed for rotor angle stability analysis [1]. Maximal power transfer happens for $\delta = 90°$, although the angle must be much lower for stability purposes, usually below 30° [69]. Losses are basically negligible.

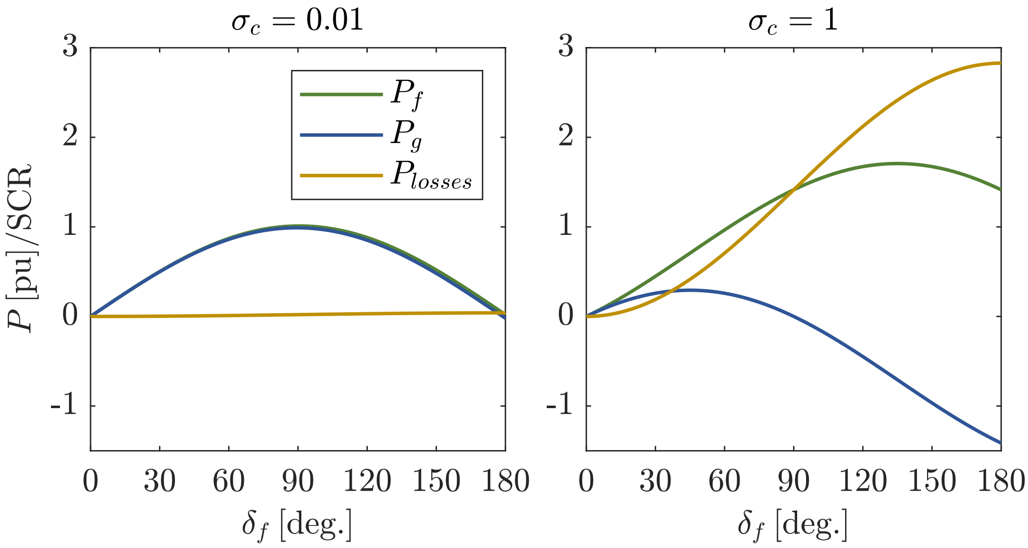

Figure 2.2: Impact of R/X ratio: P as a function of δ

It is interesting to observe, though, how different this $P - \delta$ relation can become if the R/X ratio is equal to one, as seen in Figure 2.2 (for $\sigma_c = 1$), which illustrates (2.6) without approximations. Now, the power delivered when $\delta = 90°$ is almost zero; losses are consuming all the power injected by the IBR.

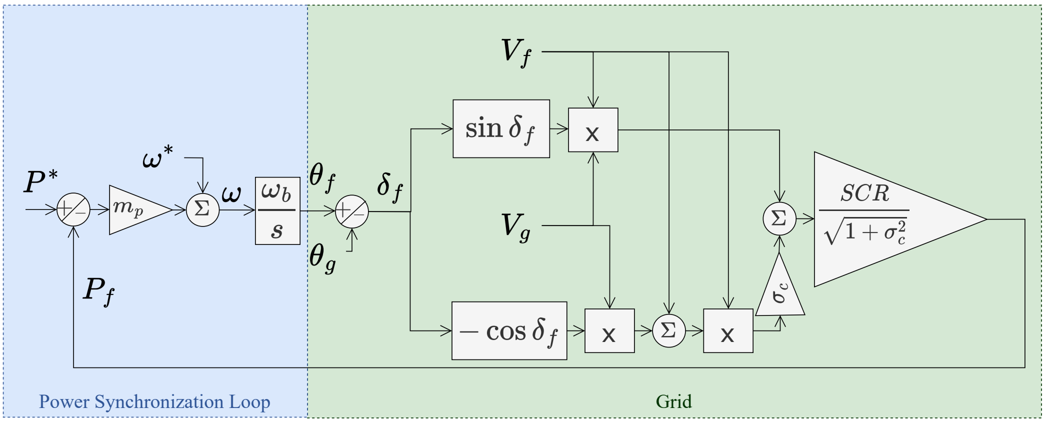

Figure 2.3: Conceptual representation of a Power Synchronization Loop

There are a few implications stemming from the non-linear $P - \delta$ relation under non-negligible R/X ratio. Although a PSL is still possible, P-Q coupling is unavoidable. When applying a PSL, IBR controllers measure the injected power P and compare it with a reference P^*, as indicated in Figure 2.3. The error is then multiplied by a droop factor, providing a frequency ω, which is integrated to provide a phase θ, and thus a phase-angle δ. In other words, PSL regulates δ in order to achieve $P = P^*$, which indirectly leads to synchronization. This is still possible for $\sigma_c \approx 1$, as in MVDGs, since changes in δ still have a major impact on P. However, if the R/X ratio is too high, i.e., $\sigma_c >> 1$, as in low-voltage distribution grids, P would not be sensitive to deviations in δ and this control method would be ineffective.

A deviation in δ, however, also has a major impact on the reactive power Q for $\sigma_c \approx 1$. This means the PSL will allow for synchronization and active power control, but will inevitably lead to an injection of reactive power. This can be counteracted by changing V_f, even if deviations in voltage are usually undesirable. A systematic solution is to virtually modify the R/X ratio using a control-based "virtual impedance" [21], further discussed in Section 2.3.2.

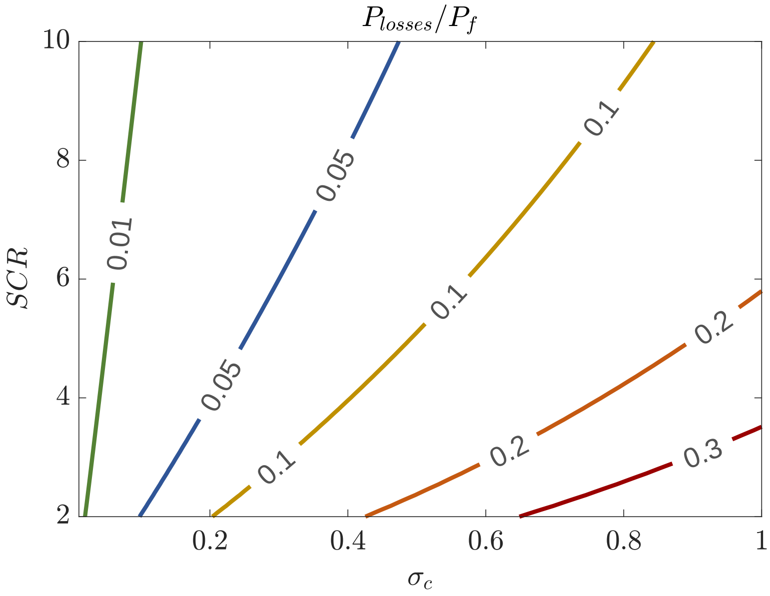

Figure 2.4: Relative power losses as a function of SCR and R/X ratio σ_c

Considering that the IBR is supposed to deliver power to the grid[1], relative losses may be expressed as:

$$\frac{P_{losses}}{P_f} = \frac{P_g - P_f}{P_f} = \frac{\sigma_c \left(V_f^2 + V_g^2 - 2\, V_f\, V_g\, \cos\delta_f\right)}{\sigma_c\, V_f\, (V_f - V_g\, \cos\delta_f) + V_f\, V_g\, \sin\delta_f} \tag{2.7}$$

As can be seen in Figure 2.4, which is a contour plot for (2.7), a combination of low SCR with high R/X ratio ($\sigma_c > 0.5$, for instance) may lead to losses above 20 %. While,

---

[1] This is a hypothesis adopted in this chapter: consumption is supposed to take place in the infinite bus, i.e., the main objective of the IBR is to inject power upstream. Evidently, in practice, load centers could be nearby, but this situation illustrates an interesting scenario for stability studies.

theoretically, a PLL instability could also happen in MVDGs – long-distance MV lines can lead to low SCR (see example in next subsection) – it is worth mentioning that these lines, unlike their HV counterparts, would be generating considerable losses in normal operation. The use of extremely long MV lines to connect IBRs is unlikely to be an economically viable solution. This is why we restrict our analysis to feeder lengths of at most 20 km, which could happen in scenarios involving PV plants in rural areas [89], for instance.

Nonetheless, as it is a common practice to consider "extreme" cases in stability studies, remote PV plants with a capacity of around 10 MW could provide such scenarios in an MVDG. It will be necessary, however, in such instances, to consider power losses of up to 20% as being "acceptable" from the point of view of the producer.

2.1.2 Key figures for SCR and R/X ratio in a MV distribution grid

In France, short-circuit power (SSC) at the outpost of HV/MV substations is of the order of a few hundred MVA [5][2]. Most equipment installed in MV is designed to handle a short-circuit current of 12.5 kA [88], which, for a voltage equal to 20 kV, leads to SSC = 443 MVA; for long MV feeders, i.e., distances reaching 20 km, SSC at the POI is as low as 30 MVA, regardless of cable/line material, HV/MV transformer rating or short-circuit power upstream from the substation [88]. For a 10-MW-rated IBR, this means SCR = 3.

Parameter	Description	Value
SSC_{up}	Short-circuit power upstream from substation	[100 - 500] MVA
σ_{up}	R/X ratio upstream from substation	0.01
d	MV Distribution feeder length	[0 - 20] km
X_l	MV line reactance	0.37 Ω/km (Overhead Line) 0.72 Ω/km (Underground Cable)
σ_{line}	R/X ratio for MV line	1.4 (Overhead Line) 0.7 (Underground Cable)
S_t	MV/LV transformer rating	10 MVA
x_t	MV/LV transformer leakage reactance	5 %

Table 2.1: Typical parameter values for MV distribution grid [5], [90], [91]

An IBR connected to the MVDG sees an impedance comprised of three components: the impedance of the power grid upstream from the substation, including an HV/MV transformer, which can be obtained from the SSC using (2.2), an MV/LV transformer, and an MV distribution line between substation and POI. For aluminum-based MV lines and cables, reactance is close to 0.37 and 0.72 Ω/km, respectively [90]; the R/X ratio may vary but is usually close to

---

[2] Cigre TF C6.04.02 recommends 100-1000 MVA for MV studies, hence the same order of magnitude [90].

one [91][3]. Taking all of this into account, some key values have been adopted in this chapter, as presented in Table 2.1.

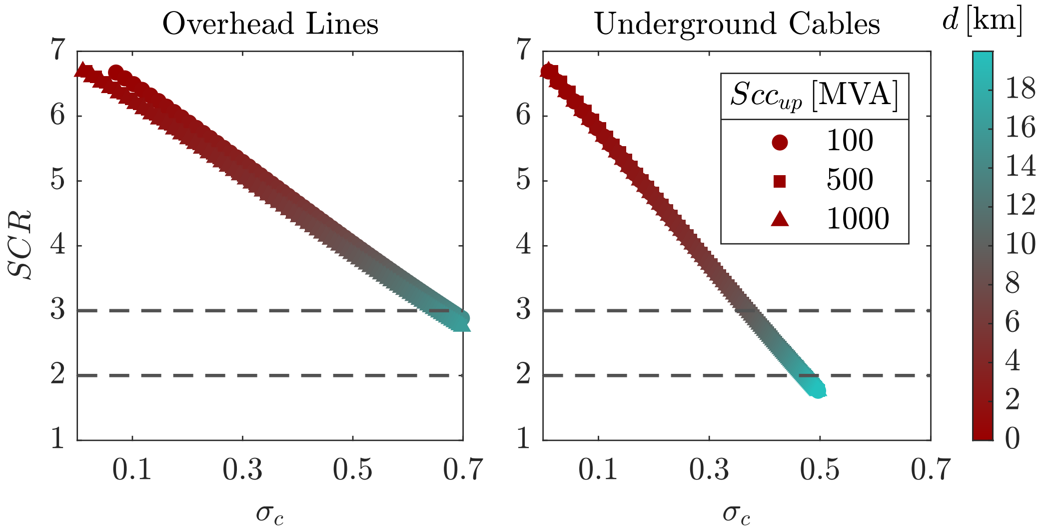

Figure 2.5: SCR and σ_c for different MV feeder lengths. Each curve is obtained by sweeping the feeder length d from 0 to 20 km.

Figure 2.5 illustrates SCR and σ_c for different MV feeder lengths, going from a distance between substation and POI of 0 up to 30 km. As the distance increases, SCR goes down and σ_c goes up, hence the POI sees a weaker grid with an elevated R/X ratio. The minimum SCR for overhead lines is just below 3, as expected [88], and below 2 (very weak grid) for underground cables, while the maximum is equal to 0.75, approximately. It is also visible that high values of upstream short-circuit power SSC_{up} do not prevent a weak grid situation if the feeder length is very long ($d > 20$ km).

Some authors consider IBRs as PQ buses in load-flow analysis, regardless of their operation mode. However, if Q-V droop control in GFMs is neglected, as it often is [70], they are actually capable of imposing a steady-state voltage at the POI, which could offer significant advantages in maintaining an adequate voltage profile in an MVDG. In order to provide a comparison, therefore, we will consider GFLs as PQ buses and GFMs as PV buses throughout this chapter.

2.2 Grid-following inverters

Two major static issues concern GFL inverters, namely their difficulty in maintaining adequate steady-state voltages under stringent conditions, which could be solved using GFMs, and their

---

[3] Cigre TF C6.04.02 recommends 0.4-2 [90], without the LV/MV transformer, which, with a reactance of about 5 %, and negligible losses, decreases the R/X ratio considerably.

synchronization instability when facing power transfer limitations (weak grids), which is an inherent limitation faced by GFMs as well. Both are described in detail in the subsections below, where the latter is analyzed through two sensitivities: V-Q and P-I.

2.2.1 Voltage levels

In France, medium-voltage distribution networks are mostly operated at 20 kV[4]. This choice relies on historical, technical, and economic factors, notably to maximize continuity of supply and minimize losses; in a sense, higher voltages would be difficult to operate in urban areas, while lower voltages would not be enough for rural regions [88]. Producers connected to the MV grid must keep voltages under a 5 % range around the contractual voltage, which should itself be within 5 % of the nominal voltage [92] [93]. Hence, in most cases, MV producers must keep voltages under 5 to 10 % of the nominal value of 20 kV.

Commonly employed methods for voltage regulation include capacitor banks and OLTC, in the HV/MV substation, and reactive power regulation from DGs at a local level [5]. The amount of reactive power to inject depends on a contractual agreement between DSO and producer; it could either be a fixed rate, proportional to the active power, in a method called "tan(ϕ)", or a closed-loop deadband control called $Q(U)$[5]. For the latter, an IBR connected to the MV grid is expected to inject up to 0.4 pu of reactive power to deal with under-voltage events and absorb up to 0.5 pu in case of overvoltages [6].

POI voltage, in per-unit amplitude V_f and phase δ_f, can be obtained using (2.6), with $V_g = 1\,\text{pu}$, for different combinations of SCR and σ_c. This is done numerically by solving load-flow equations. In Figure 2.6, the GFL is set to inject $P_f^* = 1\,\text{pu}$ and $Q_f^* = 0$. It is clear that, for weak grids (low SCR), a small R/X ratio leads to undervoltage, with $V_f < 0.95$, while a high R/X ratio leads to overvoltage. A combination of SCR ≈ 3 and $\sigma_c \approx 0.7$, possible for MV networks (Figure 2.5), gives rise to severe overvoltages, beyond $V_f = 1.1\,\text{pu}$.

A logical solution, in this case, is to control the GFL to absorb reactive power, which, as we see in Figure 2.7, brings those voltages back to approximately $V_f = 1\,\text{pu}$. More extreme situations, where $\sigma_c \approx 1$, may lead to $V_f > 1.05\,\text{pu}$ even when the IBR is absorbing $Q_f = 0.5\,\text{pu}$. This is highly unlikely, however; in most cases, GFLs with a volt-var control must be able to handle long-term overvoltages, although these will not be enough to solve short-term issues. From a static point-of-view, GFMs offer the advantage of keeping voltages tightly under control, even in weak grids with high R/X ratios.

---

[4] Voltage regulation in the French distribution grid was already discussed at the end of Section 1.1.1, this is a short recapitulation.

[5] $Q(U)$ is a form of Volt-Var control, as they are usually called in the literature. These are slow-acting controllers, in the order of tens of seconds [6].

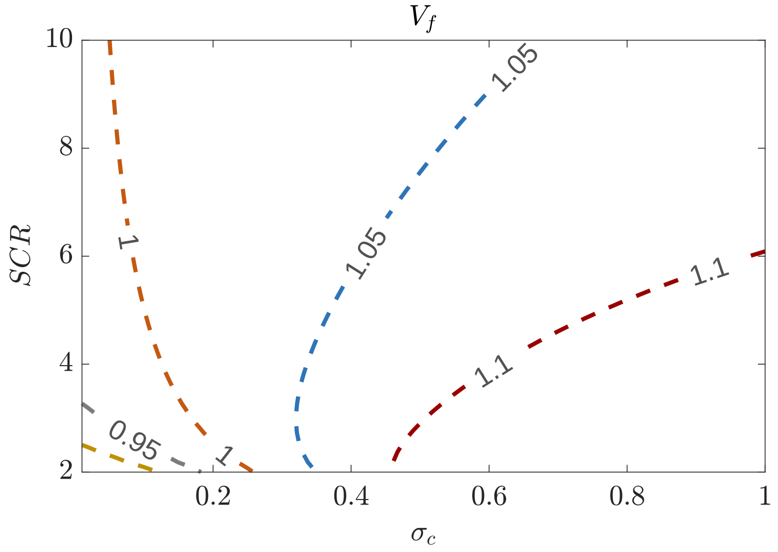

Figure 2.6: POI Voltage V_f as a function of SCR and σ_c, with $Q_f^* = 0$

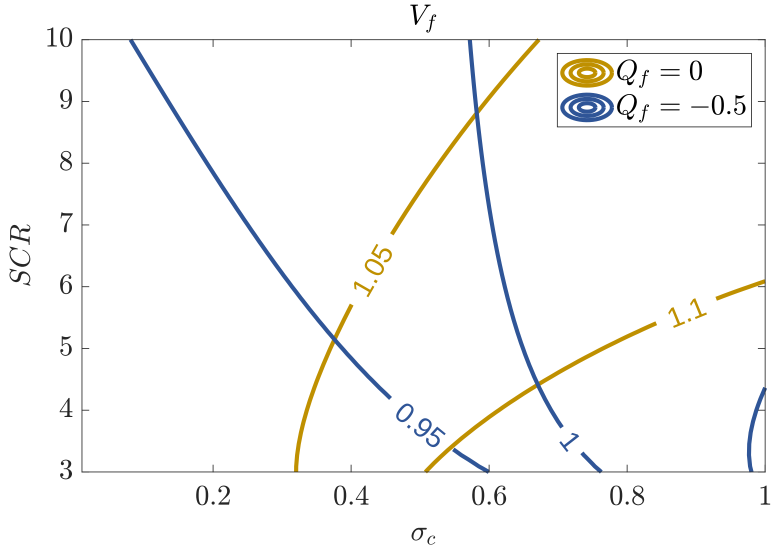

Figure 2.7: V_f as a function of SCR and σ_c, with $Q_f^* = \{-0.5, 0\}$ pu

2.2.2 V-Q sensitivity

Whenever two voltage sources are connected through an impedance, there is a maximum amount of power that can be exchanged between them. Because GFLs are PQ buses in steady-state, they may experience the same problem as constant-power loads trying to withdraw more power than the maximum deliverable[6]. This problem, which is a typical form of voltage instability [1], can also be expressed in terms of reactive power. An increase in injected reactive power is supposed to be accompanied by an increase in voltage; if not, the power system will experience instability. Hence, it would be interesting to assess the V-Q sensitivity of a GFL connected to the grid, making sure this sensitivity is positive, so as to assure stable operation. This sensitivity can be obtained by linearizing (2.6):

$$\begin{aligned} \Delta P_f &= J_{p\,\delta}\,\Delta\,\delta_f + J_{p\,v}\,\Delta\,V_f \\ \Delta\,Q_f &= J_{q\,\delta}\,\Delta\,\delta_f + J_{q\,v}\,\Delta\,V_f \end{aligned} \tag{2.8}$$

and computing J_r [1]:

$$J_r = J_{q\,v} - J_{q\,\delta}\,{J_{p\,\delta}}^{-1}\,J_{p\,v} \tag{2.9}$$

where

$$J_{p\,\delta} = \frac{\partial P_f}{\partial \delta_f}, \qquad J_{p\,v} = \frac{\partial P_f}{\partial V_f} \qquad J_{q\,\delta} = \frac{\partial Q_f}{\partial \delta_f} \qquad J_{q\,v} = \frac{\partial Q_f}{\partial V_f} \tag{2.10}$$

Obtaining J_r – the reduced jacobian – we can assess V-Q sensitivity through its inverse matrix J_r^{-1}. However, for a simple system such as Figure 2.1, J_r is a scalar and $J_r > 0$ serves as a stability criterion.

As seen in Figure 2.8, for $Q_f^* = 0$, J_r approaches the stability limit $J_r = 0$ for very weak grids (SCR = 2) under low R/X ratio. Figure 2.9 illustrates how this situation may deteriorate for $Q_f^* = -0.5\,\text{pu}$, where low R/X ratios are already approaching instability for SCR = 3; in fact, lower values of SCR lead to load-flow convergence issues, thus an equilibrium cannot be computed. Nevertheless, weak grids with low R/X ratios are not likely to be the case for MVDGs. Power transfer limitations may also be assessed as the sensitivity between active power and injected current, a more pertinent representation for GFLs, as explained in the next subsection.

2.2.3 P-I sensitivity

To begin, we may represent the phasor diagram from Figure 1.14 using (2.11), with $\overline{I_g} = \overline{I_f}$:

---

[6] In fact, certain loads, such as an EV charging station, could also be considered grid-following converters, representing the exact same voltage stability problem introduced in [1].

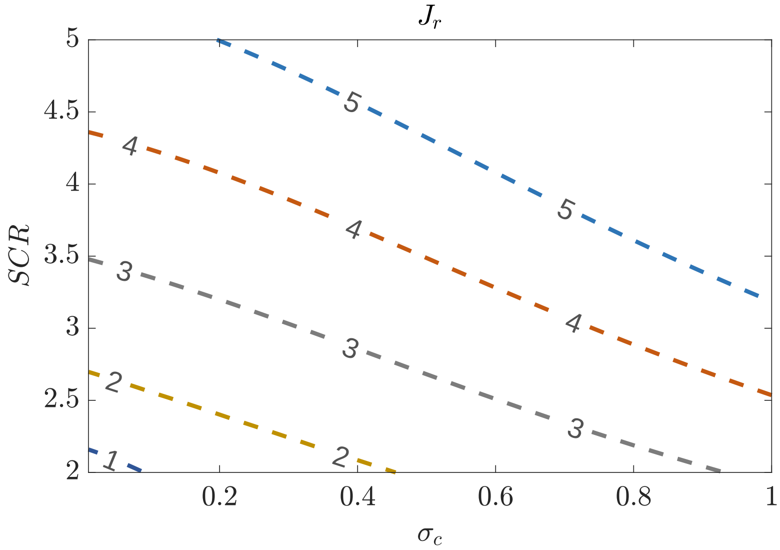

Figure 2.8: Reduced jacobian J_r as a function of SCR and σ_c, with $Q_f^* = 0$

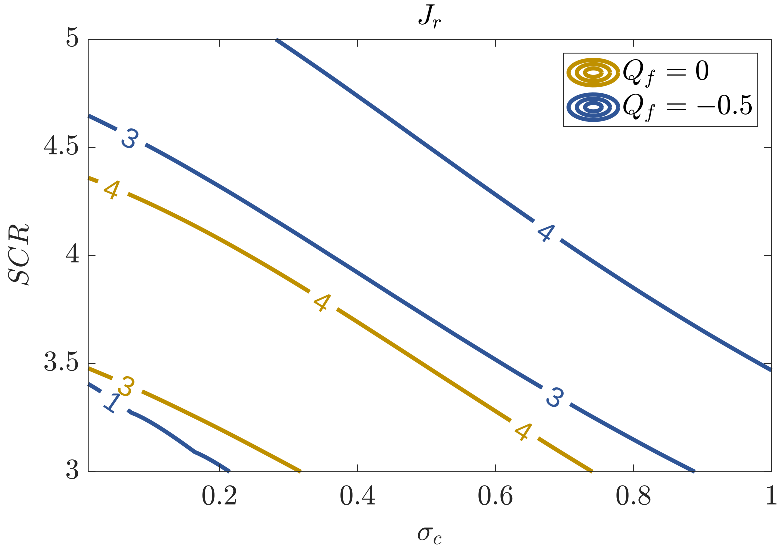

Figure 2.9: J_r as a function of SCR and σ_c, with $Q_f^* = -0.5\,\text{pu}$

$$\overline{V_f} = \overline{V_g} + \overline{Z_c}\,\overline{I_f}, \qquad \overline{I_f} = I_f \underline{/\delta_i} \tag{2.11}$$

Since GFLs use $\overline{V_f}$ as a reference for synchronization, we may rewrite (2.11) as (2.12), rotating the phasor diagram by δ_f clock-wise (negative rotation):

$$V_f = \overline{V_g}\, e^{-j\,\delta_f} + (R_c + j\,X_c)\,(I_d + j\,I_q) \tag{2.12}$$

where

$$I_d + j\,I_q = \overline{I_f}\, e^{-j\,\delta_f} = I_f \underline{/\delta_i - \delta_f} \tag{2.13}$$

In this way, the inverter can inject direct-axis, also called "active", current I_d, and quadrature-axis, "reactive", current I_q, independently. Active power P_f is computed as:

$$P_f = \Re(\overline{V_f}\,\overline{I_f}^*) = \Re(V_f\,(I_f\,e^{-j\,\delta_f})^*) = V_f\,\Re((I_d + j\,I_q)^*) = V_f\,I_d \tag{2.14}$$

A GFL inverter has to inject $P_f = P_f^*$ according to setpoint P_f^* defined by the producer. If $P_f^* > P_f$, the inverter should increase its power output in order to match the setpoint, which means an increase in direct-axis current I_d. According to (2.14), if V_f is kept somewhat constant, which is the case for strong grids, an increase in I_d will lead to an increase in P_f. If this increase in active current induces a drop in V_f, however, power injection may actually decline, resulting in instability. This situation may arise for weak grids [42], [51], [70].

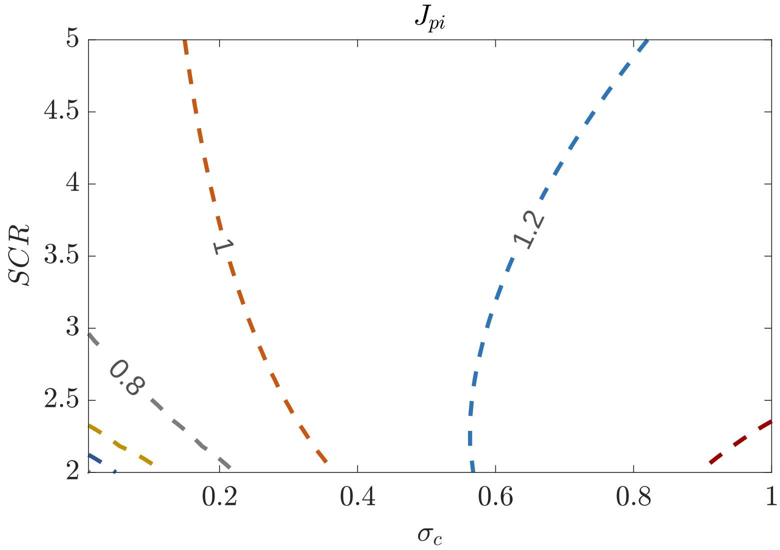

Figure 2.10: P-I sensitivity J_{pi} as a function of SCR and σ_c, with $Q_f^* = 0$

To understand this instability, we may proceed by rewriting (2.12):

$$\begin{aligned} V_f &= V_g \cos\delta_f + R_c\, I_d - X_c\, I_q \\ 0 &= -V_g \sin\delta_f + X_c\, I_d + R_c\, I_q \end{aligned} \tag{2.15}$$

which, for $I_q = 0$, i.e. no injection of reactive power, yields:

$$V_f = R_c\, I_d + \sqrt{V_g^2 - X_c^2\, I_d^2} \tag{2.16}$$

and, applying (2.16) in (2.14), we obtain:

$$P_f = R_c\, {I_d}^2 + I_d \sqrt{V_g^2 - X_c^2\, I_d^2} \tag{2.17}$$

From (2.17), P_f is a function of I_d. A stable operation requires a positive P-I sensitivity; an increase in I_d should be followed by an increase in P_f. This can be assessed by taking the partial derivative of P_f with respect to I_d, hereby named J_{pi}, in which we apply the notions of SCR and σ_c from (2.3) and (2.5):

$$J_{pi} = \frac{\partial P_f}{\partial I_d} = \frac{2\,\sigma_c\, I_d}{SCR\,\sqrt{1+\sigma_c^2}} + \frac{V_g^2 - 2\left(\frac{I_d}{SCR\,\sqrt{1+\sigma_c^2}}\right)^2}{\sqrt{V_g^2 - \left(\frac{I_d}{SCR\,\sqrt{1+\sigma_c^2}}\right)^2}} \tag{2.18}$$

Once again, it would be interesting to assess J_{pi} as a function of SCR and σ_c from a graphical point of view, using a contour plot. For $P_f^* = 1\,\text{pu}$ and $Q_f^* = 0$, one can obtain I_d via load-flow and apply it to (2.18), which results in the plot from Figure 2.10.

As for the Q-V sensitivity J_r (Figure 2.8), P-I sensitivity J_{pi} is also positive for all scenarios with SCR > 2, although it approaches zero when both SCR and R/X ratio are very low. For extreme cases, nonetheless, as can be seen in Figure 2.11, J_{pi} may become negative. This happens for SCR < 2 and $\sigma_c = 0.1$, for instance. As before, this situation does not correspond to most MVDGs[7].

---

[7] In a sense, both V-Q and P-I sensitivities are related to power transfer limitations, which are associated with inductive networks. It is interesting to observe that PLL instability, from this point of view, because of the underlying issue of power transfer limitations, can also be a form of voltage instability. There is indeed a significant overlap between power system stability categories.

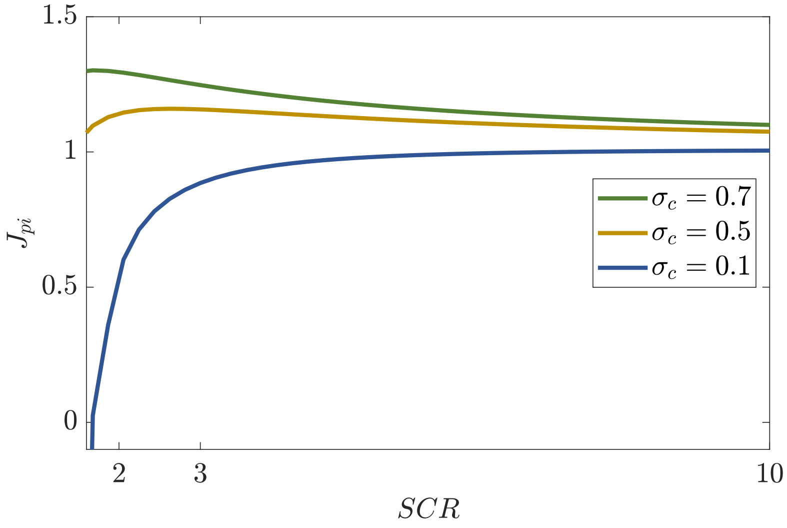

Figure 2.11: P-I sensitivity J_{pi} as a function of SCR, for various σ_c

2.2.4 A short remark on PLL instability under weak grids

The mechanism by which these power transfer limitations lead to instability is usually a synchronization issue [30]. GFLs are equipped with PLLs, which fail to synchronize in weak grids. When V-Q or P-I sensitivities are negative, this issue is just a reflection of the impossibility of injecting the reference power, but it is worth keeping in mind that PLL stability is still a *dynamic* issue. A badly-tuned PLL may lead to instability in weak grids with a higher R/X ratio as well, even if there is not necessarily a power transfer limitation, as shown in Figure 2.12. Here, the grid configuration is one that could take place in an MVDG, but a fast PLL still leads to instability. More details on PLL modeling and PLL instability will be given in future chapters[8].

2.3 Grid-forming inverters

Besides the power transfer limitations leading to synchronization instability [30], already described in the context of GFLs, grid-forming inverters may present an inadequate P-Q decoupling in steady-state due to the close-to-one R/X ratio of MVDGs, as was pointed out in Section 2.1. This is a particularity of GFMs, given that the current-source nature of GFLs allows them to inject I_d and I_q independently, hence perfectly decoupling active and reactive power injection. This issue is discussed in detail in the subsection below, followed by a tech-

---

[8] For more details on PLL tuning, please refer to Section A.1.3 in Appendix A.1

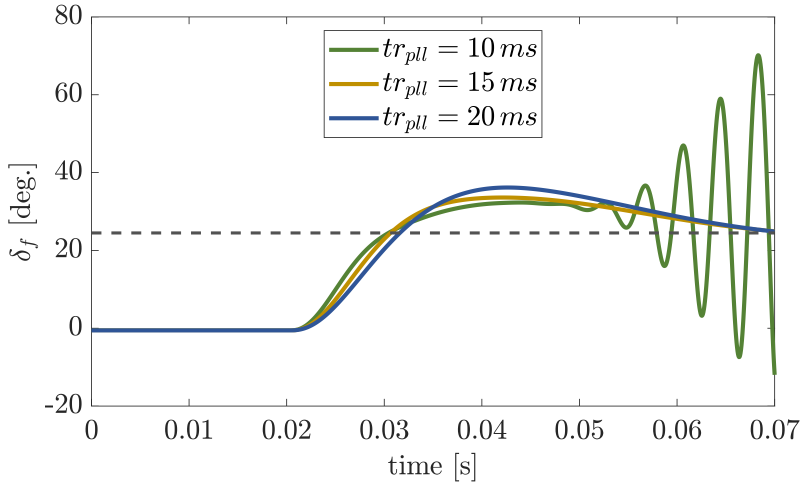

Figure 2.12: Time-domain simulation for a GFL connected to a grid with $SCR = 2$ and $\sigma_c = 0.7$. This is a step response for P^*, which goes from 0 to 1 in $t = 0.02\,s$.

nique to handle it, namely a steady-state virtual impedance (SSVI), for which we introduce a tuning criterion. By the end of this section, there remains a debate as to whether P-Q decoupling is even necessary, given the ability of GFMs to impose the voltage levels at their POIs. Steady-state P-Q coupling is a problem *only if* GFMs are employed as PQ buses, for which, in most cases, GFLs would have been a better choice.

2.3.1 P-Q coupling

GFMs are supposed to provide active power control while behaving as voltage sources [69]. Thus, in steady-state, both P_f and V_f in (2.6) are fixed by the IBR controller, usually at 1 pu; both Q_f and δ_f are to be determined by the static conditions of the system. GFMs do not comply with specific reactive power requirements unless the voltage V_f can be taken to values other than nominal, which is not normally the purpose. If voltage levels are already guaranteed through controllers, the role of reactive power control, which is mainly employed in voltage support, is unclear. In any case, assuming the DSO may require Q support from GFM inverters for other reasons, it is still interesting to investigate how much steady-state P-Q coupling may occur in MVDGs. For this, we adopt the following metric, taking Q_f and P_f from (2.6):

$$\frac{Q_f}{P_f} = \frac{V_f\,(V_f - V_g\,\cos\delta_f) - \sigma_c\,V_f\,V_g\,\sin\delta_f}{\sigma_c\,V_f\,(V_f - V_g\,\cos\delta_f) + V_f\,V_g\,\sin\delta_f} \tag{2.19}$$

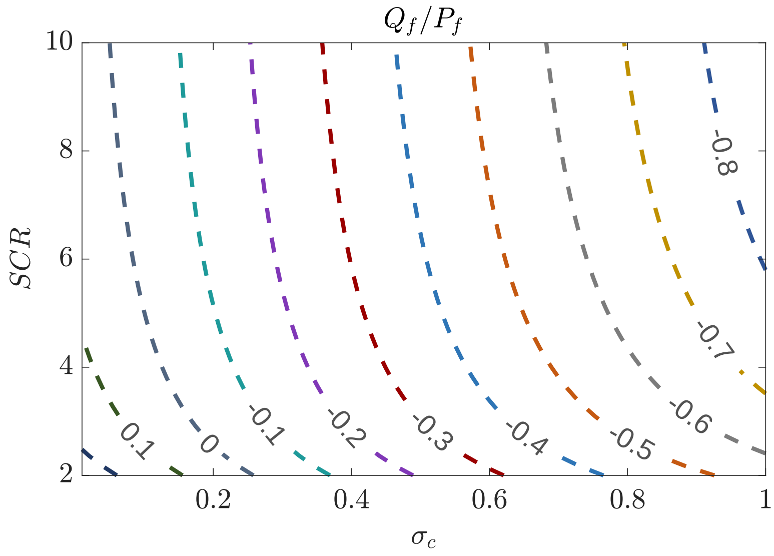

Figure 2.13: Steady-state P-Q coupling Q_f/P_f as a function of SCR and σ_c

From (2.19), since δ_f depends on static conditions (SCR and σ_c), P-Q coupling is a function of both metrics. This relation can be visualized in Figure 2.13, where this coupling is mostly influenced by the R/X ratio σ_c. For $P_f = 1\,\text{pu}$ and $V_f = 1\,\text{pu}$, the reactive power injection can reach $Q_f = -0.4\,\text{pu}$ for a weak grid with $\sigma_c = 0.7$. A stronger grid would increase the coupling from 0.4 to 0.6 pu, in this case. P-Q coupling increases with both SCR and σ_c.

An intuitive way to solve this issue is to decrease the R/X ratio to acceptable values. For example, if $SCR = 3$, a R/X ratio of $\sigma_c \approx 0.2$ would basically eliminate P-Q coupling. This can be done by inserting an inductive device in series to the IBR, which is costly. A better solution is to alter the R/X ratio virtually, by changing the impedance seen by the GFM controllers. This will essentially give the same result as a Q-V droop, which means the voltage V_f would not be equal to 1 pu anymore. A trade-off between V_f and Q_f is, of course, a physical constraint of this system. Nevertheless, if V_f is kept under acceptable limits, using a Virtual Impedance (VI)[9] may grant the advantage of improving P-δ coupling as well. This allows us to employ the same control methods used in transmission-level GFMs, such as PSC, which requires a good P-δ coupling.

---

[9] The expressions “steady-state virtual impedance” (SSVI) and “virtual impedance (VI)” are used interchangeably in this dissertation, with SSVI mostly designating the method and VI referring to the impedance itself. It is important to distinguish them from Transient Virtual Impedance (TVI) [70], however, which is a current-limitation technique, used for different purposes.

2.3.2 Steady-state virtual impedance

Adding a Virtual Impedance (VI) to the GFM from Figure 1.16 gives the diagram from Figure 2.14, where $\overline{Z_v}$ is the VI itself, while $\overline{V_v}$ and $\overline{S_v}$ are virtual variables for voltage and power, respectively.

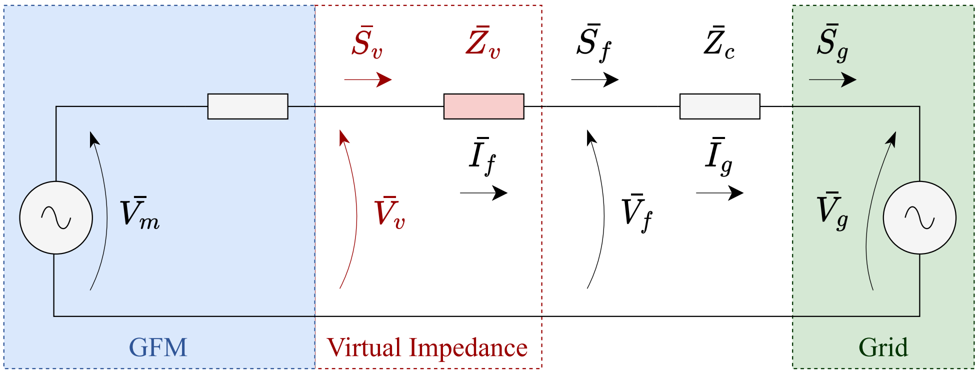

Figure 2.14: GFM inverter diagram, including a virtual impedance $\overline{Z_v}$

$\overline{Z_v}$ may be written in terms of its resistive and reactive components:

$$\overline{Z_v} = R_v + j\,X_v \tag{2.20}$$

Obtaining the total impedance $\overline{Z_t}$ seen by the IBR controllers:

$$\overline{Z_t} = \overline{Z_v} + \overline{Z_c} = R_t + j\,X_t = (R_v + R_c) + j\,(X_v + X_c) \tag{2.21}$$

From $\overline{Z_t}$, using (2.5) and (2.3), yields both the *perceived* R/X *ratio* σ_t:

$$\sigma_t = \frac{R_t}{X_t} = \frac{\sigma_c + \frac{R_v}{X_c}}{1 + \frac{X_v}{X_c}} \tag{2.22}$$

and the *perceived short-circuit ratio* SCRt:

$$\mathrm{SCR}_t = \frac{1}{|\overline{Z_t}|} = \frac{1}{\sqrt{\frac{1}{\mathrm{SCR}^2} + R_v^2 + X_v^2 + 2\,X_c\,(\sigma_c\,R_v + X_v)}} \tag{2.23}$$

$\overline{V_v}$ may be written in terms of amplitude V_v and phase-angle δ_v. GFM controllers will ensure a voltage-source behavior by controlling V_v, while δ_v is obtained via PSC. In fact, power synchronization control relies on a strong P-δ coupling. While P_f and δ_f may not be perfectly coupled, given that the R/X ratio σ_c in MVDGs can be close to one, a VI can artificially decrease the perceived R/X ratio σ_t, providing a better coupling between P_f and, in this case, δ_v.

Adding a VI leads to a virtual power $\overline{S_v}$, which can be written in terms of P_v and Q_v:

$$\begin{aligned} P_v &= \frac{\mathrm{SCR}_t}{\sqrt{1+\sigma_t^2}}\left(\sigma_t\, V_v\,(V_v - V_g\,\cos\delta_v) + V_v\,V_g\,\sin\delta_v\right) \\ Q_v &= \frac{\mathrm{SCR}_t}{\sqrt{1+\sigma_t^2}}\left(V_v\,(V_v - V_g\,\cos\delta_v) - \sigma_t\,V_v\,V_g\,\sin\delta_v\right) \end{aligned} \tag{2.24}$$

In practice, the GFM will inject $\overline{S_f}$ at its POI, previously defined in (2.6). Rewriting it as a function of virtual parameters R_v and X_v, as well as virtual metrics σ_t and SCRt, yields:

$$\begin{aligned} P_f &= \frac{\mathrm{SCR}_t}{\sqrt{1+\sigma_t^2}}\left(\sigma_t V_v\,(V_v - V_g\cos\delta_v) + V_v V_g \sin\delta_v - \frac{R_v}{X_t}\left(V_v^2 + V_g^2 - 2V_v V_g\cos\delta_v\right)\right) \\ Q_f &= \frac{\mathrm{SCR}_t}{\sqrt{1+\sigma_t^2}}\left(V_v\,(V_v - V_g\cos\delta_v) - \sigma_t V_v V_g \sin\delta_v - \frac{X_v}{X_t}\left(V_v^2 + V_g^2 - 2V_v V_g\cos\delta_v\right)\right) \end{aligned} \tag{2.25}$$

Since our goal is to decrease the actual R/X ratio σ_c to a lower perceived R/X ratio σ_t, only a virtual reactance X_v is required. Hence, we adopt $R_v = 0$ throughout this chapter. Taking $V_v = V_g = 1\,\mathrm{pu}$, and $\delta_v = \pi - \arctan\left(\frac{1}{\sigma_t}\right)$ in (2.25), the maximum active power that a GFM with VI can inject into the POI is expressed in (2.26). This is a useful stability metric. If a GFM is set to inject $P_f = 1\,\mathrm{pu}$, and σ_t is chosen to ensure a certain level of P-Q coupling, (2.26) can give us the minimum SCRt required to inject P_f. If a VI is not tuned properly, $P_{f_{max}}$ may be lower than 1 pu, which will lead to an unstable synchronization loop.

$$P_{f_{max}} = \mathrm{SCR}_t\left(1 + \frac{\sigma_t}{\sqrt{1+\sigma_t^2}}\right) \tag{2.26}$$

From (2.25), a new formula for P-Q coupling is given in (2.27).

$$\frac{Q_f}{P_f} = \frac{V_v\,(V_v - V_g\cos\delta_v) - \sigma_t V_v V_g \sin\delta_v - \frac{X_v}{X_t}\left(V_v^2 + V_g^2 - 2V_v V_g\cos\delta_v\right)}{\sigma_t V_v\,(V_v - V_g\cos\delta_v) + V_v V_g \sin\delta_v - \frac{R_v}{X_t}\left(V_v^2 + V_g^2 - 2V_v V_g\cos\delta_v\right)} \tag{2.27}$$

Once again, one may plot the P-Q coupling as a function of static conditions (SCR and σ_c), as was done in Section 2.3.1. However, since a VI can reduce this coupling, it is more

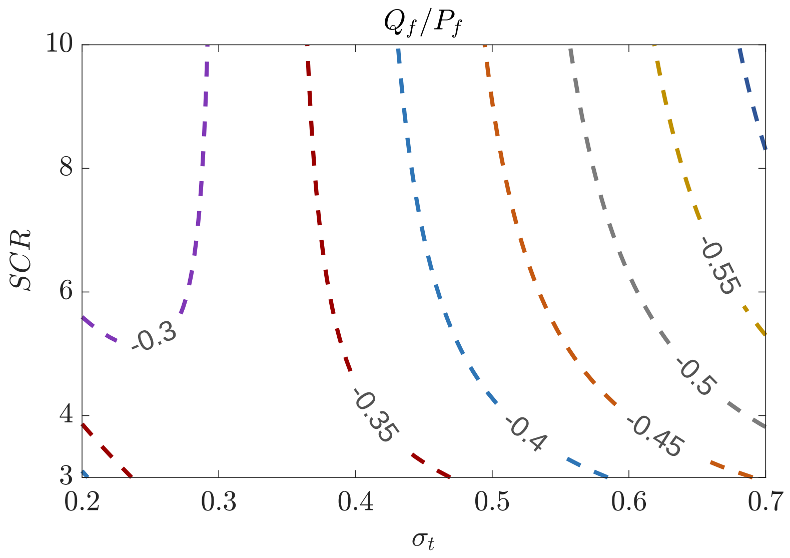

Figure 2.15: P-Q coupling as a function of σ_t, with original R/X ratio $\sigma_c = 0.7$

interesting to plot it as a function of σ_t, as shown in Figure 2.27. Here, the original R/X ratio is kept constant at $\sigma_c = 0.7$.

Comparing Figure 2.15 to 2.13, we can see that a grid with SCR $= 8$ and $\sigma_c = 0.7$, which previously injected almost $Q_f = -0.6\,\text{pu}$ for $P_f = 1\,\text{pu}$, may now inject less than $Q_f = -0.3\,\text{pu}$, depending on the choice of σ_t. If the perceived R/X ratio is chosen as $\sigma_t = 0.3$, injected reactive power goes from $Q_f = -0.6$ to $Q_f = -0.3\,\text{pu}$, inducing 50 % less P-Q coupling. For weaker grids, this improvement is less remarkable but still close to 20 %.

2.3.2.1 Tuning

Figure 2.15 may serve to define a target R/X ratio σ_t, which, given $R_v = 0$, can provide a virtual reactance X_v via (2.22). This can be a tuning criterion for adopting a VI that leads to optimal P-Q coupling, although there are two side effects to keep in mind. First of all, one must assure that V_f, which is not held at $V_f = 1\,\text{pu}$ anymore, is still under a proper range. This can be checked in Figure 2.16, where we observe that POI voltage V_f, for our study case with $\sigma_c = 0.7$, is always below 1.05 pu, for any σ_t between 0.2 and 0.7.

A more relevant side-effect is the perceived short-circuit ratio SCR$_t$, defined in (2.23). When adding a VI between the IBR and the grid, GFM control loops will perceive a weaker POI. This may lead to an unstable synchronization loop, as the maximum active power $P_{f_{max}}$ dangerously approaches 1 pu. As mentioned previously, a PSC-type control achieves synchronization when the injected power P_f is equal to its setpoint. A virtually weakened POI will

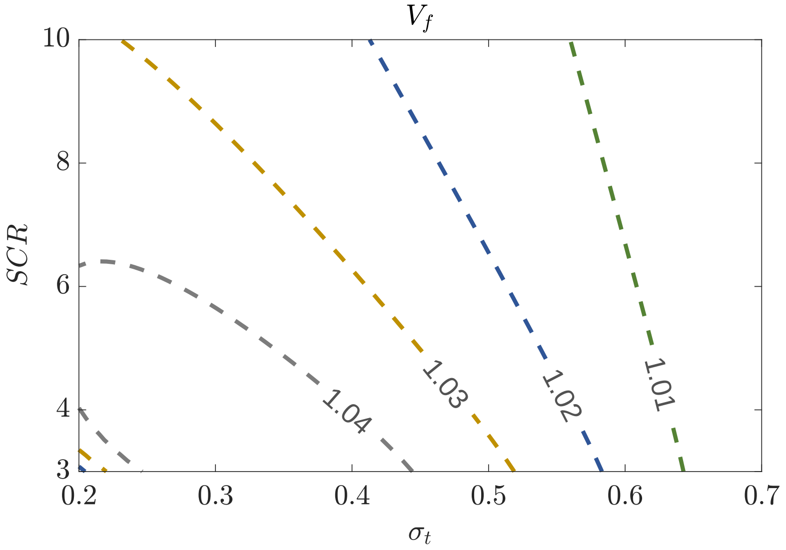

Figure 2.16: V_f as a function of σ_t, with original R/X ratio $\sigma_c = 0.7$

lead to high values of δ_v for $P_f = 1$ pu; as this weakness approaches SCRt = 2, δ_v may surpass 30°, which is usually unacceptable in power systems. In Figure 2.17, going from $\sigma_c = 0.7$ to $\sigma_t = 0.3$ in a grid with SCR = 3, for instance, would lead to a perceived short-circuit ratio considerably below SCRt = 2, which is undesirable from the point-of-view of stability.

Taking the aforementioned factors into account, namely the P-Q coupling (Figure 2.15), POI voltage V_f (2.16), and perceived short-circuit ratio SCRt (2.17), we propose a tuning method summarized in Figure 2.18. Superposing the three previous plots, it is possible to assess, for a range of situations (SCR and σ_c), which R/X ratio target σ_t would lead to a maximum reduction in P-Q coupling, while still keeping V_f below a given value – here taken as 1.04 pu, to keep a safety margin below the 5% defined by the DSO – and perceived SCR above SCRt = 2 or, for stronger grids, SCRt = 3.

As an example, taking $\sigma_c = 0.7$ in a grid with SCR = 3, as shown in Figure 2.18, P-Q coupling is reduced from 45 to 35%, which is an improvement of 22%. In this case, $\sigma_t = 0.45$ produces the best results, since SCRt is kept above SCRt = 2, and POI voltage is still below $V_f = 1.04$ pu. It is interesting to notice that a lower R/X ratio target σ_t would neither achieve a better decoupling nor allow for a safer stability margin.

Of course, the use of a virtual impedance has its drawbacks. Even if P-Q coupling is reduced, the effect is quite limited, and, as mentioned before, this decoupling may not even be intended if the IBR is able to behave as a voltage source. This method also requires a good estimation of grid impedance, which may not always be the case, although one could still argue that VI is only necessary for situations with R/X approaching $\sigma_c = 1$, usually

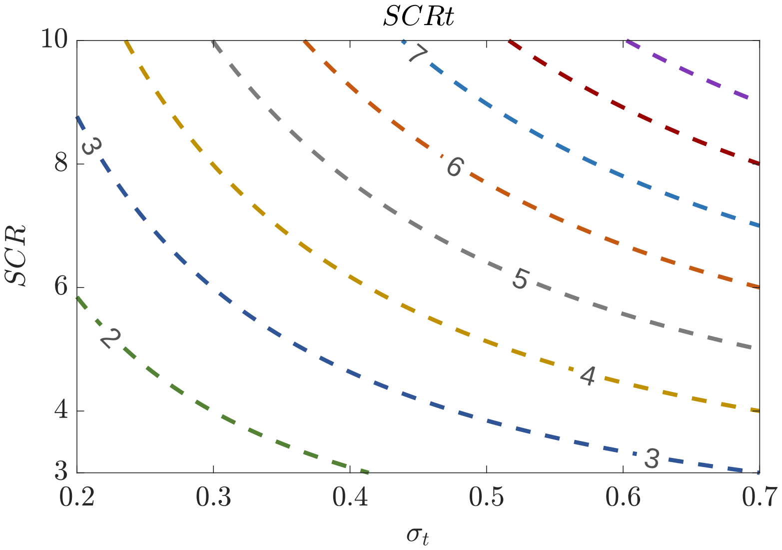

Figure 2.17: SCRt as a function of σ_t, with original R/X ratio $\sigma_c = 0.7$

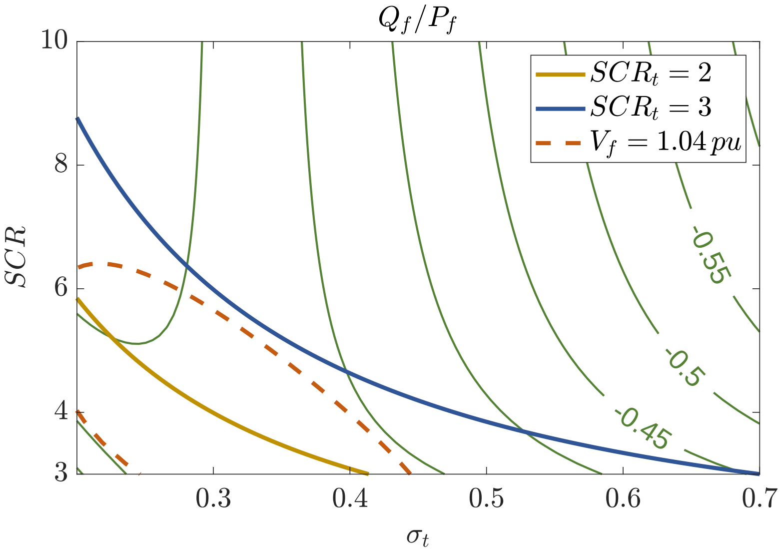

Figure 2.18: Comparative plot for VI tuning, with original R/X ratio $\sigma_c = 0.7$

related to long distribution lines; in such scenarios, information about the line/cable material (R and L per km), as well the length of the feeder, would be enough to provide an impedance estimation. Finally, VI also has an implication on small-signal stability, which should be taken into account.

2.3.2.2 Time-domain simulation

For a GFM connected to a grid with SCR $= 3$ and $\sigma_c = 0.7$, a target R/X ratio $\sigma_t = 0.45$ yields the best P-Q decoupling. This result can be confirmed via time-domain simulations, as shown in Figure 2.19. Four scenarios are used as case studies, with a setpoint of $P_f = 1\,\text{pu}$. As expected, $\sigma_t = 0.7$, i.e., no virtual impedance, results in a coupling of 45 %, while P_f has a very slight overshoot before reaching 1 pu; $\sigma_t = 0.45$ and $\sigma_t = 0.4$ lead to almost identical results, with coupling reduced by approximately 20 % and P_f step response without overshoot. If R/X ratio target is reduced to $\sigma_t = 0.2$, however, some serious consequences may arise. Both P_f and Q_f have a very slow response, indicative of a weak system; also, P_f stops short of reaching $P_f = 1\,\text{pu}$, which means the IBR might lose stability if kept at this setpoint for longer.

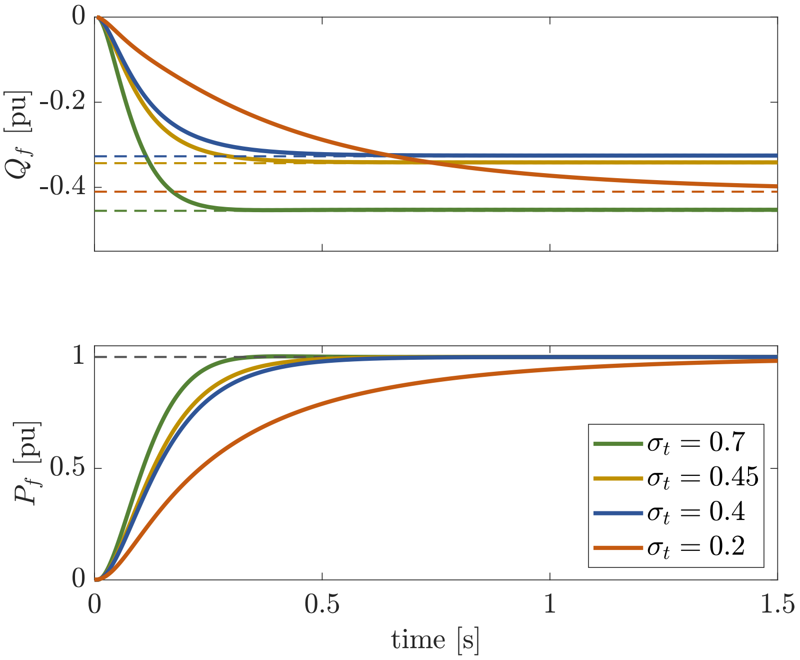

Figure 2.19: Time-domain simulation, with SCR $= 3$ and $\sigma_c = 0.7$

2.3.3 A short remark on droop-related GFM instability under strong grids

As in Section 2.2.4, it is worth discussing a topic that, although dynamic in nature, is still related to static parameters of a system consisting of a GFM inverter connected to the grid. Once again, as with PLL instability, this issue is related to the strength at the POI, hence to the SCR. However, for GFMs, the instability arises for strong interconnections rather than weak ones. This has been reported in literature [24], [30], [72], and has been explained using a conceptual duality between the PSC, used by GFMs, and the PLL, used by GFLs [71].

To understand this, let us refer back to Figure 2.3. Using POI power measurements P_f and comparing them to setpoint P_f^*, the GFM will apply a droop m_p to obtain a frequency variation δ_ω. This is then added to a setpoint ω_f^* ($2\,\pi\,50$ rad/s, for instance), resulting in a frequency ω_f to be integrated in order to obtain a phase θ_f. When P_f stabilizes at P_f^*, frequency ω_f will stabilize at ω_f^*, and the GFM will achieve synchronization with the grid. The most important parameter here is the droop m_p, usually up to $m_p = 0.05$ [66], which translates into a $5\,\%$ frequency variation for a full-load power injection $P_f = 1\,\text{pu}$. High droop values lead to better power-sharing between devices, but may also result in instability: they may cause the GFM to overreact to small power variations.

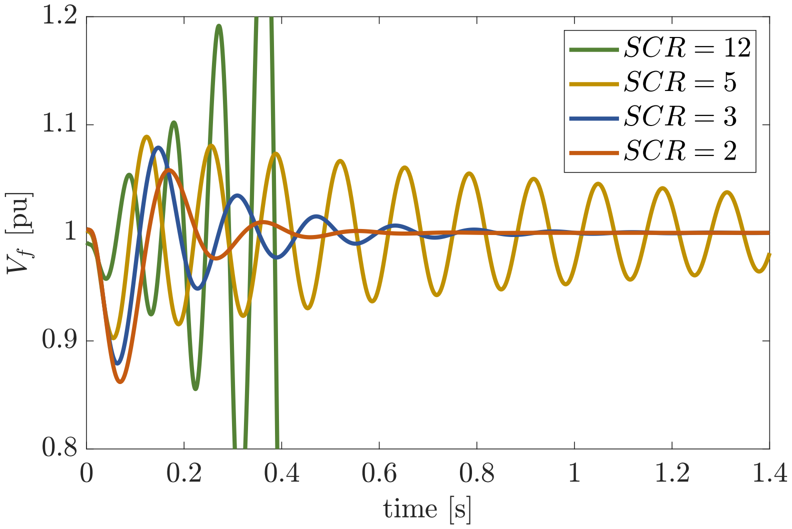

Figure 2.20: Time-domain simulation for a GFM connected to a grid with $\sigma_c = 0.1$, with droop level $m_p = 0.05$

In weak grids, a given deviation in δ_f would lead to a small variation in injected power P_f. In a strong grid, on the other hand, even small deviations in δ_f can lead to large variations in P_f. If the voltage V_f is kept constant, this would translate into a volatile current, which is the effect dual of the volatile voltage observed in GFLs connected to weak grids [71]. Hence, a large droop results in an overreactive response from the GFM, while a strong grid leads to further power variations following the change in voltage phase angle; this can result in an unstable closed loop, with undamped oscillations, as shown in Figure 2.20. Once again, this topic is tangential to the context of this chapter and will be readdressed in future chapters.

2.4 Chapter summary

Summing up this chapter, here are some takeaway points:

- Static parameters may be relevant for small-signal stability, particularly short-circuit ratio (SCR) and R/X ratio. Contemporary power systems, even with a high presence of IBRs, are still dominated by SGs, hence SCR remains a useful tool for detecting weak POIs. An R/X ratio close to one, i.e., $\sigma_c \approx 1$, is a structural trait of MVDGs and has implications on stability.
- MVDGs may experience SCR below 3 (weak grid) or even below 2 (very weak grid), depending on the choice of conductors, if feeders are long (approaching 20 km), regardless of the upstream short-circuit power. There is thus no reason to suppose that weak-grid instabilities, e.g., PLL instability, are not feasible in MVDGs.
- GFLs do not provide a tight voltage control, acting thus as PQ buses in steady-state. Even in the presence of Volt-Var mechanisms, e.g., $Q(U)$, voltage levels may reach unacceptable values under low-SCR and high-σ_c scenarios. GFMs without Q-V droop may solve this issue, acting effectively as PV buses from a load-flow point-of-view.
- For GFLs, voltage instability due to negative V-Q or P-I sensitivity, representing a power transfer limitation, is related to low SCR and low R/X ratio, hence possible in transmission-level weak-grid POIs, yet highly unlikely in MVDGs. Other forms of PLL instability, however, especially when PLLs are tuned for short response times, are still possible in MVDGs.
- If GFMs are to be operated as PQ buses instead of PV, they may suffer from P-Q coupling issues due to the close-to-one R/X ratio in MVDGs. A steady-state virtual impedance (SSVI) may provide a systematic way of correcting the R/X ratio from the controllers' point of view.
- A proper tuning of the SSVI should take three factors into account: P-Q coupling, POI voltage V_f, and perceived short-circuit ratio SCR_t. Improvements in P-Q coupling are achievable at the expense of strict voltage levels.
- Strong POI may lead GFMs to instability when their droop is high. This is the dual effect of weak-grid PLL instability in GFLs.

Chapter 3

Modeling of IBRs connected to the Distribution Grid

Contents

After ascertaining the feasibility of a given equilibrium point via static analysis, as presented in Chapter 2, one should proceed to evaluate its small signal stability, for which it is imperative to adequately model the system. This chapter is thus aimed at modeling IBRs connected to an MVDG, intending to use it in SSSA. For such, we enumerate all the differential and algebraic equations required for the state-space representation of the system, allowing us to obtain the state matrix $\boldsymbol{A}$ necessary for SSSA. To derive the state-space matrices from the differential equations, please refer to Section 1.2.5. This modeling procedure is primarily inspired by the seminal works presented in [94] and [63].

Our choice for EMT models rather than RMS has already been discussed in Section 1.2, hence we may begin by listing out some key hypotheses to simplify this modeling. First, for the sake of standardization, we adopt a benchmark network for our studies: Cigre Task-Force C6.04.02 Medium Voltage Distribution Network Benchmark [90], European Configuration, presented in Figure 3.1. Our choice relies on three factors: this benchmark network is simple, with a relatively small number of nodes, yet accurate enough for our purposes, since it is based on a real rural network in Germany; moreover, all parameters are coherent with respect to typical MV networks in France; finally, this network has two main branches, one composed of overhead lines (nodes 12-14), depicting a rural feeder, and one with underground cables, depicting a nearby village. This scenario, more challenging than an urban network with high short-circuit power in all nodes, is in pair with our objectives when studying stability.

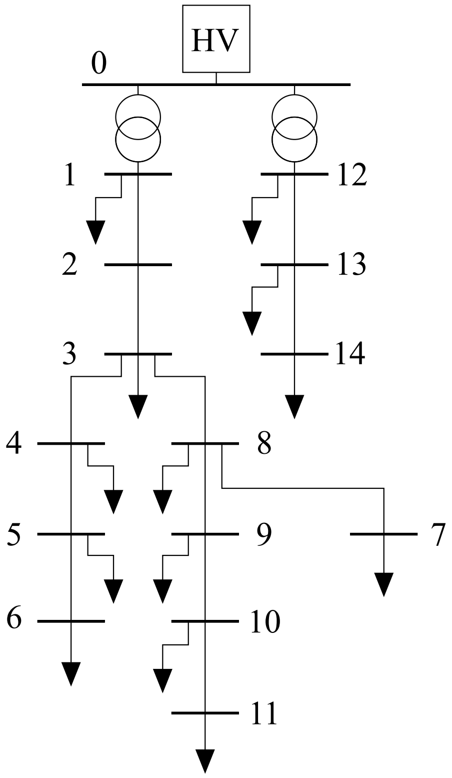

Figure 3.1: Cigre Task-Force C6.04.02: Medium Voltage Distribution Network Benchmark

From all possible configurations, we opt for the one from Figure 3.1: both feeders are isolated from each other, hence the network is radial. All IBRs are assumed to be connected to the same feeder (generally the one departing from Node 1), which is a more interesting scenario in terms of small-signal interactions, due to the proximity between IBRs.

In addition to the aforementioned assumptions, this present work relies on three major hypotheses, which are explained and justified below.

Hypothesis 1: the HV upstream network can be taken as an infinite bus

Since our MVDG includes several IBRs, it may be taken as an active distribution network (ADN). If these IBRs are large enough with respect to the network upstream, it may lead to interactions between the ADN and the HV grid. An obvious example would be an interaction between droop-based GFMs in the ADN and SGs in the network upstream, given that they would both react to frequency deviations shared among all elements in the system.

Nevertheless, our case study consists of large IBRs[1] interacting with each other in a rural French MVDG. We thus consider the upstream network to be the Continental European Transmission Grid, with a short-circuit power in the order of thousands of MVA at the HV side of the substation. A single SG in the upstream network injects between one and two orders of magnitude more power than the largest IBR connected to our MVDG; hence we may safely assume that, from the point of view of the MV network, interactions between the IBRs themselves will be more relevant than those between them and the network upstream.

Since the dynamics of the upstream network are ignored, we take it to be an infinite bus providing a perfect voltage, with a frequency of $f = 50\,\text{Hz}$. A small impedance is added to reproduce the short-circuit power ($S_{sc} = 5000\,\text{MVA}$) and R/X ratio ($\sigma_c = 0.1$).

Hypothesis 2: except for IBRs, the MVDG is entirely passive

This hypothesis implies many assumptions. In reality, MV networks may have several dynamic elements, most notably capacitor banks, OLTCs, PE-based loads, and induction machines. However, in order to study slow interactions, our time scale of interest is from a few milliseconds up to a second, and within this time scale, one may assume that slower devices have already settled into a steady state, from which they will gradually evolve onto a new state; this is the case of capacitor banks, which can be represented as regular capacitors, and OLTCs, displayed as static inductances.

With respect to loads, this assumption is less rigorous: PE-based loads may have a dynamic behavior within the same time scale as IBRs. In this case, we consider the loads to be passive because a load-IBR interaction would be too complex to generalize, especially because loads may not be aggregated into a single bundle if their dynamic behavior is not the same. Here, a case-by-case analysis may be necessary, which is out of our scope. A similar logic applies to induction machines, which are the dominant dynamic elements in industrial loads, to which we add the fact that only around 25 % of the loads in our system, in terms of active power, are industrial. Therefore, we take all loads as PQ buses in our static studies, converting them to equivalent constant-impedance loads during our dynamic simulations, assuming they present a passive behavior for our time scale of interest. Our MVDG serves as a passive interface

---

[1] For a French MVDG, this means an installed capacity of up to $P_n = 12\,\text{MW}$, as mentioned in Section 1.1.1.

between IBRs, who dictate the dynamics of the system.

Hypothesis 3: aggregated passive elements can be replaced by RLC circuits

This final hypothesis would be unnecessary if we were to use RMS models for the IBRs, or if we were to use an EMT model of the *entire* network, including the nodes downstream and the adjacent feeders (assembled in Nodes 1 and 12). However, because the network includes aggregated loads, we are compelled to tolerate a certain level of approximation by replacing these loads with RLC circuits for EMT modeling, unless we can accurately depict the LV network downstream, which would add a disproportionate layer of complexity to the problem. Hence, our EMT modeling implies that all the lines are represented by their "π-models", while the loads are substituted by RLC circuits.

In terms of dynamic behavior, a full representation of the network and a simplified representation using equivalent RLC circuits may lead to some discrepancies. However, they can be taken as equivalent if our EMT simulations are restricted to situations that could be accurately simulated using QSS approximations, which excludes all high-frequency phenomena, or in situations that are not too far from the fundamental frequency. Given that our objective is to study SICDS, these approximations are acceptable. It is worth mentioning that most IBR models available in the literature are in EMT rather than RMS, which is yet another motivating factor to keep this hypothesis. We will, therefore, employ the model shown in Figure 3.2, further explored in the following sections.

3.1 Modeling of inverter-based resources

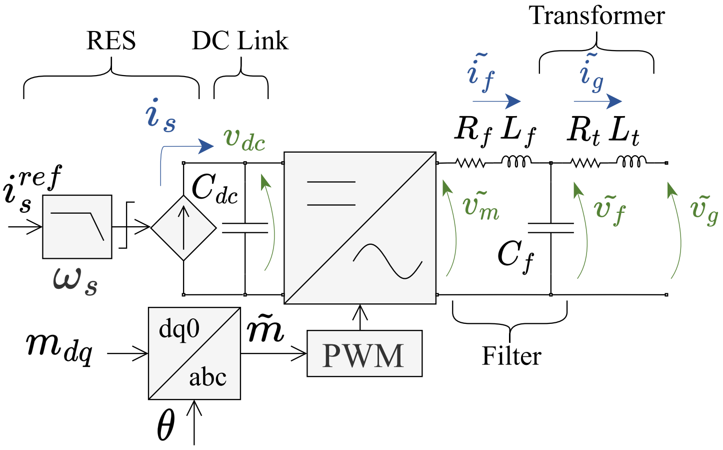

Figure 3.2: Physical model of an inverter-based resource

A three-phase PWM-controlled voltage-source converter (VSC) can be described by the following equations [79]:

$$L_f \, \dot{i_{f_k}} = v_{mk} - v_{f_k} - R_f \, i_{f_k}, \; \forall k \in \{a, b, c\} \tag{3.1}$$

$$C_{dc} \, \dot{v_{dc}} = i_s - i_{sw} \tag{3.2}$$

Considering a set of bipolar switching functions $u_k \in \{-1, 1\}$, an inverter may be represented by a generalized average model where the AC components of v_{dc} are neglected, as well as the DC component and higher-order harmonics in the three-phase currents i_{f_k}.

$$\boldsymbol{T}(\theta) = \frac{2}{3} \begin{bmatrix} \cos(\theta) & \cos(\theta - \frac{2\pi}{3}) & \cos(\theta + \frac{2\pi}{3}) \\ -\sin(\theta) & -\sin(\theta - \frac{2\pi}{3}) & -\sin(\theta + \frac{2\pi}{3}) \\ \frac{1}{2} & \frac{1}{2} & \frac{1}{2} \end{bmatrix} \tag{3.3}$$

$$\boldsymbol{x_{dq0}} = \begin{bmatrix} x_d \\ x_q \\ x_0 \end{bmatrix} = \boldsymbol{T}(\theta) \, \tilde{\boldsymbol{x}} = \boldsymbol{T}(\theta) \begin{bmatrix} x_a \\ x_b \\ x_c \end{bmatrix} \tag{3.4}$$

We may then apply a power-variant Park transformation (3.3)-(3.4), also called "*dq*0 transformation" [95], in order to obtain the VSC equations in a *dq*-frame rotated by a phase equal to θ_{ibr}, with an angular speed of ω_{ibr}. Assuming a balanced three-phase output from the inverter (no zero-sequence component), we get:

$$L_f \, \dot{i_{f_d}} = \frac{1}{2} \, v_{dc} \, m_d - v_{f_d} - R_f \, i_{f_d} + \omega_{ibr} \, L_f \, i_{f_q} \tag{3.5}$$

$$L_f \, \dot{i_{f_q}} = \frac{1}{2} \, v_{dc} \, m_q - v_{f_q} - R_f \, i_{f_q} - \omega_{ibr} \, L_f \, i_{f_d} \tag{3.6}$$

$$C_{dc} \, \dot{v_{dc}} = i_s - \frac{3}{4} \, (i_{f_d} m_d + i_{f_q} m_q) \tag{3.7}$$

with

$$\boldsymbol{v_{mdq}} = \frac{1}{2} \, v_{dc} \, \boldsymbol{m_{dq}} \tag{3.8}$$

$$i_{sw} = \frac{3}{4} \, (i_{f_d} m_d + i_{f_q} m_q) \tag{3.9}$$

Equations (3.5)-(3.7) can be rewritten in per-unit, using the base from Table 3.1, and taking $\{m_d, m_q\}$[2] to denote the *dq* components of the per-unit three-phase modulation function $\tilde{\boldsymbol{m}}$, leading to (3.10)-(3.12).

---

[2] From here on, the notation $\tilde{\boldsymbol{x}}$ or $\boldsymbol{x_{dq}}$ is equivalent to either the set of *dq* components $\{x_d, x_q\}$, or the component vector $[x_d, x_q]^t$.

$$\frac{L_f}{\omega_b}\,\dot{i}_{f_d} = v_{dc}\, m_d - v_{f_d} - R_f\, i_{f_d} + \omega_{ibr}\, L_f\, i_{f_q} \tag{3.10}$$

$$\frac{L_f}{\omega_b}\,\dot{i}_{f_q} = v_{dc}\, m_q - v_{f_q} - R_f\, i_{f_q} - \omega_{ibr}\, L_f\, i_{f_d} \tag{3.11}$$

$$C_{dc}\,\dot{v}_{dc} = i_s - i_{f_d}\, m_d - i_{f_q}\, m_q \tag{3.12}$$

Now it is possible to formulate a state-space representation for the VSC. Adding a capacitor to the output filter, two more equations are included:

$$\frac{C_f}{\omega_b}\,\dot{v}_{f_d} = i_{f_d} - i_{g_d} + \omega_{ibr}\, C_f\, v_{f_q} \tag{3.13}$$

$$\frac{C_f}{\omega_b}\,\dot{v}_{f_q} = i_{f_q} - i_{g_q} - \omega_{ibr}\, C_f\, v_{f_d} \tag{3.14}$$

Parameter	Symbol	Formula
Base AC power	S_{base}	10 MVA
Nominal RMS line voltage	U_l	20 kV
Base frequency	f_{base}	50 Hz
Base angular frequency	ω_b	$2\,\pi\, f_{base}$
Nominal RMS line current	I_l	$S_{base}/(\sqrt{3}\, U_l)$
Base voltage: peak nominal phase voltage	V_{base}	$\sqrt{2}\, U_l/\sqrt{3}$
Base current: peak nominal line current	I_{base}	$\sqrt{2}\, I_l$
Base impedance	Z_{base}	V_{base}/I_{base}
Base inductance	L_{base}	Z_{base}/ω_b
Base capacitance	C_{base}	$1/(\omega_b\, Z_{base})$
Base DC-side voltage	V_{basedc}	$2\, V_{base}$
Base DC-side current	I_{basedc}	$3\, I_{base}/4$
Base DC-side impedance	Z_{basedc}	V_{basedc}/I_{basedc}
Base DC-side inductance	L_{basedc}	Z_{basedc}
Base DC-side capacitance	C_{basedc}	$1/Z_{basedc}$

Table 3.1: Per-unit base expressions for a given IBR

Assuming an LV/MV transformer with no phase shift, we may use an RL circuit to represent it (R_t and L_t in Figure 3.2), which also includes a short line with negligible capacitance connecting the IBR transformer to the POI, yielding two more equations:

$$\frac{L_t}{\omega_b}\,\dot{i}_{g_d} = v_{f_d} - v_{g_d} - R_t\, i_{g_d} + \omega_{ibr}\, L_t\, i_{g_q} \tag{3.15}$$

$$\frac{L_t}{\omega_b}\,\dot{i}_{g_q} = v_{f_q} - v_{g_q} - R_t\, i_{g_q} - \omega_{ibr}\, L_t\, i_{g_d} \tag{3.16}$$

3.1.1 Source and DC side

As discussed in Section 1.1.2, Enedis envisions a RES capacity of up to 275 GW by 2050, most of which (around 84 %) is expected to be in the form of PV [11]. Some of these PV plants will presumably be coupled with Battery Energy Storage Systems (BESS). Hence, our RES is modeled so as to emulate PV and BESS, disregarding certain source-side stability concerns, which are usually associated with Wind Power Plants (WPP) [96]. Although certain authors might employ a constant DC source for both transient [97] and small-signal analysis [98] of IBRs, or to propose and validate IBR controllers [99], we have opted for a representation that includes some DC-side dynamics, since they may have an impact on small-signal stability [63]. As shown in Figure 3.2, we have adopted a controlled current-source model, based on [63], where a first-order delay with a time constant $\tau_s = 1/\omega_s$, in addition to a saturation block, is used to represent the dynamics related to the source-side DC/DC converter. A reference current i_s^{ref} is provided by an MPPT algorithm or by the IBR controller. A DC-link capacitor is used as an energy buffer between the source and the converter. This is a common representation for generic controllable sources, either an energy storage plant or a RES with sufficient headroom, and is commonly employed in the literature [100]–[102]. A differential equation related to the source may thus be added to our model:

$$\dot{i_s} = -\omega_s \, i_s + \omega_s \, i_s^{ref} \tag{3.17}$$

It is worth mentioning that this model may still be useful for representing Type-4 WPPs in certain applications. For instance, authors in [103], aiming to provide a stability assessment for GFMs with limited DC-side current provision, compared this simplified DC-side model with a detailed Type-4 WPP, concluding that the representation is accurate for reproducing v_{dc} instability if the source current limitation is in accordance with the maximum power point of the WPP; otherwise, if this power limitation is not respected, dynamic events could lead the rotor to stall. Moreover, a small-signal stability assessment for offshore WPPs connected to HVDC rectifiers, operating as GFL and GFM, was conducted in [104], arriving at similar conclusions as the next chapter in this dissertation, namely the key role played by GFL PLL gains and GFM droop constant in the dominant modes of the system. More specifically, for the study of low-frequency dynamics (below 10 Hz) in WPPs connected to weak grids, it is common for researchers to ignore DC-side dynamics entirely [52], since the root cause of such stability issues can be accurately explained via simplified models.

For our purposes, it is nevertheless crucial to reproduce the imperfections of the DC source. Since v_{dc} is sensitive to power imbalances, it must be kept under control by regulating either i_s, namely a Machine-side Control (MSC), or i_{sw}, usually called Converter-side Control (CSC). GFLs are able to apply CSC to regulate v_{dc}, which allows them to inject an i_s^{ref} provided by an MPPT. This is not normally the case for GFMs, which have to control v_{dc} via the source, having to send a reference i_s^{ref} from its own controller, which can lead to stability issues when the source is not capable of responding fast enough, or i_s^{ref} is above the maximum current.

3.1.2 Translating dq reference frames

It is worth noting that all variables in dq must be referred to the dq-frame of the IBR, which is rotating at ω_{ibr}. An external voltage, such as $\tilde{\boldsymbol{v}}_{\boldsymbol{g}}$ in Figure 3.2, must be rotated from the global dq-frame, denoted by the superscript "g", to the reference frame of the IBR.

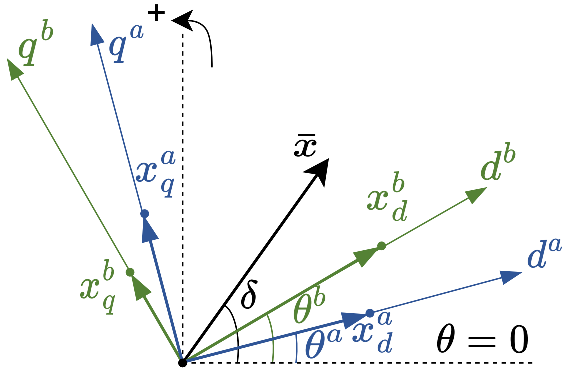

Figure 3.3: Representation of $\bar{x}$ on different dq reference frames

From Figure 3.3, we derive:

$$\boldsymbol{x}^{\boldsymbol{a}}_{\boldsymbol{dq}} = x_d^a + j\,x_q^a = |\bar{x}|\,e^{j\,(\delta-\theta^a)} \tag{3.18}$$

$$\boldsymbol{x}^{\boldsymbol{b}}_{\boldsymbol{dq}} = x_d^b + j\,x_q^b = |\bar{x}|\,e^{j\,(\delta-\theta^b)} \tag{3.19}$$

Dividing (3.19) by (3.18), we obtain:

$$\boldsymbol{x}^{\boldsymbol{b}}_{\boldsymbol{dq}} = e^{j\,(\theta^a-\theta^b)}\,\boldsymbol{x}^{\boldsymbol{a}}_{\boldsymbol{dq}} = \boldsymbol{R}(\theta^a-\theta^b)\,\boldsymbol{x}^{\boldsymbol{a}}_{\boldsymbol{dq}} \tag{3.20}$$

where $\boldsymbol{R}(\theta)$ denotes a counterclockwise rotation of θ:

$$\boldsymbol{R}(\theta) = \begin{bmatrix} \cos\theta & -\sin\theta \\ \sin\theta & \cos\theta \end{bmatrix} \tag{3.21}$$

Hence, the external voltage $\tilde{\boldsymbol{v}}_{\boldsymbol{g}}$ may be taken from a global dq frame $\{v_{g_d}^{g}, v_{g_q}^{g}\}$, which rotates at a global frequency ω_g, to the reference frame of the IBR $\{v_{g_d}, v_{g_q}\}$, rotating at ω_{ibr}, by applying (3.20):

$$\begin{bmatrix} v_{g_d} \\ v_{g_q} \end{bmatrix} = \begin{bmatrix} \cos\left(\theta_g - \theta_{ibr}\right) & -\sin\left(\theta_g - \theta_{ibr}\right) \\ \sin\left(\theta_g - \theta_{ibr}\right) & \cos\left(\theta_g - \theta_{ibr}\right) \end{bmatrix} \begin{bmatrix} v_{g_d}^{g} \\ v_{g_q}^{g} \end{bmatrix} \tag{3.22}$$

Taking all aforementioned equations into account, notably the differential equations (3.10)-(3.17), it is possible to build a state-space model for the physical components in an IBR branch as shown in Figure 3.2, with *state* vector $\boldsymbol{x}$, *input* vector $\boldsymbol{u}$, and *parameter* vector $\boldsymbol{p}$:

$$\boldsymbol{x} = \begin{bmatrix} i_{f_d} & i_{f_q} & v_{dc} & v_{f_d} & v_{f_q} & i_s & i_{g_d} & i_{g_q} \end{bmatrix}^t \tag{3.23}$$

$$\boldsymbol{u} = \begin{bmatrix} i_s^{ref} & m_d & m_q & \theta_{ibr} & \omega_{ibr} & v_{g_d}^{g} & v_{g_q}^{g} & \theta_g \end{bmatrix}^t \tag{3.24}$$

$$\boldsymbol{p} = \begin{bmatrix} \omega_b & R_f & L_f & C_f & R_t & L_t & C_{dc} & \omega_s \end{bmatrix}^t \tag{3.25}$$

This state-space will be further expanded by including an IBR controller, which will provide a set of variables $\{i_s^{ref}, m_d, m_q, \theta_{ibr}, \omega_{ibr}\}$ according to its operation mode: GFL or GFM.

3.2 Modeling of IBR controllers

3.2.1 Grid-following control

A GFL controller is composed of three blocks: external control, internal control, and phase-locked loop (PLL). Although there are variations, a standard configuration usually involves control of active and reactive power, providing current references in a dq frame, which are used in determining a modulation function for the PWM. This dq frame is obtained through a PLL, with the purpose of achieving synchronization with the input voltage $\tilde{\boldsymbol{v}}_{\boldsymbol{f}}$. An illustrative diagram is presented in Figure 3.4.

Starting from the external loop, we may write down the following equations:

$$\dot{\gamma_{v_{dc}}} = v_{dc}^{ref} - v_{dc} \tag{3.26}$$

$$\dot{q_m} = -\omega_{iq}\, q_m + \omega_{iq}\, q \tag{3.27}$$

$$\dot{\gamma_{i_q^{ref}}} = q_{ref} - q_m \tag{3.28}$$

where

$$q = v_{f_q} i_{f_d} - v_{f_d} i_{f_q} \tag{3.29}$$

leading to

$$i_{f_d}{}^{ref} = K_p{}^{vdc}\,(v_{dc}^{ref} - v_{dc}) + K_i{}^{vdc}\,\gamma_{vdc} \tag{3.30}$$

$$i_{f_q}{}^{ref} = K_p{}^{iq}\,(q_{ref} - q_m) + K_i{}^{iq}\,\gamma_{i_q^{ref}} \tag{3.31}$$

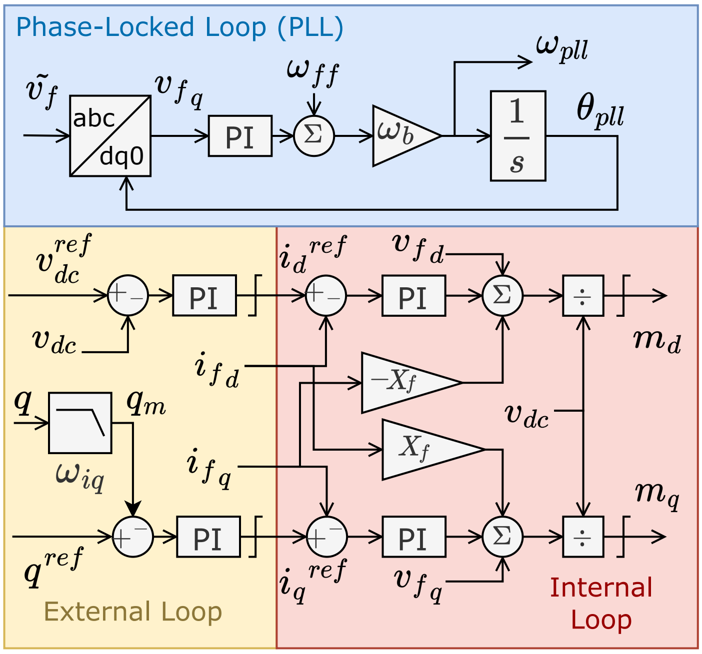

Figure 3.4: Control diagram for a GFL inverter

It is worth noting that the control of active power, unlike the reactive power, is done in an indirect manner, by regulating the DC-link voltage v_{dc}. By using this method, a GFL is able to keep v_{dc} under control while injecting whichever power is being provided by the source. This grants us the freedom to choose i_s^{ref} according to an MPPT algorithm, without any risk over v_{dc}. If, on the other hand, the IBR was to regulate P directly, then there should be an additional loop to control v_{dc}, which would give us a reference i_s^{ref} for the source. In the case of the RES being incapable of providing this current, v_{dc} could collapse. Moreover, since most GFM inverters require a machine-side v_{dc} control, it is interesting to use a GFL model which allows for a converter-side control, in order to provide a comparison. Hence, our choice for a generic GFL model uses this type of external loop.

Once the references $\{{i_f}_d^{ref}, {i_f}_q^{ref}\}$ are available, an internal control loop uses the measurements of $\{{i_f}_d, {i_f}_q\}$ to generate a modulation function for the PWM:

$$\dot{\gamma}_{i_{f_d}} = {i_f}_d^{ref} - {i_f}_d \tag{3.32}$$

$$\dot{\gamma}_{i_{f_q}} = {i_f}_q^{ref} - {i_f}_q \tag{3.33}$$

which leads to

$$v_{dc}\, m_d^{ref} = K_p^i\,({i_f}_d^{ref} - {i_f}_d) + K_i^i\,\gamma_{i_{f_d}} + {v_f}_d - \omega_{ff}\, L_f\, {i_f}_q \tag{3.34}$$

$$v_{dc}\, m_q^{ref} = K_p^i\,({i_f}_q^{ref} - {i_f}_q) + K_i^i\,\gamma_{i_{f_q}} + {v_f}_q + \omega_{ff}\, L_f\, {i_f}_d \tag{3.35}$$

Obviously, no measurement is promptly available in a dq frame suitable for the IBR. To be able to convert $\tilde{\boldsymbol{i_f}}$ into a dq frame that coincides with the active and reactive axis of this IBR, without which the injected current would be inaccurate, meaning a current-source behavior for the VSC would be unachievable, we have to resort to a PLL, whose equations are below:

$$\dot{\gamma_{pll}} = v_{f_q} \tag{3.36}$$

$$\dot{\theta_{pll}} = \omega_b \left(K_p^{pll}\, v_{f_q} + K_i^{pll}\, \gamma_{pll} + \omega_{ff}\right) \tag{3.37}$$

An algebraic equation gives us the frequency of the rotating dq frame:

$$\omega_{pll} = K_p^{pll}\, v_{f_q} + K_i^{pll}\, \gamma_{pll} + \omega_{ff} \tag{3.38}$$

Although v_{f_q} in (3.36)-(3.37) is usually a state variable, as defined in (3.14), if no capacitor is used in the output filter, it is possible to obtain it as an algebraic variable using (3.42). In this case, (3.10)-(3.11) and (3.15)-(3.16) would have to be grouped into a single pair of equations since $\tilde{\boldsymbol{i_f}}$ would be equal to $\tilde{\boldsymbol{i_g}}$, allowing us to dismiss $\{i_{g_d}, i_{g_q}\}$. This would reduce the order of our system by four, resulting in (3.39)-(3.40) instead of $\{$(3.10)-(3.11),(3.15)-(3.16)$\}$.

$$\frac{(L_f + L_t)}{\omega_b}\, \dot{i_{f_d}} = v_{dc}\, m_d - v_{g_d} - (R_f + R_t)\, i_{f_d} + \omega_{ibr}\, (L_f + L_t)\, i_{f_q} \tag{3.39}$$

$$\frac{(L_f + L_t)}{\omega_b}\, \dot{i_{f_q}} = v_{dc}\, m_q - v_{g_q} - (R_f + R_t)\, i_{f_q} - \omega_{ibr}\, (L_f + L_t)\, i_{f_d} \tag{3.40}$$

Differential equations (3.13)-(3.14) would be replaced by their algebraic counterparts (3.41)-(3.42), taking $\{\dot{i_{f_d}}, \dot{i_{f_q}}\}$ from (3.39)-(3.40):

$$v_{f_d} = v_{g_d} + \frac{L_t}{\omega_b}\, \dot{i_{f_d}} + R_t\, i_{f_d} - \omega_{pll}\, L_t\, i_{f_q} \tag{3.41}$$

$$v_{f_q} = v_{g_q} + \frac{L_t}{\omega_b}\, \dot{i_{f_q}} + R_t\, i_{f_q} + \omega_{pll}\, L_t\, i_{f_d} \tag{3.42}$$

Nevertheless, to avoid instabilities when feed-forwarding $\{v_{f_d}, v_{f_q}\}$ to the internal control loop (3.34)-(3.35), a small delay (e.g. $\tau_{vi} = 1/\omega_{vi} = 0.1\, ms$) should be added to these voltages, creating two additional state variables (3.43)-(3.44), and modifying PWM reference $\{m_d^{ref}, m_q^{ref}\}$ (3.45)-(3.46)[3]. This parameter would also add a realistic representation of measurement delays for $\tilde{v_f}$, which, although fast, are not instantaneous.

$$\dot{v_{f_{di}}} = -\omega_{vi}\, v_{f_{di}} + \omega_{vi}\, v_{f_d} \tag{3.43}$$

$$\dot{v_{f_{qi}}} = -\omega_{vi}\, v_{f_{qi}} + \omega_{vi}\, v_{f_q} \tag{3.44}$$

$$v_{dc}\, m_d^{ref} = K_p^i\, ({i_{f_d}}^{ref} - i_{f_d}) + K_i^i\, \gamma_{i_{f_d}} + v_{f_{di}} - \omega_{ff}\, L_f\, i_{f_q} \tag{3.45}$$

$$v_{dc}\, m_q^{ref} = K_p^i\, ({i_{f_q}}^{ref} - i_{f_q}) + K_i^i\, \gamma_{i_{f_q}} + v_{f_{qi}} + \omega_{ff}\, L_f\, i_{f_d} \tag{3.46}$$

---

[3] In the presence of a capacitor C_f in the output filter, equations (3.39)-(3.46) should be dismissed.

Finally, considering an instantaneous PWM, since our time scale of interest is considerably slower than the switching frequency, leads us to the following set of algebraic equations:

$$0 = m_d - m_d^{ref} \tag{3.47}$$

$$0 = m_q - m_q^{ref} \tag{3.48}$$

$$0 = \omega_{pll} - (K_p{}^{pll}\, v_{f_q} + K_i{}^{pll}\, \gamma_{pll} + \omega_{ff}) \tag{3.49}$$

Considering all these relations, we may update the state-space for the IBR by including all equations related to GFL control, notably substituting $\{\omega_{ibr}, \theta_{ibr}\}$ by $\{\omega_{pll}, \theta_{pll}\}$, which leads us to state vector $\boldsymbol{x}$, input vector $\boldsymbol{u}$, algebraic vector $\boldsymbol{z}$, and parameter vector $\boldsymbol{p}$:

$$\boldsymbol{x} = \Big[i_{f_d} \quad i_{f_q} \quad v_{dc} \quad v_{f_d} \quad v_{f_q} \quad i_s \quad i_{g_d} \quad i_{g_q} \quad \gamma_{v_{dc}} \quad q_m \quad \gamma_{i_q^{ref}} \quad \gamma_{i_{f_d}} \quad \gamma_{i_{f_q}} \quad \gamma_{pll} \quad \theta_{pll} \Big]^t \tag{3.50}$$

$$\boldsymbol{u} = \Big[i_s^{ref} \quad v_{dc}{}^{ref} \quad q^{ref} \quad v_{p_d}^{g} \quad v_{p_q}^{g} \quad \theta_g \Big]^t \tag{3.51}$$

$$\boldsymbol{z} = \Big[m_d \quad m_q \quad \omega_{pll} \Big]^t \tag{3.52}$$

$$\boldsymbol{p} = \Big[\omega_b \quad R_f \quad L_f \quad C_f \quad R_t \quad L_t \quad C_{dc} \quad \omega_s \quad \omega_{ff} \quad \omega_{iq} \quad K_p{}^{vdc} \quad K_i{}^{vdc} \quad K_p{}^{iq} \quad K_i{}^{iq} \quad K_p{}^{i} \quad K_i{}^{i} \quad K_p{}^{pll} \quad K_i{}^{pll} \Big]^t \tag{3.53}$$

In the absence of a filter capacitor, some of these vectors are slightly modified:

$$\boldsymbol{x} = \Big[i_{f_d} \quad i_{f_q} \quad v_{dc} \quad i_s \quad \gamma_{v_{dc}} \quad q_m \quad \gamma_{i_q^{ref}} \quad \gamma_{i_{f_d}} \quad \gamma_{i_{f_q}} \quad \gamma_{pll} \quad \theta_{pll} \quad v_{f_{di}} \quad v_{f_{qi}} \Big]^t \tag{3.54}$$

$$\boldsymbol{p} = \Big[\omega_b \quad R_f \quad L_f \quad R_t \quad L_t \quad C_{dc} \quad \omega_s \quad \omega_{ff} \quad \omega_{iq} \quad K_p{}^{vdc} \quad K_i{}^{vdc} \quad K_p{}^{iq} \quad K_i{}^{iq} \quad K_p{}^{i} \quad K_i{}^{i} \quad K_p{}^{pll} \quad K_i{}^{pll} \quad \omega_{vi} \Big]^t \tag{3.55}$$

This state-space could provide $\tilde{\boldsymbol{i_g}}$ as its output, so that multiple IBRs connected to the MVDG may be grouped into a single state-space. These variables would have to be rotated onto a global dq frame, with phase θ_g, giving us an output vector $\boldsymbol{y}$ (3.56). If there is no filter capacitor, $\{i_{f_d}, i_{f_q}\}$ must replace $\{i_{g_d}, i_{g_q}\}$.

$$\boldsymbol{y} = \begin{bmatrix} i_{g_d}^{g} \\ i_{g_q}^{g} \end{bmatrix} = \begin{bmatrix} \boldsymbol{R}(\theta_{pll} - \theta_g) & \boldsymbol{0_2} \\ \boldsymbol{0_2} & \boldsymbol{R}(\theta_{pll} - \theta_g) \end{bmatrix} \begin{bmatrix} i_{g_d} \\ i_{g_q} \end{bmatrix} \tag{3.56}$$

3.2.2 Grid-forming control

A GFM controller, on the other hand, is also composed of an external and internal loop, although the primary objective of the latter is to regulate an output voltage $\tilde{\boldsymbol{v_f}}$ instead of a current. However, this can be done either in a direct manner, by controlling the modulation signal $\tilde{\boldsymbol{m}}$ directly from voltage errors, or in an indirect manner, by going through a fast current control loop. While there are advantages in adopting the first method, especially if the switching frequency cannot be substantially higher than the fastest control loop, the second method has the advantage of allowing for a simple way of limiting the output current, which is crucial for a safe operation of a GFM. Because the second method, a cascaded control loop, is generic and representative enough for our purposes, assuming that switching frequency will not be a limiting factor for most MV applications, it will be adopted throughout this report, resulting in the scheme presented in Figure 3.5.

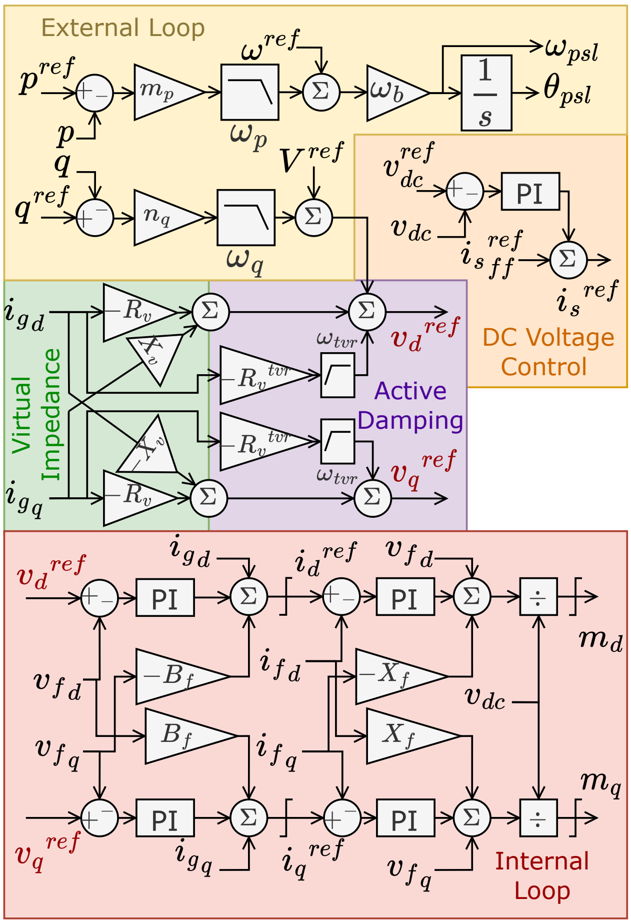

Figure 3.5: Control diagram for a GFM inverter

In microgrids, some GFM applications require IBRs to inject any value of active power, if available, in order to keep voltage and frequency under control, particularly when this GFM is the only voltage source in the network. When multiple GFMs are interconnected, however, this stiff control should be replaced by a droop-based mechanism, which emulates synchronous generators in their way of sharing power and reacting to power variations via frequency. But SGs react according to a swing equation, due to their rotating mass and its inertial effect when subjected to power imbalances; this leads to slow variations in frequency, which can only be emulated by GFMs if a low-pass filter is added to the droop control, in a method denominated "Virtual Synchronous Machine".

For interconnected networks, we may thus adapt this control method to ensure a voltage-source behavior and a synchronization capability, in addition to active power control, in what is called "Power-Synchronization Control" or "Power-Synchronization Loop" (PSL). An interconnected GFM is hence capable of injecting a specific active power, which comes as a reference P^{ref}, being then compared to the measured power P and, after passing through a droop m_p and a low-pass filter with cut-off frequency ω_p, determines a frequency deviation from reference ω_{ref}. The resulting frequency ω_{psl} is then integrated onto a phase θ_{psl}, serving as a reference dq frame for the GFM. Adding a reactive power control loop in line with these principles, although with respect to the voltage instead of the frequency, we complete the external loop, as described in the following equations:

$$\dot{\gamma_p} = -\omega_p\,\gamma_p + \omega_p\,m_p\,(p^{ref} - p) \tag{3.57}$$

$$\dot{\theta_{psl}} = \omega_b\,(\gamma_p + \omega^{ref}) \tag{3.58}$$

$$\dot{\gamma_q} = -\omega_q\,\gamma_q + \omega_q\,n_q\,(q^{ref} - q) \tag{3.59}$$

where

$$p = v_{f_d}\,i_{g_d} + v_{f_q}\,i_{g_q} \tag{3.60}$$

$$q = v_{f_q}\,i_{g_d} - v_{f_d}\,i_{g_q} \tag{3.61}$$

If our voltage source is to keep a stiff voltage, we may provide a reference V^{ref} directly to the internal loop. However, multiple additional control features may be integrated to improve the dynamic behavior of the GFM. Most commonly, we may take advantage of this flexibility to add virtual resistances or inductances, either for steady-state corrections, as a Virtual Impedance (VI), or transient improvements, such as a Transient Virtual Resistor (TVR). For MV purposes, where resistance and reactance seen from an IBR may be of the same order, a VI may prove useful in enabling an "R/X ratio correction", virtually lowering this ratio to improve dynamic performance, as discussed in Section 2.3.2. A TVR [36], [70], which is a virtual resistor coupled with a high-pass filter with cut-off frequency ω_{tvr}, serves as an active damping method to reduce power oscillations in strong reactive networks, which may still be useful in MV applications, especially for POIs near the substation. Given that these additional loops may prove mandatory for a stable and dynamically coherent behavior of a GFM, they are included in our generic model as a pair of differential equations,

$$\dot{\gamma_{\mathrm{TVR}_d}} = -\omega_{tvr}\,\gamma_{\mathrm{TVR}_d} + \omega_{tvr}\,R_v^{tvr}\,i_{g_d} \tag{3.62}$$

$$\dot{\gamma_{\mathrm{TVR}_q}} = -\omega_{tvr}\,\gamma_{\mathrm{TVR}_q} + \omega_{tvr}\,R_v^{tvr}\,i_{g_q} \tag{3.63}$$

and algebraic equations,

$$\gamma_{\mathrm{VI}_d} = -R_v \, i_{g_d} + X_v \, i_{g_q} \tag{3.64}$$

$$\gamma_{\mathrm{VI}_q} = -R_v \, i_{g_q} - X_v \, i_{g_d} \tag{3.65}$$

Taking these additional loops into account, we may determine our voltage references in dq:

$$ {v_f}_d^{ref} = V^{ref} + \gamma_q + \gamma_{\mathrm{VI}_d} + \gamma_{\mathrm{TVR}_d} - R_v^{tvr} \, i_{g_d} \tag{3.66}$$

$$ {v_f}_q^{ref} = \gamma_{\mathrm{VI}_q} + \gamma_{\mathrm{TVR}_q} - R_v^{tvr} \, i_{g_q} \tag{3.67}$$

These can then be sent to an internal voltage control loop:

$$\dot{\gamma}_{v_{f_d}} = {v_f}_d^{ref} - {v_f}_d \tag{3.68}$$

$$\dot{\gamma}_{v_{f_q}} = {v_f}_q^{ref} - {v_f}_q \tag{3.69}$$

Once again, we may obtain a set of references

$$ {i_f}_d^{ref} = K_p^v \, ({v_f}_d^{ref} - {v_f}_d) + K_i^v \, \gamma_{v_{f_d}} + i_{g_d} - \omega_{ff} \, C_f \, {v_f}_q \tag{3.70}$$

$$ {i_f}_q^{ref} = K_p^v \, ({v_f}_q^{ref} - {v_f}_q) + K_i^v \, \gamma_{v_{f_q}} + i_{g_q} + \omega_{ff} \, C_f \, {v_f}_d \tag{3.71}$$

which in turn go through a current control loop:

$$\dot{\gamma}_{i_{f_d}} = {i_f}_d^{ref} - {i_f}_d \tag{3.72}$$

$$\dot{\gamma}_{i_{f_q}} = {i_f}_q^{ref} - {i_f}_q \tag{3.73}$$

Finally, it is worth mentioning that a GFM is not able to comply with any of these control requirements if the DC-link voltage v_{dc} is not kept under control. Since this voltage is sensitive to power imbalances, and active power is already controlled by an external loop, which means the current i_{sw} from Figure 3.2 is being determined by the GFM controller, the only way to regulate v_{dc} is via the source current i_s. Hence, this source should receive commands from the IBR and react accordingly, which is done by means of a DC voltage control loop:

$$\dot{\gamma}_{v_{dc}} = {v_{dc}}^{ref} - v_{dc} \tag{3.74}$$

Although v_{dc} and i_s still follow the dynamics described in (3.12) and (3.17), respectively, we should now substitute ${i_s}^{ref}$ by

$$ {i_s}^{ref} = {K_p}^{v_{dc}} \, ({v_{dc}}^{ref} - v_{dc}) + {K_i}^{v_{dc}} \, \gamma_{v_{dc}} + {i_s}^{ff} \tag{3.75}$$

where we could define a feed-forward DC current:

$$ {i_s}^{ff} = \frac{p^{ref}}{{v_{dc}}^{ref}} \tag{3.76}$$

Because both GFL and GFM employ an inner current control loop, we have an identical expression for PWM references $\{m_d^{ref}, m_q^{ref}\}$, given in (3.34)-(3.35). Once again, since our PWM is taken as instantaneous, we get the following algebraic equations:

$$0 = m_d - m_d^{ref} \tag{3.77}$$

$$0 = m_q - m_q^{ref} \tag{3.78}$$

$$0 = \omega_{psl} - (\gamma_p + \omega^{ref}) \tag{3.79}$$

If using a GFM, we must update the state-space for the IBR branch by substituting $\{\omega_{ibr}, \theta_{ibr}\}$ with $\{\omega_{psl}, \theta_{psl}\}$. Taking into account all differential equations from this subsection, in addition to (3.10)-(3.17), we get to the following set of state-space vectors:

$$\begin{aligned} x = \Big[& i_{f_d} \quad i_{f_q} \quad v_{dc} \quad v_{f_d} \quad v_{f_q} \quad i_s \quad i_{g_d} \quad i_{g_q} \\ & \gamma_p \quad \theta_{psl} \quad \gamma_q \quad \gamma_{\text{TVR}_d} \quad \gamma_{\text{TVR}_q} \quad \gamma_{v_{f_d}} \\ & \gamma_{v_{f_q}} \quad \gamma_{i_{f_d}} \quad \gamma_{i_{f_q}} \quad \gamma_{v_{dc}} \Big]^t \end{aligned} \tag{3.80}$$

$$u = \Big[i_s^{ref} \quad p^{ref} \quad V^{ref} \quad q^{ref} \quad {v_{dc}}^{ref} \quad \omega^{ref} \quad v_{gd}^{g} \quad v_{gq}^{g} \quad \theta_g \Big]^t \tag{3.81}$$

$$z = \Big[m_d \quad m_q \quad \omega_{psl} \Big]^t \tag{3.82}$$

$$\begin{aligned} p = \Big[& \omega_b \quad R_f \quad L_f \quad C_f \quad R_t \quad L_t \quad C_{dc} \quad \omega_s \quad \omega_{ff} \quad \omega_p \\ & m_p \quad \omega_q \quad n_q \quad \omega_{tvr} \quad R_v^{tvr} \quad R_v \quad X_v \quad {K_p}^v \quad {K_i}^v \\ & {K_p}^i \quad {K_i}^i \quad {K_p}^{vdc} \quad {K_i}^{vdc} \Big]^t \end{aligned} \tag{3.83}$$

According to the same principles applied at the end of subsection 3.2.1, we obtain an output vector $\boldsymbol{y}$:

$$\boldsymbol{y} = \begin{bmatrix} {i_{gd}}^g \\ {i_{gq}}^g \end{bmatrix} = \begin{bmatrix} \boldsymbol{R}(\theta_{psl} - \theta_g) & \boldsymbol{0_2} \\ \boldsymbol{0_2} & \boldsymbol{R}(\theta_{psl} - \theta_g) \end{bmatrix} \begin{bmatrix} i_{g_d} \\ i_{g_q} \end{bmatrix} \tag{3.84}$$

3.2.2.1 Generic modeling of GFM controllers: recent developments

Although our modeling choices have already been justified throughout this section, it is worth extending the discussion on the validity of these models when considering the plethora of GFM control methods available in the literature.

Despite the challenge of establishing a unified model for IBR controllers, researchers have made considerable progress in recent years toward the generic modeling of IBRs. In [87], authors have provided a summary of this topic. Most notably, generic models, usually employed in planning studies, are supposed to be vendor-agnostic and should be able to approximately depict the dynamic behavior of IBRs when properly parameterized. For such, these models take advantage of some fundamental building blocks, which are capable of portraying a wide range of behaviors. In GFLs, for instance, these would be the PLL and the inner current control loop; by adding these two components to the preexisting generic models, it is possible to accurately depict SICDS issues in simulations [34], and in small-signal stability analysis [35]. Generic models also exploit some inherent similarities between control methods, such as a Virtual Oscillator Control (VOC) and a PLL [105], or a PSL and a VSM [106]. These similarities allow us to parameterize the models in such a way as to emulate the behavior of different control methods. This is particularly interesting from the point of view of system operators, given that they can establish standardized requirements for a generic control strategy that can be further "translated" onto different control methods.

With respect to GFMs in particular, to unify the wide range of control strategies proposed in the literature, researchers have been suggesting some broad classifications. In [87], there are categories for Droop-based control (DBC) [80], VSM [82], Matching Control (MC) [74], and VOC [83]. This is a subject of debate, and this list is not exhaustive, be it because of the existence of other categories (PLL-based GFM, for instance [106]) or due to further similarities between the aforementioned categories, which could lead to a different clustering: a VSM, for example, is a droop-based control with added inertial effect [107], and they can be made equivalent in terms of small-signal stability [108].

These categories are helpful in light of the comparative analyses provided in the literature. For example, EMT implementations led to slight differences in transient behavior in [87], suggesting nonetheless the possibility of unifying the controllers in positive sequence through the parameterization of generic models. For our purposes, however, since we are interested in the assessment of small-signal interactions in a distribution grid with GFMs, the most important conclusions can be taken from [63] and [100]. Mentioning the same categories as [87], the authors of [63] argue that all these strategies lead to equivalent small-signal behavior (an idea that is further elaborated in [109]) and can be thus reduced to a droop-based controller. Focusing specifically on the comparison of such GFM control methods, including "advanced methods" (as presented in [84], namely MC and dispatchable VOC), the authors of [100] concluded that the addition of low-pass filters allows for an equivalent representation of dVOC, VSM, and DBC. In any case, the authors were able to tune these four controllers so as to ensure similar dynamic behavior, which suggests the possibility of using a common droop-based model for representing GFMs in small-signal studies.

3.3 Modeling of an MV distribution grid

As mentioned at the beginning of this chapter, all lines of the MVDG in our case studies will be represented by their π-model, whereas loads, all of which are resistive-inductive, will be taken as RL circuits, as indicated in Figure 3.6. It is worth mentioning that MV lines, although short, may present significant capacitance when employing underground cables, namely a susceptance of 47.5 μS/km[4] in the Cigre benchmark network [90]. This calls for an accurate representation of such capacitances, hence the use of π-models, which are also convenient for a modular state-space representation of the MVDG, given that node voltages are then state variables rather than algebraic.

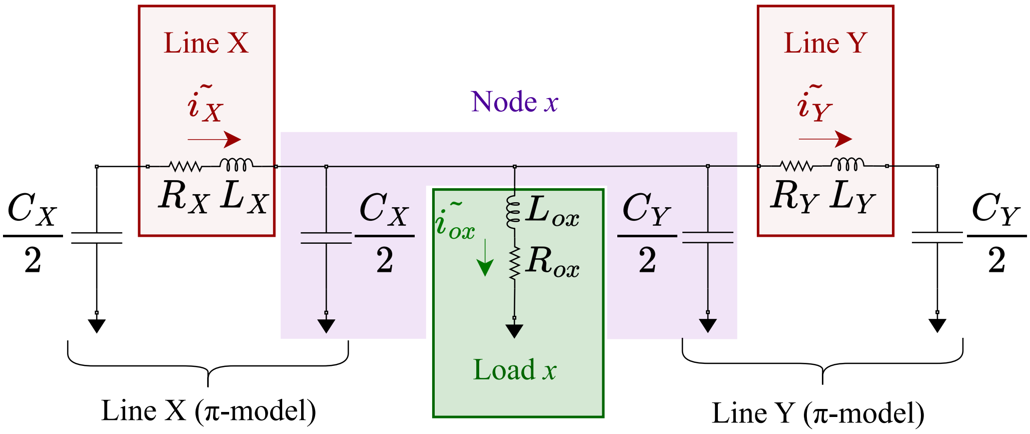

Figure 3.6: π-representation for MV distribution lines

An MVDG may thus be subdivided into nodes, loads, and lines, as indicated in Figure 3.7. Each node contains the bundled capacitances of all π-model lines connected to it, hence the state-space will consider the capacitor voltage as a state, and all inwards and outwards currents as inputs, as in Figure 3.7a. These currents include the line and load currents, as well as the currents injected by IBRs into the node. For each load, as indicated in Figure 3.7b, the nodal voltage is an input, while the load current is a state variable. Finally, for lines, the state variables are their currents, while two node voltages serve as inputs, as shown in Figure 3.7c. All differential equations describing each of these components are given below, after a brief note on the global dq reference frame.

Global reference frame

A global frequency reference ω_g is given as an input for the grid model and passed to all IBR state-spaces as a phase θ_g:

$$\dot{\theta}_g = \omega_b\, \omega_g \tag{3.85}$$

While ω_g is an input, ω_{g0} is a *parameter*, and both are always assumed to have the same value, i.e, $\omega_g = \omega_{g0}$[5]. Using ω_{g0} as a parameter allows for the grid model to be linear,

---

[4] For overhead lines, the susceptance is of 3.2 μS/km [90], almost 15 times lower.

[5] They are both adopted as 1 pu, i.e., 50 Hz, or 314 rad/s.

exempting us from yet another linearization. Because all state variables within the grid model are already in the global reference frame, they do not require a superscript "g" and they are not rotated onto a different dq frame when used as outputs.

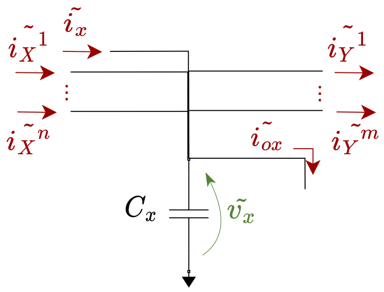

(a) Node

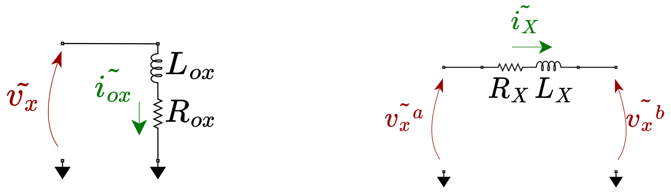

(b) Load (c) Line

Figure 3.7: Building blocks within the grid model

Nodes

$$\frac{C_x}{\omega_b}\,\dot{v}_{xd} = i_{xd} + \sum_{X\in\mathcal{X}_x} i_{X\,d} - \sum_{Y\in\mathcal{Y}_x} i_{Y\,d} - i_{ox\,d} + \omega_{g0}\,C_x\,v_{xq} \tag{3.86}$$

$$\frac{C_x}{\omega_b}\,\dot{v}_{xq} = i_{xq} + \sum_{X\in\mathcal{X}_x} i_{X\,q} - \sum_{Y\in\mathcal{Y}_x} i_{Y\,q} - i_{ox\,q} - \omega_{g0}\,C_x\,v_{xd} \tag{3.87}$$

A node x in an MVDG, in addition to its parameter vector $\boldsymbol{p} = [C_x]$, as shown in Figure 3.7a, may be represented by the following state-space vectors, derived from the differential equations (3.86)-(3.87):

$$\boldsymbol{x} = \boldsymbol{y} = \begin{bmatrix} v_{xd} & v_{xq} \end{bmatrix}^t \tag{3.88}$$

$$\begin{aligned}\boldsymbol{u} = \Big[& i_{xd}^{g} \quad i_{xq}^{g} \quad i_{X\,d}^{1} \quad i_{X\,q}^{1} \quad \ldots \quad i_{X\,d}^{n} \quad i_{X\,q}^{n} \\ & i_{Y\,d}^{1} \quad i_{Y\,q}^{1} \quad \ldots \quad i_{Y\,d}^{m} \quad i_{Y\,q}^{m} \quad i_{ox\,d} \quad i_{ox\,q} \Big]^t\end{aligned} \tag{3.89}$$

Note that the currents i_{xdq} are injected by the IBRs connected at node x, hence they should be rotated to the common reference frame, i.e., $\{i_{xd}^{g}, i_{xq}^{g}\}$, before being associated with the state-spaces of their respective nodes. In (3.89), we assume a total of n lines entering the node x and m lines exiting it, as depicted in Figure 3.7a.

Loads

$$\frac{L_{ox}}{\omega_b}\,\dot{i}_{oxd} = v_{xd} - R_{ox}\,i_{oxd} + \omega_{g0}\,L_{ox}\,i_{oxq} \tag{3.90}$$

$$\frac{L_{ox}}{\omega_b}\,\dot{i}_{oxq} = v_{xq} - R_{ox}\,i_{oxq} - \omega_{g0}\,L_{ox}\,i_{oxd} \tag{3.91}$$

A load x, in turn, with $\boldsymbol{p} = [R_{ox}\ L_{ox}]^t$, as shown in Figure 3.7b, is given by these vectors, also derived from its differential equations (3.90)-(3.91):

$$\boldsymbol{x} = \boldsymbol{y} = \begin{bmatrix} i_{oxd} & i_{oxq} \end{bmatrix}^t \tag{3.92}$$

$$\boldsymbol{u} = \begin{bmatrix} v_{xd} & v_{xq} \end{bmatrix}^t \tag{3.93}$$

Lines

$$\frac{L_X}{\omega_b}\,\dot{i}_{X\,d} = v_{x\,d}^{\,a} - v_{x\,d}^{\,b} - R_X\,i_{X\,d} + \omega_{g0}\,L_X\,i_{X\,q} \tag{3.94}$$

$$\frac{L_X}{\omega_b}\,\dot{i}_{X\,q} = v_{x\,q}^{\,a} - v_{x\,q}^{\,b} - R_X\,i_{X\,q} - \omega_{g0}\,L_X\,i_{X\,d} \tag{3.95}$$

Finally, a line X, surrounded by nodes x^a and x^b, with $\boldsymbol{p} = [R_X\ L_X]^t$, as in Figure 3.7c, considering the equations (3.94)-(3.95), yields the following state-space vectors:

$$\boldsymbol{x} = \boldsymbol{y} = \begin{bmatrix} i_{X\,d} & i_{X\,q} \end{bmatrix}^t \tag{3.96}$$

$$\boldsymbol{u} = \begin{bmatrix} v_{x\,d}^{\,a} & v_{x\,q}^{\,a} & v_{x\,d}^{\,b} & v_{x\,q}^{\,b} \end{bmatrix}^t \tag{3.97}$$

3.4 Modeling of the upstream network

Our chosen representation for the upstream network is an infinite bus with an inductive impedance, as in Figure 3.8. A more complex representation could rely on an equivalent model of a synchronous generator, with varying degrees of inertia, or even a multi-machine system. However, for the purpose of studying small-signal control interactions in the MV grid, as explained at the beginning of this chapter, a voltage-behind-impedance model is sufficient[6].

---

[6] We shall reiterate that our case study does not involve a low-inertia transmission network upstream from the substation. In such a case, an infinite bus would not be an adequate representation of the upstream network. Further work is necessary to extend our conclusions for these situations.

Here we adopt the hypothesis of a “perfect” upstream network, which is capable of providing power without any kind of dynamic constraints, limiting our scope to instabilities caused by interactions between IBRs themselves – the only dynamic devices in this system – rather than including interactions with the HV network upstream.

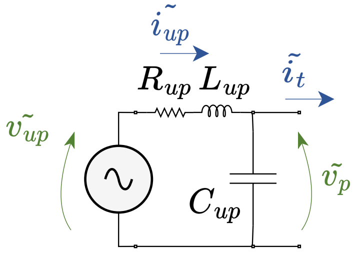

Figure 3.8: Physical model of an equivalent upstream network

A frequency ω_{up} is given as an input to the upstream network, yielding a phase θ_{up}:

$$\dot{\theta_{up}} = \omega_b \, \omega_{up} \tag{3.98}$$

An impedance, which in EMT is modeled by an RL circuit, reproduces power transfer limitations, as well as the damping properties of the network upstream:

$$\frac{L_{up}}{\omega_b} \, \dot{i_{up}}_d^g = V_{up} - {v_p}_d^g - R_{up} \, {i_{up}}_d^g + \omega_{up} \, L_{up} \, {i_{up}}_q^g \tag{3.99}$$

$$\frac{L_{up}}{\omega_b} \, \dot{i_{up}}_q^g = -{v_p}_q^g - R_{up} \, {i_{up}}_q^g - \omega_{up} \, L_{up} \, {i_{up}}_d^g \tag{3.100}$$

A small capacitor is included to simplify the dynamic equations and to represent a capacitor bank in the substation if such is the case:

$$\frac{C_{up}}{\omega_b} \, \dot{v_p}_d^g = {i_{up}}_d^g - {i_t}_d^g + \omega_{up} \, C_{up} \, {v_p}_q^g \tag{3.101}$$

$$\frac{C_{up}}{\omega_b} \, \dot{v_p}_q^g = {i_{up}}_q^g - {i_t}_q^g - \omega_{up} \, C_{up} \, {v_p}_d^g \tag{3.102}$$

As for the IBRs and the MVDG, the upstream network also translates into a state-space:

$$\boldsymbol{x} = \begin{bmatrix} \theta_{up} & {i_{up}}_d^g & {i_{up}}_q^g & {v_p}_d^g & {v_p}_q^g \end{bmatrix}^t \tag{3.103}$$

$$\boldsymbol{u} = \begin{bmatrix} \omega_{up} & V_{up} & {i_t}_d^g & {i_t}_q^g & \theta_g \end{bmatrix}^t \tag{3.104}$$

$$\boldsymbol{p} = \begin{bmatrix} \omega_b & R_{up} & L_{up} & C_{up} \end{bmatrix}^t \tag{3.105}$$

For the output, we may take $\{v_{p_d}^g, v_{p_q}^g\}$, which is the voltage at Node 0 in Figure 3.1:

$$\boldsymbol{y} = \begin{bmatrix} v_{p_d}^g & v_{p_q}^g \end{bmatrix}^t \tag{3.106}$$

3.5 State-space association technique (SSAT)

3.5.1 General method

Considering a set of n state-spaces, either linear or linearized[7], written in the form:

$$\dot{\boldsymbol{x_i}} = \boldsymbol{A_i}\,\boldsymbol{x_i} + \boldsymbol{B_i}\,\boldsymbol{u_i}, \qquad \forall i \in [1, n] \tag{3.107}$$

$$\boldsymbol{y_i} = \boldsymbol{C_i}\,\boldsymbol{x_i} + \boldsymbol{D_i}\,\boldsymbol{u_i} \tag{3.108}$$

We may consider them as a single system, which may be written in an open-loop form, hereby denoted by subscript "L":

$$\dot{\boldsymbol{x_L}} = \boldsymbol{A_L}\,\boldsymbol{x_L} + \boldsymbol{B_L}\,\boldsymbol{u_L} \tag{3.109}$$

$$\boldsymbol{y_L} = \boldsymbol{C_L}\,\boldsymbol{x_L} + \boldsymbol{D_L}\,\boldsymbol{u_L} \tag{3.110}$$

where

$$\boldsymbol{x_L} = \begin{bmatrix} \boldsymbol{x_1} \\ \boldsymbol{x_2} \\ \vdots \\ \boldsymbol{x_{n_s-1}} \\ \boldsymbol{x_{n_s}} \end{bmatrix} \qquad \boldsymbol{u_L} = \begin{bmatrix} \boldsymbol{u_1} \\ \boldsymbol{u_2} \\ \vdots \\ \boldsymbol{u_{n_i-1}} \\ \boldsymbol{u_{n_i}} \end{bmatrix} \qquad \boldsymbol{y_L} = \begin{bmatrix} \boldsymbol{y_1} \\ \boldsymbol{y_2} \\ \vdots \\ \boldsymbol{y_{n_o-1}} \\ \boldsymbol{y_{n_o}} \end{bmatrix} \tag{3.111}$$

and

$$\boldsymbol{A_L} = \begin{bmatrix} \boldsymbol{A_1} & \boldsymbol{0} & \dots & \boldsymbol{0} & \boldsymbol{0} \\ \boldsymbol{0} & \boldsymbol{A_2} & \dots & \boldsymbol{0} & \boldsymbol{0} \\ \vdots & \vdots & \ddots & \vdots & \vdots \\ \boldsymbol{0} & \boldsymbol{0} & \dots & \boldsymbol{0} & \boldsymbol{A_n} \end{bmatrix} \qquad \boldsymbol{B_L} = \begin{bmatrix} \boldsymbol{B_1} & \boldsymbol{0} & \dots & \boldsymbol{0} & \boldsymbol{0} \\ \boldsymbol{0} & \boldsymbol{B_2} & \dots & \boldsymbol{0} & \boldsymbol{0} \\ \vdots & \vdots & \ddots & \vdots & \vdots \\ \boldsymbol{0} & \boldsymbol{0} & \dots & \boldsymbol{0} & \boldsymbol{B_n} \end{bmatrix} \tag{3.112}$$

$$\boldsymbol{C_L} = \begin{bmatrix} \boldsymbol{C_1} & \boldsymbol{0} & \dots & \boldsymbol{0} & \boldsymbol{0} \\ \boldsymbol{0} & \boldsymbol{C_2} & \dots & \boldsymbol{0} & \boldsymbol{0} \\ \vdots & \vdots & \ddots & \vdots & \vdots \\ \boldsymbol{0} & \boldsymbol{0} & \dots & \boldsymbol{0} & \boldsymbol{C_n} \end{bmatrix} \qquad \boldsymbol{D_L} = \begin{bmatrix} \boldsymbol{D_1} & \boldsymbol{0} & \dots & \boldsymbol{0} & \boldsymbol{0} \\ \boldsymbol{0} & \boldsymbol{D_2} & \dots & \boldsymbol{0} & \boldsymbol{0} \\ \vdots & \vdots & \ddots & \vdots & \vdots \\ \boldsymbol{0} & \boldsymbol{0} & \dots & \boldsymbol{0} & \boldsymbol{D_n} \end{bmatrix} \tag{3.113}$$

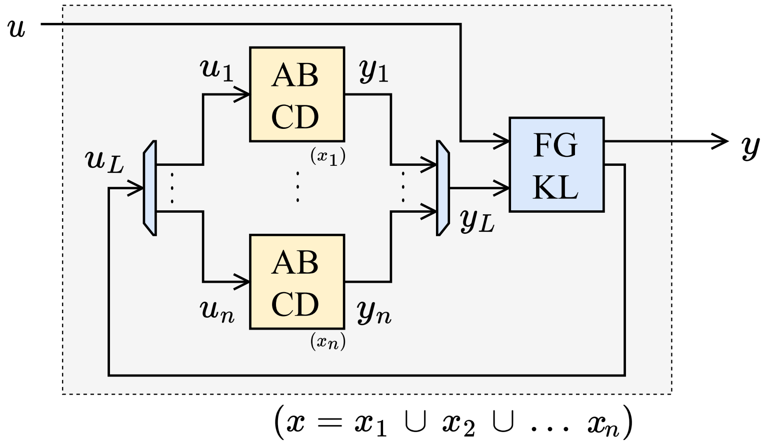

Figure 3.9: State-space association technique

An open-loop association does not consider any relation between individual state-spaces. In order to obtain a global state-space that takes them into account, we must first select a set of global inputs $\boldsymbol{u}$ and define a set of global outputs $\boldsymbol{y}$. All states must be included in the global state-space: $\boldsymbol{x} = \boldsymbol{x_L}$[8]. Since the set of open-loop inputs $\boldsymbol{u_L}$ contains the closed-loop input vector $\boldsymbol{u}$ (or a combination of it with local outputs), it may be written as a function of $\boldsymbol{u}$ and $\boldsymbol{y_L}$. Similarly, closed-loop output vector $\boldsymbol{y}$ may also be written as a function of $\boldsymbol{u}$ and $\boldsymbol{y_L}$, as expressed below:

$$\boldsymbol{u_L} = \boldsymbol{F}\,\boldsymbol{u} + \boldsymbol{G}\,\boldsymbol{y_L} \tag{3.114}$$

$$\boldsymbol{y} = \boldsymbol{K}\,\boldsymbol{u} + \boldsymbol{L}\,\boldsymbol{y_L} \tag{3.115}$$

Replacing (3.114) in (3.110):

$$\boldsymbol{y_L} = \boldsymbol{E_L}\,(\boldsymbol{C_L}\,\boldsymbol{x_L} + \boldsymbol{D_L}\,\boldsymbol{F}\,\boldsymbol{u}) \tag{3.116}$$

where

$$\boldsymbol{E_L} = (\boldsymbol{I} - \boldsymbol{D_l}\,\boldsymbol{G})^{-1} \tag{3.117}$$

Now using (3.116) in (3.114), with $\boldsymbol{x} = \boldsymbol{x_L}$:

$$\boldsymbol{u_L} = (\boldsymbol{G}\,\boldsymbol{E_L}\,\boldsymbol{C_L})\,\boldsymbol{x} + (\boldsymbol{F} + \boldsymbol{G}\,\boldsymbol{E_L}\,\boldsymbol{D_L}\,\boldsymbol{F})\,\boldsymbol{u} \tag{3.118}$$

Finally, substituting $\boldsymbol{u_L}$ from (3.118) into (3.109), and $\boldsymbol{y_L}$ from (3.116) into (3.115), we derive a closed-loop state-space:

---

[7] Following the procedure outlined in Section 1.2.5.

[8] Remember that, as defined in Section 1.2.5, state variables represent the minimum information necessary to describe the dynamics of a system, hence we cannot eliminate states without losing information.

$$\dot{\boldsymbol{x}} = \boldsymbol{A}\,\boldsymbol{x} + \boldsymbol{B}\,\boldsymbol{u} \tag{3.119}$$

$$\boldsymbol{y} = \boldsymbol{C}\,\boldsymbol{x} + \boldsymbol{D}\,\boldsymbol{u} \tag{3.120}$$

where

$$\boldsymbol{A} = \boldsymbol{A_L} + \boldsymbol{B_L}\,\boldsymbol{G}\,\boldsymbol{E_L}\,\boldsymbol{C_L} \tag{3.121}$$

$$\boldsymbol{B} = (\boldsymbol{B_L}\,\boldsymbol{G}\,\boldsymbol{E_L}\,\boldsymbol{D_L} + \boldsymbol{B_L})\,\boldsymbol{F} \tag{3.122}$$

$$\boldsymbol{C} = \boldsymbol{L}\,\boldsymbol{E_L}\,\boldsymbol{C_L} \tag{3.123}$$

$$\boldsymbol{D} = \boldsymbol{L}\,\boldsymbol{E_L}\,\boldsymbol{D_L}\,\boldsymbol{F} + \boldsymbol{K} \tag{3.124}$$

3.5.2 SSAT applied to an MVDG with IBRs

For our case study, where IBRs are connected to the Cigre benchmark MVDG with an infinite-bus HV network upstream, as displayed in Figure 3.10, the objective is to obtain a state matrix $\boldsymbol{A}$ whose eigenvalues will provide information about the system's small-signal stability, as explained in Section 1.2.5. This could be done in two steps.

Step 1: reduce the MVDG to a single state-space

First, we should utilize the state-space association technique (SSAT) to obtain a single state-space for the MVDG from the individual state-spaces of its components, i.e., nodes, loads, and lines. This means employing the open-loop vectors $\boldsymbol{u_L}$ and $\boldsymbol{y_L}$ from (3.125)-(3.126) in addition to the close-loop vectors $\boldsymbol{u}$ and $\boldsymbol{y}$ from (3.128)-(3.129) in the equations (3.114)-(3.115), obtaining the matrices $\boldsymbol{F}$, $\boldsymbol{G}$, $\boldsymbol{K}$, and $\boldsymbol{L}$, which will provide a single closed-loop state-space for the MVDG through equations (3.121)-(3.124). This procedure is illustrated in Figure 3.11.

These are the generic open-loop input and output vectors for the MVDG:

$$\boldsymbol{u_L} = \begin{bmatrix} \boldsymbol{u_1^{\mathcal{N}}} & \dots & \boldsymbol{u_{14}^{\mathcal{N}}} & \boldsymbol{u_1^{\mathcal{O}}} & \dots & \boldsymbol{u_{14}^{\mathcal{O}}} & \boldsymbol{u_A^{\mathcal{L}}} & \dots & \boldsymbol{u_N^{\mathcal{L}}} & \omega_g \end{bmatrix}^t \tag{3.125}$$

$$\boldsymbol{y_L} = \begin{bmatrix} \boldsymbol{y_1^{\mathcal{N}}} & \dots & \boldsymbol{y_{14}^{\mathcal{N}}} & \boldsymbol{y_1^{\mathcal{O}}} & \dots & \boldsymbol{y_{14}^{\mathcal{O}}} & \boldsymbol{y_A^{\mathcal{L}}} & \dots & \boldsymbol{y_N^{\mathcal{L}}} & \theta_g \end{bmatrix}^t \tag{3.126}$$

where the superscripts $\mathcal{N}$, $\mathcal{O}$, and $\mathcal{L}$, designate nodes (3.88)-(3.89), loads (3.92)-(3.93), and lines (3.96)-(3.97), respectively.

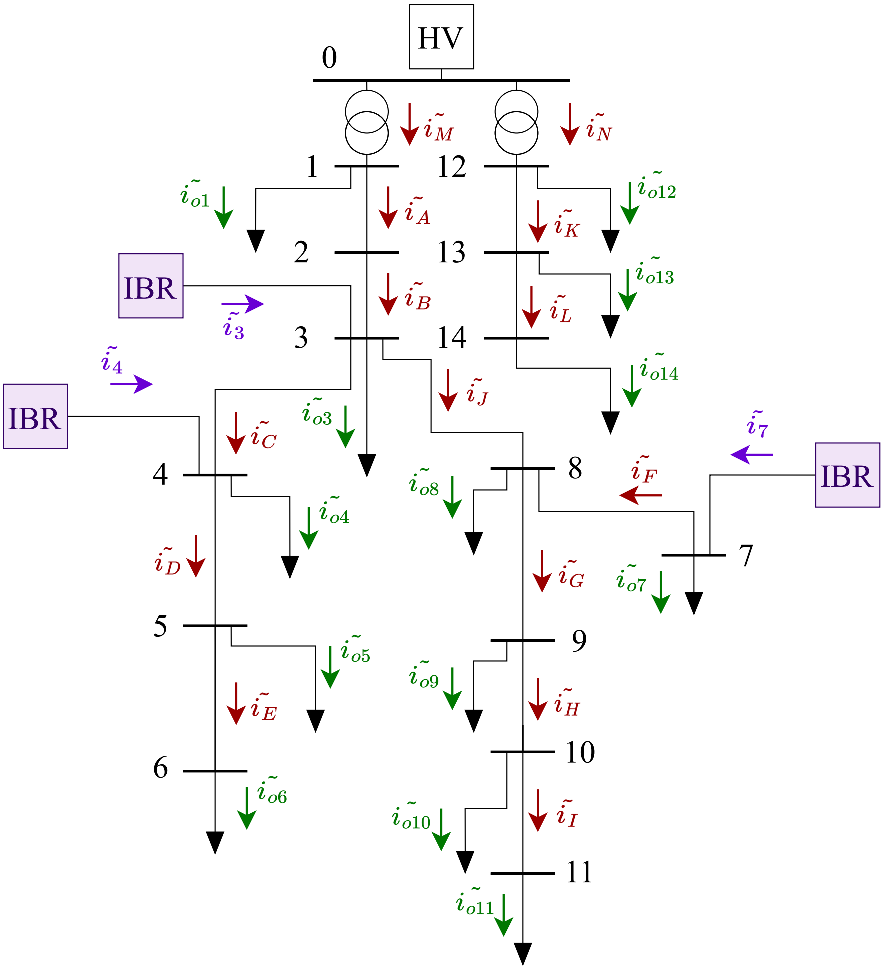

Figure 3.10: Nomenclature and convention for current directions in the Cigre benchmark MVDG. Three IBRs are positioned arbitrarily to illustrate the direction of injected currents. Line currents are named with capital letters, while load currents are named with the letter "*o*" and the node number, and injected currents are named as their node number exclusively.

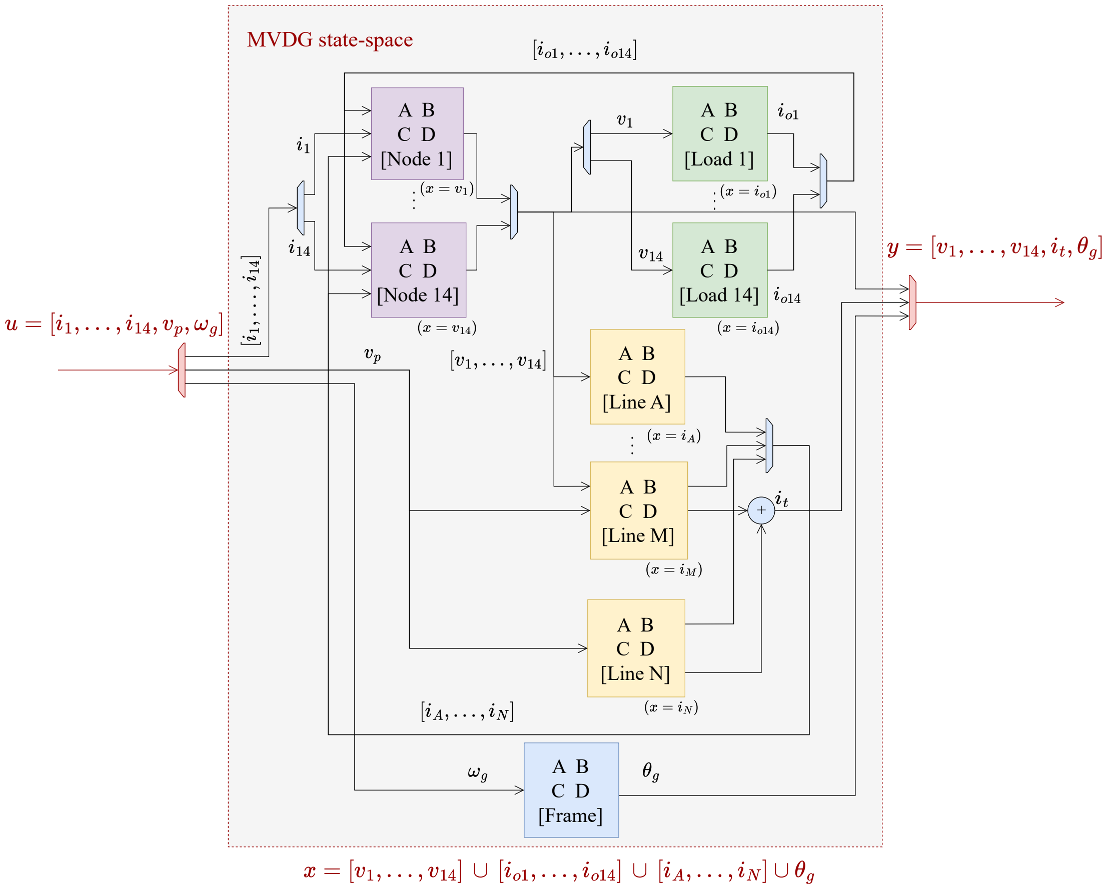

Figure 3.11: SSAT applied to the benchmark MVDG

A *closed-loop* MVDG representation, on the other hand, leads to the following vectors:

$$\boldsymbol{x} = \begin{bmatrix} v_{1d} & v_{1q} & \dots & v_{14d} & v_{14q} & i_{o1d} & i_{o1q} & \dots & i_{o14d} & i_{o14q} \\ & & & & & i_{Ad} & i_{Aq} & \dots & i_{Nd} & i_{Nq} & \theta_g \end{bmatrix}^t \tag{3.127}$$

$$\boldsymbol{u} = \begin{bmatrix} i_{1d} & i_{1q} & \dots & i_{14d} & i_{14q} & v_{pd}^{g} & v_{pq}^{g} & \omega_g \end{bmatrix}^t \tag{3.128}$$

$$\boldsymbol{y} = \begin{bmatrix} v_{1d} & v_{1q} & \dots & v_{14d} & v_{14q} & i_{td} & i_{tq} & \theta_g \end{bmatrix}^t \tag{3.129}$$

Step 2: obtain the final state-space with IBRs, MVDG, and upstream network

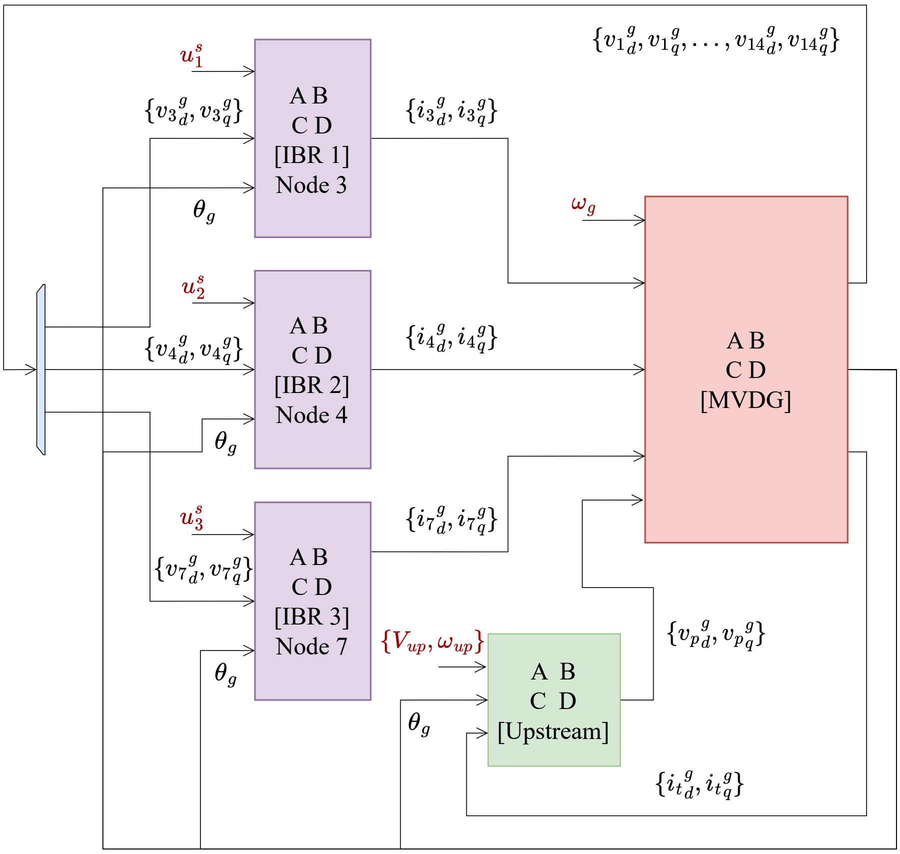

Figure 3.12: SSAT applied to the entire system, using the example from Figure 3.10 where IBRs are connected to nodes 3, 4, and 7.

The following step is to associate all individual state-spaces of each IBR to the state-space of the MVDG and the upstream network, as shown in Figure 3.12, where, for the k^{th} IBR, the input sub-vector $\boldsymbol{u_k^s}$ represents its setpoints:

$$\boldsymbol{u_k^s} = \begin{bmatrix} i_s^{ref} & {v_{dc}}^{ref} & q^{ref} \end{bmatrix}^t \qquad \text{if GFL} \tag{3.130}$$

$$\boldsymbol{u_k^s} = \begin{bmatrix} i_s^{ref} & p^{ref} & V^{ref} & q^{ref} & {v_{dc}}^{ref} \end{bmatrix}^t \qquad \text{if GFM} \tag{3.131}$$

The final system, considering a generic number of n IBRs, will present the following open-loop input and output vectors:

$$\begin{aligned} \boldsymbol{u_L} = \Big[& \boldsymbol{u_1^s} \quad {v_1}_d^g \quad {v_1}_q^g \quad \theta_g \quad \dots \quad \boldsymbol{u_n^s} \quad {v_n}_d^g \quad {v_n}_q^g \quad \theta_g, \\ & \qquad \boldsymbol{u_L}^{\text{MVDG}}, \quad \boldsymbol{u_{up}^s} \quad {i_t}_d^g \quad {i_t}_q^g \quad \theta_g \Big]^t \end{aligned} \tag{3.132}$$

$$\boldsymbol{y_L} = \begin{bmatrix} {i_1}_d^g & {i_1}_q^g & \dots & {i_n}_d^g & {i_n}_q^g, & \boldsymbol{y_L}^{\text{MVDG}}, & {v_p}_d^g & {v_p}_q^g \end{bmatrix}^t \tag{3.133}$$

where $\boldsymbol{u_L}^{\text{MVDG}}$ and $\boldsymbol{y_L}^{\text{MVDG}}$ are given by (3.125) and (3.126), respectively.

Here, $\boldsymbol{u_{up}^s} = \begin{bmatrix} V_{up} \; \omega_{up} \end{bmatrix}^t$ could be taken as the setpoint vector for the upstream network.

A closed-loop input vector would consist exclusively of setpoints, noting that the only setpoint for the closed-loop MVDG state-space is ω_g:

$$\boldsymbol{u} = \begin{bmatrix} \boldsymbol{u_1^s} & \dots & \boldsymbol{u_n^s} & \omega_g & \boldsymbol{u_{up}^s} \end{bmatrix}^t \tag{3.134}$$

The state vector of the final state-space, defined in (3.135), is just an ensemble of all the state variables in the system, including all IBRs, either GFL, as in (3.50) or (3.54), or GFM, as in (3.80), as well as the MVDG, (3.127), and the upstream network, (3.103).

$$\boldsymbol{u} = \begin{bmatrix} \boldsymbol{x_1}^{\text{IBR}} & \dots & \boldsymbol{x_n}^{\text{IBR}}, & \boldsymbol{x}^{\text{MVDG}}, & \boldsymbol{x}^{\text{up}} \end{bmatrix}^t \tag{3.135}$$

Using the vectors $\boldsymbol{u}$, $\boldsymbol{uL}$, and $\boldsymbol{y_L}$ from (3.134), (3.132), and (3.133), respectively, in (3.114), one may obtain the matrix $\boldsymbol{G}$, which, combined with $\boldsymbol{E_L}$ from (3.116), yields the final state matrix $\boldsymbol{A}$ via (3.121). All other matrices are unnecessary, this matrix $\boldsymbol{A}$ is the only one to be deployed in the SSSA.

3.6 Sizing and parameterization

All the steps necessary for building the $\boldsymbol{A}$ matrix have already been prescribed, yet the *numerical values* of its entries still depend on the sizing of passive IBR components, namely the output filter and DC-link capacitor, as well as the parameterization of IBR controllers, either GFL or GFM. This final step, notably the tuning of certain control loops, is crucial for the

SSSA, inasmuch as it defines the parameters used in the sensitivity analyses. Some of these parameters will eventually constitute the guidelines for the DSO to prevent SICDS in MVDGs. With this in mind, following a discussion on the sizing of physical elements, we provide a brief overview of the tuning of PI controllers for first-order systems, deriving basic formulas that will be applied in tuning the controllers. Because the tuning in itself is a straightforward process, the application of these formulas for each control loop is available as a supplement to this dissertation, in the Appendix A.

A detailed sizing of output filters and LV/MV transformers in particular is out of scope for this chapter, mostly focused on the parameterization of IBR controllers, but because their sizing may also have an impact on small-signal stability, our main choices are summarized below.

First, since producers connected to MVDGs in France are allowed to inject up to 12 MW [5], we adopt an IBR with rated power $S_{ibr} = 10\,\text{MVA}$, as expressed in Table 3.2, so that there is a 20 % margin for active power control if needed. This rated power is relatively high for most PV plants connected to distribution networks, but since our goal is to study stability problems, it is reasonable to consider large installations, which would have a higher dynamic impact on the system. It is also worth mentioning that here, considering what is usually done in literature, we assume a single "equivalent" inverter connecting the PV plant to the grid. Under certain conditions, it may be interesting to reproduce plant architecture in more detail, but this is not in accordance with our objective of building a generic model, hence we adopt a single aggregated inverter, primarily based on ABB Central Solar Inverter, Model: PVS980-58 [110]. Since this is a 5 MVA inverter, we assume two of them aggregated into a single model.

Parameter	Symbol	Value
Rated Power	S_{ibr}	10 MVA
Nominal RMS Line Voltage (MV)	U_{ibr}^{MV}	20 kV
Nominal RMS Phase Voltage (LV)	V_{ibr}^{LV}	400 V
Nominal DC Voltage	V_{ibr}^{DC}	1127 V

Table 3.2: Converter rating

A basic LV/MV transformer, as described in Table 3.3, is enough for our purposes. Since the rated power is not very high, an inductance of $L_t = 0.05\,\text{pu}$ is considered reasonable. We also assume transformer losses to be almost negligible, especially in comparison to MV lines, hence the series resistance is merely 1 % of the reactance.

Taking Figure 3.2, ignoring load and line, if the IBR was directly connected to an infinite bus, power transfer in steady-state would follow the classic formula: $P = V_f\, V_l\, \sin(\delta)/(\omega\,(L_f + L_t))$. For $P = 1\,\text{pu}$, with rated voltages and frequency, δ must be kept under 30°, hence $L_f + L_t < 0.5\,\text{pu}$, which translates into $L_f^{max} = 0.45\,\text{pu}$. On the other hand, L_f must be

Parameter	Symbol	Value
Rated Power	S_t	10 MVA
Nominal RMS Line Voltage (MV)	U_t^{MV}	20 kV
Nominal RMS Line Voltage (LV)	U_t^{LV}	690 V
Series inductance	L_t	0.05 pu
Series resistance	R_t	0.0005 pu

Table 3.3: Transformer rating

large enough to keep output current ripples under an acceptable range. From (3.136) [69], considering $V_{dc} = 1127\,\text{V}$, $f_{sw} = 5\,\text{kHz}$ and $L_{base} = 0.15\,\text{mH}$, we get to $L_f^{min} = 0.08\,\text{pu}$. From now on, we adopt $L_f = 0.1\,\text{pu}$, which is about 30 % higher than the minimum, in order to avoid overtly high short-circuit currents, but low enough to avoid power delivery issues.

$$L_f^{min} = \frac{1}{8}\,\frac{V_{dc}}{\Delta i_f\, f_{sw}\, L_{base}} \tag{3.136}$$

For proper harmonics attenuation, i.e., a total harmonic distortion (THD) below 5 %, the cut-off frequency related to the LC components of the output filter $f_{LC} = 2\pi\, f_n/\sqrt{L_f\, C_f}$ must be between $10\, f_n$ and $0.1\, f_{sw}$ [69], where $f_n = 50\,\text{Hz}$ is the nominal frequency; this leads to $C_f^{min} = 0.02\,\text{pu}$ (3.137). Applying the same formula with $L_f = 0.1\,\text{pu}$ instead of L_f^{max} leads to $C_f = 0.1\,\text{pu}$, which implies $f_{LC} \approx 17\, f_n$ thus above $10\, f_n$. We may therefore adopt $C_f = 0.1\,\text{pu}$ for the rest of this dissertation.

$$C_f^{min} = \frac{100\, f_n^2}{L_f^{max}\, f_{sw}^2} \tag{3.137}$$

Finally, since losses for inductive filters are on the order of 1 %, we adopt $R_f = 0.01\,\text{pu}$. Results are summarized in Table 3.4. Once again, precise and thorough sizing of the output filter is out of the scope of this report, for further explanations and details concerning this topic, please refer to [69].

A final component to design is the DC-link capacitor C_{dc}, which has strong implications in both small-signal and large-signal stability, especially due to its "inertial" effect. This capacitor is designed to minimize voltage ripples Δv_{dc}. We may thus employ a formula provided in [111], which corresponds to 1/6 of the minimal capacitance required by a single-phase inverter:

$$C_{dc}^{min} = \frac{1}{6}\,\frac{P_n}{\omega_b\, v_{dc}^n\, \Delta v_{dc}} \tag{3.138}$$

Considering $v_{dc}^n = 1127\,\text{V}$ and $v_{dc}^{max} = 1500\,\text{V}$, we get a ripple of $\Delta v_{dc} = 2\,(v_{dc}^{max} - v_{dc}^n) = 746\,\text{V}$, which is almost 2/3 of the nominal v_{dc}, hence a very relaxed estimate. For $P_n = 10\,\text{MW}$, we obtain $C_{dc}^{min} = 6.3\,\mathrm{mF}$. We adopt therefore a larger capacitance, namely 50 times the minimum: $C_{dc} = 315\,\mathrm{mF}$. For a DC-side capacitance base of $C_{basedc} = 7.88\,\mathrm{F}$, this translates into $C_{dc} = 0.04\,\mathrm{pu}$, which will be our standard from here on. This capacitance leads to a ripple of about $\Delta v_{dc} = 1.3\,\%$. In terms of energy, this capacitance corresponds to $W_{dc} = 0.2\,\mathrm{MWs}$, which means this DC-link is able to provide $P_n = 10\,\mathrm{MW}$ during 20 ms, i.e., one full cycle. In this report, DC-link losses are neglected, hence no conductance is required on the DC-side diagrams or equations. Once again, because this topic is out of the scope, for further information on DC-link design in PV installations, please refer to [111].

Parameter	Symbol	Value
Series inductance	L_f	0.1 pu
Series resistance	R_f	0.01 pu
Shunt capacitance	C_f	0.1 pu
DC-link capacitance	C_{dc}	0.04 pu

Table 3.4: IBR sizing parameters

3.6.1 Tuning a PI controller for first-order systems

A first-order system is characterized by a gain K_0 and a time-constant τ_0:

$$H_p(s) = \frac{Y(s)}{U(s)} = \frac{K_0}{\tau_0\, s + 1} \tag{3.139}$$

For a unitary step response $U(s) = \frac{1}{s}$, an inverse Laplace transform would yield, for $t > 0$, an output $y(t)$:

$$y(t) = K_0(1 - e^{-\frac{1}{\tau_0}\,t}) \tag{3.140}$$

Hence, τ_0 is the period it takes for the output y to reach 63 % of K_0, whereas the gain K_0 is the steady-state output for $t \to \infty$. In order to assess a time response for this system, we may compute $t_r^{5\%} = 3\,\tau_0$ or $t_r^{1\%} = 5\,\tau_0$, which corresponds to the time it takes for this system to reach 95 % and 99 % of K_0, respectively. From here on, unless mentioned otherwise, “time response” will always be taken as $t_r = t_r^{5\%}$.

A first-order system can be easily controlled via a proportional-integral (PI) controller, where a proportional gain allows for reference tracking and an integrator eliminates the steady-state error. A PI controller can be described by a transfer function:

$$H_c(s) = K_p + \frac{K_i}{s} \tag{3.141}$$

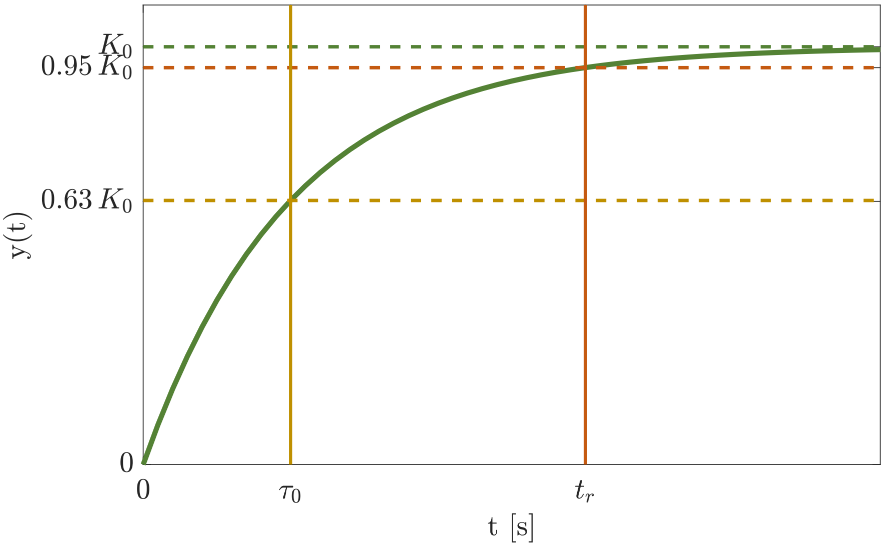

Figure 3.13: Step response for a 1st order system

Which leads to a closed-loop transfer function:

$$H(s) = \frac{H_c(s)\,H_p(s)}{1 + H_c(s)\,H_p(s)} = \frac{N(s)}{D(s)} \tag{3.142}$$

where

$$D(s) = s^2 + 2\,\zeta\,\omega_n\,s + \omega_n^2 \tag{3.143}$$

Here, $H(s)$ is a second-order system characterized by a damping factor ζ and a natural frequency ω_n; we may thus find K_p and K_i to satisfy requirements for ζ and ω_n. However, a more intuitive requirement would be a time-response $t_r = t_r^{5\%}$, also called "settling time":

$$t_r \approx 3\,\tau = \frac{3}{\zeta\,\omega_n} \tag{3.144}$$

In fact, (3.144) is valid for underdamped systems with $\zeta \leq 0.707$; it indicates the time it takes for the step response of an underdamped system to settle within a 5 % band ($b = 0.05$) around the final output y_f, stemming from the formula of exponential decay: $e^{-\zeta\,\omega_n\,t_r} = b$. For different bands, one should apply:

$$t_r^b = \frac{-\ln(b)}{\zeta\,\omega_n} \tag{3.145}$$

For systems with higher damping, this time response obtained via (3.144) is underestimated. In Figure 3.14, we observe how it actually takes about 50 % more than t_r for a step response to reach the desired band when damping is critical ($\zeta = 1$). Nevertheless, it is a common practice to adopt $\zeta = 1/\sqrt{2} = 0.707$, since it usually provides an acceptable trade-off between speed of response and damping of transient oscillations, as can be seen in Figure 3.14. This will be done throughout this dissertation, reducing our degree of freedom by half for every PI controller, which will be tuned exclusively based on t_r. We opt for this approach because we intend to study small-signal stability problems related to interactions between IBRs: a low damping factor would evidently lead to sub-optimal stability, hence it is a conservative assumption to consider this parameter to be properly tuned. Our tuning criteria rely on a desired time-response t_r, which, unlike ζ, is not a simple choice.

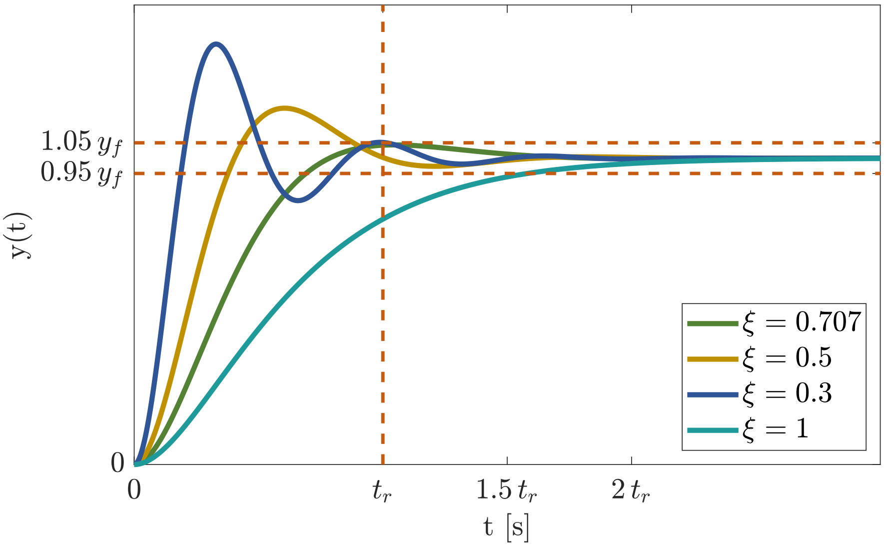

Figure 3.14: Step response for a 2nd order system

We may thus find K_p and K_i based on the characteristics of our first-order plant, namely K_0 and τ_0, and our desired time response t_r, by applying both (3.139) and (3.141) to (3.142):

$$K_p = \frac{1}{K_0}\left(\frac{6\,\tau_0}{t_r} - 1\right), \qquad K_i = \frac{9\,\tau_0}{K_0\,\zeta^2\,t_r^2} \tag{3.146}$$

If the plant is just an integrator:

$$H_p(s) = \frac{Y(s)}{U(s)} = \frac{K_0}{s} \tag{3.147}$$

applying (3.147) to (3.142) would rather lead to the following gains:

$$K_p = \frac{6}{K_0\,t_r}, \qquad K_i = \frac{9}{K_0\,\zeta^2\,t_r^2} \tag{3.148}$$

Most controllers in our generic models can be tuned using (3.146) and (3.148), based on time-response requirements, which entails a significant advantage in terms of standardization. Detailed tuning of each IBR control loop following these rules is provided in Appendix A.

3.6.2 Standard configurations for GFL and GFM inverters

Based on the detailed tuning of IBRs (Appendix A), the following values are adopted as the "standard" tuning for GFLs and GFMs. This configuration will serve as a reference, being compared to multiple situations that deviate from it, and assessing their effects on small-signal stability. It is worth noting that there is no consensus over the ideal tuning of IBRs, especially in light of their dependence on grid conditions, e.g., SCR at the POI. Our standard choice is thus empirical, based on small-signal studies and time-domain simulations.

IBR	Parameter	Standard Value
GFL	$t_r^{v_{dc}}$	100 ms
	$t_r^{i_q}$	100 ms
	t_r^{pll}	50 ms
	t_r^{i}	10 ms
	τ_{q_m}	30 ms
	ω_s	1000 rd/s
GFM	m_p	0.01
	ω_p	31.4 rd/s
	$\tau_{v_{dc}}$	5 ms
	n_q	0
	ω_q	31.4 rd/s
	t_r^{v}	10 ms
	t_r^{i}	0.5 ms
	ω_{tvr}	62.8 rd/s
	R_v^{tvr}	0.03 pu
	X_v	0
	R_v	0
	ω_s	1000 rd/s

Table 3.5: Standard values for IBR tuning parameters

3.7 Chapter summary

This chapter provided a detailed guide for modeling an MVDG with IBRs. Here are some takeaway points:

- SICDS phenomena occur in the intersection between EMT and RMS modeling methodologies, but using EMT models allows us to work with higher precision, venturing into frequency ranges not well-reproduced by RMS models. EMT models are also vastly available in the literature regarding IBRs.

- A benchmark network is required for our case studies, for which we adopted the European configuration of the Cigre MV distribution grid.

- Three major hypotheses are postulated for our models:

  1. The HV network upstream can be taken as an infinite bus: we are interested in interactions between the IBRs themselves rather than the interactions between the distribution grid and the network upstream.
  2. Except for IBRs, the MVDG is entirely passive: OLTCs and capacitor banks are too slow to be taken into account for SICDS studies, while load dynamics are considered out of scope. In our case studies, the dynamics are driven primarily by the IBR controllers.
  3. Aggregated passive elements can be replaced by RLC circuits: a common assumption in EMT studies, this is a necessary hypothesis insofar as the loads from the benchmark network are already aggregated, i.e., we do not have an accurate representation of the LV networks downstream.

- Due to Enedis' perspectives for 2050, our case studies are based on PV and BESS rather than WPPs. The source model is generic enough to include Type-4 wind turbines, but Type-3 turbines require specific models and are out of the scope of this dissertation.

- GFLs are modeled according to the prevalent models available in the literature. For the control of active power, we have opted for a v_{dc} control rather than a straightforward P control, given that the former method provides an interesting comparison with respect to GFMs. The building blocks of a GFL are the external and internal control loops, in addition to a PLL.

- GFMs, in terms of their external control, are modeled as a power-synchronization loop coupled with a low-pass filter for virtual inertia, hence a virtual synchronous machine. Multiple models are available in the literature, but they present similar small-signal behavior. Our model of choice is judged as being generic enough for SSSA, being easily "translated" into other control methods, which might be an advantage for the DSO.

- GFMs also have an internal control loop, for which we adopted a cascaded structure, as well as additional control loops for active damping and R/X ratio correction. A v_{dc} control loop is also added to the GFM, since it may have an impact on SICDS.

- Each IBR yields a state-space representation based on its differential and algebraic equations, all of which are provided in this chapter. The MVDG state-space can be obtained through a modular representation, using the state-space association technique.

All of these may then be assembled into the final state-space, whose $\boldsymbol{A}$ matrix will be employed in the SSSA.

- All information required for sizing and parameterization is also available in this chapter. IBR controllers in our models are mostly PI-based, hence they may be tuned using first-order approximations. Criteria are mostly expressed in terms of time responses, which could be used as guidelines by the DSO. Detailed tuning of all IBR controllers is provided in Appendix A.

Chapter 4

Small Signal Stability of a Distribution Grid with IBRs

Contents

Having modeled an MVDG with IBRs, we may finally proceed to the stability analysis. We recall that our main interest is to study slow-interaction converter-driven stability, which, as defined in Section 1.2.4, concerns *slow* dynamic interactions between IBR controllers and other components of the power system. These interactions are in the range of a few hertz up to several tens of hertz, approaching the fundamental frequency of 50 Hz, encompassing thus both low-frequency and sub-synchronous oscillations. Opting for an accurate modeling of the system and a detailed assessment of the physics behind SICDS issues, we resort to the well-known method of small-signal stability analysis, for which all mathematical notions have already been summarized in Section 1.2.5.

The chapter begins with a detailed study of a 1-IBR system in Section 4.1, examining the interactions between an IBR, be it a GFL or a GFM, and the MVDG itself. Justifying our choice of scenarios with the notion of SCR-based weakness of a POI, already explained in Chapter 2, we proceed to the characterization of a 1-IBR system through its modal maps, tracing a "cartography" of major SICDS-related modes and the IBR states associated with them. Going back to the tuning parameters defined in Chapter 3, which are swept over a range of values, we are able to assess the behavior of the targeted modes. These sensitivities serve both as a means to understand the physical causes of SICDS issues and determine which are the most consequential parameters. The importance of detecting key parameters and defining their bound values is a core idea of this thesis, being first introduced in this section and addressed thoroughly in Chapter 5. For illustration, two instabilities are examined in detail, demonstrating the interest in using SSSA, namely the high-$t_r^{v_{dc}}$ instability in GFLs and high-droop instability in GFMs.

In order to broaden the analysis to include interactions *between* IBRs, one could resort to a multi-IBR configuration, the simplest of which consists of only two converters, as in Section 4.2. Now the choice of scenarios depends not only on the SCR at their POIs but also on the electrical proximity between IBRs, especially when involving GFMs. The concept of modal maps is once again employed to identify the SICDS-related modes in which both IBRs have a marked contribution, constituting a small-signal interaction. Assessing the same sensitivities as for the 1-IBR system, but now in the presence of another IBR, in what we designate as *single-parameter sensitivities*, we are able to unveil the particularities of multi-IBR configurations, aiming once more at outlining the physical origin of SICDS issues, while refining the acceptable values for the aforementioned key parameters. Certain interactions seem to be of particular interest, such as the worsening of high-$t_r^{v_{dc}}$ instability in GFLs in the presence of a GFM, or the destabilizing interaction between high-droop GFMs (even for droop levels within the typical 5 % range), or else the positive interaction between slow-PLL GFLs and neighboring GFMs. These interactions are hence addressed in detail.

Finally, bearing in mind the SICDS issues in a 2-IBR system and how they are affected by certain control parameters, an empiric yet systematic DSO-oriented methodology is proposed at the end of this chapter, in Section 4.3. Considering divergent interests between MV-connected producers and the DSO, where the former intend to tune their IBRs according to their own needs, whereas the latter is primarily concerned about the overall SICDS in the MVDG, it is crucial to ensure that the ranges of key parameters do not entail unstable or low-damping boundary configurations, i.e., scenarios in which each key parameter in every IBR is either at its lower or upper bound value. The methodology is aimed at improving these bound values, culminating in an optimization method in Chapter 5. First demonstrated in a 2-IBR configuration, leading to recognizable gains in stability, this methodology is applied to a larger system in Appendix C.

4.1 1-IBR system: interactions between IBR and grid

4.1.1 Choice of scenarios

Bus	Without IBR		With IBR	
	SCR	R/X	SCR	R/X
3	5.36	0.64	4.28	0.48
4	5.03	0.65	4.07	0.49
5	4.75	0.66	3.88	0.50
6	4.11	0.67	3.45	0.53
7	4.02	0.67	3.39	0.53
8	4.71	0.66	3.85	0.51
9	4.57	0.67	3.76	0.51
10	4.26	0.67	3.55	0.53
11	4.13	0.67	3.46	0.53

Table 4.1: SCR and R/X ratio for different buses in the MVDG. All loads are modeled as constant impedances.

Going back to the MVDG from Figure 3.1, although we are starting with only one IBR, when tackling a multi-IBR configuration it would be more realistic to consider the IBRs connected to the feeder departing from Node 1 instead of the one from Node 12, given that it is more extensive and has more loads connected to it, hence our scenarios are restricted to this feeder. As mentioned in Chapter 2, there are two crucial static characteristics of the POI for small-signal stability, namely SCR and R/X ratio, both of which are given in Table 4.1, for each bus in the chosen feeder. Noting that the presence of an IBR has a significant impact on these parameters due to the impedance of its LV/MV transformer, we observe that the R/X ratio is similar for all buses, ranging from 0.48 to 0.53. Short-circuit ratio, on the other hand, may vary between 3.39 for the weakest bus, namely Bus 7, and 4.28 for the strongest, i.e., Bus 3. Therefore, these two buses are the candidates for our scenarios of choice. The present subsection elucidates this choice based on the SSSA of a GFL and a GFM connected to different buses in the MVDG, shown in Figures 4.1 and 4.2, respectively.

For a GFL, we may adopt the standard configuration from Table 3.5 and compare it with a fast-PLL configuration, where $t_r^{pll} = 10\,\text{ms}$ rather than $50\,\text{ms}$. As expected, the standard configuration presents satisfactory damping regardless of which bus the GFL is connected to, as shown in Figure 4.1a. A fast-PLL configuration, however, crosses the $5\,\%$ damping line for Bus 7, indicating a weak-grid-related issue: PLL instability, as mentioned in previous chapters, is a combination of a low SCR at the POI and a low t_r^{pll}. In fact, Figure 4.1b confirms that the most unstable situations happen for Buses 7, 6, 11, and 10; these are the four buses with the lowest SCR, in this exact same order, as described in Table 4.1.

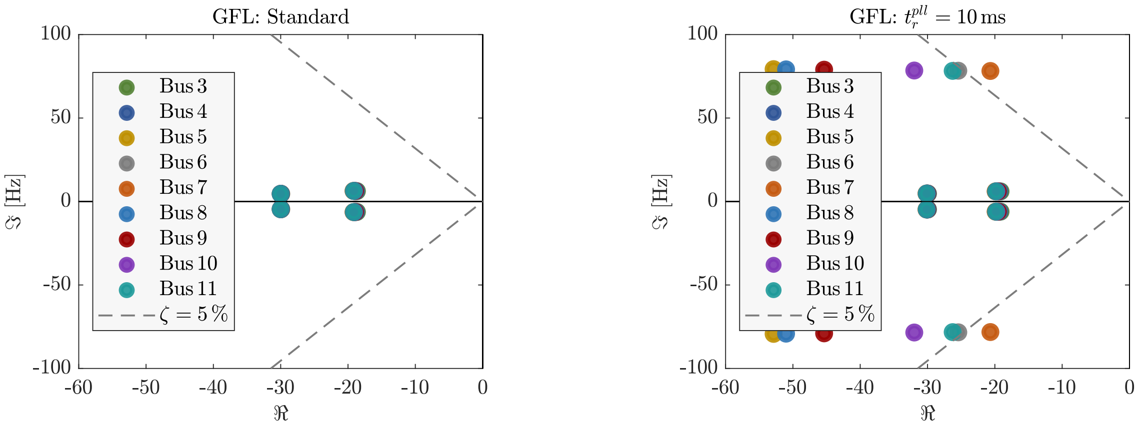

(a) Standard configuration (b) Fast-PLL configuration

Figure 4.1: SSSA of a GFL connected to different buses in the MVDG. Fast-PLL GFL presents low damping when connected to the weakest buses in the system.

For a GFM, we may once again assume the standard configuration from Table 3.5, but now we compare it with a high-droop configuration, where $m_p = 0.2$ rather than 0.01. This is an unrealistically high droop value, not expected to be adopted in real-life situations, but may help in justifying the choice of scenarios. The standard configuration yields proper damping regardless of the bus, as in Figure 4.2a, while a high-droop configuration crosses the 5 % damping line for Buses 3 and 4, indicating a strong-grid-related issue. As discussed in Chapter 2, GFMs may experience strong-grid instability when the droop is too high. This time, Buses 3, 4, 5, and 8 are the ones closest to the imaginary axis, as depicted in Figure 4.2b, while being the ones with the highest SCR according to Table 4.1, in this exact same order.

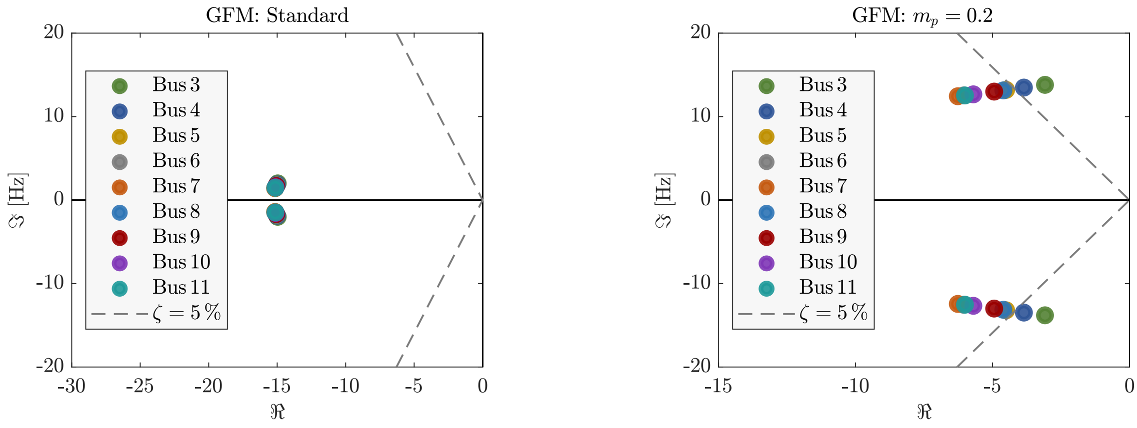

(a) Standard configuration (b) High-droop configuration

Figure 4.2: SSSA of a GFM connected to different buses in the MVDG. High-droop GFM presents low damping when connected to the strongest buses in the system.

Figures 4.1 and 4.2 corroborate our previous assertion: Buses 3 and 7 are good candidates for the SSSA, since they constitute the most extreme situations. Therefore, most of our single-IBR studies will involve a GFL connected to Bus 7 or a GFM connected to Bus 3.

4.1.2 Modal maps

A logical first step in SSSA is to characterize the modes of a given system. We may start by mapping all the eigenvalues of a 1-IBR system, as is done in Figures 4.3 and 4.4 for a GFL and a GFM, respectively. There is not much information to be gained from such an abundant plot, except that both configurations yield eigenvalues in a wide range of frequencies. It is more interesting to observe what happens under a targeted frequency range, namely the mapping of *dominant* modes, as in Figures 4.5 and 4.6. These are the modes associated with SICDS which should be "tagged" with respect to their most participative states.

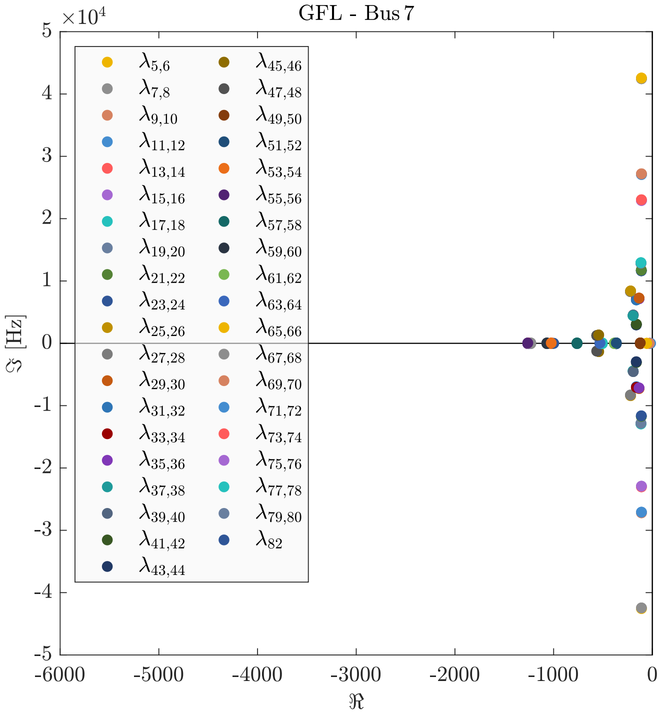

Figure 4.3: Modal maps for a standard GFL connected at Bus 7

Figure 4.5a presents a modal map for a GFL inverter, restricted to eigenvalues with frequencies under 300 Hz, with two transversal lines indicating a damping ratio of $\zeta = 70.7\,\%$, adopted as a tuning criterion for time-response-based controllers in Appendix A, and $\zeta = 3\,\%$, considered as the minimum acceptable damping in power systems. Zooming into the frequency range of SICDS phenomena, we observe three dominant modes: $\lambda_{71,72}$, $\lambda_{69,70}$, and $\lambda_{65,66}$.

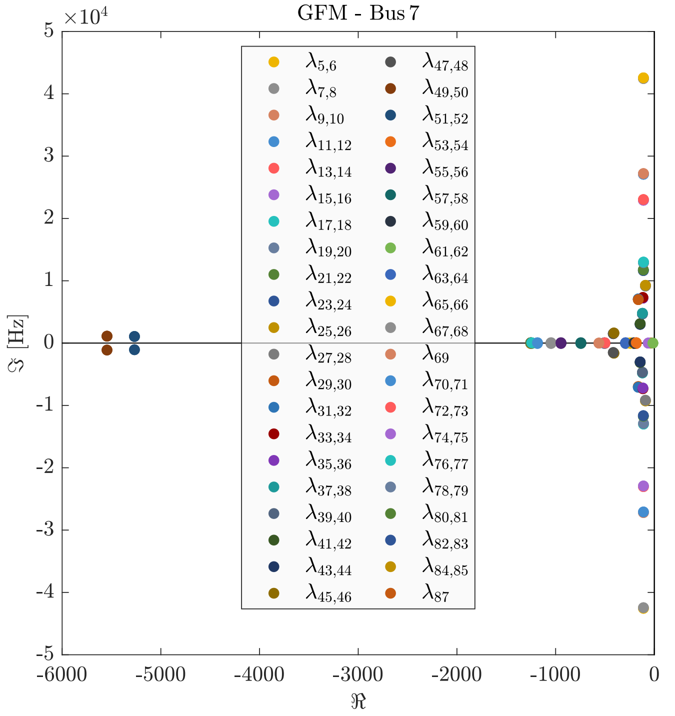

Figure 4.4: Modal maps for a standard GFM connected at Bus 7

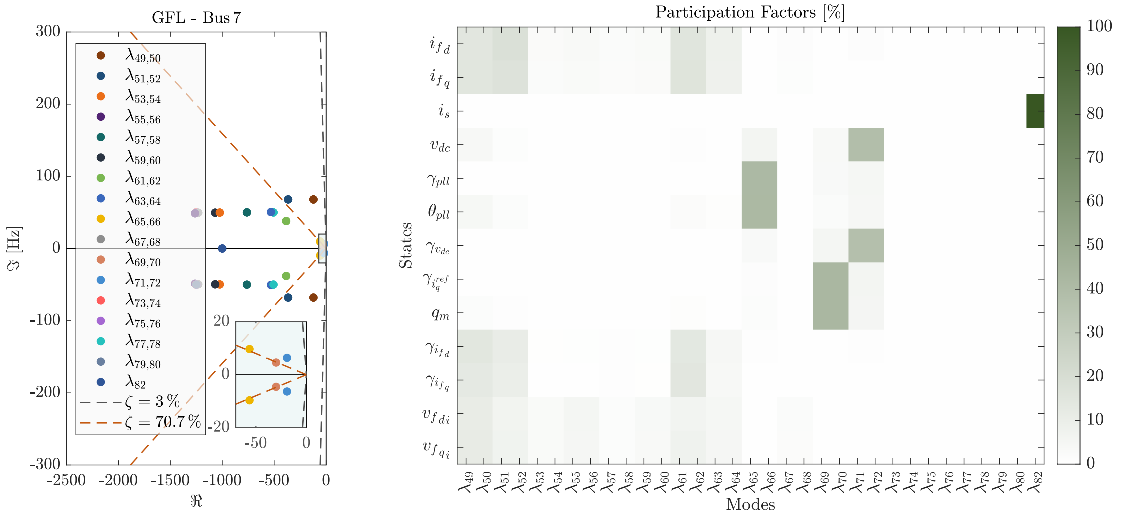

(a) Selected modal map

(b) Participation matrix

Figure 4.5: Mode characterization for a GFL inverter

A participation matrix, as in Figure 4.5b, is useful for characterizing such modes: $\lambda_{71,72}$ is associated with $\gamma_{v_{dc}}$ and v_{dc}, hence it refers to the external P-control loop[1], whereas $\lambda_{69,70}$ is associated with $\gamma_{i_q}^{ref}$ and q_m, referring to the Q-control loop, and $\lambda_{65,66}$ is related to γ_{pll} and θ_{pll}, state variables of the PLL. The three SICDS-related modes (external control loops and PLL) are also the dominant ones, dictating the dynamics of the IBR, which hints at the importance of this frequency range. It comes as no surprise that all of these modes are located in proximity with the $\zeta = 70.7\,\%$ line, since they have all been tuned for such damping. It is also no surprise that a standard GFL has no weakly-damped mode, i.e., they are all sufficiently distant from $\zeta = 3\,\%$.

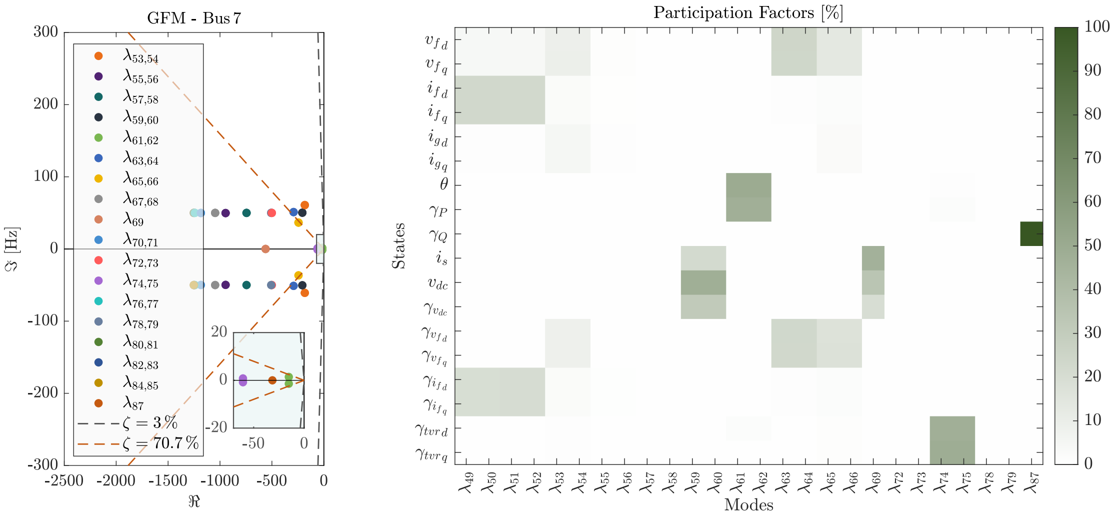

(a) Selected modal map

(b) Participation matrix

Figure 4.6: Mode characterization for a GFM inverter

Figure 4.6a provides the same information for a GFM inverter, where the dominant modes are now $\lambda_{61,62}$, λ_{87}, and $\lambda_{74,75}$. Here, $\lambda_{61,62}$ is the most important SICDS-related mode, associated with m_p and θ, hence the external P-control mode; λ_{87} is just a delay, i.e., a non-oscillatory mode related to the external Q-control, whereas $\lambda_{74,75}$ is associated with the active damping loop (TVR[2]). In the standard configuration, the mode related to the v_{dc} control ($\lambda_{59,60}$) is located in the higher frequency range, close to 50 Hz, not far from $\lambda_{53,54}$, $\lambda_{59,60}$, and $\lambda_{65,66}$. These modes are related to the internal voltage control loop. All of these are located around the $\zeta = 70.7\,\%$ line, given that they are also tuned for this damping.

---

[1] Let us recall that we have adopted an *indirect* P-control loop, via the control of v_{dc}, as discussed in Section 3.2.1.

[2] A virtual resistor coupled with a high-pass filter, aimed at mitigating power oscillations in strong reactive networks. For more details, please refer back to Section 3.2.2.

4.1.3 Selected sensitivities

Once the major SICDS-related modes have been characterized, we may proceed by analyzing the impact of key parameters by means of sensitivity analysis, or *eigen-sensitivity*, which consists of sweeping the given parameter over a certain range and assessing the trajectory traced by the system's eigenvalues. Our objective is twofold: understanding the physics behind certain SICDS phenomena and determining which are the key parameters that have a significant impact on SICDS. We may also define the initial ranges for these key parameters, to be further refined in the 2-IBR system when including the effects of inter-IBR interactions. Among the multiple sensitivity studies performed for this section, two of them are analyzed in detail below, due to the insights they provide about the physical causes of SICDS issues in 1-IBR systems. These are the SICDS instability caused by high $t_r^{v_{dc}}$ in GFLs and the one caused by high m_p in GFMs (high-droop instability).

Special note: For all the sensitivity plots in this chapter, eigenvalue maps indicate the *initial* location of each eigenvalue, whereas their evolution is represented by a green line. In most cases, a zoomed box provides the same plot confined to the SICDS frequency range, focusing on the dominant modes.

4.1.3.1 High-$t_r^{v_{dc}}$ instability in GFLs

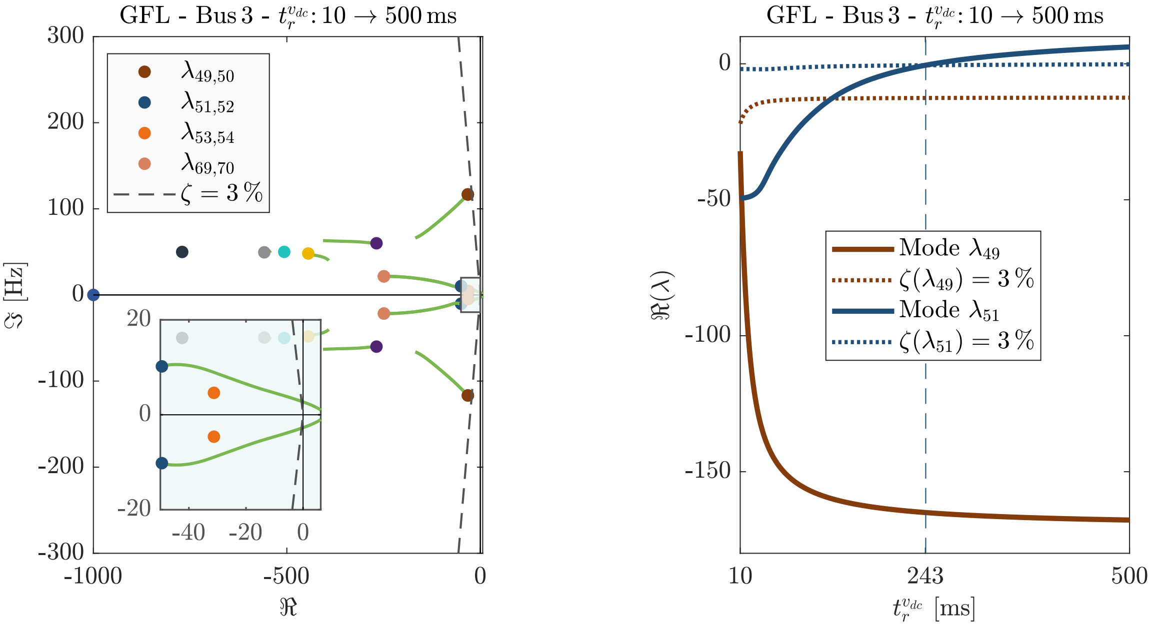

(a) Sensitivity (b) Eigenvalue trajectory

Figure 4.7: Eigen-sensitivity for $t_r^{v_{dc}}$ in a GFL

Figure 4.7 reveals that a GFL may become unstable if the v_{dc} control time response is high. As explained in Section 3.2.1, there are multiple advantages in applying a converter-side control to the DC-link voltage in GFLs, especially when the source-side converter is following an MPPT algorithm, but one must first verify if the DC-link capacitor is large enough to sustain v_{dc} while this same voltage is being controlled via i_d, as seen in Figure 3.4. Alternatively, this control loop should be fast enough to control v_{dc} in accordance with the energy storage in the capacitor.

In order to find a relation between $t_r^{v_{dc}}$ and C_{dc}, let us go back to (3.12):

$$C_{dc}\,\dot{v_{dc}} = i_s - i_{f_d}\,m_d - i_{f_q}\,m_q \tag{4.1}$$

where $\{m_d, m_q\}$, as shown in Figure 3.4 (ignoring the saturation), are given by:

$$m_d = \frac{v_{md}}{v_{dc}} \qquad\qquad m_q = \frac{v_{mq}}{v_{dc}} \tag{4.2}$$

and $\{v_{md}, v_{mq}\}$, in steady-state, can be written as:

$$v_{md} = v_{f_d} + R_f\,i_{f_d} - X_f\,i_{f_q} \tag{4.3}$$

$$v_{mq} = v_{f_q} + X_f\,i_{f_d} + R_f\,i_{f_q} \tag{4.4}$$

Now linearizing (4.3), with a steady AC voltage ($\Delta v_{f_d} = 0$) and no change in reactive current ($\Delta i_{f_q} = 0$):

$$\Delta v_{md} = \Delta v_{f_d} + R_f\,\Delta i_{f_d} - X_f\,\Delta i_{f_q} \approx R_f\,\Delta i_{f_d} \tag{4.5}$$

which we may substitute into the linearization of m_d (4.2), with $v_{md0} = m_{d0}\,v_{dc0}$:

$$\Delta m_d = \frac{1}{v_{dc0}}\,\Delta v_{md} - \frac{v_{md0}}{v_{dc0}^2}\,\Delta v_{dc} \approx \frac{R_f}{v_{dc0}}\,\Delta i_{f_d} - \frac{m_{d0}}{v_{dc0}}\,\Delta v_{dc} \tag{4.6}$$

Finally, linearizing (4.1):

$$C_{dc}\,\Delta\dot{v}_{dc} = \Delta i_s - \Delta i_{f_d}\,m_{d0} - i_{f_{d0}}\,\Delta m_d - \Delta i_{f_q}\,m_{q0} - i_{f_{q0}}\,\Delta m_q \tag{4.7}$$

Once again, we may neglect any change in source current ($\Delta i_s = 0$), as well as q-axis controls ($\Delta i_{f_q} = \Delta m_q = 0$), and substitute Δm_d with (4.6):

$$C_{dc}\,\Delta\dot{v}_{dc} = -m_{d0}\,\Delta i_{f_d} - i_{f_{d0}}\left(\frac{R_f}{v_{dc0}}\,\Delta i_{f_d} - \frac{m_{d0}}{v_{dc0}}\,\Delta v_{dc}\right) \tag{4.8}$$

Writing (4.8) in the s-domain, we get a transfer function between Δi_{f_d} and Δv_{dc}:

$$H_p(s) = \frac{\Delta v_{dc}(s)}{\Delta i_{f_d}(s)} = \frac{K_0}{\tau_0\,s - 1} \tag{4.9}$$

where

$$K_0 = -\Big(\frac{v_{dc0}}{i_{f\,d0}} + \frac{R_f}{m_{d0}}\Big) \qquad \tau_0 = \frac{C_{dc}\, v_{dc0}}{i_{f\,d0}\, m_{d0}} \tag{4.10}$$

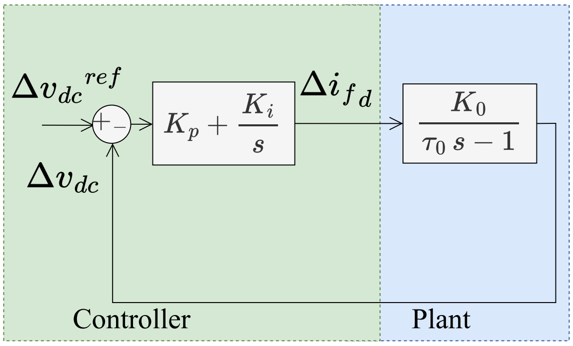

Figure 4.8: Simplified representation of a GFL v_{dc} control

From Figure 4.8, we derive a closed-loop transfer function between Δv_{dc} and Δv_{dc}^{ref}:

$$H(s) = \frac{\Delta v_{dc}(s)}{\Delta v_{dc}^{ref}(s)} = \frac{(K_p + \frac{K_i}{s})\,\frac{K_0}{\tau_0\, s - 1}}{1 + (K_p + \frac{K_i}{s})\,\frac{K_0}{\tau_0\, s - 1}} = \frac{\frac{K_p\, K_0}{\tau_0}\, s + \frac{K_i\, K_0}{\tau_0}}{s^2 + (\frac{K_p\, K_0 - 1}{\tau_0})\, s + \frac{K_i\, K_0}{\tau_0}} \tag{4.11}$$

Roots of the characteristic equation, i.e., the denominator of (4.11), are given by:

$$s_{1,2} = \frac{\frac{1 - K_p\, K_0}{\tau_0} \pm \sqrt{(\frac{K_p\, K_0 - 1}{\tau_0})^2 - \frac{4\, K_i\, K_0}{\tau_0}}}{\frac{2\, K_i\, K_0}{\tau_0}} \tag{4.12}$$

Assuming an oscillatory mode, i.e., $(\frac{K_p\, K_0 - 1}{\tau_0})^2 < \frac{4\, K_i\, K_0}{\tau_0}$, as well as non-null values for K_0, K_i, and τ_0, with $\tau_0 > 0$, these roots will have a negative real part only if $K_p\, K_0 > 1$. Using the method presented in the Appendix A, Section A.1.2, we may rewrite K_p as:

$$K_p = -\frac{6\, C_{dc}}{m_{d0}\, t_r^{v_{dc}}} \tag{4.13}$$

Hence, the stability criterion $K_p\, K_0 > 1$, considering K_p as in (4.12) and K_0 as in (4.10), translates into the following:

$$t_r^{v_{dc}} < 6\, C_{dc}\, \frac{v_{dc0}\, m_{d0} + R_f\, i_{f\,d0}}{i_{f\,d0}\, m_{d0}^2} \tag{4.14}$$

which may be further simplified, taking $v_{dc0} = m_{d0} = i_{f\,d0} \approx 1\,\text{pu}$, and $R_f << 1\,\text{pu}$:

$$t_r^{v_{dc}} < 6\, C_{dc} \tag{4.15}$$

This is a useful "rule-of-thumb" to determine if the v_{dc} control loop is fast enough with respect to the DC-link capacitor. For C_{dc} equal to 0.02, 0.04, and 0.08 pu we would get a minimum $t_r^{v_{dc}}$ of 120, 240, and 480 ms, respectively. As can be seen in Figure 4.9, these are reasonably accurate estimates. The actual values for which the IBR becomes unstable are slightly higher than the ones displayed in the figure, since they happen when $\zeta = 0$, i.e., $\Re(\lambda) = 0$, rather than $\zeta = 3\,\%$, but these are visibly in close proximity to each other. In any case, our simple formula provided a conservative estimate. It is worth remarking that this issue is not dependent on the SCR at the POI or any other grid parameter.

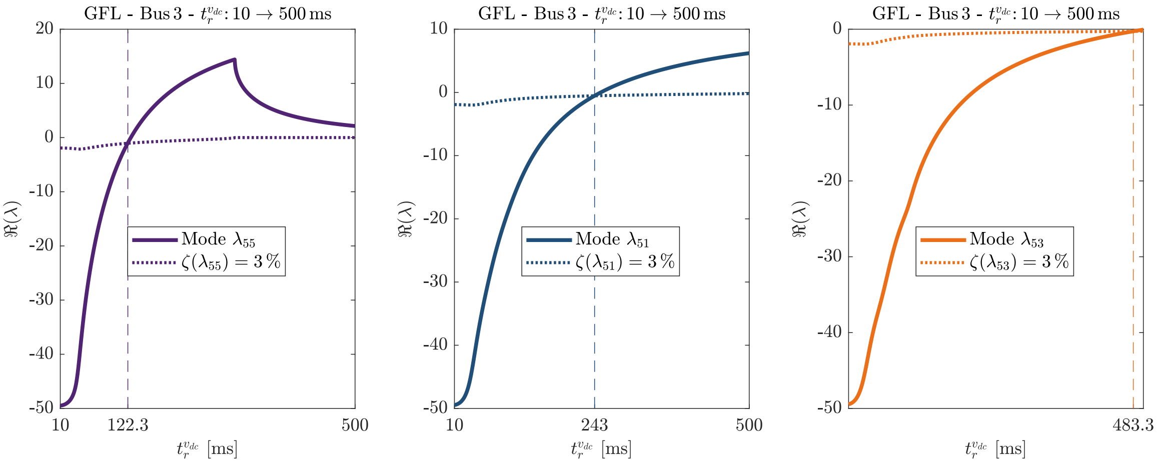

(a) $C_{dc} = 0.02\,\text{pu}$ (b) $C_{dc} = 0.04\,\text{pu}$ (c) $C_{dc} = 0.08\,\text{pu}$

Figure 4.9: Eigenvalue trajectory for different values of C_{dc}

To conclude: a high $t_r^{v_{dc}}$ may lead to instability or low damping if the DC-link capacitor is too small. Since the external control loop should be sufficiently slower than the inner loop, which itself is limited by the switching frequency of the converter, it is reasonable to assume that $t_r^{v_{dc}}$ cannot be faster than 10 ms, approximately, which means that C_{dc} should be above 0.002 pu. An important implication here is that for a DSO to properly assess this sort of stability, it should have an estimate of the DC-link capacitance of the most important IBRs in the system.

4.1.3.2 High-m_p instability in GFMs

As observed in Figure 4.10 and mentioned in previous chapters, GFMs may experience high-droop instability under high-SCR conditions. To understand this phenomenon in a 1-IBR system, one may resort to the analogy between the GFM external control loop and a synchronous generator, as in Section A.2.2 from Appendix A. Going back to (3.57) and (3.58), and considering $\omega = \gamma_p + \omega^{ref}$ as the per-unit frequency of the GFM, we get:

$$\Delta\dot{\omega}_r = \omega_p\, m_p\, (p^{ref} - p) - \omega_p\, \Delta\omega_r \tag{4.16}$$

$$\dot{\delta} = \omega_b\, \Delta\omega_r \tag{4.17}$$

where $\Delta\omega_r = \omega - \omega^{ref}$, with $\omega^{ref} = 1\,\text{pu}$, and $\delta = \theta - \theta_g$, with $\theta_g(t) = \omega_{base}\, t$ being a reference phase rotating at synchronous frequency. We may rewrite (4.16) as:

$$2\, H\, \Delta\dot{\omega}_r = (p^{ref} - p) - K_D\, \Delta\omega_r \tag{4.18}$$

where

$$H = \frac{1}{2\, m_p\, \omega_p} \qquad\qquad K_D = \frac{1}{m_p} \tag{4.19}$$

This formulation is the classical "swing equation" for SGs [1], where H is the inertia and K_D is the damping factor. For GFMs, since there is no rotating mass, H is a *virtual* inertia. Insomuch as K_D is inversely proportional to m_p, it is clear that high values for m_p will decrease the damping of the virtual synchronous machine.

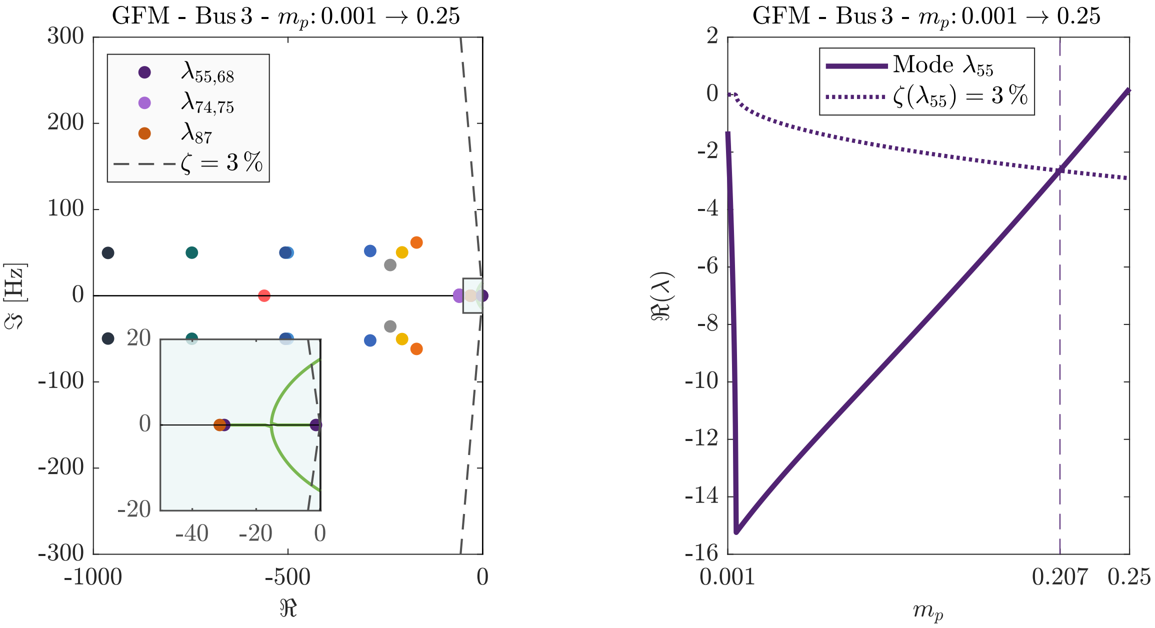

(a) Sensitivity (b) Eigenvalue trajectory

Figure 4.10: Eigen-sensitivity for m_p in a GFM

Now, given that a GFM acts as a voltage source in steady-state, let us return to (2.6), where σ_c is the R/X ratio seen by the IBR:

$$P = \frac{\text{SCR}}{\sqrt{1+\sigma_c^2}} \left(\sigma_c\, V_f\, (V_f - V_g\, \cos\delta) + V_f\, V_g\, \sin\delta \right) \tag{4.20}$$

Linearizing this equation and expressing it in the s-domain, with $s = 0$ (steady-state), we find a relation between a variation in the POI voltage angle $\Delta\delta$ and the consequent variation in the power injected by the IBR ΔP:

$$H_{p\delta}(0) = \frac{\Delta P(0)}{\Delta\delta(0)} = \frac{\mathrm{SCR}}{\sqrt{1+\sigma_c^2}}(V_{f0}\,V_g\,\cos\delta_0 + \sigma_c\,V_{f0}\,V_g\,\sin\delta_0) = k^p\,\frac{\mathrm{SCR}}{\sqrt{1+\sigma_c^2}} \tag{4.21}$$

$H_{p\delta}(0)$ is the portion of ΔP due to $\Delta\delta$, hence it is an expression of the (also virtual) *synchronizing torque* (K_S in [1]) provided by the IBR. For a single-machine infinite-bus (SMIB) analysis, as is the case in the present example, the author of [1] offers the following expression for the damping ratio ζ stemming from the dynamics of the swing equation:

$$\zeta = \frac{1}{2}\,\frac{K_D}{\sqrt{2\,K_S\,H\,\omega_{base}}} \tag{4.22}$$

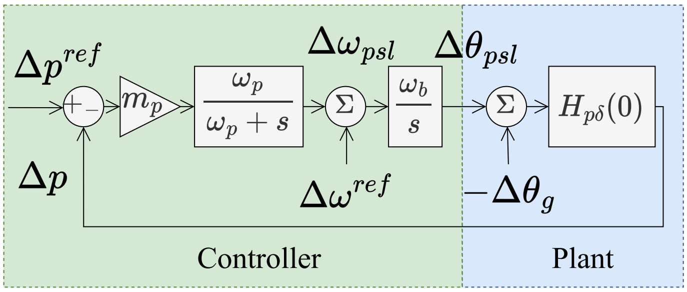

Figure 4.11: Linearized GFM external control loop: active power

We find this same expression by computing the transfer function between ΔP and ΔP^{ref} for the external P-control loop of a GFM, as depicted in Figure 4.11:

$$H_p^p(s) = \frac{\Delta p(s)}{\Delta p^{ref}(s)} = \frac{\frac{K_0}{\tau_0}}{s^2 + \frac{1}{\tau_0}\,s + \frac{K_0}{\tau_0}} \tag{4.23}$$

where

$$K_0 = m_p\,\omega_b\,H_{p\delta}(0) \qquad\qquad \tau_0 = \frac{1}{\omega_p} \tag{4.24}$$

Considering (3.142) and (3.144) for (4.23), we get:

$$\zeta = \frac{1}{2}\sqrt{\frac{\omega_p}{m_p\,\omega_b\,H_{p\delta}(0)}} = \frac{1}{2}\sqrt{\frac{\omega_p\,\sqrt{1+\sigma_c^2}}{m_p\,\omega_b\,k^p\,\mathrm{SCR}}} \tag{4.25}$$

From (4.19), and knowing that $K_S = H_{p\delta}(0)$, we find the exact same expression as (4.25) when using (4.22), demonstrating the interest of using the GFM-SG analogy.

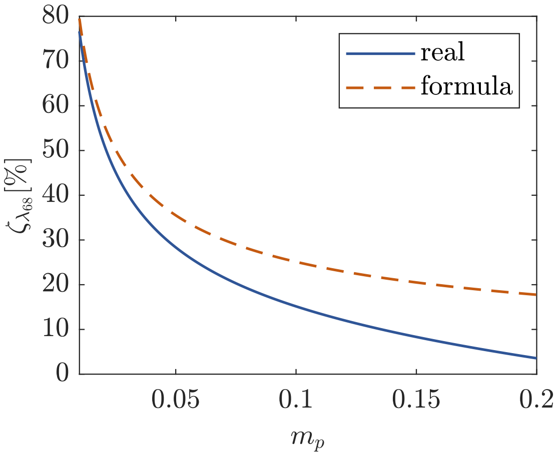

Figure 4.12: Damping of the droop-related mode (λ_{68}) for a GFM connected to Bus 3

The most important conclusion here is that, according to (4.25), the damping of the pair of eigenvalues associated with the GFM external P-control loop is inversely proportional to both m_p and SCR: a high droop and a strong POI may both lead to a weakly-damped mode.

For most cases, with an m_p of up to 5 %, the formula (4.25) serves as a sufficiently accurate rule-of-thumb to assess the damping of a GFM-SMIB scenario. However, if the droop is *exaggeratedly* high (crossing a 10 % threshold, for instance), the real damping observed in the SSSA deviates considerably from the one obtained using the formula, as shown in Figure 4.12. Unlike (4.15), this time the formula does not provide a conservative estimate: the damping from (4.25) is *overestimated*, hence a proper assessment of high-droop instability requires a detailed representation of the system. This formulation has nonetheless allowed us to explore the physics behind this instability, which was one of our main objectives.

4.1.4 Key parameters for SICDS

By performing small-signal sensitivities to all the tuning parameters presented in Chapter 3, one is able to define an initial range for such parameters, assessing their impact on SICDS. These ranges should be refined when more IBRs are added to the system, but a 1-IBR system already offers some insight. As shown in Table 4.2, three tuning parameters for GFLs ($t_r^{v_{dc}}$, $t_r^{i_q}$, t_r^{pll}) lead to low-damping situations with frequencies close to those of SICDS phenomena. Their ranges may be updated so as to avoid these situations. For GFMs, on the other hand, numerous tuning parameters seem to have little impact on SICDS, given that their sensitivity analyses, considering their initial ranges, do not provoke low-damping situations. There are two parameters (m_p, $\tau_{v_{dc}}$), however, that do relate to SICDS; to these, we add ω_p, which, as expressed in Figure 4.14 may also lead to SICDS issues under specific circumstances.

IBR	Parameter	Bus	Initial range	Value for $\zeta = 3\,\%$	Frequency for $\zeta = 3\,\%$
GFL	$t_r^{v_{dc}}$	7	$10 - 500\,\mathrm{ms}$	$11.3\,\mathrm{ms}$ $249.3\,\mathrm{ms}$	$111.5\,\mathrm{Hz}$ $2.8\,\mathrm{Hz}$
	$t_r^{i_q}$	7	$20 - 1000\,\mathrm{ms}$	$24.9\,\mathrm{ms}$	$65.8\,\mathrm{Hz}$
	t_r^{pll}	7*	$10 - 1000\,\mathrm{ms}$	$17.9\,\mathrm{ms}$	$64.6\,\mathrm{Hz}$
	t_r^{i}	7	$0.5 - 20\,\mathrm{ms}$	$0.5\,\mathrm{ms}$	$970.0\,\mathrm{Hz}$
GFM	m_p	3	$0.001 - 0.250$	0.207	$14.0\,\mathrm{Hz}$
	ω_p	3	$1 - 100\,\mathrm{rd/s}$	–	–
	n_q	3	$0 - 0.5$	–	–
	ω_q	3	$1 - 100\,\mathrm{rd/s}$	–	–
	ω_{tvr}	3	$1 - 100\,\mathrm{rd/s}$	–	–
	$\tau_{v_{dc}}$	3	$5 - 100\,\mathrm{ms}$	$74.9\,\mathrm{ms}$	$3.0\,\mathrm{Hz}$
	t_r^{v}	3	$1 - 50\,\mathrm{ms}$	–	–
	t_r^{i}	3	$0.5 - 20\,\mathrm{ms}$	$1.1\,\mathrm{ms}$	$1868.0\,\mathrm{Hz}$

Table 4.2: Summary of sensitivities for 1-IBR system.

Since GFLs are prone to weak grid instabilities, all sensitivities for GFLs in Table 4.2 consider them to be connected to Bus 7, the one with the lowest SCR in the benchmark MVDG, namely SCR $= 3.39$. For all of these, we have adopted a short distance between the POI and the grid (only $d = 10\,\mathrm{m}$), except when performing the t_r^{pll} sensitivity, for which we considered a 5 km line in between, rendering the POI much weaker, i.e., SCR $= 2.48$. If not, there would be no PLL instability, which is a phenomenon we prefer to retain in our studies, due to its importance, or even prominence, in real-life SICDS events. It is worth noting that a 5 km line connecting an IBR to an MVDG, although unlikely, may still take place in practice. The aforementioned instability may be visualized in Figure 4.13.

When reading Table 4.2, one would imagine that ω_p has little impact on SICDS for a single-GFM system, given that, when sweeping the parameter from 1 to 100 rd/s, the minimal damping of the system remained above $\zeta = 3\,\%$. This situation is quite different when the droop is relatively high, e.g. $m_p = 0.2$ (once again, unrealistically high for practical situations, but serves our purpose in this example), for which an intermediary range of values for ω_p may lead to low damping, namely between 22.3 and 92.7 rd/s, as indicated in Figure 4.14. For a DSO trying to find a range of values to serve as a guideline for the multiple IBRs connected to an MVDG, this situation requires special care, since the problem is not necessarily an overtly high or low value for the parameter, but a specific range. Ways in which one could deal with this issue will be further explored in future chapters.

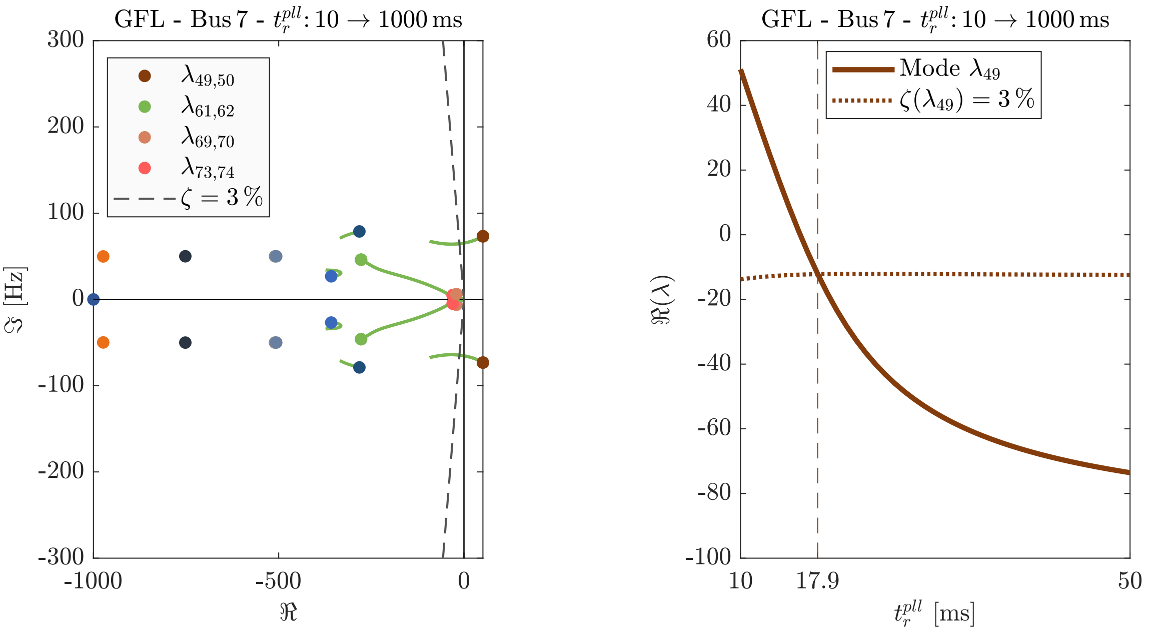

(a) Sensitivity (b) Eigenvalue trajectory

Figure 4.13: Eigen-sensitivity for t_r^{pll} in a GFL connected through a 5 km line (SCR = 2.48)

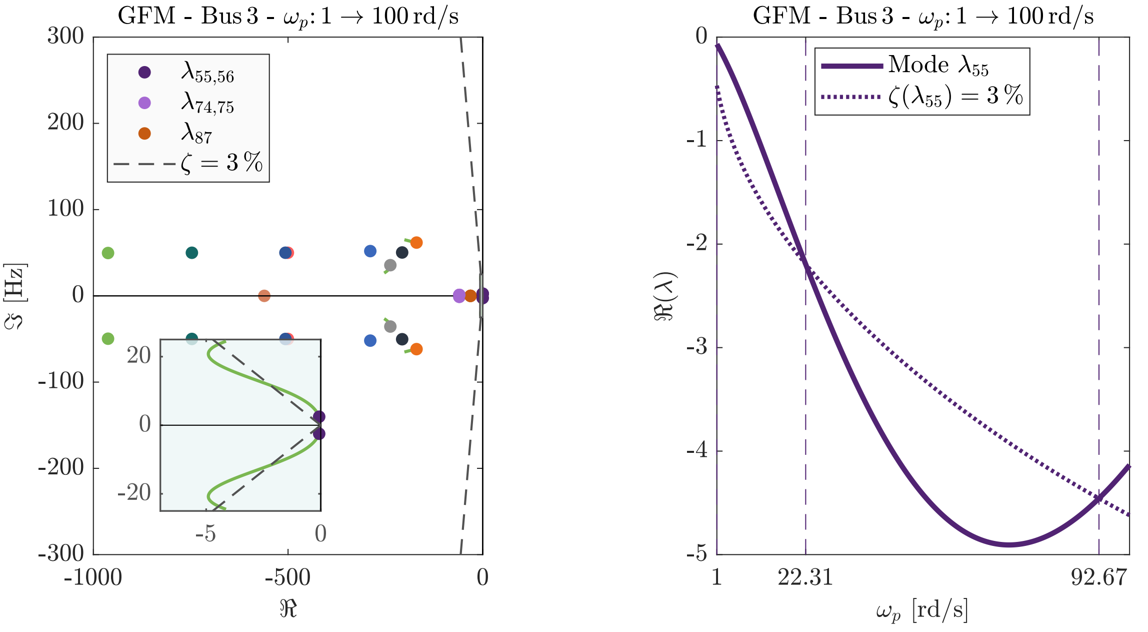

(a) Sensitivity (b) Eigenvalue trajectory

Figure 4.14: Eigen-sensitivity for ω_p in a GFM with $m_p = 0.2$

Therefore, two sets of tuning parameters are chosen as the "key parameters" for SICDS, as expressed in (4.26). From now on, these will be the only parameters we will explore. Although the small-signal sensitivities from Table 4.2 were the main criteria to demarcate the most relevant parameters, other factors have also been taken into consideration, such as the interest of a given parameter for our purposes, e.g., Q-control parameters in GFMs are of little interest, seen that GFMs may possibly be exempted from such task inasmuch as they can strictly control the voltage at their POI. Another factor is the "genericity" of a given parameter, i.e., the likelihood of it being applied in other control strategies: an active-damping loop, such as the TVR, is not always present in the models found in the literature, whereas a droop constant and a low-pass filter are much more commonly employed.

$$\boldsymbol{p_t}^{\text{GFL}} = \begin{bmatrix} t_r^{v_{dc}} & t_r^{i_q} & t_r^{pll} \end{bmatrix}^t \qquad\qquad \boldsymbol{p_t}^{\text{GFM}} = \begin{bmatrix} m_p & \omega_p & \tau_{v_{dc}} \end{bmatrix}^t \tag{4.26}$$

4.2 2-IBR system: interactions between IBRs

4.2.1 Choice of scenarios

A 2-IBR system is ideal to study the interactions between IBRs connected to an MVDG. For such, it is important to select interesting scenarios, capable of representing the most extreme situations from the point-of-view of stability. Whereas these were mostly dependent on the SCR seen by the POI for a 1-IBR system (see Table 4.1), now we must also assess the electrical distance between the buses onto which the IBRs are connected. This can be done by computing the bus-to-bus impedance $\bar{Z}_{ab}$ between Bus a and Bus b:

$$\bar{Z}_{ab} = \boldsymbol{Z_{bus}}(a,a) + \boldsymbol{Z_{bus}}(b,b) - 2\,\boldsymbol{Z_{bus}}(a,b) \tag{4.27}$$

where $\boldsymbol{Z_{bus}}$ is the *nodal impedance matrix*, commonly employed in load-flow analysis or short-circuit studies [112]. The lower the $\bar{Z}_{ab}$ between two buses, the closer they are from an electrical point-of-view. This might increase the chances of SICDS issues related to the IBRs connected to these buses. Figure 4.15 provides $\bar{Z}_{ab}$ for all pairs of buses in the main feeder of our benchmark MVDG, and Table 4.3 summarizes the major pairs.

Starting with a GFL/GFL configuration, we observe how a standard tuning will once again yield satisfactory stability for all connection scenarios, as depicted in Figure 4.16a. If the PLL time response is reduced, however, as in Figure 4.16b, some connections will lead to low damping. Figure 4.17a provides an explanation: situations with the lowest minimal-damping (darkest points in the scatter plot) happen whenever at least one of the buses has a low SCR. The pair of buses 10/11 is the most extreme of these scenarios, where both buses are weak and in proximity to each other; it will thus be adopted as our "S3" scenario in Table 4.4. It is worth noting that, for a GFL/GFL configuration, the distance between IBRs does not necessarily correlate with low damping, as shown in Figure 4.17b: buses 3/4, for instance, have a $\bar{Z}_{ab}$ similar to 10/11, but their minimum damping is eight times higher.

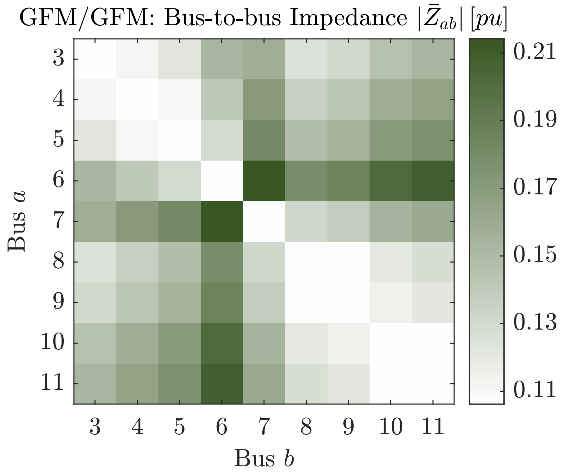

Figure 4.15: Bus-to-bus impedance for a 2-IBR system

For a GFM/GFM configuration with high droops, on the other hand, the minimal damping seems to be almost perfectly correlated with the distance between IBRs, as demonstrated in Figure 4.19b. Even if the SCR still plays an important role, as shown in Figure 4.19a, where most of the low-damping configurations involve at least one high-SCR bus, a short distance between high-droop GFMs is the most relevant factor for SICDS: buses 8/9 are weaker than 3/4, but closer to each other, leading to lower damping. Both of these pairs constitute interesting scenarios, hence they are both included in Table 4.4 as “S5” and “S1”, respectively. It is worth mentioning that GFMs with standard tuning are also far from the low-damping region, as seen in Figure 4.18a. The “high-droop” scenario, which was previously considered to happen for exaggeratedly high values, e.g. $m_p = 0.2$ for a 1-IBR system, now may take place for $m_p = 0.04$, as in Figure 4.18b, a value that is within the 5 % range considered as “typical”. This indicates that GFMs may indeed interact in a way that renders the system prone to small-signal instabilities.

Nearest pairs of buses			Furthest pairs of buses		
Bus a	Bus b	$\bar{Z}_{ab}$ [pu]	Bus a	Bus b	$\bar{Z}_{ab}$ [pu]
8	9	0.1062	6	7	0.2142
10	11	0.1064	6	11	0.2087
4	5	0.1107	6	10	0.2018
3	4	0.1116	6	9	0.1859
9	10	0.1146	5	7	0.1821

Table 4.3: $\bar{Z}_{ab}$ for major pairs of buses in the benchmark MVDG

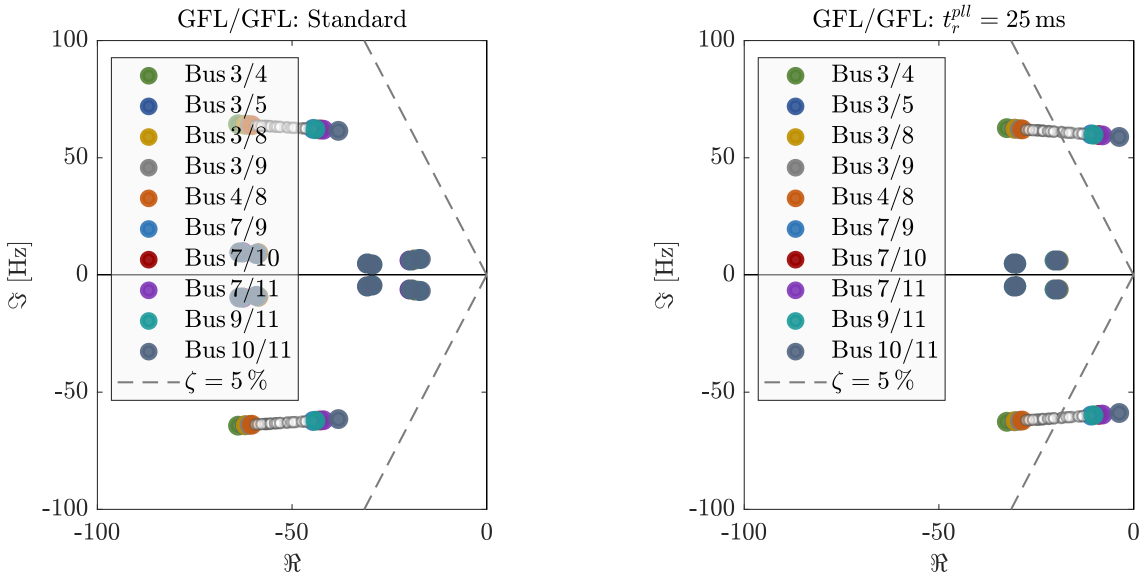

(a) Standard configuration

(b) Fast-PLL configuration

Figure 4.16: SSSA of a pair of GFLs connected to different buses in the MVDG. Fast-PLL GFLs present low damping when connected to the weakest buses in the system.

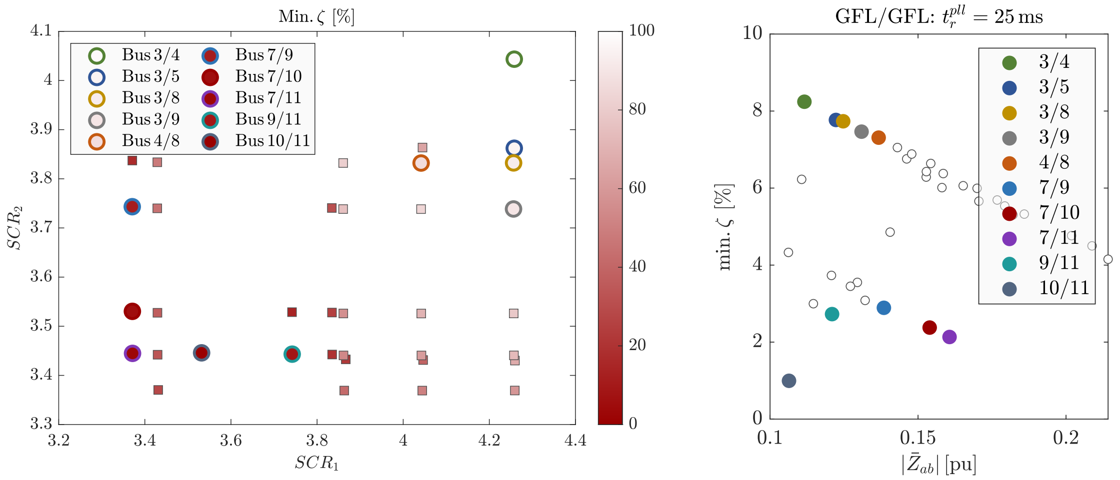

(a) Min. ζ as function of SCRs

(b) Min. ζ as function of $\overline{Z}_{ab}$

Figure 4.17: Minimum damping as a function of SCR for both POIs, as well as the impedance between the IBRs (both are GFLs).

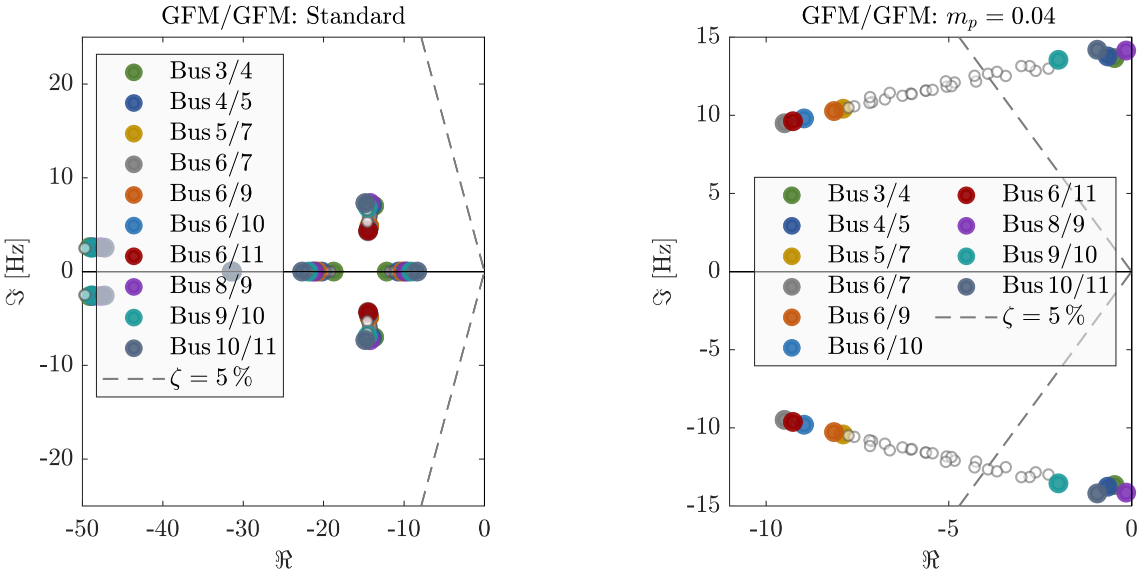

(a) Standard configuration

(b) High-droop configuration

Figure 4.18: SSSA of a pair of GFMs connected to different buses in the MVDG. High-droop GFMs present low damping when connected to the strongest buses in the system or when in close proximity to each other.

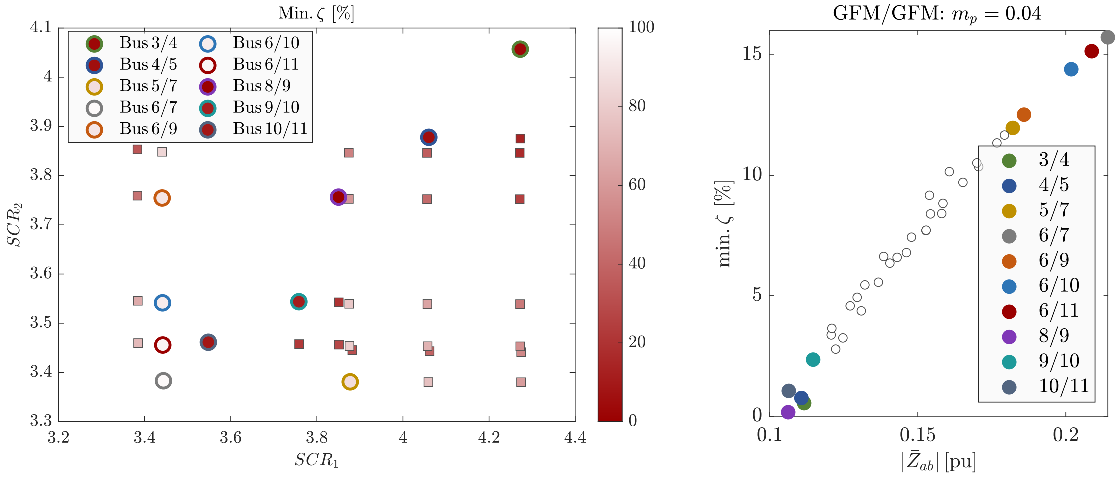

(a) Min. ζ as function of SCRs

(b) Min. ζ as function of $\overline{Z}_{ab}$

Figure 4.19: Minimum damping as a function of SCR for both POIs, as well as the impedance between the IBRs (both are GFMs).

Scenario	Bus a	Bus b	Distance [km]	$\bar{Z}_{ab}$ [pu]	SCR a	SCR b	Description
S1	3	4	0.8	0.1116	4.28	4.07	Strong and nearby
S2	3	5	1.4	0.1223	4.28	3.88	Strong and far
S3	10	11	0.5	0.1064	3.55	3.46	Weak and nearby
S4	7	11	3.3	0.1606	3.39	3.46	Weak and far
S5	8	9	0.3	0.1062	3.85	3.76	Nearest buses

Table 4.4: Selected scenarios for a 2-IBR system

To conclude, five scenarios are selected for further studies, considered to be sufficiently representative of the most extreme, yet feasible, situations in our benchmark MVDG, from the point-of-view of SICDS. These are presented in Table 4.4.

4.2.2 Modal maps

As in Section 4.1.2, we may proceed by characterizing the major modes in a 2-IBR system, especially those in which both IBRs present a significant participation, indicative of an interaction between them. A comparison between the modal maps of the three possible configurations (GFL/GFL, GFL/GFM, and GFM/GFM), as well as a comparison with respect to the situation with only one IBR (Figures 4.5 and 4.6), could also provide some insight into the root cause of certain SICDS issues.

Let us begin with a GFL/GFL configuration, for which Figure 4.20a indicates two fairly-stable dominant modes in the SICDS frequency range, namely $\lambda_{83,84}$ and $\lambda_{89,90}$, both of which, according to Figure 4.20b, involve the P-control loop of *both* IBRs, hinting at a possible interaction. Other low-frequency modes are in the vicinity of the $\zeta = 70.7\,\%$ damping line, involving both the Q-control loop ($\lambda_{87,88}$, $\lambda_{91,92}$) and the PLL ($\lambda_{81,82}$, $\lambda_{85,86}$). As for the 1-IBR systems, these control loops are the most relevant for SICDS involving GFLs.

For a GFL/GFM configuration, depicted in Figure 4.21, modes are mostly related to only one IBR, almost as a superposition of Figures 4.5a and 4.6a, with few exceptions, e.g., $\lambda_{69,70}$, $\lambda_{72,73}$, $\lambda_{76,77}$, and $\lambda_{78,79}$, in which an interaction is clear, although these are mostly high-frequency modes. This situation may change under different grid conditions, as will be further explored in this chapter. The most relevant SICDS-related modes are $\lambda_{90,91}$, $\lambda_{92,93}$, and $\lambda_{94,95}$. Mode $\lambda_{90,91}$ is mostly associated with the P-control loop from the GFM, with slight participation from the GFL's counterpart ($\gamma_{v_{dc}}$). Modes $\lambda_{92,93}$ and $\lambda_{94,95}$ are related to the GFL's P and Q-control loops, respectively. Once again, external loops play a major role.

A GFM/GFM configuration, as the one with two GFLs, also presents multiple interaction modes, as depicted in Figure 4.22. Unsurprisingly, the major players are the external control loops (λ_{91}, λ_{92}) and the TVR ($\lambda_{89,90}$), just as in a 1-IBR system. From Figure 4.22b, it is interesting to observe the difference between *interaction* modes, such as λ_{91} and λ_{92}, and *single-IBR* modes, such as $\lambda_{95,96}$ and $\lambda_{97,98}$. While the former modes, related to the P-control loop, involve both IBRs, the latter ones, associated with the v_{dc} control, are concentrated on only one IBR each, with no interaction between them. Evidently, interaction modes are of special interest in this section, given that they are particularities of a multi-IBR system.

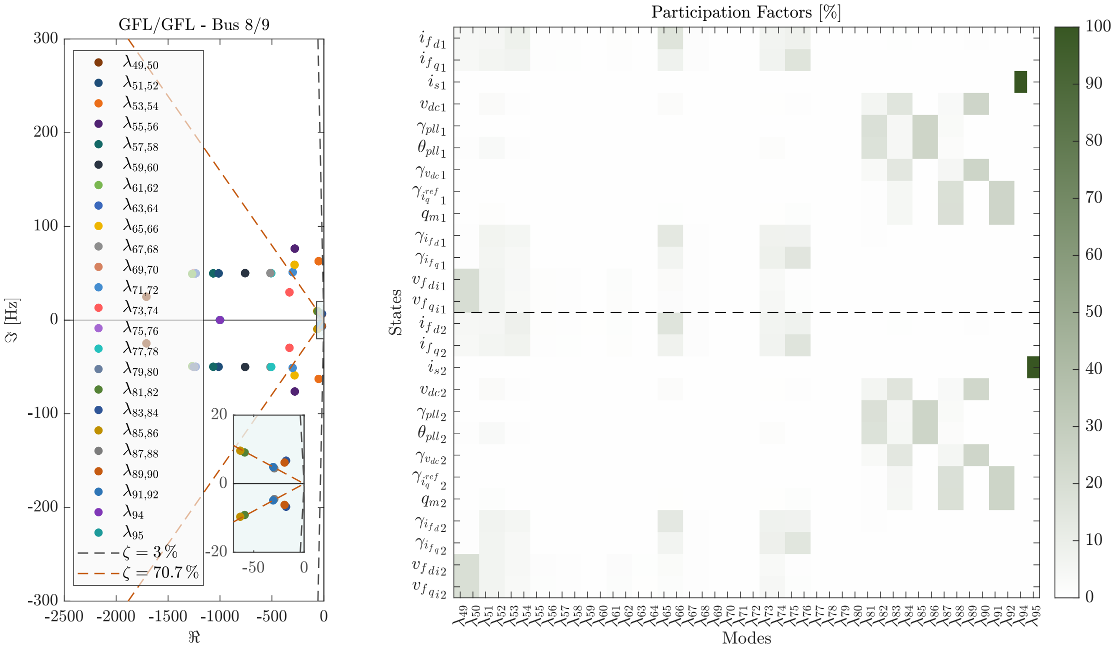

(a) Selected modal map

(b) Participation matrix

Figure 4.20: Mode characterization for a GFL/GFL configuration

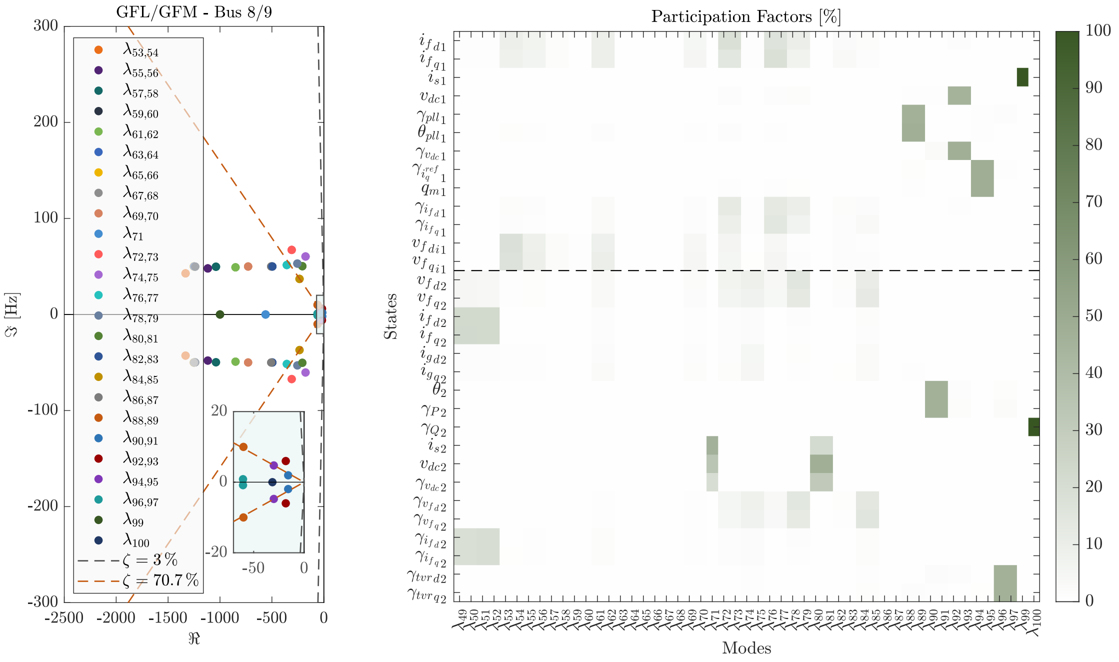

(a) Selected modal map

(b) Participation matrix

Figure 4.21: Mode characterization for a GFL/GFM configuration

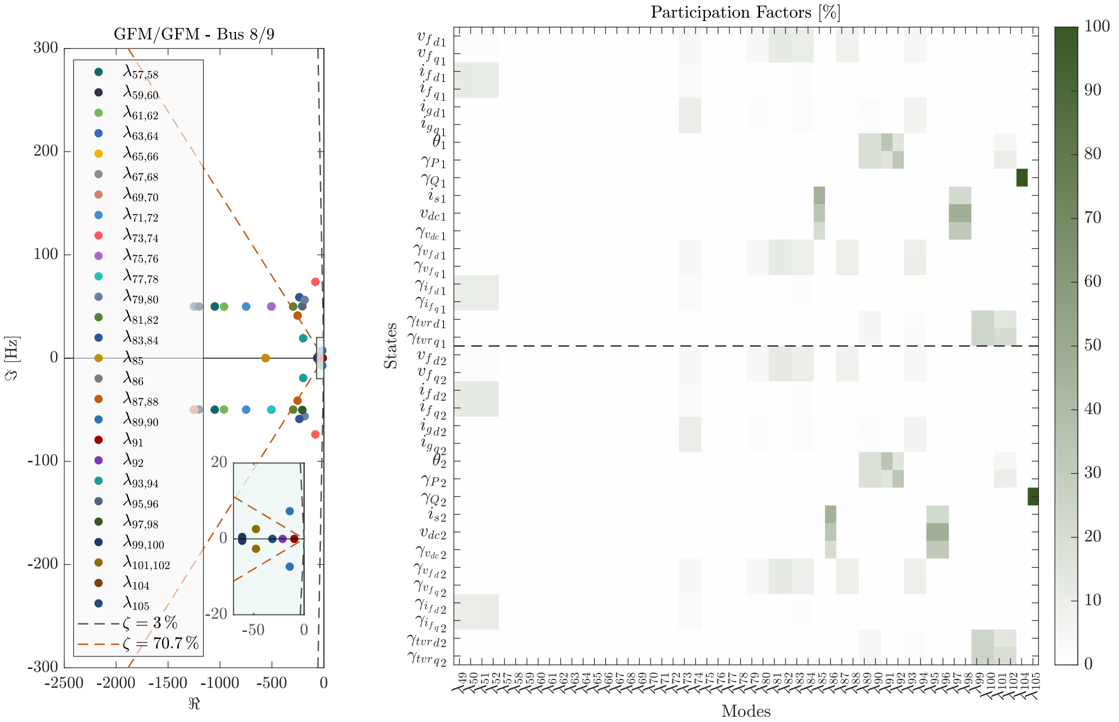

(a) Selected modal map

(b) Participation matrix

Figure 4.22: Mode characterization for a GFM/GFM configuration

4.2.3 Selected sensitivities

As for the 1-IBR system in Section 4.1.3, a series of eigen-sensitivities may provide further insight into the root causes of certain small-signal interactions between IBRs. Although we have narrowed our set of parameters to just three per IBR (Section 4.1.4), an extensive small-signal study calls for a large number of sensitivities, both *single-parameter sensitivities* (SPS), i.e., only a given parameter of one single IBR is swept within a range, while the other IBR remains constant[3], or *double-parameter sensitivities* (DPS), where a given parameter that exists in both IBRs is swept for both at the same time. The present section is dedicated to SPS, where we attempt to compare a given 1-IBR sensitivity to the same sensitivity when performed in the presence of another IBR; the differences between them will reveal the manner in which the second IBR affects the behavior of the first one. Three special cases will be investigated in detail, all of which were already presented for a 1-IBR system in Section 4.1.3: high-$t_r^{v_{dc}}$ instability in GFLs, high-droop instability in GFMs, and fast-PLL instability in weakly-connected GFLs. Besides apprehending the physics behind each of these interactions, our goal is to refine the parameter ranges from Table 4.2 and advance towards a more systematic methodology to improve them.

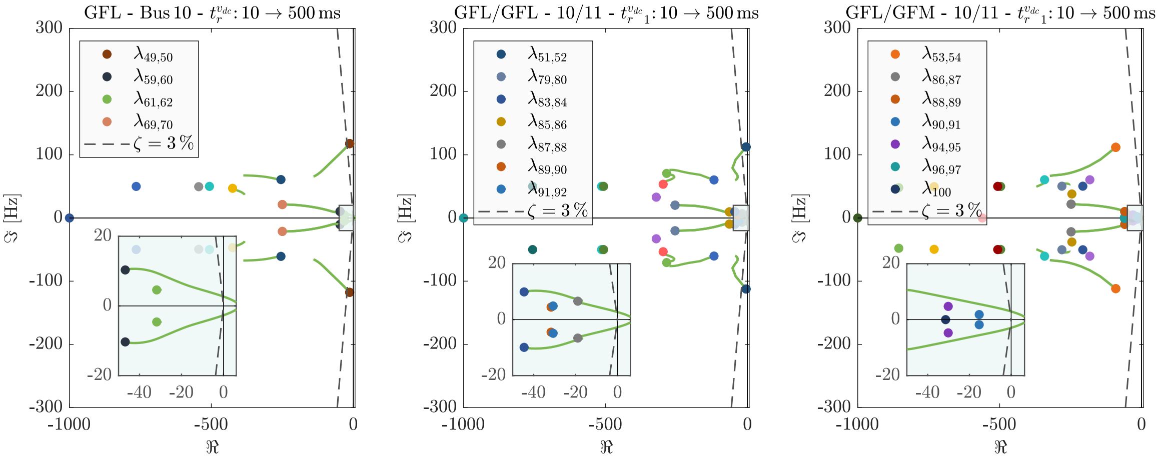

(a) Only GFL (b) GFL/GFL (c) GFL/GFM

Figure 4.23: Single-parameter eigen-sensitivity for $t_r^{v_{dc}}$ in a GFL under three configurations (only one GFL, two GFLs, and a GFL with a GFM).

4.2.3.1 High-$t_r^{v_{dc}}$ instability in GFLs in the presence of another IBR

Let us begin by repeating the sensitivity from Section 4.1.3.1 for a single GFL connected to Bus 10, sweeping $t_r^{v_{dc}}$ from 10 to 500 ms, as displayed in Figure 4.23a. Ignoring the high-

---

[3] In this section, the additional IBR is always tuned as per its “standard” configuration, given in Table 3.5.

frequency mode $\lambda_{49,50}$ which is unstable for a very small value of $t_r^{v_{dc}}$ (10 ms is just as fast as the inner loop), the SICDS-related mode $\lambda_{59,60}$ crosses the $\zeta = 3\,\%$ damping line when $t_r^{v_{dc}} \approx 248\,\text{ms}$, as indicated in Figure 4.24a, leading to 3 Hz oscillations. When another GFL is added, connected to Bus 11 (Scenario S3 in Table 4.4), there is no major difference with respect to this mode, the sensitivity remains virtually the same, with mode $\lambda_{87,88}$ crossing the $\zeta = 3\,\%$ line at $t_r^{v_{dc}} = 248\,\text{ms}$ in Figure 4.24b.

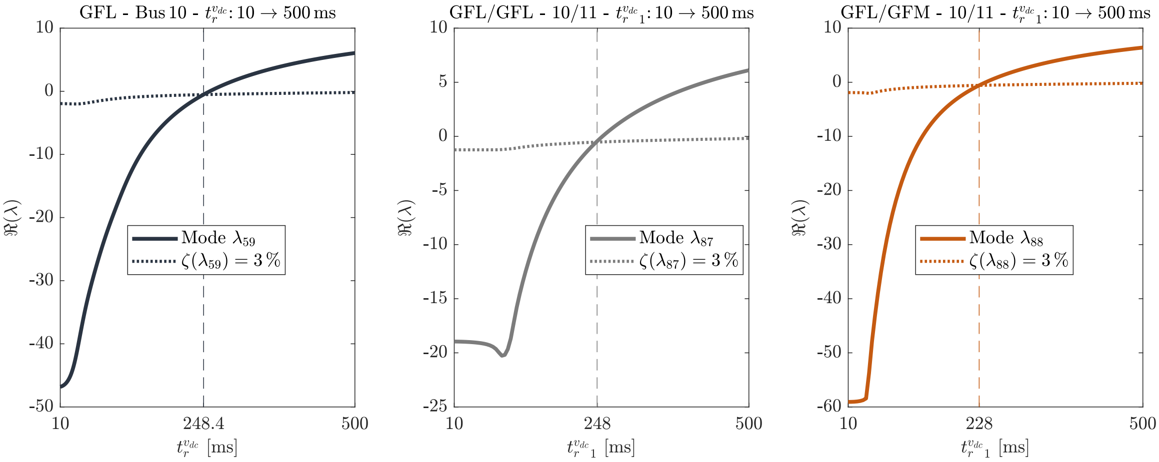

(a) Only GFL (b) GFL/GFL (c) GFL/GFM

Figure 4.24: Eigenvalue trajectory for $t_r^{v_{dc}}$ in a GFL under three configurations (only one GFL, two GFLs, and a GFL with a GFM)

We may recall that a rule-of-thumb was established to avoid such instabilities in (4.15), according to which, for $C_{dc} = 0.04\,\text{pu}$, $t_r^{v_{dc}}$ should remain below 240 ms. Figures 4.24a and 4.24b both corroborate with this formula, since the instability only occurs when $t_r^{v_{dc}}$ is above this value. Interestingly, the situation gets *worse* when a GFM is added, leading to a lower threshold for this instability: from Figure 4.24c, $t_r^{v_{dc}}$ has to remain below 228 ms to avoid a low-damping situation. In this case, (4.15) is incapable of providing a conservative estimate for stable operation. Although omitted here, participation factors for mode $\lambda_{88,89}$ in Figure 4.23c relate them to the P-control loop in both the GFL and the GFM, hinting at a P-related interaction between the IBRs, which is confirmed by the time-domain simulation (TDS) in Figure 4.25. Whereas the GFL/GFL configuration experiences weakly-damped power oscillations exclusively in IBR 1 when its $t_r^{v_{dc}}$ is high, a GFL/GFM configuration has to deal with oscillations in *both* IBRs, indicating an interaction. This is a rare situation in which a GFL-related SICDS issue is aggravated by the presence of a GFM, upholding the complexity of the subject. In most cases, a GFL/GFM configuration is the most stable.

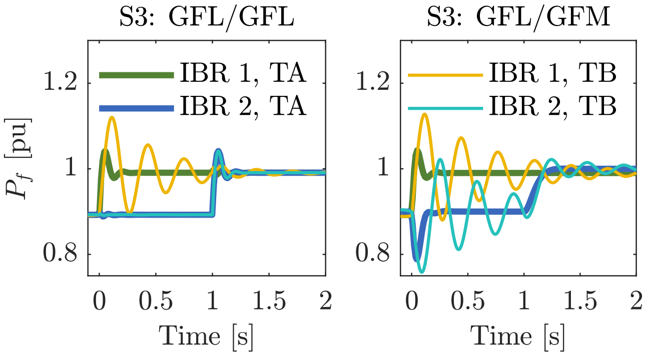

Figure 4.25: Time-domain simulation to illustrate the results from Figure 4.23. Here, "IBR 1" and "IBR 2" represent the injected power P_f for each inverter, following a 0.1 pu step on p^{ref} for IBR 1 (at $t = 0$ s) and IBR 2 ($t = 1$ s). "TA" and "TB" are tuning configurations: "TA" is the standard configuration ($t_r^{v_{dc}} = 100$ ms for both IBRs), whereas "TB" presents a modified tuning for IBR 1: $t_r^{v_{dc}} = 220$ ms.

4.2.3.2 High-m_p instability in GFMs in the presence of another IBR

Now repeating the sensitivity from Section 4.1.3.2, sweeping the droop constant m_p from 0.1 % to 25 % for a single GFM connected to Bus 10, we derive the plot from Figure 4.26a, where even the excessively elevated $m_p = 0.25$ is not able to drive the system to a damping ratio below $\zeta = 3\,\%$. Indeed, since this is a relatively weak bus (see Table 4.1), a 1-IBR system with a GFM is expected to be particularly stable. When another GFM is connected to Bus 11, however, even a droop just below 6 % in the first GFM, as in Figure 4.27b, is enough to lead mode $\lambda_{92,93}$ to weakly-damped 13 Hz oscillations. Because of the low-frequency small-signal interactions between nearby-connected GFMs, the maximum allowable droop is reduced to less than a quarter of its value in a 1-IBR system. Defining this maximum droop is one of the main challenges in integrating GFMs into MVDGs: future sections will elucidate this topic, demonstrating why even the typical droop range of up to 5 % may still entail SICDS risks under stringent grid conditions.

If the additional IBR is a GFL, however, Figure 4.26c does not indicate a low-damping situation; in fact, a GFM/GFL configuration is even more stable than a single GFM, given that mode $\lambda_{92,93}$ in Figure 4.27c is further away from $\zeta = 3\,\%$ than mode $\lambda_{55,56}$ in Figure 4.27a when m_p is at its maximum value. Once again, a TDS is provided in Figure 4.28 to further corroborate these conclusions, namely the superiority of a GFM/GFL configuration when compared to a GFM/GFM, with respect to small-signal stability in high-droop situations.

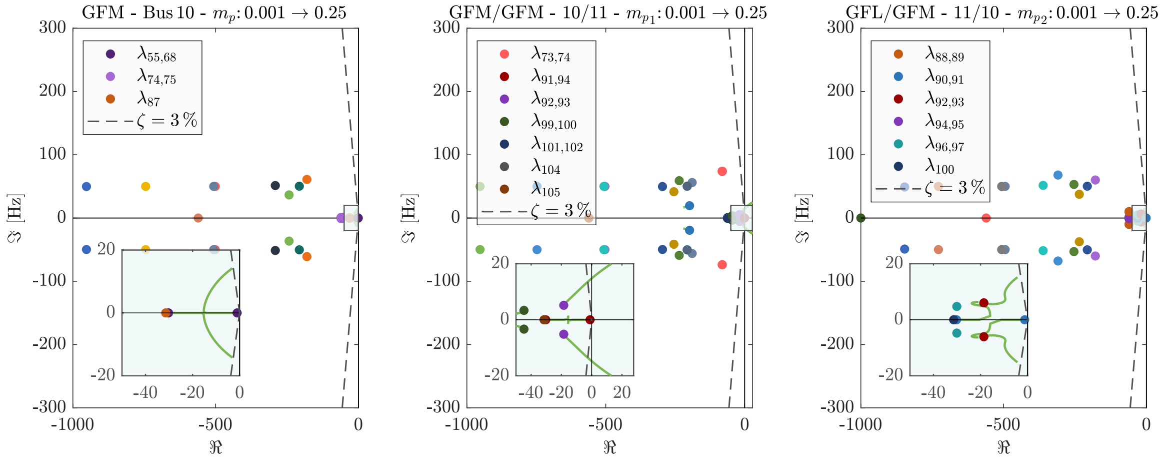

(a) Only GFM (b) GFM/GFM (c) GFM/GFL

Figure 4.26: Single-parameter eigen-sensitivity for m_p in a GFM under three configurations (only one GFM, two GFMs, and a GFM with a GFL).

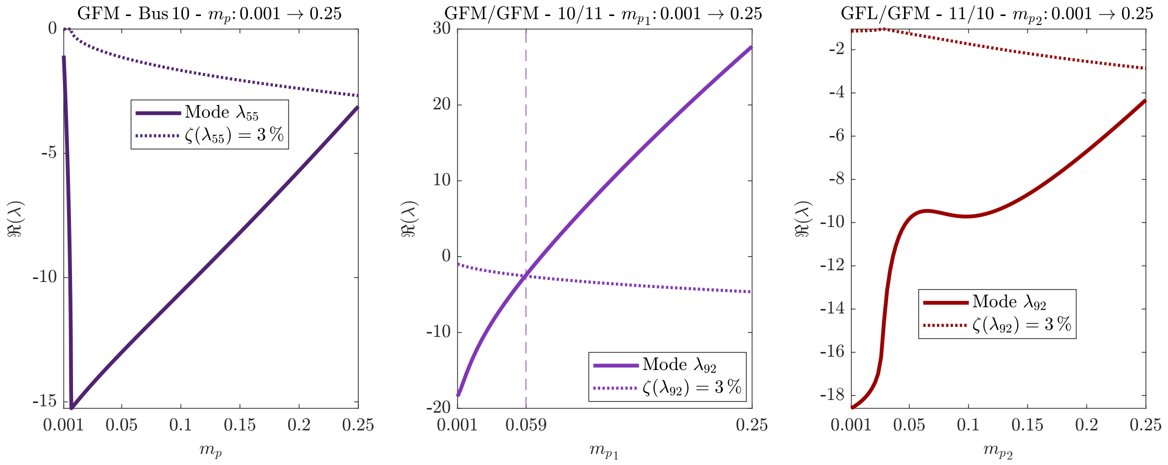

(a) Only GFM (b) GFM/GFM (c) GFM/GFL

Figure 4.27: Eigenvalue trajectory for m_p in a GFM under three configurations (only one GFM, two GFMs, and a GFM with a GFL)

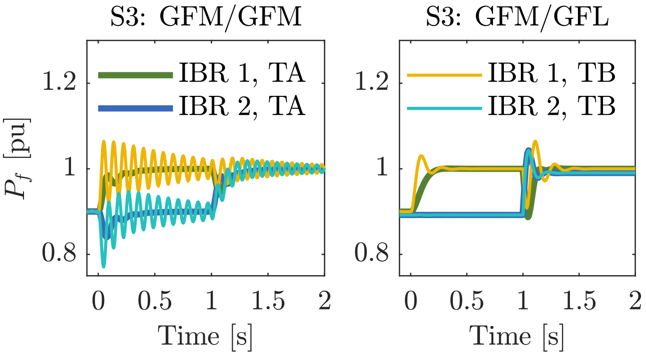

Figure 4.28: Time-domain simulation to illustrate the results from Figure 4.26. P_f for both IBRs following a 0.1 pu step on p^{ref} for IBR 1 (at $t = 0$ s) and IBR 2 ($t = 1$ s). Once again, "TA" is the standard tuning configuration ($m_p = 0.01$ for both IBRs), while "TB" is modified for IBR 1: $m_p = 0.045$.

4.2.3.3 Low-t_r^{pll} instability in GFLs in the presence of another IBR

Our final single-parameter sensitivity deals with the phenomenon briefly discussed in Section 4.1.4, Figure 4.13, when a GFL is connected to a weak bus in the MVDG through a 5 km line, rendering its POI weak enough for the IBR to experience PLL instability if t_r^{pll} is low enough. We repeat this sensitivity in Figure 4.29a for a single GFL connected to Bus 11 through the same 5 km line. As indicated in Figure 4.30a, a t_r^{pll} just below 18 ms is enough to cause weakly-damped oscillations at 60 Hz. Adding a standard GFL, connected at Bus 10, further decreases the SCR at the POI of the first IBR, which leads to a narrower margin for the PLL, i.e., the minimum t_r^{pll} is now as high as 30 ms according to Figure 4.30b.

Replacing the additional GFL with a GFM results in a completely different situation, as indicated in Figure 4.29c, where there is no instability even for the fastest PLL. A GFM is capable of increasing the strength of the POI for the GFL in its vicinity, constituting a *positive* interaction. This time, rather than yet another TDS to validate these results, we provide an additional SPS for the GFL/GFM configuration in Figure 4.31, where the GFM is now connected to Bus 7 rather than Bus 10. As observed in Figure 4.31b, a t_r^{pll} of 11 ms now leads to unsatisfactory damping, which was not the case in Figure 4.30c. This reiterates the fact that the GFM increases the POI strength for the GFLs *in its vicinity*. If the GFM is too distant, this additional strength may not be enough to avoid PLL instability. It remains nonetheless impressive that a GFM in a neighboring bus is capable of stabilizing a GFL located more than 5 km away, which suggests that GFM may serve as a powerful asset for DSOs.

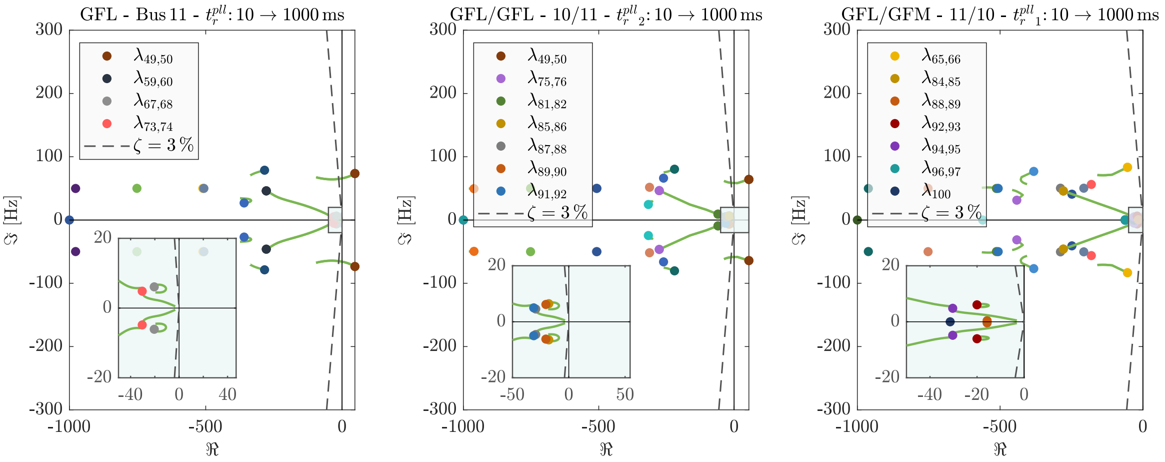

(a) Only GFL (b) GFL/GFL (c) GFL/GFM

Figure 4.29: Single-parameter eigen-sensitivity for t_r^{pll} in a GFL under three configurations (only one GFL, two GFLs, and a GFL with a GFM).

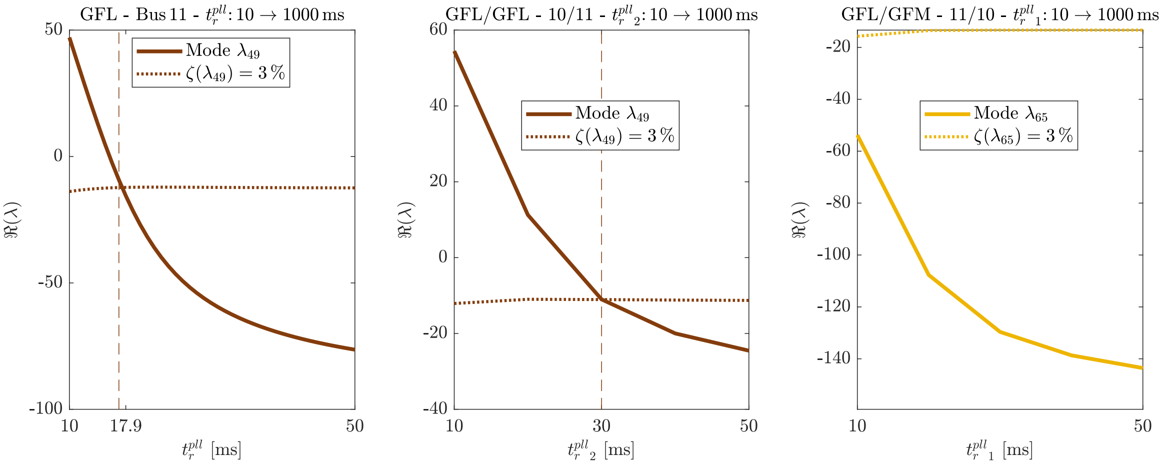

(a) Only GFL (b) GFL/GFL (c) GFL/GFM

Figure 4.30: Eigenvalue trajectory for t_r^{pll} in a GFL under three configurations (only one GFL, two GFLs, and a GFL with a GFM)

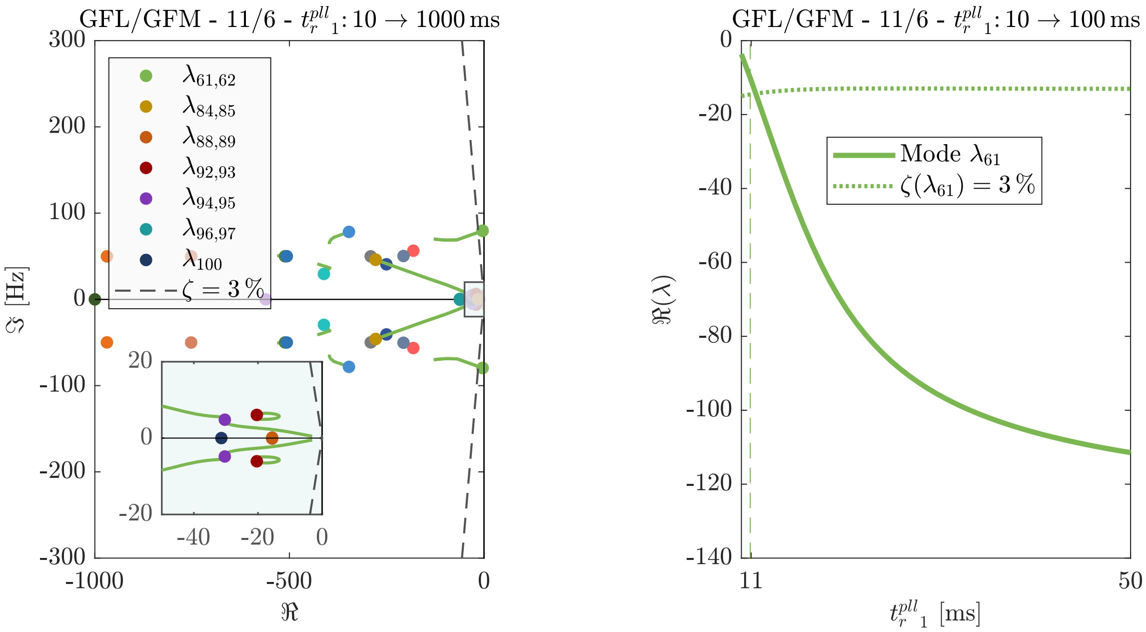

(a) Sensitivity (b) Eigenvalue trajectory

Figure 4.31: Eigen-sensitivity for t_r^{pll} in a GFL for a GFL/GFM configuration. Here, the GFL is connected at Bus 11, while the GFM is connected at Bus 7.

4.3 Improving parameter bounds for small-signal stability

From Section 4.1.4, as defined in (4.26), we know that certain key parameters play a major role in SICDS. In Section 4.2.3, we have assessed their impact on a 2-IBR system, stressing the importance of limiting their values within a reasonable range. In practice, producers may be compelled to tune their IBRs according to their own needs, for which they might employ a 1-IBR equivalent model for the system, such as in Section 4.1. The presence of an additional IBR, however, may lead to a shift in system dynamics, rendering the previous parameterization unsatisfactory in terms of stability. In such situations, the DSO could arbitrate among the different requirements of individual producers by imposing *ranges* (or *bounds*) for the aforementioned key parameters, with the purpose of preventing SICDS issues.

In order to present a methodology for the DSO to impose such bounds, we may begin with a case study consisting of two IBRs connected to buses 10 and 11 (Scenario S3 in Table 4.4), tuned within the ranges presented in Table 4.5. These initial bounds stem from the single-parameter sensitivities presented in Section 4.2.3, already constituting an improvement with regards to Table 4.2, but our objective is to improve them further. A reasonable first step is to ensure that all the different IBR configurations in which the key parameters are either at their minimum or maximum values, i.e., boundary configurations (BC)[4], are sufficiently stable, which we define as a minimum damping of $\zeta \geq 3\,\%$ for all eigenvalues with frequencies under 500 Hz. Logically, the next step, explored in the next chapter, would be to ensure a stable operation *within* the proposed parameter ranges, updating the bounds if necessary.

IBR	Parameter	Minimum	Maximum	Standard
GFL	$t_r^{v_{dc}}$	50 ms	220 ms	100 ms
	$t_r^{i_q}$	50 ms	1000 ms	100 ms
	t_r^{pll}	20 ms	1000 ms	50 ms
GFM	m_p	0.005	0.05	0.01
	ω_p	3.14 rd/s	62.8 rd/s	31.4 rd/s
	$\tau_{v_{dc}}$	3 ms	70 ms	5 ms

Table 4.5: Original bounds for key tuning parameters

4.3.1 Extreme configurations

For ensuring the stable operation of BCs, we follow an empirical yet systematic methodology, assessing *extreme configurations* (EC) and improving their stability via *multi-parameter sensitivities* (MPS)[5] or, in this specific case (with only two IBRs), *double-parameter sensitivities* (DPS). ECs are a subset of all the BCs, comprising only the most stringent configurations. Although we assess the small-signal stability of all BCs, there is no need to apply MPS to all of them, but only to the worst cases, i.e., the ECs. Considering our 2-IBR case study, where each IBR has three key parameters, there are 64 BCs in total, from which we have selected, according to the sensitivity studies described below, three ECs for GFLs (GFLB, GFLC, GFLD) and one for GFMs (GFMB), as presented in Table 4.6. These are added to the standard configurations (GFLA, GFLB), tuned according to Table 3.5.

Parameter	GFLA	GFLB	GFLC	GFLD	Parameter	GFMA	GFMB
$t_r^{v_{dc}}$	100 ms	220 ms	220 ms	50 ms	m_p	0.01	0.05
$t_r^{i_q}$	100 ms	50 ms	1000 ms	50 ms	ω_p	31.4 rd/s	62.8 rd/s
t_r^{pll}	50 ms	20 ms	1000 ms	20 ms	$\tau_{v_{dc}}$	5 ms	70 ms

Table 4.6: Extreme configurations (EC) for GFLs and GFMs

An additional constraint for DSOs is to adopt "simple" requirements for key parameters,

---

[4] The concept of "boundary configuration" will be examined in detail in the next chapter.

[5] An MPS is nothing but a sensitivity study where the same parameter is swiped from minimum to maximum for *all* IBRs. If there are two GFLs, for instance, the MPS for t_r^{pll} would modify the t_r^{pll} for both GFLs, as in Figure 4.32b, in contrast to Figure 4.29b, where t_r^{pll} for the first GFL was kept constant.

which we define as requirements that apply *equally* to all the pertinent IBRs[6] in a given system. This means that, in most cases, a DSO is expected to impose the same bounds for t_r^{pll}, for instance, on all the pertinent GFLs connected to a certain MVDG, the ranges are not personalized for each IBR. The distinction between GFL and GFM remains important, nonetheless, i.e., requirements for GFLs and GFMs are not the same, given that they have different key parameters.

4.3.2 Multi-parameter sensitivities

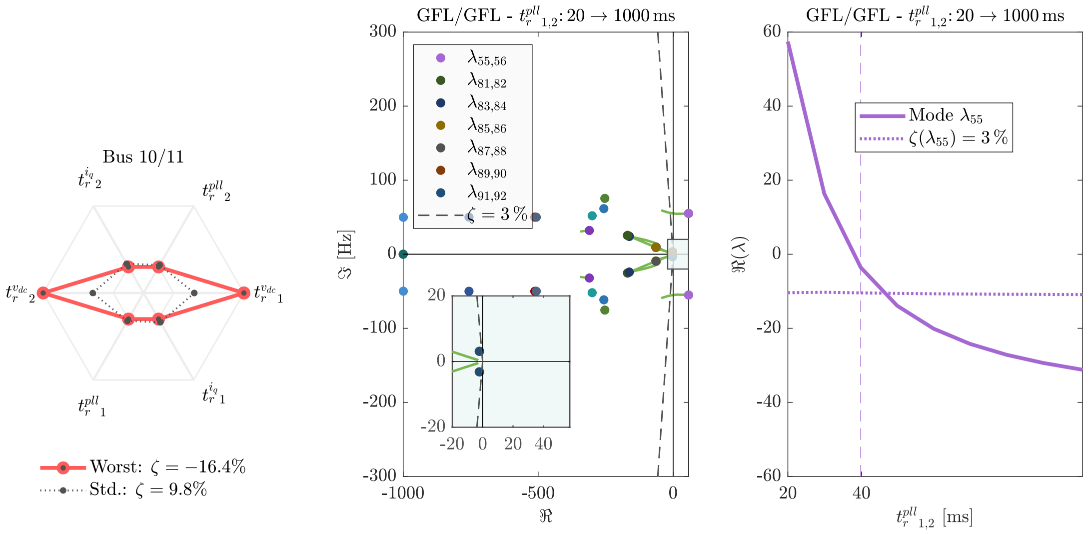

(a) Worst configuration (b) DPS for $t_r^{pll}{}_{1,2}$ (c) Eigenvalue trajectory

Figure 4.32: Worst combination between bound values for a GFL/GFL configuration, leading to a damping of $\zeta = -16.4\,\%$, and an eigen-sensitivity for t_r^{pll} in both GFLs, aiming to find a *minimal* t_r^{pll} to improve the worst-case damping.

Let us begin with a GFL/GFL configuration, as presented in Figure 4.32. Using the original bounds from Table 4.5, among all the 64 BCs, the one depicted in Figure 4.32a yields the worst damping $\zeta = -16.4\,\%$, which is actually negative, i.e., unstable. This BC is constituted of two GFLs with minimum $t_r^{i_q}$ and t_r^{pll}, and maximum $t_r^{v_{dc}}$. Because such a BC is the worst-case scenario for a GFL/GFL configuration, it has been adopted as an EC in Table 4.6, namely “GFLB”. In order to mitigate this issue, we should detect which key parameters are capable of bringing the system back to stability. PFs indicate that mode $\lambda_{55,56}$ in Figure 4.32b is associated with the PLLs of both GFLs, hence we may apply a DPS for t_r^{pll}, finding a range which would drive this EC to stable operation. Figure 4.32c indicates that

---

[6] A “pertinent” IBR is one that is expected to comply with specific DSO requirements. These could be, for example, IBRs located in particularly weak POIs, IBRs that have a considerable installed capacity, or IBRs in close proximity with other IBRs.

increasing the minimum t_r^{pll} to a value above 40 ms could ensure proper damping. We may thus adopt $\min(t_r^{pll}) = 45\,\mathrm{ms}$ in Table 4.7.

Now reassessing all the BCs for the same GFL/GFL configuration, with bound values still as in Table 4.5, but with $\min(t_r^{pll}) = 45\,\mathrm{ms}$, we get a new worst-case BC in Figure 4.33a. This time it consists of all three parameters at their maximum values, being adopted as the EC named "GFLC" in Table 4.6. Using the exact same procedure in Figure 4.33b, we observe a low-frequency mode (λ_{89} in Figure 4.33c) becoming weakly-damped when t_r^{pll} is too high. Unlike previous situations of PLL-related instability, this time we observe a *slow*-PLL low-damping issue, effectively in the frequency range of SICDS phenomena. According to Figure 4.33c, a maximum t_r^{pll} below 662 ms for both GFLs could solve this issue. We therefore adopt $\max(t_r^{pll}) = 600\,\mathrm{ms}$ in Table 4.7.

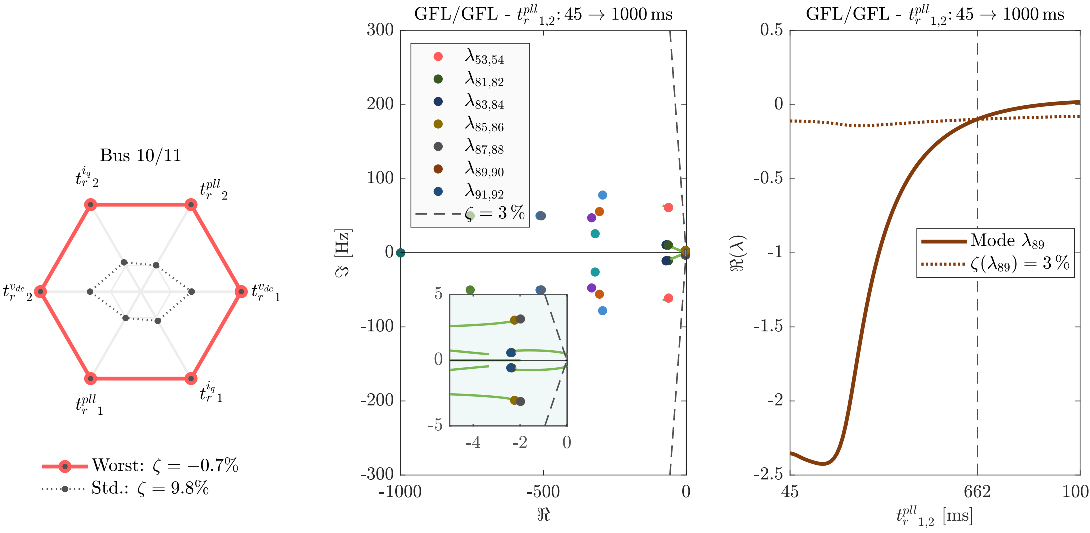

(a) Worst configuration (b) DPS for $t_r^{pll}{}_{1,2}$ (c) Eigenvalue trajectory

Figure 4.33: Worst combination between bound values for a GFL/GFL configuration (after updating the minimal t_r^{pll}), leading to a damping of $\zeta = -0.7\,\%$, and an eigen-sensitivity for t_r^{pll} in both GFLs, aiming to find a *maximal* t_r^{pll} to improve the worst-case damping.

Reapplying the method for a third time, using the values of Table 4.5 with $\min(t_r^{pll}) = 45\,\mathrm{ms}$ and $\max(t_r^{pll}) = 600\,\mathrm{ms}$, the resulting worst-case (third EC for GFLS, named as "GFLD" in Table 4.6) is characterized by all parameters fixed at their minimum values, as depicted in Figure 4.34a. The worst-case damping is now positive, although still below 3 %. PFs now indicate mode $\lambda_{55,56}$ in Figure 4.34b related to the Q-control loop, hence we may apply a DPS on $t_r^{i_q}$ to obtain a better range. Figure 4.34c suggests a minimum $t_r^{i_q}$ slightly above 50 ms. We adopt $\min(t_r^{i_q}) = 60\,\mathrm{ms}$ in Table 4.7. Further improvements for the GFL/GFL configuration will be unnecessary: the worst-case configuration when employing the updated bounds from Table 4.7 is presented in Figure 4.36a, where the minimum damping is finally above 3 %.

The same logic applies to a GFM/GFM configuration, as indicated in Figure 4.35. Here, the worst BC is the one in which all parameters are at their maximum, i.e., the EC named "GFMB" in Table 4.6, which is the configuration for GFM 2 in Figure 4.35a. As indicated in Figure 4.35c, the maximum droop should be reduced to values below 3.8 % to stabilize mode $\lambda_{94,95}$, hence we adopt $\max(m_p) = 0.035$ in Table 4.7. Luckily, the worst-case BC when considering the updated bounds in this GFM/GFM configuration results in a damping of $\zeta = 4.5\,\%$, as in Figure 4.36b, satisfactory for our purposes.

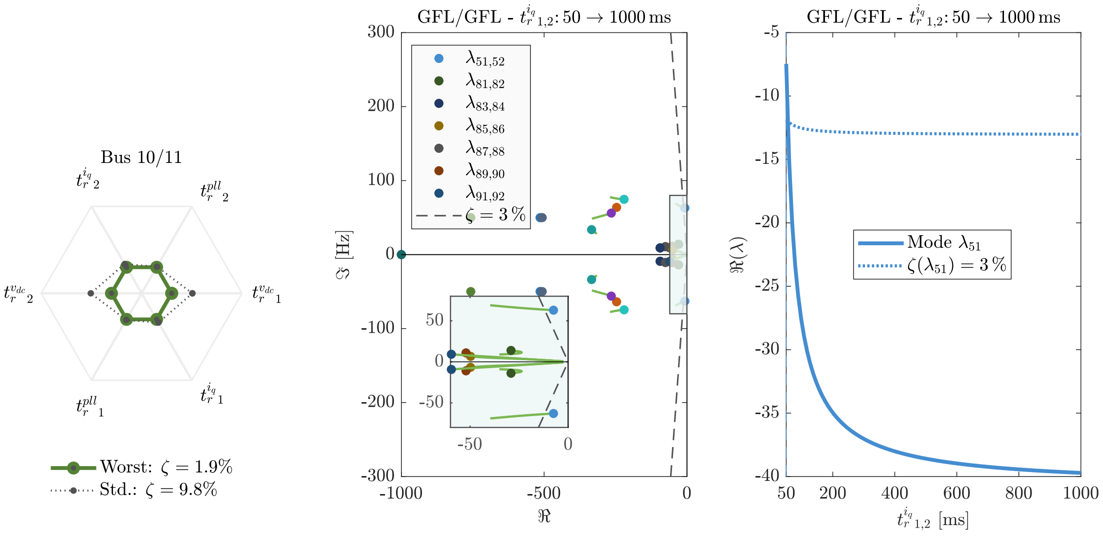

(a) Worst configuration (b) DPS for $t_r^{iq}{}_{1,2}$ (c) Eigenvalue trajectory

Figure 4.34: Worst combination between bound values for a GFL/GFL configuration (after updating the minimal and maximal t_r^{pll}), leading to a damping of $\zeta = 1.9\,\%$, positive but still below 3 %, and an eigen-sensitivity for t_r^{iq} in both GFLs, aiming to find a *minimal* t_r^{iq} to improve the worst-case damping.

Extending the analysis to Scenarios S1, S2, and S4 (defined in Table 4.4), there is a remarkable difference between the minimum damping presented in Figure 4.37, where the bounds are taken as in Table 4.5, and Figure 4.38, where they are updated in accordance to the DPSs presented above, summarized in Table 4.7. Whereas the original bounds could not prevent multiple combinations between ECs leading to low damping, or even instability, the new bounds have succeeded in ensuring their stability. It is worth noting that there is a significant disparity within the scenarios, hinting at the importance of grid conditions when defining appropriate parameter bounds, as well as between different IBR operation modes, e.g., there is no instability in GFL/GFM situations. Once again, results suggest an advantage of having a mix with both GFL and GFM.

The most important conclusion, however, is that, while the parameters chosen in Section 4.1.4 were the only ones considered in this analysis, their re-tuning was capable of stabilizing the most stringent BCs stemming from the original bounds. This corroborates our claim that these are indeed the most relevant parameters for SICDS. Had they not been suitably appointed, they would not have been able to stabilize these scenarios.

IBR	Parameter	Minimum	Maximum	Standard
GFL	$t_r^{v_{dc}}$	50 ms	220 ms	100 ms
	$t_r^{i_q}$	60 ms	1000 ms	100 ms
	t_r^{pll}	45 ms	600 ms	50 ms
GFM	m_p	0.005	0.035	0.01
	ω_p	3.14 rd/s	62.8 rd/s	31.4 rd/s
	$\tau_{v_{dc}}$	3 ms	70 ms	5 ms

Table 4.7: Improved bounds for key tuning parameters

It is also worth mentioning that this methodology is applicable to systems with more IBRs, an example of which is presented in Appendix C, where we have two GFMs and three GFLs. Interestingly, certain interactions in this 5-IBR system were already foreseen by analyzing the 2-IBR system, namely the interaction between external loops in the GFL/GFM configuration (Section 4.2.3.1), as well as the high-droop issues involving two GFMs (Section 4.2.3.2). In this example, the stability of worst-case BCs is improved by applying MPS to m_p and $t_r^{v_{dc}}$, leading to a minimum damping of $\zeta = 9\,\%$ when the bound values are updated. This illustrates the usefulness of a simplified 2-IBR assessment of inter-IBR interactions.

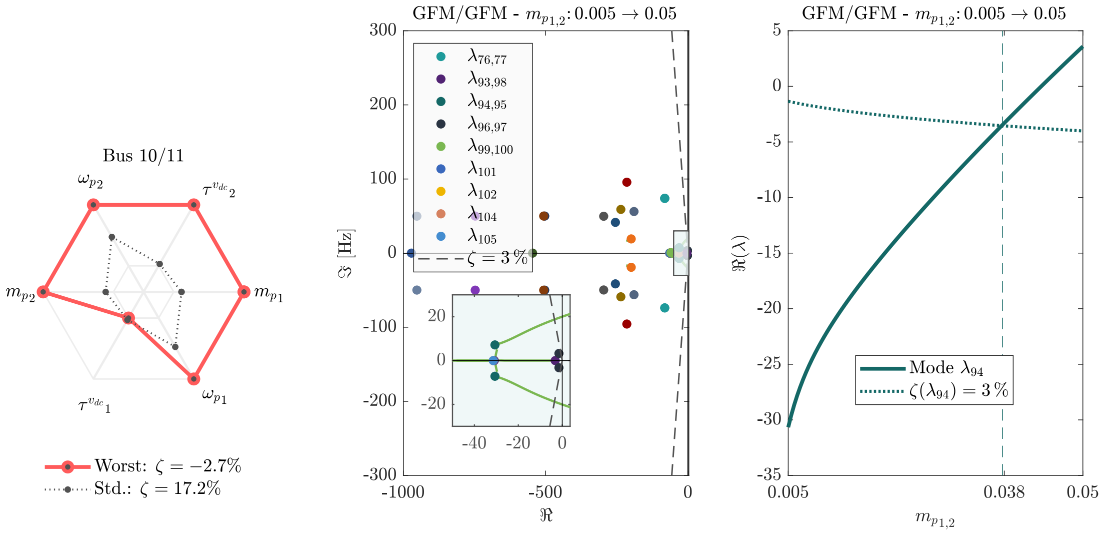

(a) Worst configuration (b) DPS for $m_{p_{1,2}}$ (c) Eigenvalue trajectory

Figure 4.35: Worst combination between bound values for a GFM/GFM configuration, leading to a damping of $\zeta = -2.7\,\%$, and an eigen-sensitivity for m_p in both GFMs, aiming to find a *maximal* m_p to improve the worst-case damping.

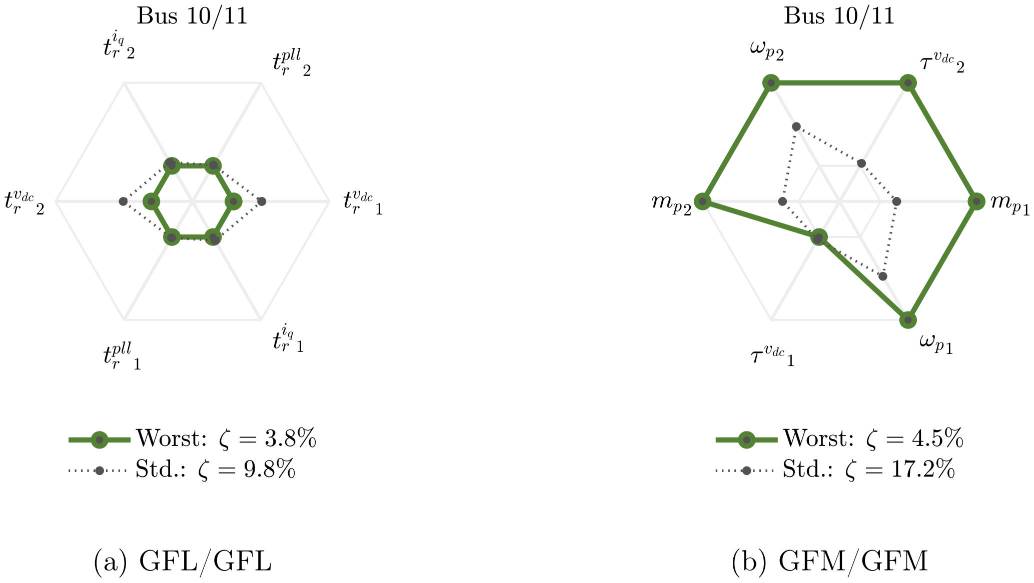

Figure 4.36: Worst configuration for GFL/GFL and GFM/GFM configurations after updating the parameter bounds from Table 4.5 to Table 4.7. Both configurations present a satisfactory minimum damping $\zeta \geq 3\,\%$.

4.4 Chapter summary

This chapter presented a detailed small-signal stability analysis of an MVDG with IBRs, with the objective of investigating SICDS issues. Here are some takeaway points:

- An interesting scenario for SSSA should be realistic but “extreme”, representing the most stringent condition. For a 1-IBR system, this depends primarily on the SCR at the POI. For a GFL, we opt for buses with the lowest SCR, e.g., Bus 7, while for a GFM we opt for those with the highest SCR, e.g., Bus 3.

- A modal map is useful in characterizing the major modes in a 1-IBR system. We may restrict our analysis to eigenvalues within the frequency range of SICDS phenomena. Examining their participation factors, we may also “tag” these modes with respect to the IBR states associated with them.

- Dominant modes for a GFL are related to its external control loops (P and Q), as well as the PLL. Dominant modes for a GFM are also related to its external control loops, in addition to the TVR. DC-link voltage control may also entail a dominant mode if the time response is particularly slow.

- Sensitivity studies, in conjunction with PFs, are helpful in detecting key parameters for SICDS. They are also useful in explaining the physical causes of certain instabilities.

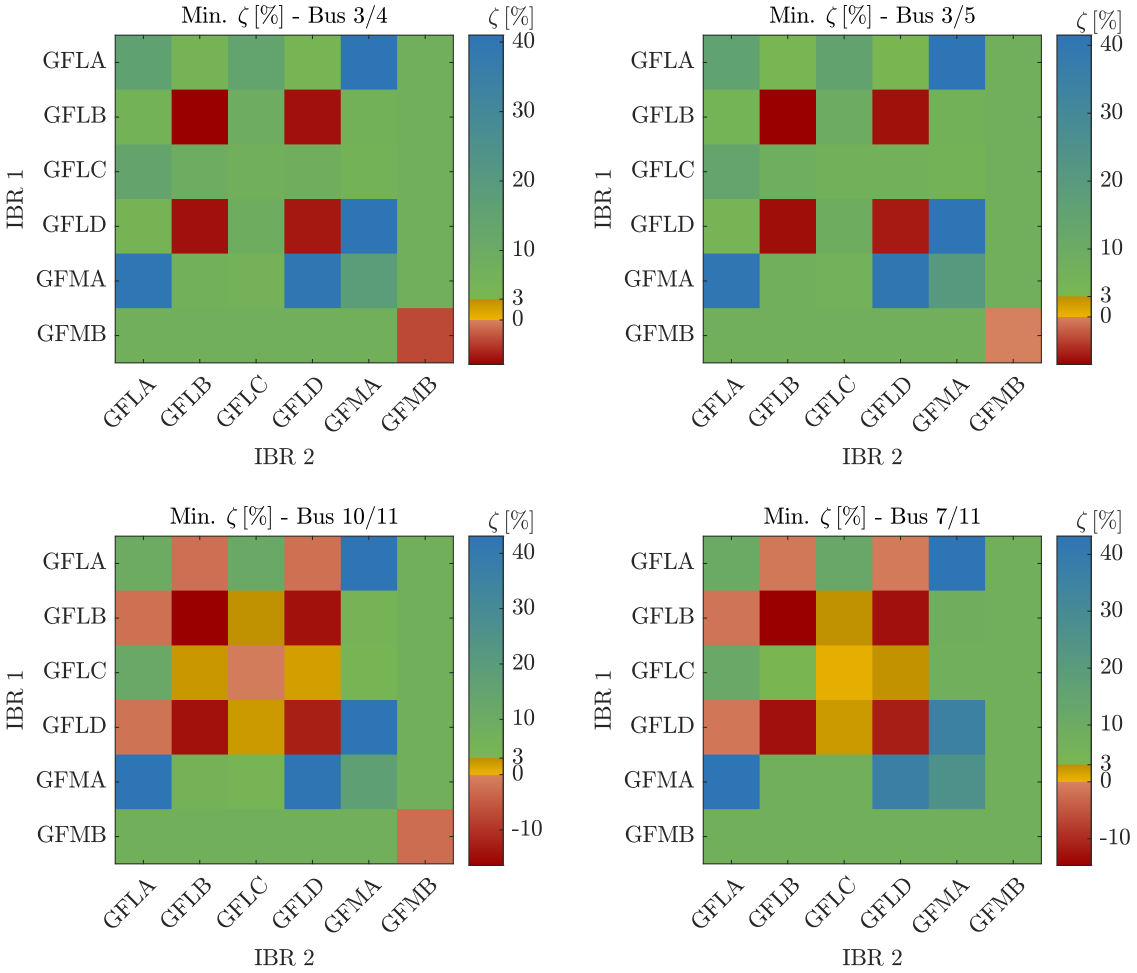

Figure 4.37: Combinations between a set of IBR configurations, as presented in Table 4.6, for scenarios S1-S4 from Table 4.4. Each square represents the minimum damping ratio among all eigenvalues under 500 Hz for the correspondent combination between IBR1 and IBR2. Here, the parameter ranges are the original ones (Table 4.5), leading to multiple instances of instability (red squares) and low damping (yellow squares).

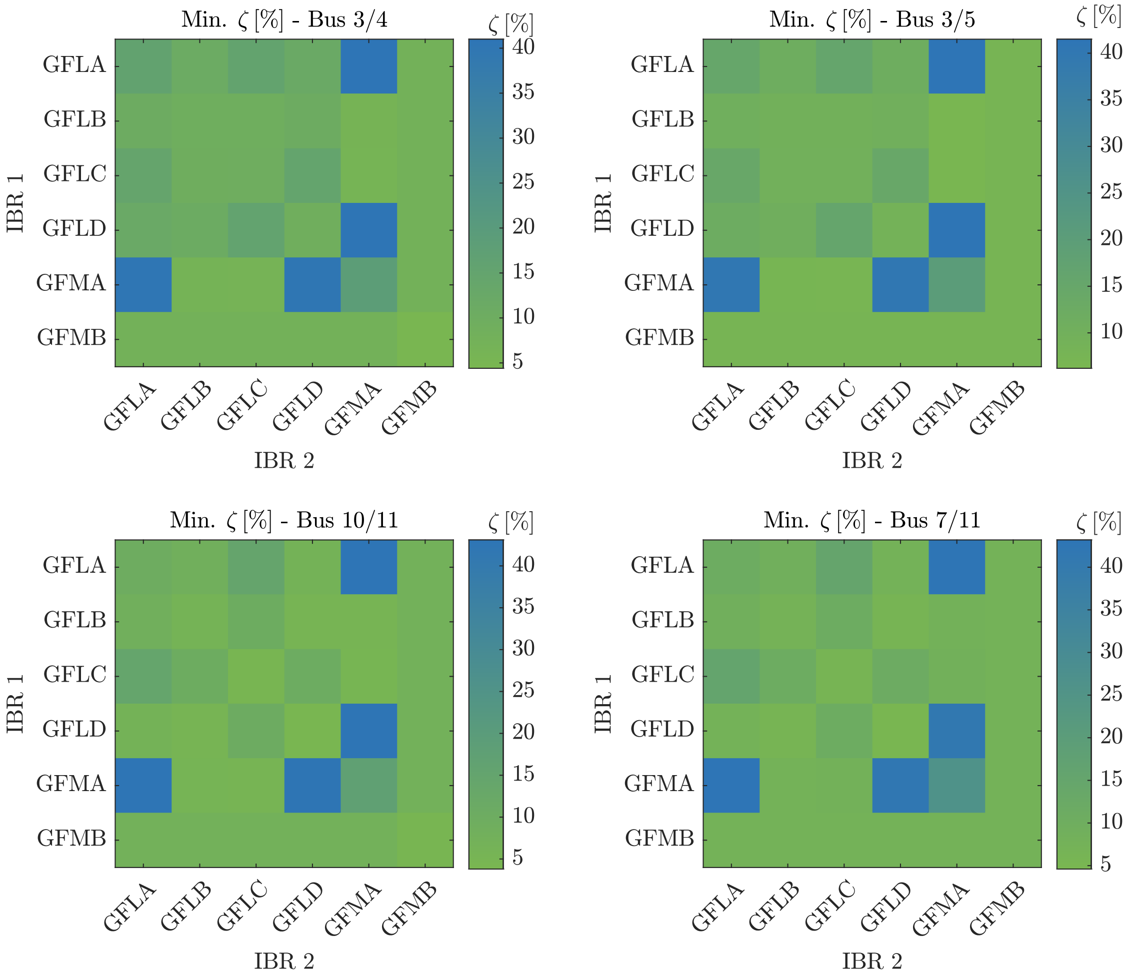

Figure 4.38: Combinations between a set of IBR configurations, for scenarios S1-S4. Now, the parameter ranges are the improved ones (Table 4.7), resulting in stable outcomes (green/blue squares) for all configurations.

- High $t_r^{v_{dc}}$ may lead GFLs to instability, regardless of the SCR at the POI. A GFL requires a large enough DC-link capacitance to hold v_{dc} while the inverter is injecting an i_d current responsible for regulating the same v_{dc}. As a rule-of-thumb, this loop remains stable if $t_r^{v_{dc}}$ is below $6\,C_{dc}$.

- High m_p may lead GFMs to instability when the POI is too strong. For a single GFM connected to the benchmark MVDG, this only happens under unrealistically high droop values (close to 20 %). An analogy between GFM and SG can be used to determine a formula for the damping ratio of this droop-related mode. This formula is only accurate when m_p is relatively low, which is true in most real-life situations ($m_p \leq 5\,\%$).

- PLL instability is unlikely for a single GFL connected to this MVDG. If the connecting line is long (5 km, for instance), a low t_r^{pll} (around 18 ms) may lead to instability.

- According to these sensitivities, the key parameters for SICDS in GFLs are the time responses of the external loops and the PLL, namely $t_r^{v_{dc}}$, $t_r^{i_q}$, and t_r^{pll}.

- Key parameters for GFMs are m_p and ω_p, i.e., droop and virtual inertia, both related to the PSL, as well as $\tau_{v_{dc}}$.

- A 2-IBR system is useful for studying interactions between IBRs. Conclusions for this simple configuration may be extended to larger systems (see Appendix C).

- When choosing scenarios for a 2-IBR system, it is useful to assess the electrical distance between IBRs, in addition to the SCR at their POIs. This can be done via a bus-to-bus equivalent impedance $|\bar{Z}_{ab}|$. Lower values for $|\bar{Z}_{ab}|$ indicate nearby IBRs, which are more prone to interactions, especially if they are GFMs.

- Modal maps in 2-IBR systems can reveal SICDS-related modes that involve both IBRs, i.e., *interaction* modes. In a GFL/GFM configuration, for instance, one of the dominant modes includes states related to the P-control loop in GFLs ($t_r^{v_{dc}}$ and $\gamma_{t_r^{v_{dc}}}$) and the same loop in GFMs (θ and γ_P).

- Single-parameter sensitivities (SPS), i.e., sensitivities where one of the IBRs is kept constant, can elucidate the differences between a 1-IBR and 2-IBR system.

- SPS for $t_r^{v_{dc}}$ in a GFL indicate that a GFL/GFM configuration may actually worsen the high-$t_r^{v_{dc}}$ instability. For a GFL with $C_{dc} = 0.04\,\text{pu}$, a $t_r^{v_{dc}}$ of 240 ms was not enough to keep $\zeta \geq 3\,\%$ in the presence of a GFM. This is a rare instance when a mix of GFL and GFM seems to deteriorate SICDS.

- SPS for m_p in a GFM indicates that a GFM/GFM configuration with nearby IBRs is much more prone to instability than a single GFM. Now, a droop level of just 4 % is enough for the damping to become unsatisfactory. High droop levels do not lead to instability in a GFM/GFL configuration, though.

- SPS for t_r^{pll} in a GFL connected to the MVDG via a 5 km line indicates that a GFM in the vicinity can effectively eliminate the PLL instability. This is an instance of positive interaction between IBRs.
- Having selected the key parameters for SICDS, a DSO could define their ranges. In such cases, it is important to ensure that all boundary configurations (BC), i.e., situations in which each key parameter in every IBR is either at its lower or upper bound value, are sufficiently stable.
- Assessing the worst-case BCs, we may define the extreme configurations (EC) for each IBR. The goal is then reduced to ensuring the stability of all combinations between ECs. This can be done via multi-parameter sensitivities using the key parameters, finding new bound values capable of ensuring SICDS.
- This methodology is applicable to systems with more IBRs, as illustrated in Appendix C. Certain interactions in this 5-IBR system were already foreseen by analyzing the 2-IBR system, demonstrating the usefulness of a simplified 2-IBR assessment of inter-IBR interactions.
- It is worth noting that improving bound values for ensuring the stability of BCs is not enough to guarantee the stability for *all* possible IBR tunings *within* these bound values. Such a problem requires an optimization-based solution, as proposed in the next chapter.

CHAPTER 5

Parameter Bounds for SICDS

An optimization-based method

Contents

In the previous chapter, particularly in Section 4.3[1], we have introduced the notion of boundary configurations, i.e., situations in which the key parameters in all IBRs are tuned at their bound values. These key parameters, defined in Section 4.1.4, are crucial for SICDS in multi-IBR systems, as was demonstrated in the aforementioned sections. A fundamental question remains unanswered, however: by improving the ranges of key parameters so that the BCs are stabilized, are we effectively avoiding the *worst-case* situation? In other words, can we actually ensure that the worst combination between key parameters is indeed a BC? As argued in Section 5.1, the answer is “no”: there are situations in which intermediary values of key parameters actually yield a less stable scenario than the worst among all BCs.

---

[1] This notion is also explored in Appendix C, applied to a larger system.

Nevertheless, determining these ranges is important for DSOs. Since they do not usually own the IBRs, they are unable to ensure a specific parameterization for their controllers. If DSOs are to *impose* certain dynamic constraints, this might be detrimental to the interest of producers. A possible compromise is for DSOs to provide *ranges* for these key parameters, allowing for producers to tune their IBRs according to their own needs, as long as the ranges are respected. What the DSO would require in such a scenario is a method to ensure that the *worst* combination of values for key parameters, *within these ranges*, is sufficiently stable (minimum damping above 3 %, for instance). The first step is to ensure that all BCs in these ranges are stable, as was done in Section 4.3, but we still have to assess the stability of non-BC situations. This requires an optimization method capable of finding the worst combination among all the key parameters, i.e., a " worst-case optimization", as defined in Section 5.1.1.

Going further, the DSO should also be capable of providing ranges that are as large as possible, giving the maximum amount of freedom for producers to tune their IBRs, while still ensuring SICDS. This is yet another optimization problem, a "bound surface optimization", where the worst-case optimization is actually a constraint, as described in Section 5.1.2. This is a highly complex optimization problem, compelling us to employ metaheuristic methods, such as a Genetic Algorithm (GA) or a Particle Swarm Optimization (PSO), which are computationally demanding. As a faster and simpler alternative, we propose another heuristic-based method in Section 5.2, where the concepts from Section 4.3 serve as an inspiration for a gradient-based BC-modification algorithm. This method is compared to the metaheuristic algorithms in Section 5.3, yielding satisfactory results in terms of SICDS, with a gain of almost two orders of magnitude in computation time. While Section 4.3 provided an empirical method to improve SICDS in MVDGs with IBRs, this chapter extends it onto a rigorous, systematic, and computationally-efficient algorithm.

5.1 Preliminaries

Assuming that IBRs can be accurately represented through generic models, as the ones presented in Chapter 3, reducing their parameterization to the tuning of a set of key parameters, as in Section 4.1.4, it would be helpful to provide the bounds for these parameters in such a way as to ensure small signal stability. Our objective would thus be to define the largest range for these key parameters, within which all possible combinations are sufficiently stable. This would ensure a reasonable degree of freedom for producers to tune their IBRs according to their own needs while guaranteeing a stability margin for the system comprising all IBRs.

This method requires initialization of all parameter ranges, which we perform in accordance with Table 5.1. These ranges stem from the SSSA performed in Chapter 4, e.g. Table 4.5, although the upper bounds for GFL parameters have been limited to more realistic values[2].

IBR	Par.	Standard	Range
GFL	$t_r^{v_{dc}}$	50 ms	50 – 250 ms
	$t_r^{i_q}$	100 ms	50 – 250 ms
	t_r^{pll}	100 ms	20 – 250 ms
GFM	m_p	0.01	0.005 – 0.05
	ω_p	31.4 rd/s	3.14 – 62.8 rd/s
	$\tau_{v_{dc}}$	5 ms	3 – 70 ms

Table 5.1: Standard values and initial bounds for chosen tuning parameters

Let us start by defining a *bound surface* χ using all m normalized parameter ranges:

$$\chi(\boldsymbol{l},\boldsymbol{u}) = \sum_{j=1}^{m}(\tilde{u}_j - \tilde{l}_j)^2 \tag{5.1}$$

where the j^{th} bound value, lower l_j or upper u_j, is normalized with respect to the initial bounds $(\boldsymbol{l_o},\boldsymbol{u_o})_j$:

$$\tilde{l}_j = \frac{l_j - (l_o)_j}{(u_o)_j - (l_o)_j} \text{ and } \tilde{u}_j = \frac{u_j - (l_o)_j}{(u_o)_j - (l_o)_j} \tag{5.2}$$

Our goal of finding the largest range for the key parameters may be written as an optimization problem, where the objective function is the maximization of bound surface $\chi(\boldsymbol{l},\boldsymbol{u})$ and a constraint function ensures stable operation for all parameter combinations within the bounds $(\boldsymbol{l},\boldsymbol{u})$, for all IBRs in the system.

Here, "sufficiently stable" means that the minimum damping $\bar{\zeta}(\boldsymbol{P})$ among all q non-zero eigenvalues λ_k, as defined in (5.4)-(5.5), is greater than a predefined stability criterion κ:

$$\bar{\zeta} > \kappa \tag{5.3}$$

Negative $\bar{\zeta}$ indicates instability, so $\kappa = 0$ could be taken as a theoretical limit. In practice, however, the minimum acceptable damping κ in power systems is generally around 3% [14].

$$\bar{\zeta}(\boldsymbol{P}) = \min[\zeta_1, \zeta_2, \dots, \zeta_q] \tag{5.4}$$

where, as defined in (1.25),

$$\zeta_k = \frac{-\Re(\lambda_k)}{\sqrt{\Re(\lambda_k)^2 + \Im(\lambda_k)^2}}, \; \forall k \in [1, q] \tag{5.5}$$

---

[2] Even though time responses as slow as 1 s (as in Table 4.5) did not entail instabilities, they are unlikely to satisfy the dynamic requirements for IBRs in real-life applications. As mentioned in Chapter 3, both IBR external controls and the PLL are usually tuned in the order of tens to hundreds of milliseconds.

In (5.4), $\boldsymbol{P}$ is a parameter matrix with elements p_{ij}:

$$p_{ij} \in [l_j, u_j],\ \forall j \in [1, m],\ \forall i \in [1, n] \tag{5.6}$$

where each row designates the i^{th} of n IBRs, and each column the j^{th} among m parameters.

In Section 4.3, we proposed evaluating every configuration in which the parameters are either at their lower or upper bounds for each IBR. Each of these is hereby denoted as a "boundary configuration" (BC) and represented by the matrix $\boldsymbol{\mathcal{P}}$, with elements ρ_{ij}[3]:

$$\rho_{ij} \in \{l_j, u_j\},\ \forall j \in [1, m],\ \forall i \in [1, n] \tag{5.7}$$

Besides the large number of evaluations required for systems with multiple IBRs, guaranteeing stability for all BCs is not enough to ensure stable operation within bounds $(\boldsymbol{l}, \boldsymbol{u})$. Certain parameter configurations p_{ij} within these bounds may infringe the stability constraints, even if all the BCs satisfy it, as we see in Figure 5.1. Here, we consider two GFMs, connected to buses 10 and 11 in the network from Figure 3.1, both with fixed m_p and τ_{vdc}, taking ω_p to be the only variable tuning parameter, with bounds $(\boldsymbol{l}, \boldsymbol{u}) = (5, 50)\,\mathrm{rad/s}$. Assuming a stability criterion $\kappa = 3\,\%$, we observe that there is an unsatisfactory region within these bounds for which $\bar{\zeta} \leq \kappa$. There is an unstable "hole" within a region enclosed by stable BCs, an idea we had already suggested in Section 4.1.4, Figure 4.14a.

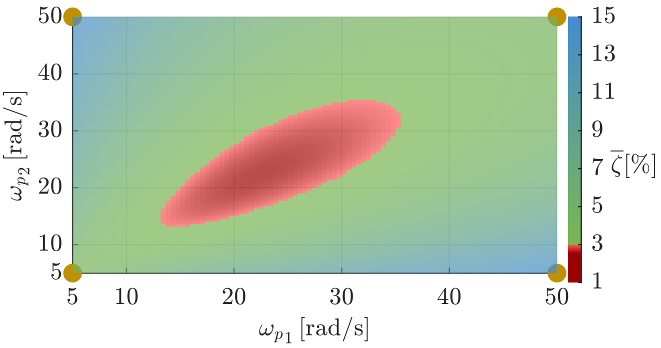

.

Figure 5.1: $\bar{\zeta}$ as a function of ω_p for each IBR, illustrating a sub-region with unsatisfactory stability within a region defined by stable BCs (indicated by the circles in the corners). Here we consider a scenario with GFMs connected to nodes 10 and 11, both of them tuned with $m_p = 0.027$ and $\tau_{vdc} = 5\,\mathrm{ms}$.

---

[3] Please note the distinction between p_{ij} and ρ_{ij}. While p_{ij} is the j^{th} parameter for the i^{th} IBR in *any* configuration, hence a value *between* the lower bound l_j and upper bound u_j, ρ_{ij} is the given parameter for *boundary configurations only*, being *equal to* either l_j or u_j.

5.1.1 Worst-case optimization

A more accurate approach to ensure that a given set of parameter bounds $(\boldsymbol{l}, \boldsymbol{u})$ is stable over the entire domain it defines, would consist in considering all possible parameter combinations $\boldsymbol{P}$ within these bounds rather than relying solely on BCs. This may be described as an optimization problem:

$$\begin{aligned} \min_{P} \quad & \bar{\zeta}(\boldsymbol{P}) \\ \text{s.t.} \quad & l_j \leq p_{ij} \leq u_j, \\ & \qquad \forall j \in [1, m], \, \forall i \in [1, n] \end{aligned} \tag{5.8}$$

We may take $\bar{\zeta}^w$ to designate a *worst-case damping*, i.e., the minimum $\bar{\zeta}(\boldsymbol{P})$ among all configurations within bounds $(\boldsymbol{l}, \boldsymbol{u})$, obtained using (5.8). Similarly, $\boldsymbol{P^w}$ indicates the worst-case parameter matrix $\boldsymbol{P}$, for which $\bar{\zeta}(\boldsymbol{P}) = \bar{\zeta}^w$. This is a constrained nonlinear optimization, the results presented in this chapter were obtained using Sequential Quadratic Programming (SQP) in *Matlab*, where the algorithm is executed repeatedly for different initial points, picked randomly within $(\boldsymbol{l}, \boldsymbol{u})$.

5.1.2 Bound surface optimization

The larger optimization problem may be written as in (5.9), where we maximize the normalized boundary surface $\chi(\boldsymbol{l}, \boldsymbol{u})$ from (5.1) while ensuring that the worst-case $\bar{\zeta}^w$ from (5.8) satisfies a stability criterion κ. All parameter combinations $\boldsymbol{P}$ within bounds $(\boldsymbol{l}, \boldsymbol{u})$ comply with a predefined stability margin, hence those bounds can be safely adopted as guidelines.

$$\begin{aligned} \max_{\boldsymbol{l}, \boldsymbol{u}} \quad & \chi(\boldsymbol{l}, \boldsymbol{u}) \\ \text{s.t.} \quad & \bar{\zeta}^w(\boldsymbol{l}, \boldsymbol{u}) > \kappa \end{aligned} \tag{5.9}$$

This is a complex optimization where the nonlinear constraint function $\bar{\zeta}^w(\boldsymbol{l}, \boldsymbol{u})$ is in itself an optimization problem, as defined in (5.8). Algorithms such as an Interior Point Method (IPM) or the aforementioned SQP, commonly employed for such problems, may either fail to converge to a feasible point or demand too much computation. A logical alternative is to use metaheuristic methods, e.g., GA and PSO, although these may also present sub-optimal results, as discussed in Section 5.3.

Still, having recourse to BCs, as described in (5.7), in addition to the worst-case optimization from (5.8), it is possible to minimally reduce the original bounds $(\boldsymbol{l_o}, \boldsymbol{u_o})$, while verifying $\bar{\zeta}^w > \kappa$, which indirectly provides a surface χ close to optimal. This heuristic method is described in the section below.

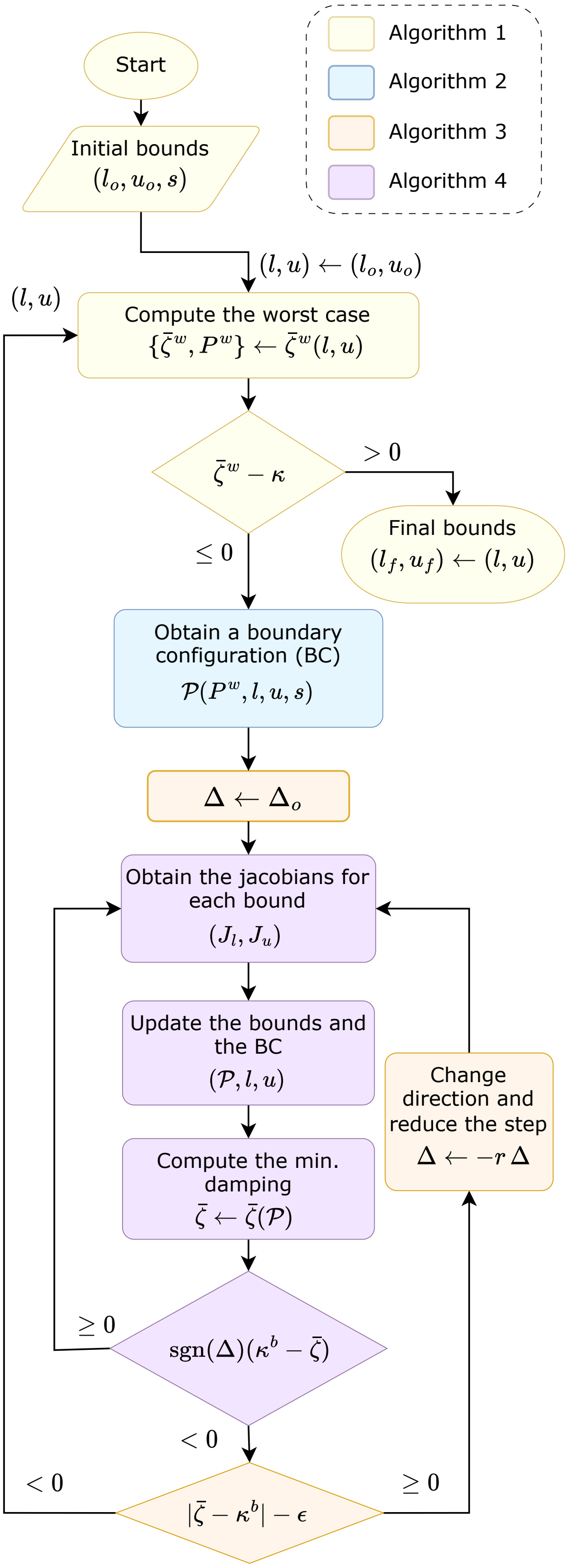

Figure 5.2: Flow-chart for the heuristic method

5.2 Heuristic method

In order to perform this bound-surface optimization in a faster and simpler way, when compared to metaheuristic algorithms, a tailored heuristic is proposed in this section.

5.2.1 Overview

As shown in Figure 5.2 and codified in Algorithm 1, this method takes three inputs, namely $\boldsymbol{l_o}$, $\boldsymbol{u_o}$, and $\boldsymbol{s}$, which are arrays containing the initial values for lower and upper bounds, as well as a set of standard values for all the key parameters, respectively. By default, the numerical values for these arrays are given in Table 5.1.

Algorithm 1 Main algorithm to find the optimal bounds $\{\boldsymbol{l_f}, \boldsymbol{u_f}\}$

```
Input: $\boldsymbol{l_o}, \boldsymbol{u_o}, \boldsymbol{s}$
Output: $\boldsymbol{l_f}, \boldsymbol{u_f}$
$\{\bar{\zeta}^w, \boldsymbol{P^w}\} \leftarrow \bar{\zeta}^w(\boldsymbol{l_o}, \boldsymbol{u_o})$
$\boldsymbol{l} \leftarrow \boldsymbol{l_o}$, $\boldsymbol{u} \leftarrow \boldsymbol{u_o}$
while $\bar{\zeta}^w \leq \kappa$ do
    $\{\boldsymbol{\mathcal{P}}, \mathcal{L}, \mathcal{U}\} \leftarrow \textsc{Boundary}(\boldsymbol{P^w}, \boldsymbol{l}, \boldsymbol{u}, \boldsymbol{s})$
    $\{\boldsymbol{l}, \boldsymbol{u}\} \leftarrow \textsc{Heuristic}(\boldsymbol{l}, \boldsymbol{u}, \boldsymbol{\mathcal{P}}, \mathcal{L}, \mathcal{U})$
    $\{\bar{\zeta}^w, \boldsymbol{P^w}\} \leftarrow \bar{\zeta}^w(\boldsymbol{l}, \boldsymbol{u})$
end while
$\boldsymbol{l_f} \leftarrow \boldsymbol{l}$, $\boldsymbol{u_f} \leftarrow \boldsymbol{u}$
```

After computing the original worst-case scenario $\bar{\zeta}^w = \bar{\zeta}^w(\boldsymbol{l_o}, \boldsymbol{u_o})$, if this does not satisfy a stability criterion κ, the algorithm uses $\boldsymbol{s}$ as a threshold to obtain a boundary configuration $\boldsymbol{\mathcal{P}}$ from the worst-case parameter matrix $\boldsymbol{P^w}$, as detailed in Algorithm 2. This BC is then modified progressively until it reaches satisfactory stability, providing a new set of bounds $(\boldsymbol{l}, \boldsymbol{u})$, which are reevaluated with respect to their worst-case damping $\bar{\zeta}^w$. This three-step process is repeated until $\bar{\zeta}^w$ satisfies the stability criterion from (5.3). For clarity, the main algorithm is divided into three sub-algorithms, each of which is described in detail throughout this section.

5.2.2 Approximating the worst-case scenario to a BC

As expressed in (5.7), a BC is represented by a parameter matrix $\boldsymbol{\mathcal{P}}$, where all parameters are attributed to either lower or upper bound values. In Algorithm 2, the BC is generated from the worst-case parameter matrix $\boldsymbol{P^w}$, obtained in the previous step of the heuristic. For the i^{th} IBR, whenever the j^{th} parameter p_{ij} is below its standard value s_j in the worst-case scenario, the corresponding BC parameter ρ_{ij} is taken as the lower bound value l_j; otherwise, we adopt the upper bound value u_j. Two additional arrays, $\boldsymbol{\mathcal{L}}$ and $\boldsymbol{\mathcal{U}}$, are used in order to store the indexes of $\boldsymbol{\mathcal{P}}$ in which parameters are attributed to their lower and upper bounds, respectively. These arrays are important for Algorithm 4, where we need to know which bound values should be updated.

Algorithm 2 Function to find a boundary configuration $\boldsymbol{\mathcal{P}}$

```
function BOUNDARY($\boldsymbol{P}, \boldsymbol{l}, \boldsymbol{u}, \boldsymbol{s}$)
    $\mathcal{L} \leftarrow \varnothing, \mathcal{U} \leftarrow \varnothing$
    for $i \in [1, n]$ do
        for $j \in [1, m]$ do
            if $p_{ij} < s_j$ then
                $\rho_{ij} \leftarrow l_j$
                $\mathcal{L} \leftarrow [\mathcal{L}, (i, j)]$
            else
                $\rho_{ij} \leftarrow u_j$
                $\mathcal{U} \leftarrow [\mathcal{U}, (i, j)]$
            end if
        end for
    end for
    return $\{\boldsymbol{\mathcal{P}}, \mathcal{L}, \mathcal{U}\}$
end function
```

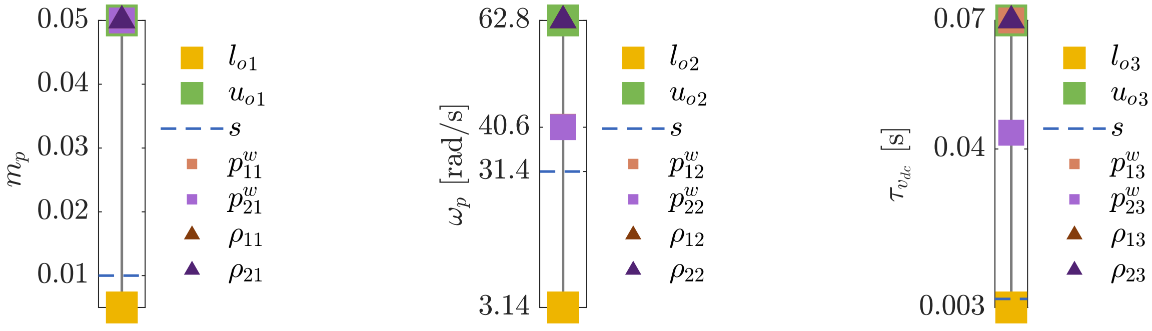

(a) m_p (b) ω_p (c) $\tau_{v_{dc}}$

Figure 5.3: Obtaining the boundary configuration for a scenario with two GFMs, connected to nodes 10 and 11

Figure 5.3 illustrates the application of Algorithm 2 for a scenario with two GFMs, hence with three parameters (m_p, ω_p and $\tau_{v_{dc}}$) for each IBR. In this scenario, the original worst-case configuration yields a set of parameters $\boldsymbol{P^w}$. Since all elements p^w_{ij} in $\boldsymbol{P^w}$, indicated by the smaller squares in Figure 5.3, are above their respective standard values (Table 3.5), indicated by the blue dashed line, the boundary configuration $\boldsymbol{\mathcal{P}}$ obtained via Algorithm 2 will have all elements ρ_{ij} equal to their original upper bounds u_o. We observe that all BC parameters ρ_{ij}, indicated by triangles in Figure 5.3, are superposing the larger green squares (upper bounds). This BC configuration is the one that most resembles the worst-case scenario, as per our definition in Algorithm 2.

5.2.3 Gradient-based method to modify the BCs

Algorithm 3 Function to apply a heuristic method in order to find satisfactory parameter bounds $\{\boldsymbol{l}, \boldsymbol{u}\}$

```
function HEURISTIC($\boldsymbol{l}, \boldsymbol{u}, \boldsymbol{\mathcal{P}}, \mathcal{L}, \mathcal{U}$)
    $\Delta \leftarrow \Delta_o$
    $\bar{\zeta}_{prev} \leftarrow \bar{\zeta}(\boldsymbol{\mathcal{P}})$
    while $|\bar{\zeta} - \kappa^b| \geq \epsilon$ do
        $\{\boldsymbol{\mathcal{P}}, \boldsymbol{l}, \boldsymbol{u}\} \leftarrow$ UPDATE($\Delta, \boldsymbol{l}, \boldsymbol{u}, \boldsymbol{\mathcal{P}}, \mathcal{L}, \mathcal{U}$)
        $\bar{\zeta} \leftarrow \bar{\zeta}(\boldsymbol{\mathcal{P}})$
        if $(\bar{\zeta} - \kappa^b)(\bar{\zeta}_{prev} - \kappa^b) < 0$ then
            $\Delta \leftarrow -r\,\Delta$
        end if
        $\bar{\zeta}_{prev} \leftarrow \bar{\zeta}$
    end while
    return $\{\boldsymbol{l}, \boldsymbol{u}\}$
end function
```

Algorithm 3 is responsible for modifying the BC, and consequently the bound values associated with it, until the configuration resulting from this procedure is sufficiently close to the alternative stability criteria κ^b, i.e., $|\bar{\zeta} - \kappa^b| < \epsilon$, where $\bar{\zeta}$ is obtained using (5.4). This is done by modifying each normalized bound value proportionally to its individual impact on $\bar{\zeta}$ (gradient-based BC modification), as described in Algorithm 4. For a step size of $\Delta = 0.05$[4], for instance, this total 5% change is shared among all the normalized bound values $\tilde{b}$ whose indices are stored in $\boldsymbol{\mathcal{L}}$ or $\boldsymbol{\mathcal{U}}$, proportionally to their sensitivity $\partial\bar{\zeta}/\partial\tilde{b}$.

Initially, one would imagine that the minimum damping $\bar{\zeta}$ is below the stability criterion κ, requiring an improvement. The process from Algorithm 4 is hence repeated until $\bar{\zeta} > \kappa^b$, which would have been enough to achieve a satisfactory BC. If the step size Δ is relatively large, however, the bound values may have been excessively altered, leaving room for a slight relaxation. In other words, a slightly *less stable* configuration could still satisfy $\bar{\zeta} > \kappa^b$. We may thus resort to a bisection method, adopting a new step size, smaller than the previous one by a factor r, and modifying the bounds in the opposite direction in order to reduce the stability while still respecting $\bar{\zeta} > \kappa^b$. This translates into repeating the procedure from Algorithm 4

---

[4] There is no need for a unit, given that all parameters are *normalized* according to (5.2).

with a negative step size: $\Delta \leftarrow -r\,\Delta$. For either positive or negative step size Δ, we should stop and change the direction of the bisection when $\bar{\zeta}$ crosses κ^b, which corresponds to the condition $(\bar{\zeta} - \kappa^b)\,(\bar{\zeta}_{prev} - \kappa^b) < 0$. In fact, when the product $(\bar{\zeta} - \kappa^b)\,(\bar{\zeta}_{prev} - \kappa^b)$ becomes negative, it may either indicate that the minimum damping $\bar{\zeta}$ is now satisfactory (if we are increasing stability) or unsatisfactory (if we are decreasing stability). In both cases, there is no need to compute further values for $\bar{\zeta}$.

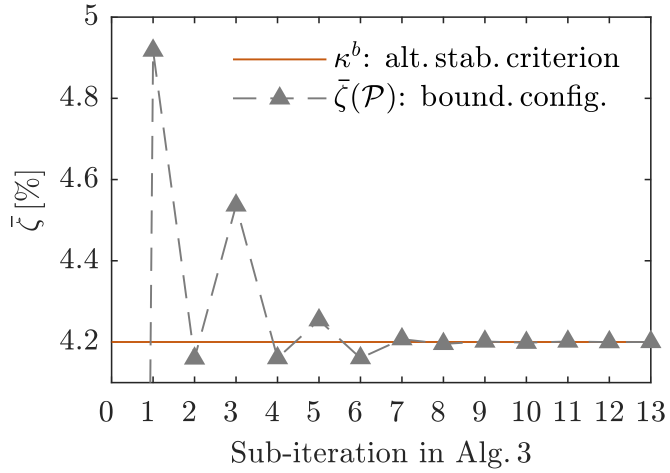

Figure 5.4: Minimum damping $\bar{\zeta}$ for each sub-iteration of the Algorithm 3, considering a scenario with GFMs connected to nodes 10 and 11, with $\kappa = 3\,\%$ and $\kappa^b = 4.2\,\%$.

Figure 5.4 illustrates this bisection method. A growth in $\bar{\zeta}$ between consecutive sub-iterations indicates a positive step size Δ. After 13 sub-iterations in Algorithm 3, the minimum BC damping, which began at $\bar{\zeta} = -7.2\,\%$, is finally close enough to $\kappa^b = 4.2\,\%$, satisfying $|\bar{\zeta} - \kappa^b| < \epsilon$. It is worth noting that each sub-iteration in Algorithm 3 consists of multiple sub-iterations in Algorithm 4, which are further explored in Figure 5.5.

Initially, this process is repeated until $\bar{\zeta} > \kappa^b$, which would have been enough to achieve a satisfactory BC. If the step size Δ is relatively large, however, the bound values may have been excessively altered, leaving room for a slight relaxation. Following a bisection method, we may thus adopt a new step size, smaller than the previous one by a factor r, modifying the bounds in the opposite direction in order to reduce the stability while still respecting $\bar{\zeta} > \kappa^b$. This translates into repeating the procedure of Algorithm 4 with a negative step size: $\Delta \leftarrow -r\,\Delta$. Further modifications are unnecessary once $|\bar{\zeta} - \kappa^b| < \epsilon$ is satisfied, indicating that the BC has reached satisfactory stability with minimal bound surface reduction.

Algorithm 4 refers to the procedure that actually updates the bound values, allowing for Algorithm 3 to modify the BCs. Each normalized bound $\tilde{b}$ is updated proportionally to its sensitivity $\partial\bar{\zeta}/\partial\tilde{b}$, with $\partial\tilde{b} = \Delta$. Because we are interested exclusively in the relative sensitivities for each bound with respect to the others, it is enough to compute the numerator $\partial\bar{\zeta}$,

Algorithm 4 Function to update bound values $\{\boldsymbol{l},\boldsymbol{u}\}$ and obtain a new boundary configuration $\boldsymbol{\mathcal{P}}$

```
function Update($\Delta, \boldsymbol{l}, \boldsymbol{u}, \boldsymbol{\mathcal{P}_o}, \mathcal{L}, \mathcal{U}$)
    $\bar{\zeta} \leftarrow \bar{\zeta}(\boldsymbol{\mathcal{P}_o})$
    $\boldsymbol{J_l} \leftarrow \mathbf{0}_{1\times m}$, $\boldsymbol{J_u} \leftarrow \mathbf{0}_{1\times m}$
    $\boldsymbol{l_{prev}} \leftarrow \boldsymbol{l}$, $\boldsymbol{u_{prev}} \leftarrow \boldsymbol{u}$, $\bar{\zeta}_{prev} \leftarrow \bar{\zeta}$, $\boldsymbol{\mathcal{P}_{prev}} \leftarrow \boldsymbol{\mathcal{P}_o}$
    while $\mathrm{sgn}(\Delta)\,(\kappa^b - \bar{\zeta}) \geq 0$ do
        for $j \in [1, m]$ do
            $\boldsymbol{l} \leftarrow \boldsymbol{l_{prev}}$, $\boldsymbol{u} \leftarrow \boldsymbol{u_{prev}}$
            $\tilde{l}_j \leftarrow \frac{l_j - (l_o)_j}{(u_o)_j - (l_o)_j} + \Delta$
            $\tilde{u}_j \leftarrow \frac{u_j - (l_o)_j}{(u_o)_j - (l_o)_j} - \Delta$
            $l_j \leftarrow \tilde{l}_j\big((u_o)_j - (l_o)_j\big) + (l_o)_j$
            $u_j \leftarrow \tilde{u}_j\big((u_o)_j - (l_o)_j\big) + (l_o)_j$
            $\boldsymbol{\mathcal{P}^{\mathcal{L}}} \leftarrow \boldsymbol{\mathcal{P}_{prev}}$, $\boldsymbol{\mathcal{P}^{\mathcal{U}}} \leftarrow \boldsymbol{\mathcal{P}_{prev}}$
            $\rho^{\mathcal{L}}_{ij} \leftarrow l_j, \forall i \in \{[1, n] \mid (i, j) \in \mathcal{L}\}$
            $\rho^{\mathcal{U}}_{ij} \leftarrow u_j, \forall i \in \{[1, n] \mid (i, j) \in \mathcal{U}\}$
            $(J_l)_j \leftarrow \bar{\zeta}(\mathcal{P}^{\mathcal{L}}) - \bar{\zeta}_{prev}$
            $(J_u)_j \leftarrow \bar{\zeta}(\mathcal{P}^{\mathcal{U}}) - \bar{\zeta}_{prev}$
        end for
        $J_s \leftarrow \sum_{j=1}^{m} |(J_l)_j| + \sum_{j=1}^{m} |(J_u)_j|$
        $\boldsymbol{l} \leftarrow \boldsymbol{l_{prev}}$, $\boldsymbol{u} \leftarrow \boldsymbol{u_{prev}}$
        for $j \in [1, m]$ do
            $\tilde{l}_j \leftarrow \frac{l_j - (l_o)_j}{(u_o)_j - (l_o)_j} + \frac{(J_l)_j}{J_s}\,|\Delta|$
            $\tilde{u}_j \leftarrow \frac{u_j - (l_o)_j}{(u_o)_j - (l_o)_j} - \frac{(J_u)_j}{J_s}\,|\Delta|$
            $l_j \leftarrow \max\{\tilde{l}_j\big((u_o)_j - (l_o)_j\big) + (l_o)_j,\ (l_o)_j\}$
            $u_j \leftarrow \min\{\tilde{u}_j\big((u_o)_j - (l_o)_j\big) + (l_o)_j, (u_o)_j\}$
        end for
        $\boldsymbol{\mathcal{P}} \leftarrow \boldsymbol{\mathcal{P}_{prev}}$
        $\rho_{ij} \leftarrow l_j, \forall i \in \{[1, n] \mid (i, j) \in \mathcal{L}\}$
        $\rho_{ij} \leftarrow u_j, \forall i \in \{[1, n] \mid (i, j) \in \mathcal{U}\}$
        $\bar{\zeta} \leftarrow \bar{\zeta}(\boldsymbol{\mathcal{P}})$
        $\boldsymbol{l_{prev}} \leftarrow \boldsymbol{l}$, $\boldsymbol{u_{prev}} \leftarrow \boldsymbol{u}$, $\bar{\zeta}_{prev} \leftarrow \bar{\zeta}$, $\boldsymbol{\mathcal{P}_{prev}} \leftarrow \boldsymbol{\mathcal{P}}$
    end while
    return $\{\boldsymbol{\mathcal{P}}, \boldsymbol{l}, \boldsymbol{u}\}$
end function
```

since the denominator Δ is the same for all parameters. These sensitivities are stored in the jacobian matrices J_l and J_u for lower and upper bounds, respectively. Normalized updated bounds will thus receive the following values, for $j \in [1, m]$ corresponding to all m parameters:

$$\begin{aligned} \tilde{l}_j &= \frac{l_j - (l_o)_j}{(u_o)_j - (l_o)_j} + \frac{(J_l)_j}{J_s} \, |\Delta| \\ \tilde{u}_j &= \frac{u_j - (l_o)_j}{(u_o)_j - (l_o)_j} - \frac{(J_u)_j}{J_s} \, |\Delta| \end{aligned} \tag{5.10}$$

where

$$J_s = \sum_{j=1}^{m} |(J_l)_j| + \sum_{j=1}^{m} |(J_u)_j| \tag{5.11}$$

and denormalized bounds ($\boldsymbol{l}$, $\boldsymbol{u}$) can be computed by applying (5.2) to ($\tilde{\boldsymbol{l}}$, $\tilde{\boldsymbol{u}}$) obtained from (5.10), using the initial bounds ($\boldsymbol{l_o}$, $\boldsymbol{u_o}$) to saturate any outstanding bound value.

To exemplify Algorithm 4, let us imagine a scenario with two GFMs in which the upper bounds of m_p and ω_p, as well as the lower bounds of both ω_p and $\tau_{v_{dc}}$ are part of the BCs. This means that there are indices related to $\overline{m_p}$ and $\overline{\omega_p}$ (upper bounds of m_p and ω_p) in $\boldsymbol{\mathcal{U}}$, and indices related to $\underline{\omega_p}$ and $\underline{\tau_{v_{dc}}}$ (lower bounds of ω_p and $\tau_{v_{dc}}$) in $\boldsymbol{\mathcal{L}}$. Now let us imagine that reducing $\overline{m_p}$ by 5 % in all IBRs whose indices are associated with m_p in $\boldsymbol{\mathcal{U}}$ leads to an increase of 20 % in the minimal damping $\bar{\zeta}$, while increasing $\underline{\omega_p}$ in all IBRs whose indices are associated with ω_p in $\boldsymbol{\mathcal{L}}$ leads to an increase of 10 % in $\bar{\zeta}$, the corresponding modifications for $\overline{\omega_p}$ and $\underline{\tau_{v_{dc}}}$ having negligible effect on $\bar{\zeta}$. Hence, for a total impact of 0.03 on $\bar{\zeta}$, $\overline{m_p}$ had an impact of 0.02, while $\underline{\omega_p}$ had an impact of 0.01. When modifying the BCs by $\Delta = 5\,\%$, therefore, $\overline{m_p}$ should take 2/3 of this modification, while $\underline{\omega_p}$ takes the remaining 1/3, respecting the proportions of their individual effect on $\bar{\zeta}$. The next BC will have a $\overline{m_p}$ reduced by 2.33 % and a $\underline{\omega_p}$ increased by 1.66 %. By following this procedure, we restrict our modifications to the most impactful bound values, avoiding unnecessary changes and rapidly converging to a configuration that satisfies our stability criterion.

Taking a simpler example, Figure 5.5 displays the iterations of Algorithm 4 between sub-iterations 0 and 1 in Algorithm 3 (displayed in Figure 5.4). In this case, the BCs consist of maximal m_p, ω_p, and $\tau_{v_{dc}}$ for both GFMs, as in Figure 5.3. When evaluating their impact on $\bar{\zeta}$, it is clear that the upper bound of m_p plays a predominant role, which is why the other parameters remain virtually unchanged. In terms of its normalized value $\tilde{m_p}$, this parameter, imposed on both IBRs, goes from 0.95 to 0.5 in 11 sub-iterations, increasing the minimum damping to $\bar{\zeta} = 4.9\,\%$. Since our goal in Algorithm 3 is to obtain a $\bar{\zeta} \approx \kappa^b = 4.2\,\%$, we may run Algorithm 3 once again, using a negative step size Δ to slightly decrease the damping.

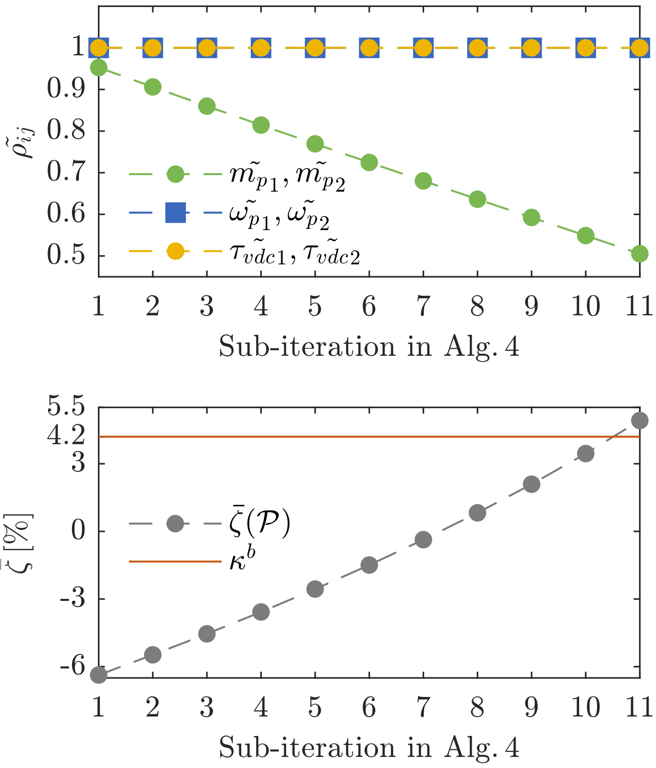

Figure 5.5: Normalized BC parameters $\rho\tilde{i}j$ for each sub-iteration of the Algorithm 4, as well as the corresponding minimal BC damping $\bar{\zeta}$, considering the scenario from Figure 3. Here, we zoom into the iterations of Algorithm 4 happening between sub-iterations 0 and 1 in Algorithm 3 (displayed in Figure 3).

5.2.4 Tuning

A set of constants is employed in this method, as indicated in Table 5.2, where the values attributed to them are the ones adopted for the examples in this chapter. In general, they should be tuned on a case-by-case basis. From all of these parameters, the tuning of κ^b is of particular relevance, as further explored in Section 5.3. As for the other parameters, while the initial step size is chosen arbitrarily ($\Delta_0 = 5\,\%$ seems to provide fast convergence in most simulations), it is important to adopt a reasonably small value to avoid "skipping holes", as the one presented in Figure 5.1. If the step size is too large, one might overlook a small unstable sub-region. A larger stopping criteria ϵ could have further accelerated the algorithm, but at the cost of a narrower bound surface, whereas the reduction rate r of $50\,\%$ is representative of a typical bisection algorithm. A larger value could once more accelerate convergence, although this would entail the same risks as a large Δ_0.

Parameter	Description	Values
κ	Stability criterion	$3\,\%$
κ^b	Alternative stability criterion for BCs	3 - 5 %
Δ_o	Initial step size for updating BCs in Algorithm 3	$5\,\%$
ϵ	Stopping criteria for BCs in Algorithm 3	10^{-6}
r	Reduction rate for step sizes in Algorithm 3	$50\,\%$

Table 5.2: Set of parameters used in the heuristic method

5.3 Results

5.3.1 Validation of the proposed heuristic method

In order to validate the method from Section 5.2, let us go back to an example with two GFMs, connected at nodes 10 and 11 in the network from Figure 3.1. Applying the method, we obtain the results presented in Figure 5.6. Each iteration of Algorithm 1, represented by squares, gradually increases the worst-case damping $\bar{\zeta}^w$ until the stability criterion is satisfied, which requires only three iterations. This means that the optimization from (5.8), which is the most time-consuming procedure in this method, was applied only four times, including the evaluation of the original scenario. In between iterations, several BCs are evaluated, indicated by triangles in Figure 5.6. Visibly, a gradient-based method is efficient in bringing these BCs sufficiently close to the alternative criterion κ^b.

The time-domain simulation in Figure 5.7 confirms the results from Figure 5.7. By computing the worst-case parameters $\boldsymbol{P}$ for the original bounds, as well as for those obtained by the heuristic method, both of which are presented in Table 5.3, we simulate the steady-state behavior of the IBRs in terms of their injected active power P_f. As we may observe, while the original worst-case configuration leads to power oscillations with growing amplitude, for a step-change of just 1 % in P^{ref} (at $t = 0.2$ s), the heuristic worst-case scenario configuration a stable operating condition.

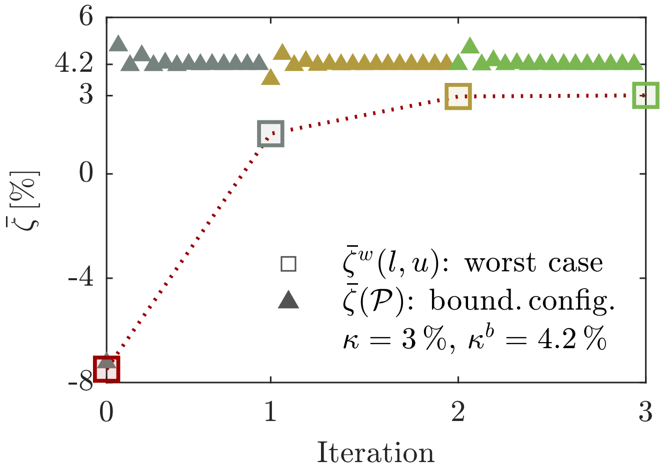

Figure 5.6: Minimum damping $\bar{\zeta}$ for each iteration of the heuristic method, considering a scenario with GFMs connected to nodes 10 and 11

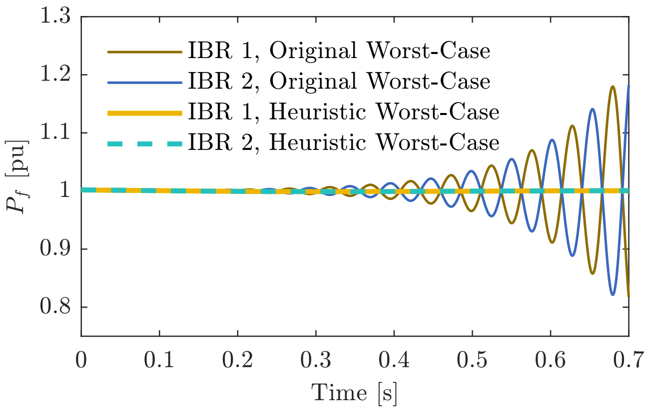

Figure 5.7: Time-domain simulation: injected power P_f in per-unit for two GFMs connected to nodes 10 and 11. Comparison between the worst-case parameterization considering the original bounds and those obtained by applying the heuristic method.

Method	m_p [pu/pu]	ω_p [rd/s]	$\tau_{v_{dc}}$ [ms]
Original Bounds	$0.0050 - 0.0500$	$3.14 - 62.8$	$3 - 70$
Heuristic	$0.0050 - 0.0263$	$3.15 - 62.6$	$3 - 70$
GA	$0.0070 - 0.0260$	$3.24 - 62.1$	$3.2 - 70$
PSO	$0.0050 - 0.0263$	$3.14 - 62.8$	$3 - 70$

Table 5.3: Comparison of methods: final bounds for GFM/GFM

Method	Parameter	Values
GA	Penalty value	10^9
	Population size	20
	Maximum stall generations	20
	Crossover fraction	0.8
PSO	Penalty value	10^9
	Swarm size	20
	Maximum stall generations	20
	Inertia factor	0.7290
	Cognitive learning factor	1.4945
	Social learning factor	1.4945

Table 5.4: Set of parameters used for tuning the metaheuristic optimization methods

5.3.2 Comparison with GA and PSO

Repeating the case study from Figure 5.6, with the same stability criterion of $\kappa = 3\,\%$, in order to provide a comparison with respect to the proposed heuristic method, let us solve the problem presented in (5.9) using metaheuristic methods, namely GA and PSO. We opt for a penalty-function approach for implementing this constrained optimization problem [113], embedding the stability constraint from (5.8) in the algorithm objective function with a penalty factor, and adapting (5.9) to the following maximization:

$$\max_{\boldsymbol{l},\boldsymbol{u}} \quad \chi(\boldsymbol{l},\boldsymbol{u}) - \alpha\, H(\boldsymbol{l},\boldsymbol{u}) \tag{5.12}$$

where

$$H(\boldsymbol{l},\boldsymbol{u}) = \Big(\max\{0,\, \kappa - \bar{\zeta}^w(\boldsymbol{l},\boldsymbol{u})\}\Big)^2 \tag{5.13}$$

Here, $H(\boldsymbol{l},\boldsymbol{u})$ is a penalty factor, whereas α is the penalty value described in Table 5.4.

As noted in Section 5.1, these methods may yield sub-optimal results. Even though all methods reach a comparable bound surface χ, as displayed in Table 5.5, both GA and PSO are considerably slower than the heuristic method. Tuned according to Table 5.4, in terms of its objective, i.e., maximal bound surface, a GA-based solution leads to a slightly smaller surface than the heuristic, while the calculation time is 86 times greater. A PSO algorithm is even slower, taking 90 times more computation time than the heuristic method to give a similar surface. Final bounds are themselves quite similar, as observed in Table 5.3. More notably though, due to the high penalty value ($\alpha = 10^9$), both methods end up converging to a feasible solution, seeing that they yield $\bar{\zeta}^w > \kappa$, even if they do not provide a substantially greater bound surface.

Method	$\bar{\zeta}^w$	χ	χ/χ_o	CPU Time
Original Bounds	-7.49 %	3	100	35 s
Heuristic	3.01 %	2.22	73.88 %	3 min
GA	3.22 %	2.15	71.53 %	4 h 53 min
PSO	3.00 %	2.22	74.12 %	5 h 7 min

Table 5.5: Comparison of methods: key figures

5.3.3 Tuning the heuristic method

As seen in Figure 5.6, in order to reach an acceptable worst-case damping $\bar{\zeta}^w > \kappa$ with $\kappa = 3\,\%$, we had to employ a different stability criterion κ^b for the BCs, namely $\kappa^b = 4.2\,\%$. If we had taken $\kappa^b = \kappa$, Algorithm 1 would have kept iterating and evaluating $\bar{\zeta}^w$, without attaining $\bar{\zeta}^w > \kappa$, as illustrated in Figure 5.8. This is due to a discrepancy between the original worst-case parameters $\boldsymbol{P^w}$ and those for the boundary configuration $\boldsymbol{\mathcal{P}}$, as shown previously in Figure 5.1. Here, aiming to stabilize the former, we are compelled to exaggerate the stability criteria for the corresponding BC.

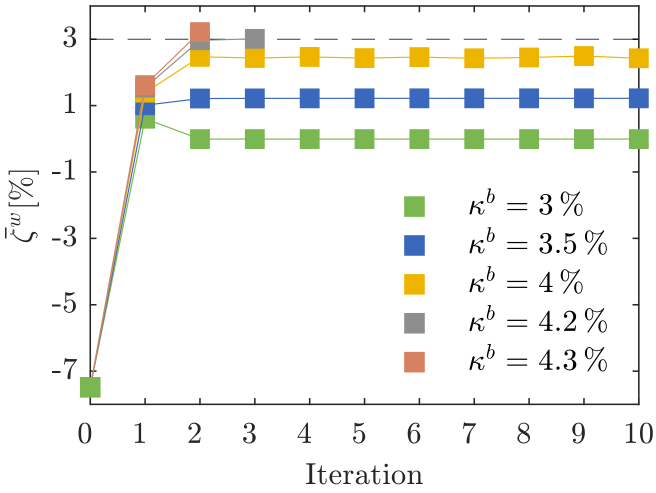

Figure 5.8: Worst-case $\bar{\zeta}$ for each iteration of the heuristic method, considering a scenario with two GFMs connected to nodes 10 and 11

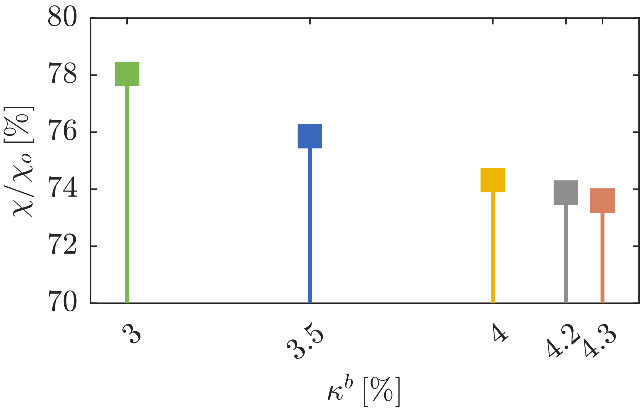

Figure 5.9: Bound surface χ as a function of the alternative stability criterion κ^b for each simulation in Figure 5.8. Here, surface χ is given as a percentage of the initial surface $\chi_o = \chi(\boldsymbol{l_o}, \boldsymbol{u_o})$.

Still, increasing κ^b implies a trade-off: a more restrictive stability criterion for BCs may lead to a smaller bound surface χ, as indicated in Figure 5.9, because the BCs are further modified in Algorithm 3, yielding narrower ranges for key parameters. Considering the values presented in Figure 5.8, the best choice for κ^b would thus be $\kappa^b = 4.2\,\%$, insofar as it provides a $0.38\,\%$ larger bound surface than $\kappa^b = 4.3\,\%$, while still securing worst-case stability ($\bar{\zeta}^w > \kappa$). We may thus reaffirm that a careful tuning of the heuristic parameters presented in Table 5.2, particularly κ^b, is fundamental for the well-functioning of the method under different circumstances.

5.3.4 Additional study case

In order to further validate the method from Section 5.2, we apply it in a different configuration, replacing the first GFM, connected at node 10, with a GFL. Sticking to the worst-case stability criterion of $\kappa = 3\,\%$, while adopting an alternative criterion of $\kappa^b = 5.8\,\%$ for the BCs, we obtain the results presented in Tables 5.6 and 5.7. Compared to the previous scenario, which presented only three parameters, given that it only included GFMs, this time we have six parameters in total, leading to a slower simulation. As observed in Figure 5.10, it takes six iterations for the bounds to satisfy $\bar{\zeta}^w > \kappa$, compared to three iterations in the previous case with two GFMs, which also contributes to a greater simulation time.

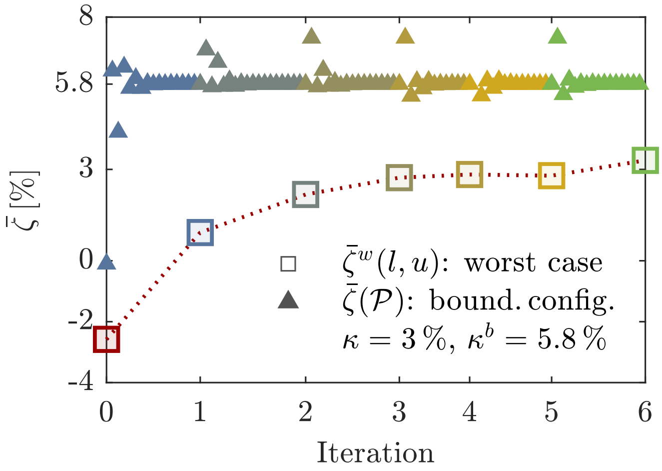

Figure 5.10: $\bar{\zeta}$ for each iteration of the heuristic method, considering a scenario with a GFL and a GFM connected to nodes 10 and 11, respectively

Method	$\bar{\zeta}^w$	χ	χ/χ_o	Sim. Time
Original Bounds	-2.58 %	6	100	46 s
Heuristic	3.30 %	5.72	95.30 %	19 min

Table 5.6: GFL/GFM: key figures

Figure 5.10 also indicates that the original scenario presents negative worst-case damping ($\bar{\zeta}^w = -2.58\,\%$, as reported in Table 5.6), implying an unstable configuration at the initial worst-case scenario. A time-domain simulation may once again confirm this, demonstrating how the heuristic method succeeds in providing a stable worst-case scenario, as shown in Figure 5.11. With respect to the original bounds provided in Table 5.1, our final bounds for a GFL/GFM configuration present a smaller range for $t_r^{v_{dc}}$ and ω_p. GFL external loop time-response $t_r^{v_{dc}}$ is limited to values below 230 ms, while GFM low-pass filter cut-off frequency ω_p should be greater than 4.78 rd/s. These minor adjustments, which reduce the original boundary surface χ by less than 5 %, are nonetheless sufficient to ensure small-signal stability for the worst-case scenario. Once again, the heuristic method is capable of providing satisfactory bounds in a suitable amount of time, demonstrating its ability to act upon the critical parameters in a system with both GFL and GFM inverters.

$t_r^{v_{dc}}$ [ms]	$t_r^{i_q}$ [ms]	t_r^{pll} [ms]	m_p [pu/pu]	ω_p [rd/s]	$\tau_{v_{dc}}$ [ms]
50 – 230	50 – 249	20 – 248	0.005 – 0.05	4.78 – 62.8	3 – 70

Table 5.7: Final bounds for GFL/GFM

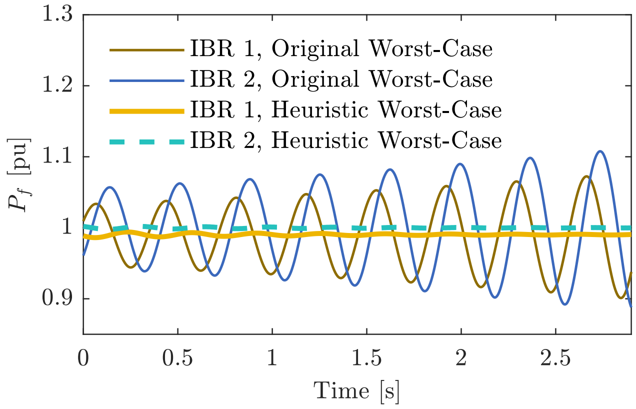

Figure 5.11: Time-domain simulation: injected power P_f in per-unit for the scenario presented in Figure 5.10.

5.4 Chapter summary

This final chapter introduced an optimization-based method to determine parameter bounds for SICDS. Here are the major takeaway points:

- Once the key parameters for SICDS have been determined, it is crucial to provide reasonable *bounds* for these parameters. Imposing their exact value would be challenging because DSOs do not usually own the IBRs, and a stability-based criterion may not be in the best interest of producers.

- The goal is thus to allow producers to tune their IBRs according to their own needs while respecting the bounds defined by the DSO for SICDS. This way, both the DSO and the producers may attain their objectives.
- Although Chapter 4 presented a method to improve parameter bounds for SICDS, ensuring the stability of worst-case BCs, this does not ensure that all parameter combinations *within* these bounds are stabilized. There are situations in which intermediary values of key parameters actually yield a less stable scenario than the worst among all BCs.
- For a given set of parameter bounds, one may write an optimization problem to find the worst parameter combination within these bounds, i.e., the situation with minimal damping. We have called this the “worst-case optimization”.
- This is a constrained nonlinear optimization, solved via Sequential Quadratic Programming (SQP) in *Matlab* for all the results presented in this chapter.
- When defining the parameter bounds, the DSO should aim at providing the largest ranges, giving producers the maximum freedom to tune their IBRs. The total “wideness” of the parameter ranges could be defined as a *surface*, namely a “bound surface”.
- The main objective can hence be translated into an optimization problem as well. Here, the objective function is the maximization of the bound surface, constrained by a stability criterion for the worst-case scenario. We want to provide the widest ranges for the key parameters while ensuring that the worst combination among them is sufficiently stable, i.e., the minimal damping is above 3 %. This is a “bound surface optimization”.
- Being a highly-complex optimization, where the constraint function is in itself an optimization problem, common algorithms such as IPM and SQP often fail to converge to a feasible solution. We may resort to metaheuristic optimization, e.g., GA and PSO.
- Even though they are less prone to convergence issues, both GA and PSO require a high number of evaluations, leading to a considerable computation time (approximately 5 h for the example in this chapter).
- Alternatively, we propose a heuristic method that uses the concepts from Chapter 4 to find an approximate solution for the bound surface optimization.
- In this method, we first apply the worst-case optimization for the initial bounds. This configuration is then approximated by the BC that best resembles it. The bounds for this BC are then modified progressively, according to a gradient, giving preference to the bounds with the highest impact on the minimal damping, hence avoiding an excessive reduction of the bound surface. The new bounds are then reevaluated with respect to their worst-case configuration. The entire process is repeated until the worst-case optimization yields a satisfactory minimal damping.

- The well-functioning of this heuristic requires careful parameterization, especially the alternative stability criterion for BCs κ^b, which is usually different from the general criterion κ. In general, the BCs should be "over-stabilized" so that the worst-case configuration within those bounds is sufficiently stable.

- Applying this method to a GFM/GFM configuration whose initial bounds lead to an unstable worst-case scenario, we are able to find parameter bounds that ensure a minimum damping of 3 % with a bound surface of 73.88 % of the initial surface.

- While the heuristic method delivers this result in only 3 minutes, both the GA and PSO lead to a similar surface (71.53 %, and 74.12 %, respectively) while taking close to 5 hours. The heuristic method is almost 100 times faster while yielding comparable results. The gains in computational efficiency are considerable.

- The heuristic method is further tested on a GFL/GFM configuration, once again yielding positive results. Minimum damping of 3 % is secured with a bound surface of 95.3 % of the initial surface.

- Further work is necessary to validate this method in larger systems, with more IBRs and/or key parameters for each IBR, assessing the gains in scalability with respect to the metaheuristic optimization algorithms.

Conclusions

Aiming to reach carbon neutrality by 2050, France is committed to integrating more RES into the grid. Enedis, the main French DSO, expects up to ten times more distribution-connected wind and solar power by 2050, where the total capacity of MV-connected PV plants could increase by up to 15 times. These perspectives are raising concerns about the stable operation of future IBR-rich MV networks, especially with respect to interactions between IBRs. Hence, this thesis provided a study of slow-interaction converter-driven stability in medium-voltage distribution grids with IBRs, assessing the impact of both grid-following and grid-forming operation modes. Our main objective was to develop a methodology for DSOs to analyze and prevent these instabilities.

5.5 Main conclusions

Our first conclusions stem directly from the literature review, serving as the basis on which we outlined the scope of this thesis in Figure 1.17. With an ever-increasing presence of IBRs, the classical categories of power system stability do not suffice for assessing the stability of MVDGs, hence our choice to focus on a new category: converter-driven stability. Due to their system-wide implications, and the fact that they might result from inter-IBR interactions, we have preferred to tackle *slow-interaction* CDS, which applies to phenomena under 50 Hz. With respect to assessment methods, our conclusion is that small-signal stability analysis, due to the powerful tools associated with it, is better suited to explain the origins of SICDS problems when detailed models are available. Given the multiple time scales of IBR controllers, it is preferable to model this system in EMT rather than RMS, allowing for a more precise representation. Finally, because of the predominance of control interactions in SICDS, one may conclude that the operation mode of IBRs, which determines the behavior of their controllers, should be taken into account in this analysis, which is why we have provided a detailed comparison between GFL and GFM inverters throughout this dissertation.

Before modeling the system for SSSA, we performed a static analysis to study the impact of grid parameters such as SCR and R/X ratio, concluding that weak-grid situations (SCR below 3) may appear for MVDGs with long feeders (close to 20 km), hence certain instabilities observed in large transmission grids, e.g., PLL instability, could also occur in MVDGs. We also concluded that, under low-SCR and high-R/X, GFLs may lead to unacceptable voltage levels, which could be solved by replacing them with GFMs. Static issues due to negative P-I sensitivity (power transfer limitation) are unlikely in a grid with high-R/X. For GFMs operated as PQ-buses, a steady-state coupling between P and Q, arising from the high R/X ratio, could require a virtual impedance (VI) for R/X ratio correction. Proper tuning of this VI should be based on P-Q coupling, POI voltage, and perceived SCR; improvements in coupling are possible, but come at the expense of strict voltage levels.

Adopting the *CIGRE* Benchmark MV Network as our MVDG, generic models for IBRs, both GFL and GFM, were provided in Chapter 3. Our studies focus on large PV and BESS installations, although conclusions may extend to Type-4 WPPs. Studying the models available in the literature, we conclude that a generic GFL should include internal and external control loops (for P and Q), in addition to a PLL, where the P-control loop could be replaced by a converter-side DC-voltage control. A generic GFM model should also comprise internal and external control loops, where the latter includes a power-synchronization loop (for P) and Q-V droop control. It is also important to consider additional control loops, such as active damping, virtual impedance, and machine-side v_{dc} control. Although multiple models are available in the literature, we conclude that their small-signal behavior may still be reproduced by means of these generic models, which is an advantage for the DSO.

With the models established, what ensues is the small-signal stability analysis, from which we derive most of the conclusions of this thesis. Using modal maps to identify the dominant modes in a 1-IBR system, we conclude that they are related to the external loops for both GFL and GFM, as well as the PLL (for a GFL) and the v_{dc} control loop (for a GFM). Using sensitivity analysis and participation factors, we are able to identify key parameters for SICDS, namely $t_r^{v_{dc}}$, $t_r^{i_q}$, and t_r^{pll} in GFLs, as well as m_p, ω_p, and $\tau_{v_{dc}}$ in GFMs. These are crucial for DSOs to prevent and mitigate SICDS issues in MVDGs. Considering a single-GFL system, we conclude that high $t_r^{v_{dc}}$ can lead to instability if the DC-link capacitance is small, while PLL instability may occur if t_r^{pll} is low and the IBR is connected to the weakest node in the MVDG through a long line, e.g., 5 km. High-droop instability may also occur for GFMs connected to strong nodes, a phenomenon explored through analogies with synchronous generators, although this only happens for unrealistically high droop values, e.g., $m_p = 0.2$.

In order to study interactions between IBRs, we resort to 2-IBR configurations, where, besides the SCR at the POI, the electrical distance between IBRs is also an important parameter. Modal maps reveal that dominant modes may result from the interaction between external loops of both IBRs. Single-parameter sensitivities are employed to refine the critical ranges for key parameters; most notably, a droop level of $m_p = 0.04$ is now enough to cause SICDS issues when two GFMs are connected to nearby nodes, indicating a relevant interaction between GFMs. Although a GFL/GFM mix seems to yield more stable scenarios than GFL/GFL or GFM/GFM configurations, there are still some negative interactions: a GFM could worsen the high $t_r^{v_{dc}}$ instability in GFLs, for instance. On the other hand, a nearby GFM can solve a PLL instability in a GFL. Extending the analysis to a system with more IBRs corroborates these findings, demonstrating the usefulness of a generic 2-IBR assessment.

Our main conclusion is that DSOs should play a major role in ensuring SICDS in MVDGs. They could do this by providing adequate ranges for key parameters. An initial methodology is to assess boundary configurations (BC), where each parameter is tuned at its minimum or maximum bound value, identifying the most critical BCs and ensuring their stability. This could be done through multi-parameter sensitivities applied to worst-case combinations between BCs. Parameter bounds should be further refined using the optimization problem defined in Chapter 5, guaranteeing the stability of all parameter combinations within these bounds. This is a complex optimization problem, where the constraint function is in itself an optimization problem. It can be solved via metaheuristic algorithms, such as GA and PSO, which are effective but computationally intensive. As a simpler alternative, we propose a heuristic method that applies a gradient-based algorithm to find an approximate solution for the same optimization problem. From the final results, we conclude that this heuristic method yields similar outcomes as the metaheuristic algorithms, but with much less computation time; in some scenarios, the heuristic method is almost 100 times faster.

5.6 Perspectives

Going back to the hypotheses presented in Chapter 3, a logical way to expand the work done in this thesis is to include the downstream dynamics in the model, by representing the MV loads and LV networks, as well as the upstream dynamics, by adding a representation of the HV network, especially in the case of low inertia. Whereas we focused on inter-IBR interactions, future work could focus on the interactions between IBRs and loads, or between the active MV distribution grid and the HV network upstream. A comparison between multiple GFM control methods to further validate the generality of the model is also worth pursuing.

Figure 1.17 provides another pathway for future work, indicating where the scope of this thesis could be extended. One could include fast-interaction CDS and explore the intersection between harmonic instability and slow interactions. Different assessment methods could also be explored, including an impedance-based approach. SICDS could also be investigated from the point of view of large-signal stability, exploring interactions related to current-limitation algorithms, frequency fluctuations due to low inertia, and black-start procedures, for instance. Development of reduced-order RMS models or methods for model-order reduction of EMT models for SICDS could also lead to interesting studies.

Finally, albeit our DSO-oriented solution was a system-level optimization problem, device-level solutions could also be considered. Additional control loops to dampen low-frequency oscillations or advanced GFM control methods could perhaps lead to a more decentralized way of dealing with SICDS. There is also room for improvement in the solution proposed in this work, given that the heuristic method still relies on empirical tuning. Application on larger systems, with more inverters, more elements in the network, and more key parameters would also be of great value. Considering the DSO's interest in temporarily islanding certain portions of the MVDG, this method could also be examined in the context of microgrids.

Bibliography

[1] P. Kundur, N. Balu, and M. Lauby, *Power System Stability and Control* (EPRI power system engineering series). McGraw-Hill Education, 1994 (cit. on pp. 5, 19, 26, 28, 30, 32, 35, 42, 44, 51, 114, 115, 188, 189).

[2] A. Doulet, "Réseaux de distribution d'électricité - présentation," *Editions TI*, no. ref. article : d4200, 2010, Base documentaire : TIP266WEB. (cit. on pp. 6, 8).

[3] M. Alvarez-Herault, V. Gouin, T. Chardin-Segui, *et al.*, *Distribution System Planning: Evolution of Methodologies and Digital Tools for Energy Transition*. Wiley, 2023 (cit. on p. 6).

[4] "Bilan électrique 2022," Enedis, Tech. Rep., 2023 (cit. on pp. 8, 9).

[5] M. Cosson, "Stabilité du réseau électrique de distribution. analyse du point de vue automatique d'un système complexe," Thèse de doctorat dirigée par Dumur, Didier Automatique Université Paris-Saclay (ComUE) 2016, Ph.D. dissertation, 2016 (cit. on pp. 9, 47, 49, 95).

[6] Enedis, "Principe et conditions de mise en oeuvre d'une régulation locale de puissance réactive pour les installations de production raccordées au réseau public de distribution hta," *Enedis NOI - RES 60*, 2016 (cit. on pp. 10, 33, 49).

[7] Ministère de la transition écologique et solidaire, *Stratégie nationale bas-carbone - synthèse*, 2020 (cit. on p. 10).

[8] "Secten, Rapport d'inventaire: Gaz à effet de serre et polluants atmosphériques - Bilan des émissions en France de 1990 à 2022," Citepa, Tech. Rep., 2023 (cit. on p. 11).

[9] "Energy pathways to 2050 - key results," RTE, Tech. Rep., 2021 (cit. on pp. 10, 12).

[10] "Bilan électrique 2022 - principaux résultats," RTE, Tech. Rep., 2023 (cit. on p. 12).

[11] "Eléments de prospective du réseau public de distribution d'électricité à l'horizon 2050," Enedis, Tech. Rep., 2021 (cit. on pp. 13, 14, 73).

[12] P. Kundur, J. Paserba, V. Ajjarapu, *et al.*, "Definition and classification of power system stability ieee/cigre joint task force on stability terms and definitions," *IEEE Transactions on Power Systems*, vol. 19, no. 3, pp. 1387–1401, 2004 (cit. on pp. 15–19, 22).

[13] J. Slotine and W. Li, *Applied Nonlinear Control*. Prentice Hall, 1991 (cit. on pp. 16, 17).

[14] J. Machowski, J. Bialek, and J. Bumby, *Power System Dynamics: Stability and Control*. Wiley, 2011 (cit. on pp. 16, 31, 147).

[15] T. van Cutsem and C. Vournas, *Voltage Stability of Electric Power Systems* (Power Electronics and Power Systems). Springer US, 2007 (cit. on p. 19).

[16] N. Hatziargyriou, J. Milanović, C. Rahmann, *et al.*, "Stability definitions and characterization of dynamic behavior in systems with high penetration of power electronic interfaced technologies," Tech. Rep., May 2020 (cit. on pp. 20–22).

[17] N. Hatziargyriou, J. Milanovic, C. Rahmann, *et al.*, "Definition and classification of power system stability – revisited extended," *IEEE Transactions on Power Systems*, vol. 36, no. 4, pp. 3271–3281, 2021 (cit. on pp. 20–23, 214).

[18] P. Aristidou, G. Valverde, and T. Van Cutsem, "Contribution of distribution network control to voltage stability: A case study," *IEEE Transactions on Smart Grid*, vol. 8, no. 1, pp. 106–116, 2017 (cit. on p. 21).

[19] A. Adrees, J. Milanović, and P. Mancarella, "Effect of inertia heterogeneity on frequency dynamics of low-inertia power systems," *IET Generation, Transmission & Distribution*, vol. 13, no. 14, pp. 2951–2958, 2019 (cit. on p. 21).

[20] F. Milano, F. Dörfler, G. Hug, D. J. Hill, and G. Verbič, "Foundations and challenges of low-inertia systems (invited paper)," in *2018 Power Systems Computation Conference (PSCC)*, 2018, pp. 1–25 (cit. on pp. 21, 44).

[21] J. Rocabert, A. Luna, F. Blaabjerg, and P. Rodríguez, "Control of power converters in ac microgrids," *IEEE Transactions on Power Electronics*, vol. 27, no. 11, pp. 4734–4749, 2012 (cit. on pp. 21, 23, 32, 36, 37, 46, 194).

[22] F. Milano, *Complex frequency*, 2021. arXiv: `2105.07769 [eess.SY]` (cit. on p. 21).

[23] J. Shair, X. Xie, L. Wang, W. Liu, J. He, and H. Liu, "Overview of emerging subsynchronous oscillations in practical wind power systems," *Renewable and Sustainable Energy Reviews*, vol. 99, pp. 159–168, 2019 (cit. on p. 22).

[24] L. Kong, Y. Xue, L. Qiao, and F. Wang, "Review of Small-Signal Converter-Driven Stability Issues in Power Systems," *IEEE Open Access Journal of Power and Energy*, vol. 9, pp. 29–41, 2022 (cit. on pp. 22, 23, 27, 28, 38, 64).

[25] X. Wang and F. Blaabjerg, "Harmonic stability in power electronic-based power systems: Concept, modeling, and analysis," *IEEE Transactions on Smart Grid*, vol. 10, no. 3, pp. 2858–2870, 2019 (cit. on p. 22).

[26] E. Ebrahimzadeh, F. Blaabjerg, X. Wang, and C. L. Bak, "Harmonic Stability and Resonance Analysis in Large PMSG-Based Wind Power Plants," *IEEE Transactions on Sustainable Energy*, vol. 9, no. 1, pp. 12–23, 2018 (cit. on p. 22).

[27] M. Lu, Y. Yang, B. Johnson, and F. Blaabjerg, "An interaction-admittance model for multi-inverter grid-connected systems," *IEEE Transactions on Power Electronics*, vol. 34, no. 8, pp. 7542–7557, 2019 (cit. on p. 22).

[28] Y. Li, L. Fan, and Z. Miao, “Wind in weak grids: Low-frequency oscillations, subsynchronous oscillations, and torsional interactions,” *IEEE Transactions on Power Systems*, vol. 35, no. 1, pp. 109–118, 2020 (cit. on pp. 23–25).

[29] L. Fan and Z. Miao, “Wind in weak grids: 4 hz or 30 hz oscillations?” *IEEE Transactions on Power Systems*, vol. 33, no. 5, pp. 5803–5804, 2018 (cit. on pp. 23–25).

[30] X. Wang, M. G. Taul, H. Wu, Y. Liao, F. Blaabjerg, and L. Harnefors, “Grid synchronization stability of converter-based resources—an overview,” *IEEE Open Journal of Industry Applications*, vol. 1, pp. 115–134, 2020 (cit. on pp. 23, 24, 26, 27, 38, 55, 64).

[31] X. Wang, L. Harnefors, and F. Blaabjerg, “Unified impedance model of grid-connected voltage-source converters,” *IEEE Transactions on Power Electronics*, vol. 33, no. 2, pp. 1775–1787, 2018 (cit. on p. 23).

[32] B. Badrzadeh, Z. Emin, E. Hillberg, *et al.*, “The need for enhanced power system modelling techniques and simulation tools,” English, *CIGRE Science & Engineering*, vol. 17, no. February, pp. 30–46, 2020 (cit. on p. 23).

[33] M. Paolone, T. Gaunt, X. Guillaud, *et al.*, “Fundamentals of power systems modelling in the presence of converter-interfaced generation,” *Electric Power Systems Research*, vol. 189, p. 106 811, 2020 (cit. on p. 23).

[34] D. Ramasubramanian, W. Wang, P. Pourbeik, *et al.*, “Positive sequence voltage source converter mathematical model for use in low short circuit systems,” *IET Generation, Transmission & Distribution*, vol. 14, no. 1, pp. 87–97, 2020. eprint: `https://ietresearch.onlinelibrary.wiley.com/doi/pdf/10.1049/iet-gtd.2019.0346` (cit. on pp. 23, 39, 83).

[35] A. Singh, V. Debusschere, and N. Hadjsaid, “Slow-interaction Converter-driven Stability in the Distribution Grid: Small Signal Stability Analysis using RMS Models,” in *IEEE Power & Energy Society General Meeting (PES-GM)*, 2022, pp. 1–5 (cit. on pp. 23, 83).

[36] L. Zhang, L. Harnefors, and H.-P. Nee, “Power-synchronization control of grid-connected voltage-source converters,” *IEEE Transactions on Power Systems*, vol. 25, no. 2, pp. 809–820, 2010 (cit. on pp. 24, 39, 44, 80, 187).

[37] J. Adams, C. Carter, and S.-H. Huang, “Ercot experience with sub-synchronous control interaction and proposed remediation,” in *PES T D 2012*, 2012, pp. 1–5 (cit. on p. 24).

[38] P.-H. Huang, M. S. El Moursi, W. Xiao, and J. L. Kirtley, “Subsynchronous resonance mitigation for series-compensated DFIG-based wind farm by using two-degree-of-freedom control strategy,” *IEEE Transactions on Power Systems*, vol. 30, no. 3, pp. 1442–1454, 2015 (cit. on p. 24).

[39] H. Liu, X. Xie, C. Zhang, Y. Li, H. Liu, and Y. Hu, “Quantitative SSR analysis of series-compensated DFIG-based wind farms using aggregated rlc circuit model,” *IEEE Transactions on Power Systems*, vol. 32, no. 1, pp. 474–483, 2017 (cit. on p. 24).

[40] A. E. Leon and J. A. Solsona, “Sub-synchronous interaction damping control for DFIG wind turbines,” *IEEE Transactions on Power Systems*, vol. 30, no. 1, pp. 419–428, 2015 (cit. on p. 24).

[41] Y. Cheng, M. Sahni, D. Muthumuni, and B. Badrzadeh, “Reactance scan crossover-based approach for investigating SSCI concerns for DFIG-based wind turbines,” *IEEE Transactions on Power Delivery*, vol. 28, no. 2, pp. 742–751, 2013 (cit. on p. 24).

[42] H. Liu, X. Xie, J. He, *et al.*, “Subsynchronous interaction between direct-drive PMSG based wind farms and weak ac networks,” *IEEE Transactions on Power Systems*, vol. 32, no. 6, pp. 4708–4720, 2017 (cit. on pp. 24, 44, 53).

[43] L. Fan and Z. Miao, “An explanation of oscillations due to wind power plants weak grid interconnection,” *IEEE Transactions on Sustainable Energy*, vol. 9, no. 1, pp. 488–490, 2018 (cit. on pp. 24, 25, 35).

[44] S.-H. Huang, J. Schmall, J. Conto, J. Adams, Y. Zhang, and C. Carter, “Voltage control challenges on weak grids with high penetration of wind generation: Ercot experience,” in *2012 IEEE Power and Energy Society General Meeting*, 2012, pp. 1–7 (cit. on p. 24).

[45] C. Li, “Unstable operation of photovoltaic inverter from field experiences,” *IEEE Transactions on Power Delivery*, vol. 33, no. 2, pp. 1013–1015, 2018 (cit. on p. 24).

[46] J. Matevosyan, J. MacDowell, N. Miller, *et al.*, “A future with inverter-based resources: Finding strength from traditional weakness,” *IEEE Power and Energy Magazine*, vol. 19, no. 6, pp. 18–28, 2021 (cit. on pp. 24, 39).

[47] NERC, “1,200 MW Fault Induced Solar Photovoltaic Resource Interruption Disturbance Report,” NERC, Tech. Rep., 2017 (cit. on p. 24).

[48] F. Arraño-Vargas, Z. Shen, S. Jiang, J. Fletcher, and G. Konstantinou, “Challenges and mitigation measures in power systems with high share of renewables - the Australian experience,” *Energies*, vol. 15, no. 2, 2022 (cit. on p. 25).

[49] P. De Rua, T. Roose, Özgür Can Sakinci, N. de Morais Dias Campos, and J. Beerten, “Identification of mechanisms behind converter-related issues in power systems based on an overview of real-life events,” *Renewable and Sustainable Energy Reviews*, vol. 183, p. 113 431, 2023 (cit. on p. 25).

[50] Y. Cheng, L. Fan, J. Rose, *et al.*, “Real-World Subsynchronous Oscillation Events in Power Grids With High Penetrations of Inverter-Based Resources,” *IEEE Transactions on Power Systems*, vol. 38, no. 1, pp. 316–330, 2023 (cit. on p. 25).

[51] Y. Li, L. Fan, and Z. Miao, “Stability control for wind in weak grids,” *IEEE Transactions on Sustainable Energy*, vol. 10, no. 4, pp. 2094–2103, 2019 (cit. on pp. 25, 35, 53).

[52] L. Fan, “Modeling type-4 wind in weak grids,” *IEEE Transactions on Sustainable Energy*, vol. 10, no. 2, pp. 853–864, 2019 (cit. on pp. 25, 73).

[53] Y. Li, L. Fan, and Z. Miao, "Replicating real-world wind farm SSR events," *IEEE Transactions on Power Delivery*, vol. 35, no. 1, pp. 339–348, 2020 (cit. on p. 25).

[54] Q. Xu, "Chapter 7 - overview of stability analysis methods in power electronics," in *Control of Power Electronic Converters and Systems*, F. Blaabjerg, Ed., Academic Press, 2021, pp. 169–197 (cit. on pp. 26–28).

[55] Q. Hu, L. Fu, F. Ma, and F. Ji, "Large signal synchronizing instability of pll-based vsc connected to weak ac grid," *IEEE Transactions on Power Systems*, vol. 34, no. 4, pp. 3220–3229, 2019 (cit. on p. 26).

[56] F. Andrade, K. Kampouropoulos, L. Romeral, J. C. Vasquez, and J. M. Guerrero, "Study of large-signal stability of an inverter-based generator using a lyapunov function," in *IECON 2014 - 40th Annual Conference of the IEEE Industrial Electronics Society*, 2014, pp. 1840–1846 (cit. on p. 26).

[57] F. Milano, *Power System Modelling and Scripting* (Power Systems). Springer Berlin Heidelberg, 2010 (cit. on pp. 27, 28, 30, 31).

[58] J. Sun, "Impedance-based stability criterion for grid-connected inverters," *IEEE Transactions on Power Electronics*, vol. 26, no. 11, pp. 3075–3078, 2011 (cit. on pp. 27, 44).

[59] X. Wang, L. Harnefors, and F. Blaabjerg, "Unified Impedance Model of Grid-Connected Voltage-Source Converters," *IEEE Transactions on Power Electronics*, vol. 33, no. 2, pp. 1775–1787, 2018 (cit. on p. 27).

[60] L. Harnefors, X. Wang, A. G. Yepes, and F. Blaabjerg, "Passivity-based stability assessment of grid-connected vscs—an overview," *IEEE Journal of Emerging and Selected Topics in Power Electronics*, vol. 4, no. 1, pp. 116–125, 2016 (cit. on p. 27).

[61] M. Amin and M. Molinas, "Small-signal stability assessment of power electronics based power systems: A discussion of impedance- and eigenvalue-based methods," *IEEE Transactions on Industry Applications*, vol. 53, no. 5, pp. 5014–5030, 2017 (cit. on pp. 27, 28).

[62] M. Gibbard, D. Vowles, and P. Pourbeik, *Small-signal stability, control and dynamic performance of power systems* (JSTOR Open Access monographs). University of Adelaide Press, 2015 (cit. on p. 28).

[63] U. Markovic, O. Stanojev, P. Aristidou, E. Vrettos, D. Callaway, and G. Hug, "Understanding Small-Signal Stability of Low-Inertia Systems," *IEEE Transactions on Power Systems*, vol. 36, no. 5, pp. 3997–4017, 2021 (cit. on pp. 32, 67, 73, 83).

[64] M. Cheah-Mane, A. Egea-Alvarez, E. Prieto-Araujo, H. Mehrjerdi, O. Gomis-Bellmunt, and L. Xu, "Modeling and Analysis Approaches for Small-Signal Stability Assessment of Power-Electronic-Dominated Systems," *WIREs Energy and Environment*, vol. 12, no. 1, e453, 2023 (cit. on p. 32).

[65] E. P. R. Institute, "Grid forming inverters: Epri tutorial," *Program 2020 174 DER Integration*, 2020 (cit. on p. 36).

[66] T. Qoria, Q. Cossart, L. Chuanye, *et al.*, "Migrate 2020 deliverable d3.2 - local control and simulation tools for large transmission systems," Dec. 2018 (cit. on pp. 36, 64, 187, 189).

[67] Kroposki, B., "UNIFI Specifications for Grid-forming Inverter-based Resources— Version 1," UNIFI, Tech. Rep., 2022 (cit. on pp. 36, 37).

[68] E. Rokrok, T. Qoria, A. Bruyere, B. Francois, and X. Guillaud, "Effect of using pll-based grid-forming control on active power dynamics under various scr," in *IECON 2019 - 45th Annual Conference of the IEEE Industrial Electronics Society*, vol. 1, 2019, pp. 4799–4804 (cit. on p. 36).

[69] G. Denis, "Les nouvelles stratégies de contrôle d'onduleurs pour un système électrique 100% interfacé par électronique de puissance," Theses, Ecole Centrale de Lille, Nov. 2017 (cit. on pp. 37, 45, 56, 96).

[70] T. Qoria, "Grid-forming control to achieve a 100% power electronics interfaced power transmission systems," Theses, HESAM Université, Nov. 2020 (cit. on pp. 37, 39, 48, 53, 57, 80, 186, 187, 189, 193).

[71] Y. Li, Y. Gu, and T. Green, "Revisiting grid-forming and grid-following inverters: A duality theory," *IEEE Transactions on Power Systems*, pp. 1–1, 2022 (cit. on pp. 38, 64).

[72] R. Rosso, X. Wang, M. Liserre, X. Lu, and S. Engelken, "Grid-forming converters: Control approaches, grid-synchronization, and future trends—a review," *IEEE Open Journal of Industry Applications*, vol. 2, pp. 93–109, 2021 (cit. on pp. 38, 64).

[73] A. Avazov, F. Colas, J. Beerten, and X. Guillaud, "Damping of torsional vibrations in a type-iv wind turbine interfaced to a grid-forming converter," in *2021 IEEE Madrid PowerTech*, 2021, pp. 1–6 (cit. on p. 38).

[74] C. Arghir and F. Dörfler, "The electronic realization of synchronous machines: Model matching, angle tracking, and energy shaping techniques," *IEEE Transactions on Power Electronics*, vol. 35, no. 4, pp. 4398–4410, 2020 (cit. on pp. 38, 39, 83).

[75] I. Subotic; and D. Groß; "Power-balancing dual-port grid-forming power converter control for renewable integration and hybrid ac/dc power systems," *IEEE Transactions on Control of Network Systems*, pp. 1–12, 2022 (cit. on p. 38).

[76] C. Cardozo, Y. Vernay, G. Denis, T. Prevost, M. Zubiaga, and J. Valera, "Osmose grid-forming performance assessment within multiservice storage connected to the transmission grid," Aug. 2020 (cit. on p. 38).

[77] T. Qoria, F. Gruson, F. Colas, X. Kestelyn, and X. Guillaud, "Current limiting algorithms and transient stability analysis of grid-forming vscs," *Electric Power Systems Research*, vol. 189, p. 106 726, 2020 (cit. on p. 38).

[78] Q. Cossart, “Tools and Methods for the Analysis and Simulation of Large Transmission Systems Using 100% Power Electronics,” Theses, Ecole nationale supérieure d’arts et métiers - ENSAM, Sep. 2019 (cit. on p. 38).

[79] S. Bacha, I. Munteanu, and A. I. Bratcu, *Power Electronic Converters Modeling and Control - with Case Studies* (Advanced Textbooks in Control and Signal Processing). Springer, Sep. 2013, p. 458 (cit. on pp. 39, 71, 183).

[80] M. Chandorkar, D. Divan, and R. Adapa, “Control of parallel connected inverters in standalone ac supply systems,” *IEEE Transactions on Industry Applications*, vol. 29, no. 1, pp. 136–143, 1993 (cit. on pp. 39, 83).

[81] J. M. Guerrero, M. Chandorkar, T.-L. Lee, and P. C. Loh, “Advanced control architectures for intelligent microgrids—part i: Decentralized and hierarchical control,” *IEEE Transactions on Industrial Electronics*, vol. 60, no. 4, pp. 1254–1262, 2013 (cit. on p. 39).

[82] J. Liu, Y. Miura, H. Bevrani, and T. Ise, “Enhanced virtual synchronous generator control for parallel inverters in microgrids,” *IEEE Transactions on Smart Grid*, vol. 8, no. 5, pp. 2268–2277, 2017 (cit. on pp. 39, 83, 187).

[83] G.-S. Seo, M. Colombino, I. Subotic, B. Johnson, D. Groß, and F. Dörfler, “Dispatchable virtual oscillator control for decentralized inverter-dominated power systems: Analysis and experiments,” in *2019 IEEE Applied Power Electronics Conference and Exposition (APEC)*, 2019, pp. 561–566 (cit. on pp. 39, 83).

[84] T. Jouini, U. Markovic, and D. Groß, “Migrate 2020 deliverable d3.3 - new options for existing system services and needs for new system services,” Dec. 2018 (cit. on pp. 39, 83).

[85] P. Unruh, M. Nuschke, P. Strauß, and F. Welck, “Overview on grid-forming inverter control methods,” *Energies*, vol. 13, no. 10, 2020 (cit. on p. 39).

[86] “IEEE guide for planning DC links terminating at AC locations having low short-circuit capacities,” *IEEE Std 1204-1997*, pp. 1–216, 1997 (cit. on pp. 43, 44).

[87] EPRI, “Grid Forming Inverters: Tutorial,” EPRI, Palo Alto, CA, Tech. Rep., 2022, 3002025483 (cit. on pp. 44, 82, 83).

[88] A. Coiffier, “Structure des réseaux de distribution,” *Techniques De L’Ingénieur Réseaux Électriques Et Applications*, vol. base documentaire : TIP302WEB. No. ref. article : d4210, 2021 (cit. on pp. 44, 47–49).

[89] E. Gain, “Réseaux De Distribution Conception Et Dimensionnement,” *Techniques De L’Ingénieur Réseaux Électriques Et Applications*, vol. base documentaire : TIP302WEB. No. ref. article : d4220, 1993, Base documentaire : TIP302WEB. (cit. on p. 47).

[90] K. Strunz, E. Abbasi, R. Fletcher, N. Hatziargyriou, R. Iravani, and G. Joos, *TF C6.04.02 : TB 575 – Benchmark Systems for Network Integration of Renewable and Distributed Energy Resources.* Apr. 2014 (cit. on pp. 47, 48, 68, 84).

[91] J. Buire, “Intégration des incertitudes liées aux prévisions de consommation et production à la gestion prévisionnelle d’un réseau de distribution,” 2018ECLI0017, Ph.D. dissertation, 2018 (cit. on pp. 47, 48).

[92] J.-L. Fraisse and L. Karsenti, “Raccordement de la production décentralisée aux réseaux de distribution conditions d’intégration,” *Techniques de l’ingénieur Réseaux électriques et applications*, vol. base documentaire : TIP302WEB. No. ref. article : d4241, 2014. eprint: `basedocumentaire:TIP302WEB.` (cit. on p. 49).

[93] Enedis, “Principes d’étude et règles techniques pour le raccordement au réseau public de distribution géré par enedis d’une installation de consommation en hta,” *Enedis PRO - RES 50*, 2010 (cit. on p. 49).

[94] N. Pogaku, M. Prodanovic, and T. C. Green, “Modeling, Analysis and Testing of Autonomous Operation of an Inverter-Based Microgrid,” *IEEE Transactions on Power Electronics*, vol. 22, no. 2, pp. 613–625, 2007 (cit. on p. 67).

[95] D. Baimel, J. Belikov, J. M. Guerrero, and Y. Levron, “Dynamic modeling of networks, microgrids, and renewable sources in the dq0 reference frame: A survey,” *IEEE Access*, vol. 5, pp. 21 323–21 335, 2017 (cit. on p. 71).

[96] D. Xie, Y. Lu, J. Sun, and C. Gu, “Small-Signal Stability Analysis for Different Types of PMSGs Connected to the Grid,” *Renewable Energy*, vol. 106, pp. 149–164, 2017 (cit. on p. 73).

[97] T. Qoria, F. Gruson, F. Colas, G. Denis, T. Prevost, and X. Guillaud, “Critical Clearing Time Determination and Enhancement of Grid-Forming Converters Embedding Virtual Impedance As Current Limitation Algorithm,” *IEEE Journal of Emerging and Selected Topics in Power Electronics*, vol. 8, no. 2, pp. 1050–1061, 2019 (cit. on p. 73).

[98] R. Liu, L. Ding, C. Xue, and Y. Li, “Small-Signal Modelling and Analysis of Microgrids with Synchronous and Virtual Synchronous Generators,” *IET Energy Systems Integration*, 2023 (cit. on p. 73).

[99] D. B. Rathnayake, R. Razzaghi, and B. Bahrani, “Generalized Virtual Synchronous Generator Control Design for Renewable Power Systems,” *IEEE Transactions on Sustainable Energy*, vol. 13, no. 2, pp. 1021–1036, 2022 (cit. on p. 73).

[100] D. A. Aragon, E. Unamuno, S. Ceballos, and J. A. Barrena, “Comparative Small-Signal Evaluation of Advanced Grid-Forming Control Techniques,” *Electric Power Systems Research*, vol. 211, p. 108 154, 2022 (cit. on pp. 73, 83).

[101] O. Stanojev, U. Markovic, P. Aristidou, and G. Hug, “Improving Stability of Low-Inertia Systems using Virtual Induction Machine Synchronization for Grid-Following Converters,” *IEEE Transactions on Power Systems*, 2022 (cit. on p. 73).

[102] A. Tayyebi, D. Groß, A. Anta, F. Kupzog, and F. Dörfler, “Frequency stability of synchronous machines and grid-forming power converters,” *IEEE Journal of Emerging and Selected Topics in Power Electronics*, vol. 8, no. 2, pp. 1004–1018, 2020 (cit. on p. 73).

[103] S. Samanta and N. R. Chaudhuri, “Stability Analysis of Grid-Forming Converters Under DC-Side Current Limitation in Primary Frequency Response Regime,” *IEEE Transactions on Power Systems*, vol. 37, no. 4, pp. 3077–3091, 2022 (cit. on p. 73).

[104] J. Martínez Turégano, S. Añó Villalba, S. Bernal Perez, R. Peña, and R. Blasco Gimenez, “Small-Signal Stability and Fault Performance of Mixed Grid Forming and Grid Following Offshore Wind Power Plants Connected to a HVDC-Diode Rectifier,” *IET Renewable Power Generation*, vol. 14, no. 12, pp. 2166–2175, 2020 (cit. on p. 73).

[105] D. Ramasubramanian and E. Farantatos, “Representation of Grid Forming Virtual Oscillator Controller Dynamics with WECC Generic Models,” in *IEEE Power & Energy Society General Meeting (PES-GM)*, 2021, pp. 1–5 (cit. on p. 83).

[106] E. Rokrok, T. Qoria, A. Bruyere, B. Francois, and X. Guillaud, “Classification and Dynamic Assessment of Droop-Based Grid-Forming Control Schemes: Application in HVDC Systems,” *Electric Power Systems Research*, vol. 189, p. 106 765, 2020 (cit. on p. 83).

[107] J. Liu, Y. Miura, and T. Ise, “Comparison of Dynamic Characteristics Between Virtual Synchronous Generator and Droop Control in Inverter-Based Distributed Generators,” *IEEE Transactions on Power Electronics*, vol. 31, no. 5, pp. 3600–3611, 2016 (cit. on p. 83).

[108] S. D’Arco and J. A. Suul, “Equivalence of Virtual Synchronous Machines and Frequency-Droops for Converter-Based MicroGrids,” *IEEE Transactions on Smart Grid*, vol. 5, no. 1, pp. 394–395, 2014 (cit. on p. 83).

[109] D. Groß, M. Colombino, J.-S. Brouillon, and F. Dörfler, “The Effect of Transmission-Line Dynamics on Grid-Forming Dispatchable Virtual Oscillator Control,” *IEEE Transactions on Control of Network Systems*, vol. 6, no. 3, pp. 1148–1160, 2019 (cit. on p. 83).

[110] *ABB Central Inverters*, PVS980-58, 9AKK107492A3104 Rev.B, ABB, Nov. 2019 (cit. on p. 95).

[111] “Dynamic modeling,” in *Photovoltaic Power System*. John Wiley & Sons, Ltd, 2017, ch. 6, pp. 173–197. eprint: `https://onlinelibrary.wiley.com/doi/pdf/10.1002/9781119280408.ch6` (cit. on pp. 96, 97).

[112] L. C. Zanetta Júnior, *Fundamentos de sistemas elétricos de potência*. Editora Livraria da Física, 2006 (cit. on p. 119).

[113] K. Parsopoulos and M. Vrahatis, “Particle Swarm Optimization Method for Constrained Optimization Problem,” in Jan. 2002, vol. 76, pp. 214–220 (cit. on p. 161).

Appendix A

Detailed Tuning of IBR Controllers

Contents

A.1 Tuning a GFL controller

From (3.53), taking $\boldsymbol{p_c}$ as a subset of the parameter vector $\boldsymbol{p}$ where only control parameters are retained, we need to find a proper value for the following:

$$\boldsymbol{p_c} = \begin{bmatrix} \omega_{ff} & \omega_{iq} & {K_p}^{vdc} & {K_i}^{vdc} & {K_p}^{iq} & {K_i}^{iq} & {K_p}^{i} & {K_i}^{i} & {K_p}^{pll} & {K_i}^{pll} \end{bmatrix}^t \tag{A.1}$$

In order to tune $\boldsymbol{p_c}$, we consider the following tuning parameters:

$$\boldsymbol{p_t} = \begin{bmatrix} t_r^i & t_r^{v_{dc}} & t_r^{i_q} & t_r^{q_m} & t_r^{pll} \end{bmatrix}^t \tag{A.2}$$

As a rule, the feed-forward frequency is defined as $\omega_{ff} = 1\,\text{pu}$. For all other parameters, we use the set of time responses $\boldsymbol{p_t}$. In general, external loops must be considerably slower than internal loops, thus $t_r^i << \{t_r^{v_{dc}}, t_r^{i_q}\}$. For stability purposes, PLLs are also tuned to be slower than internal loops: $t_r^i << t_r^{pll}$. A detailed tuning method based on these time-response requirements is presented below.

A.1.1 Internal loop

Going back to (3.10), we may describe the dynamics of the output L filter as:

$$\frac{L_f}{\omega_b}\,\dot{i}_{f_d} = v_{dc}\,m_d - v_{f_d} - R_f\,i_{f_d} + \omega_{pll}\,L_f\,i_{f_q}$$

which we linearize around an operation point “0”:

$$\frac{L_f}{\omega_b}\,\Delta\dot{i}_{f_d} = \Delta v_{dc}\,m_{d0} + v_{dc0}\,\Delta m_d - \Delta v_{f_d} - R_f\,\Delta i_{f_d} + \omega_{pll_0}\,L_f\,\Delta i_{f_q} + \Delta\omega_{pll}\,L_f\,i_{f_q}$$

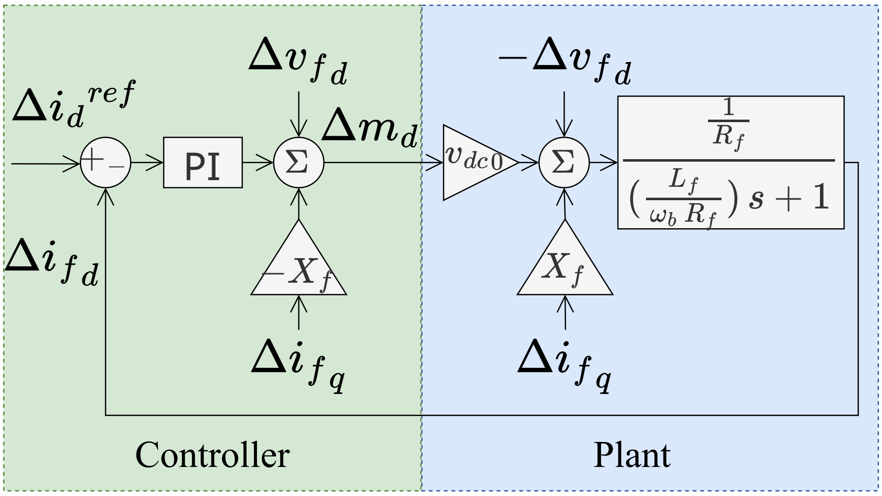

Figure A.1: Linearized GFL internal control loop

Since v_{dc} and ω_{pll} present slow variations with respect to the internal loop dynamics, we consider $\Delta v_{dc} \approx 0$ and $\Delta\omega_{pll} \approx 0$. Thus, rewriting in the Laplace domain:

$$\Delta i_{f_d}(s) = \frac{v_{dc0}}{\frac{L_f}{\omega_b}\,s + R_f}\,\Delta m_d(s) + \frac{1}{\frac{L_f}{\omega_b}\,s + R_f}\,(\omega_{pll_0}\,L_f\,\Delta i_{f_q}(s) - \Delta v_{f_d}(s)) \tag{A.3}$$

Our goal is to determine m_d in order to keep i_{f_d} under control, thus the second portion of (A.3) can be taken as a perturbation. Since we can measure i_{f_q} and v_{f_d}, it is easy to counteract the effect of this perturbation through a decoupling mechanism, as in Figure 3.4. This leads us to the following transfer function representing the plant:

$$H_p^i(s) = \frac{\Delta i_{f_d}(s)}{\Delta m_d(s)} = \frac{\frac{v_{dc0}}{R_f}}{(\frac{L_f}{\omega_b\,R_f})\,s + 1} \tag{A.4}$$

Here, $H_p^i(s)$ is in the form (3.139), so we can apply (3.146) to get K_p^i and K_i^i, considering:

$$K_0 = \frac{v_{dc0}}{R_f} \qquad \tau_0 = \frac{L_f}{\omega_b\,R_f} \qquad \zeta = 0.707$$

For $v_{dc0} = 1\,\text{pu}$, and taking $t_r^i = 10\,\text{ms}$, we get $K_p^i = 0.18$ and $K_i^i = 57.31$.

A.1.2 External loop

Active power control

Now going back to (3.12):

$$C_{dc}\,\dot{v_{dc}} = i_s - i_{f_d} m_d - i_{f_q} m_q$$

which we linearize around an operation point:

$$C_{dc}\,\Delta\dot{v}_{dc} = \Delta i_s - \Delta i_{f_d} m_{d0} - \Delta i_{f_q} m_{q0} - i_{f_{d0}} \Delta m_d - i_{f_{q0}} \Delta m_q$$

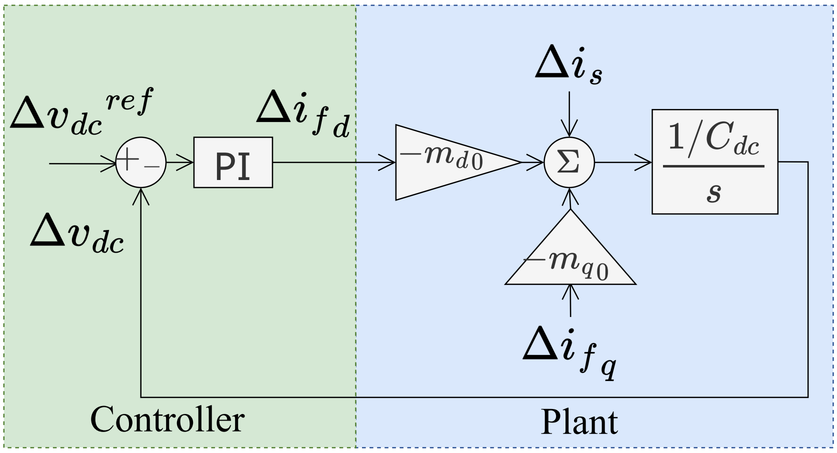

Figure A.2: Linearized GFL external control loop: active power

Once again, some simplifications are implied: $\Delta i_s \approx 0$ because the source is slow with respect to the v_{dc}-control dynamics. On the other hand, modulation signals $\{\Delta m_d, \Delta m_q\}$ are derivatives, with spikes that fade off in the time-scale of the external control [79], hence they may be ignored as well. Taking Δi_{f_q} as a disturbance, we get:

$$H_p^{v_{dc}}(s) = \frac{\Delta v_{dc}(s)}{\Delta i_{f_d}(s)} = -\frac{m_{d0}/C_{dc}}{s} \tag{A.5}$$

Because $H_p^{v_{dc}}(s)$ is in the form (3.147), we use (3.148) to get $K_p^{v_{dc}}$ and $K_i^{v_{dc}}$, with:

$$K_0 = -\frac{m_{d0}}{C_{dc}} \qquad\qquad \zeta = 0.707$$

For $m_{d0} = 1\,\text{pu}$, adopting $t_r^{v_{dc}} = 10\,t_r^i = 100\,\text{ms}$, we get $K_p^{v_{dc}} = -2.40$ and $K_i^{v_{dc}} = -72.09$.

Reactive power control

In order to keep the reactive power under control, one should find a current reference ${i_f}_q^{ref}$ which, when injected, leads the measured reactive power q_m to a setpoint q^{ref}, as shown in Figure 3.4. For this, we need a transfer function relating ${i_f}_q$ to q_m.

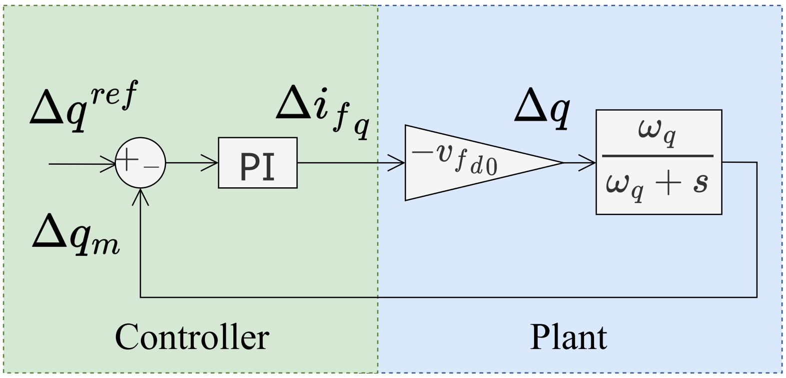

Figure A.3: Linearized GFL external control loop: reactive power

First, we take (3.29), assuming the PLL has already driven ${v_f}_q$ to zero:

$$q = {v_f}_q {i_f}_d - {v_f}_d {i_f}_q \approx -{v_f}_d {i_f}_q$$

Considering negligible variations in ${v_f}_d$, which is valid for a strong POI:

$$\Delta q(s) = -{v_f}_{d0} \Delta {i_f}_q(s) \tag{A.6}$$

Now considering a low-pass filter on the measurement of reactive power (3.27):

$$\Delta q_m(s) = \frac{1}{(1/\omega_{iq})s + 1} \Delta q(s) \tag{A.7}$$

Substituting (A.6) in (A.7), we get a transfer function for the plant:

$$H_p^{iq}(s) = \frac{\Delta q_m(s)}{\Delta {i_f}_q(s)} = \frac{-{v_f}_{d0}}{(1/\omega_{iq})s + 1} \tag{A.8}$$

Once again, we just have to apply (3.146) to get K_p^{iq} and K_i^{iq}, with:

$$K_0 = -{v_f}_{d0} \qquad \tau_0 = \frac{1}{\omega_{iq}} \qquad \zeta = 0.707$$

where

$$\frac{1}{\omega_{iq}} = \tau_{q_m} = \frac{1}{3} {t_r}^{q_m}$$

It is not mandatory for the control of reactive power to be as fast as the active power, but we may still adopt $t_r^{iq} = 100\,\mathrm{ms}$ to keep it considerably slower than the internal loop. Since t_r^{qm} is just a measurement delay for reactive power, it does not have a direct relation to t_r^{iq}; thus we adopt a value with similar order of magnitude: $t_r^{qm} = 90\,\mathrm{ms}$, which is enough to filter out high-frequency noise in reactive power measurements.

Therefore, taking $v_{f_{d0}} = 1\,\mathrm{pu}$, we get $K_p^{iq} = -0.80$ and $K_i^{iq} = -54.02$.

A.1.3 Phase-locked loop (PLL)

If v_f is a sinusoidal voltage, with peak value V_p and phase θ_f:

$$v_f(t) = V_p \cos\left(\theta_f(t)\right)$$

A dq transformation of $\mathrm{T}(\theta_{pll})$ (3.3) would yield:

$$v_{f_q}(t) = V_p \sin\left(\theta_f(t) - \theta_{pll}(t)\right)$$

Taking $V_p = 1\,\mathrm{pu}$, when θ_{pll} approaches θ_f:

$$v_{f_q}(t) \approx \theta_f(t) - \theta_{pll}(t)$$

Which, once linearized and expressed in Laplace domain, gives:

$$\Delta v_{f_q}(s) \approx \Delta\theta_f(s) - \Delta\theta_{pll}(s)$$

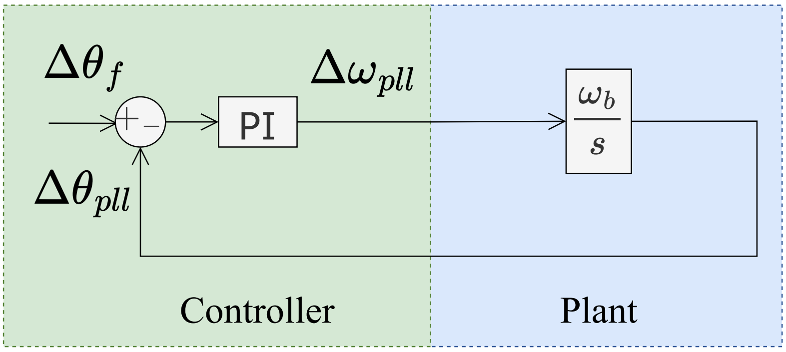

Figure A.4: Linearized PLL

Hence, taking feed-forward frequency ω_{ff} as a perturbation, we can consider our plant to be simply an integrator:

$$H_p^{pll}(s) = \frac{\Delta\theta_{pll}(s)}{\Delta\omega_{pll}(s)} = \frac{\omega_b}{s} \tag{A.9}$$

Our goal is to use a PI controller as a means to drive θ_{pll} toward a reference θ_f. Once again, we may just apply (3.148) to get K_p^{pll} and K_i^{pll}, considering:

$$K_0 = \omega_b \qquad \zeta = 0.707$$

A PLL can be tuned to have a wide range of time responses, from tens to hundreds of milliseconds [70]. For this dissertation, we mostly consider $t_r^{pll} = 50\,\text{ms}$, which results in $K_p^{pll} = 0.38$ and $K_i^{pll} = 22.93$.

A.2 Tuning a GFM controller

Taking $\boldsymbol{p_c}$ as a subset of $\boldsymbol{p}$ (3.83), this time for GFMs:

$$\boldsymbol{p_c} = \Big[\omega_{ff} \quad \omega_p \quad m_p \quad \omega_q \quad n_q \quad \omega_{tvr} \quad R_v^{tvr} \quad R_v \quad X_v \quad {K_p}^v \qquad K_i^{\,v} \quad {K_p}^i \quad K_i^{\,i} \quad {K_p}^{vdc} \quad {K_i}^{vdc}\Big]^t \tag{A.10}$$

In order to tune $\boldsymbol{p_c}$, we define the following tuning parameters:

$$\boldsymbol{p_t} = \Big[t_r^i \quad t_r^v \quad m_p \quad \omega_p \quad n_q \quad \omega_q \quad t_r^{v_{dc}} \qquad R_v^{tvr} \quad \omega_{tvr} \quad R_v \quad X_v\Big]^t \tag{A.11}$$

Unlike a GFL (A.11), where tuning parameters are reduced to only time-responses, a GFM requires some additional parameters, such as droop constants (m_p, n_q), cut-off frequencies for low and high-pass filters (ω_p, ω_q, ω_{tvr}), and virtual resistances or reactances (R_v^{tvr}, R_v, X_v). The tuning methodology for these parameters is presented below.

A.2.1 Internal loop

A GFM is expected to act as a voltage source, which inevitably requires some form of fast voltage control. We may thus follow similar steps as for the GFL internal loop, except we now apply them to the voltage, starting from (3.13),

$$\frac{C_f}{\omega_b}\,\dot{v_f}_d = {i_f}_d - {i_g}_d + \omega_{psl}\,C_f\,{v_f}_q$$

and linearizing it around an operation point:

$$\frac{C_f}{\omega_b}\,\Delta\dot{v_f}_d = \Delta{i_f}_d - \Delta{i_g}_d + \omega_{psl_0}\,C_f\,\Delta{v_f}_q + \Delta\omega_{psl}\,C_f\,{v_f}_{q0}$$

Since a relatively slow external control, namely a power-synchronization loop, is providing the frequency ω_{psl}, we may safely assume $\Delta\omega_{psl} \approx 0$ within the fast dynamics of $v_{f_{dq}}$ control. Hence, we obtain a transfer function $H_p^v(s)$,

$$H_p^v(s) = \frac{\Delta v_{f_d}(s)}{\Delta i_{f_d}(s)} = \frac{\omega_b / C_f}{s} \tag{A.12}$$

which leads to K_p^v and K_i^v via (3.148). Using $t_r^v = 10\,\text{ms}$, which is the same as t_r^i for our GFL, we get $K_p^v = 0.19$ and $K_i^v = 57.31$. However, unlike the GFL, here the internal loop will have an even faster loop within, in order to limit $i_{f_{dq}}$. Due to empirical small-signal stability constraints, this internal time-response has to be around 20 times faster than t_r^v, which is why we adopt $t_r^i = 0.5\,\text{ms}$. In order to compute gains related to this additional control loop, we follow the steps presented in Section A.1.1, getting $K_p^i = 3.81$ and $K_i^i = 22925$.

A.2.2 External loop

Active power control

There are multiple ways of tuning a power-synchronization loop. A most basic method is to just predefine a droop m_p and select a cut-off frequency ω_p for the low-pass filter in order to optimally reject measurement noise. Otherwise, we can also tune m_p and ω_p with the purpose of providing a certain damping and time-response, estimating a second-order transfer function that reproduces the low-frequency behavior of the inverter [70] [36]; in this case, m_p has significant implications on transient P-Q coupling, which may also be taken into account. However, this method requires information about the network for accurate tuning. A more generic method would consist of emulating the swing equation of SGs, tuning the GFM to provide an equivalent inertia H, and damping K_D [82] [66].

Because of its generic nature, we start from the last method, commonly named “Virtual Synchronous Machine” (VSM), following the steps from Section 4.1.3.2. Taking (3.57),

$$\dot{\gamma_p} = -\omega_p\,\gamma_p + \omega_p\,m_p\,(p^{ref} - p) \tag{A.13}$$

and defining a GFM frequency ω_{psl}, in pu:

$$\omega_{psl} = \gamma_p + \omega^{ref} \tag{A.14}$$

Substituting (A.14) in (A.13), we get:

$$2H\,\dot{\Delta\omega_r} = p^{ref} - p - K_D\,\Delta\omega_r \tag{A.15}$$

where $\Delta\omega_r = \omega_{psl} - \omega^{ref}$, and

$$H = \frac{1}{2\, m_p\, \omega_p} \qquad\qquad K_D = \frac{1}{m_p} \tag{A.16}$$

From (A.15), a PSL-based GFM is capable of emulating the classical swing equation of a synchronous generator as expressed in [1], where p^{ref} acts as the mechanical power and ω^{ref} as the rated value of the rotor angular velocity.

In order to assess the low-frequency behavior of this PSL, which translates into ignoring the grid dynamics, we may use the following closed-loop transfer function:

$$H_p^p(s) = \frac{\Delta p(s)}{\Delta p^{ref}(s)} = \frac{\frac{K_0}{\tau_0}}{s^2 + \frac{1}{\tau_0}\, s + \frac{K_0}{\tau_0}} \tag{A.17}$$

where

$$K_0 = m_p\, \omega_b\, H_{p\delta}(0) \qquad\qquad \tau_0 = \frac{1}{\omega_p} \tag{A.18}$$

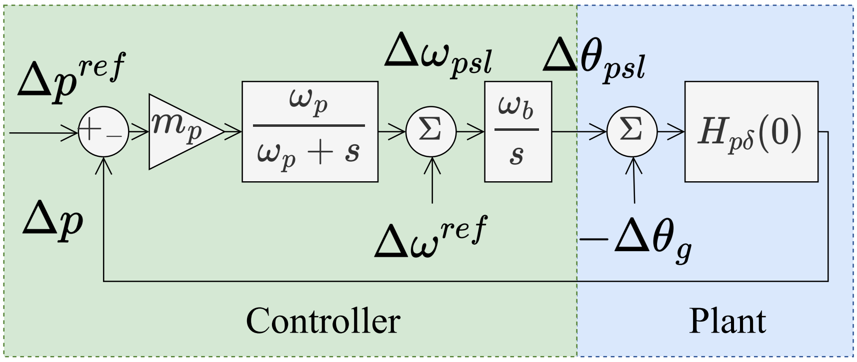

Figure A.5: Linearized GFM external control loop: active power

Here, $H_{p\delta}(0)$ is a transfer function between the phase angle $\delta = \theta_{psl} - \theta_g$ and the active power P transferred between $\bar{V}_f$ and $\bar{V}_g$, evaluated in steady-state $(s = 0)$[1]. Considering an impedance $\bar{Z}_c = R_c + j\, X_c$ between $\bar{V}_f$ and $\bar{V}_g$, $H_{p\delta}(0)$ will be equal to:

$$H_{p\delta}(0) = \frac{\text{SCR}}{\sqrt{1+\sigma_c^2}} (V_{f0}\, V_g\, \cos\delta_0 + \sigma_c\, V_{f0}\, V_g\, \sin\delta_0) = k^p\, \frac{\text{SCR}}{\sqrt{1+\sigma_c^2}} \tag{A.19}$$

Using (3.142) and (3.144), we get:

$$\zeta^2 = \frac{\omega_p}{4\, m_p\, \omega_b\, H_{p\delta}(0)} = \frac{\omega_p\, \sqrt{1+\sigma_c^2}}{4\, m_p\, \omega_b\, k^p\, \text{SCR}} \qquad\qquad t_r^p = \frac{6}{\omega_p} \tag{A.20}$$

---

[1] As explained in Section 4.1.3.2, $H_{p\delta}(0)$ acts as a virtual synchronizing torque K_S.

where SCR is the short-circuit ratio seen from the POI, i.e., SCR $= |1/\bar{Z}_c|$, and $\sigma_c = R_c/X_c$.

This means we can use ω_p to impose a time-response to the system, i.e., a delay between a change in active power and the corresponding change in frequency while regulating m_p in order to ensure a proper damping ratio. However, this ratio ζ depends on network conditions. Most notably, it increases with σ_c, which is usually higher in MV networks, but it decreases with SCR; in other words: a PSL-based GFM has worse damping in strong grids rather than weak grids. For strong networks, an optimal droop m_p for damping purposes may be too low for adequate power sharing among multiple GFMs. In practice, some additional control blocks may be employed in order to deal with this trade-off between damping and power sharing, usually involving a derivative action [70] [66]; nevertheless, for the sake of a more generic model, they have not been included in our work.

Finally, the simplest way to determine m_p is through grid requirements. Considering the droop $m_p = \Delta\omega/\Delta p$, for $\Delta p = 1\,\text{pu}$, a maximum frequency deviation $\Delta\omega$ allowed in most grid codes is around 5 %, so we could adopt m_p between 0.01 and 0.05. For the low-pass filter, it is common to tune it around 5 Hz, i.e., $\omega_p = 31.4\,\text{rad/s}$ [66], filtering out fundamental-frequency oscillations (ten times higher than the cut-off frequency).

Hence, based on empirical observations obtained via small-signal stability analysis, we adopted $m_p = 0.01$ and $\omega_p = 31.4\,\text{rad/s}$ for most of our simulations, which results in relatively low inertia constant $H = 1.6$ in comparison to SGs (4 - 10 [1]), and t_r^p around 200 ms, hence close to the time-response of GFL external loops.

Reactive power control

While active power control plays a key role in GFMs, since it serves as an SG-emulating synchronization mechanism, control of reactive power is generally neglected. Because GFMs are supposed to serve as voltage sources, it is possible to control the amplitude of v_f in a somewhat stiff manner, where the usual idea of regulating Q to attain a better V would be unnecessary. If strict P and Q control is the primary objective, a GFL could play this role in an MVDG, which is usually strong enough to ensure its operation. Another issue is the R/X ratio of MV networks, which leads to a strong steady-state coupling between P and Q, as discussed in Section 2.3.1; hence, controlling Q can have a negative impact on P, while sacrificing a strict steady-state voltage amplitude. This is why n_q is mostly taken as zero.

Nevertheless, if control of reactive power is still an objective, we may once again resort to grid requirements. Since $n_q = \Delta V/\Delta Q$, and a maximum acceptable ΔV is usually between 5 and 10 %, we may consider $n_q = 0.1$, for instance. For the low-pass filter, we consider it to be of the same order as ω_p, if P-Q coupling is low; or slower, if the grid is particularly resistive.

Ignoring both the internal control loop and grid dynamics, considerably faster than the external control, we get to an approximate closed-loop transfer function, of a first-order type:

$$H_p^q(s) = \frac{\Delta q(s)}{\Delta q^{ref}(s)} = \frac{K_0}{\tau_0\, s + 1} \tag{A.21}$$

where

$$K_0 = 1 - \frac{1}{n_q\, H_{qv}(0) + 1} \qquad \tau_0 = \frac{1}{\omega_q\,(n_q\, H_{qv}(0) + 1)} \tag{A.22}$$

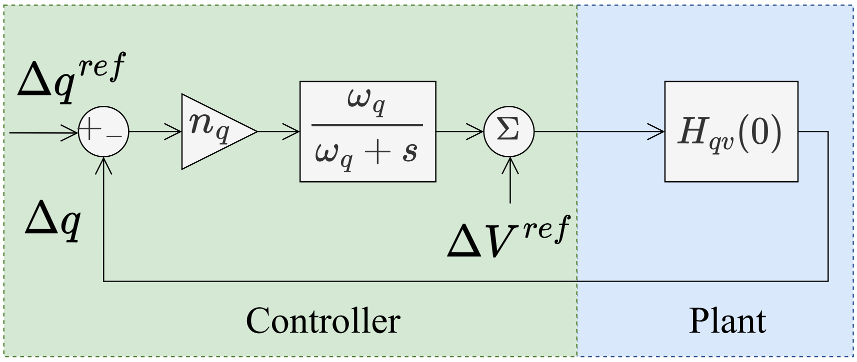

Figure A.6: Linearized GFM external control loop: reactive power

This time, $H_{qv}(0)$ is a transfer function between the voltage V_f and the reactive power Q transferred between $\bar{V_f}$ and $\bar{V_g}$, evaluated in steady-state ($s = 0$):

$$H_{qv}(0) = \frac{\text{SCR}}{\sqrt{1+\sigma_c^2}}(2V_{f0} - V_g\,\cos\delta_0 - \sigma_c\, V_g\,\sin\delta_0) = k^q\,\frac{\text{SCR}}{\sqrt{1+\sigma_c^2}} \tag{A.23}$$

Since $t_r = 3\,\tau_0$ for a first-order system:

$$t_r^q = \frac{3}{\omega_q + \omega_q\, n_q\, k^q\, \frac{\text{SCR}}{\sqrt{1+\sigma_c^2}}} \tag{A.24}$$

Hence, if there is enough information regarding short-circuit ratio and R/X, we may tune ω_q via (A.24) in order to achieve a given time-response.

In our case, opting for a GFM that provides a strict voltage level at its POI, we mostly ignore this control loop altogether, taking $n_q = 0$ and $\omega_q = 31.4\,\text{rad/s}$.

A.2.3 DC voltage control loop

Both internal and external control loops rely on a steady v_{dc}; otherwise, they would not be able to operate accurately, transferring DC-side oscillations to the AC-side or even rendering the GFM unstable. It is thus crucial to control v_{dc}. Nonetheless, a GFM has to inject a specific i_{sw} to the switches in order to comply with voltage and power control loops. This leaves us only one option to regulate v_{dc}, the source current i_s. An MPPT may still provide a reference for i_s, but only as a feed-forward value, which is to be added to the controlled portion of i_s. A GFM source has to be sufficiently flexible to ensure a stable v_{dc}, which may require sacrificing perfect compliance with an MPPT algorithm.

Starting from (3.12),

$$C_{dc}\,\dot{v_{dc}} = i_s - i_{f_d} m_d - i_{f_q} m_q = i_s - i_{sw}$$

and linearizing around an operation point “0”:

$$C_{dc}\,\Delta\dot{v}_{dc} = \Delta i_s - \Delta i_{sw}$$

Taking Δi_{sw} as a disturbance, we get:

$$\frac{\Delta v_{dc}(s)}{\Delta i_s(s)} = \frac{1/C_{dc}}{s} \tag{A.25}$$

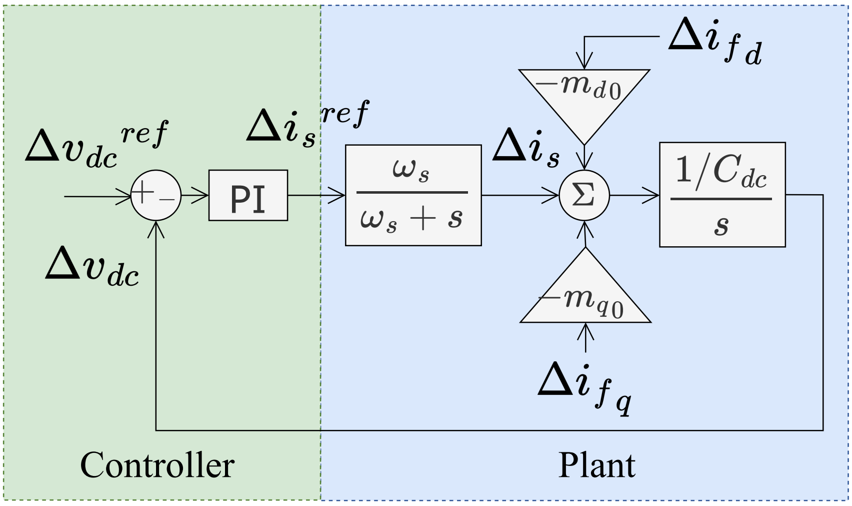

Figure A.7: Linearized GFM v_{dc} control loop

Including the dynamics of the source (3.17), we obtain an open-loop transfer function:

$$H_p^{v_{dc}}(s) = \frac{\Delta v_{dc}(s)}{\Delta i_s^{ref}(s)} = \frac{\omega_s}{s+\omega_s}\,\frac{1/C_{dc}}{s} \tag{A.26}$$

In order to simplify our tuning, we may consider an approximation that is only valid if the source is relatively fast with respect to the time-response of this control loop, i.e.,

$t_r^s \approx 3\,/\omega_s << t_r^{v_{dc}}$. In the case of PVs and BESS, there is no obvious reason to consider this source delay to be above a few milliseconds. Since we intend to take $t_r^{v_{dc}}$ in the order of tens of milliseconds, we may apply this approximation. In any case, a more complex controller (a PID, for instance) would allow for precise machine-side v_{dc} control even with slower sources, as long as the capacitor is large enough to act as an energy buffer and the source delay is properly estimated. Hence, we have:

$$H_p^{v_{dc}}(s) \approx \frac{1/C_{dc}}{s} \tag{A.27}$$

which allows us to obtain $K_p^{v_{dc}}$ and $K_i^{v_{dc}}$ via (3.148), with:

$$K_0 = \frac{1}{C_{dc}}, \qquad \zeta = 0.707$$

For most simulations, we take $t_r^{v_{dc}} = 15\,\text{ms}$, getting $K_p^{v_{dc}} = 16.02$ and $K_i^{v_{dc}} = 3204.1$.

A.2.4 Additional control loops

Active Damping: Transient virtual resistor (TVR)

As mentioned previously, it is common for GFMs to present certain additional loops, particularly for active damping of power oscillations.

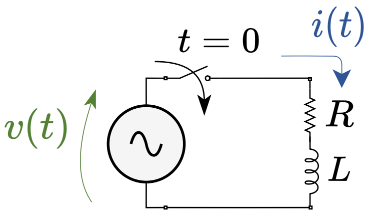

Figure A.8: RL circuit with sinusoidal input voltage

If the IBR is connected to an inductive grid, transient dynamics may be described by a simple RL circuit with input voltage $v(t) = V\cos(\omega_b\,t)$, expressed through the following differential equation:

$$\frac{d\,i(t)}{dt} + \frac{R}{L}\,i(t) = \frac{V\cos(\omega_b\,t)}{L} \tag{A.28}$$

We can find $i(t)$ by solving (A.28), denoting the initial condition as i_0:

$$i(t) = \frac{V}{R^2+\omega_b^2\,L^2}\left[R\cos(\omega_b\,t) + \omega_b\,L\sin(\omega_b\,t)\right] + \left(i_0 - \frac{V\,R}{R^2+\omega_b^2\,L^2}\right)e^{-\frac{R}{L}\,t} \tag{A.29}$$

Multiplying by v, we get an expression for instantaneous power:

$$p(t) = p_{ss}(t) + p_t(t) \tag{A.30}$$

where

$$p_{ss}(t) = \frac{1}{2}\,\frac{V^2}{R^2 + \omega_b^2\,L^2}\left[R - R\,\cos\left(2\omega_b\,t\right) + \omega_b\,L\,\sin\left(2\omega_b\,t\right)\right] \tag{A.31}$$

and

$$p_t(t) = e^{-\frac{R}{L}\,t}\left(V\,i_0 - \frac{V^2\,R}{R^2 + \omega_b^2\,L^2}\right) cos(\omega_b\,t) \tag{A.32}$$

From (A.32), we observe how the single-phase instantaneous power p has a transient portion p_t in the form of a damped sinusoid with a decay rate $\lambda = \frac{R}{L}$ and angular frequency $\omega_b = 2\pi\,50\,\text{rad/s}$, from which we get a damping ratio:

$$\zeta = \frac{R}{\sqrt{R^2 + \omega_b^2\,L^2}} \tag{A.33}$$

If a GFM is connected to an infinite-bus via $\overline{Z_c} = R_c + j\,\omega_g\,L_c$, it will observe fundamental-frequency power oscillations with a damping ratio of $\zeta = \frac{R_c}{\sqrt{R_c^2 + \omega_g^2\,L_c^2}}$, considering all variables in per-unit.

According to (A.33), resistive networks offer better damping, which is mostly an advantage in MV networks; if we are to consider POIs close to the substation, however, IBRs may perceive a strong and inductive grid instead. Hence, considering a "worst-case scenario" in which the only impedance between the IBR and the upstream network is a transformer $\overline{Z_c} \approx \overline{Z_t} \approx j\,\omega_g\,L_t$, for instance, we may need to increase R using a virtual resistor R_v^{tvr}. To avoid steady-state issues, this resistor must be coupled with a high-pass filter, ensuring it will only be active during transients. From (A.33), we may tune R_v^{tvr} using this formula:

$$R_v^{tvr} = \frac{\zeta\,L_t}{\sqrt{1-\zeta^2}} - R_t \tag{A.34}$$

Cut-off frequency ω_{tvr} for the high-pass filter must be far enough from the fundamental frequency, hence we may adopt $\omega_{tvr} = \omega_b/5$, as in [70]. For $\zeta = 0.5$ [70], and $L_t = 0.05\,\text{pu}$, we get $R_v^{tvr} = 0.028\,\text{pu}$, used for most of our simulations.

Implementation of active damping techniques is done as in Figure 3.5, where current measurements $i_{g_{dq}}$ are multiplied by R_v^{tvr} and subtracted from voltage references v_{dq}^{ref}. From the point-of-view of the IBR, this drop in its voltage reference acts as if there was an additional resistor in its POI.

Virtual impedance (VI)

A similar logic is used for the virtual impedance (VI), except we do not couple it with a high-pass filter, thus there is a steady-state effect. In MV networks, a VI may be used to emulate a lower R/X ratio at the POI [21], allowing for a better coupling between active power and voltage phase angle, which could improve the overall dynamics of the power-synchronization loop. This topic has already been explored in detail in Section 2.3.2, which tackled some static aspects of IBRs connected to MVDGs.

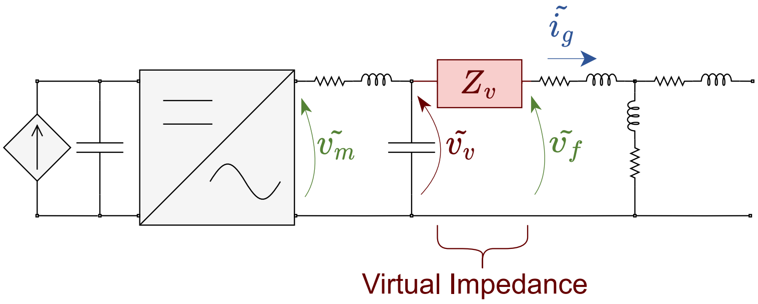

Figure A.9: IBR with virtual impedance

Adding a virtual impedance would imply a virtual voltage v_v. Because our PWM is still controlling v_f – the actual voltage – we must modify v_f^{ref} to take into account a virtual voltage drop from v_v. A GFM with VI will still behave as a voltage source, but only virtually stiff. This is summarized by the steady-state equation below:

$$\overline{V_f} = \overline{V_v} - (R_v + j\,X_v)\,\overline{I_g} \tag{A.35}$$

Rewriting (A.35) using reference values in dq:

$$v_{f_d}^{ref} + j\,v_{f_q}^{ref} = v_{v_d}^{ref} + j\,v_{v_q}^{ref} - (R_v + j\,X_v)\,(i_{g_d} + j\,i_{g_q}) \tag{A.36}$$

With $v_{v_d}^{ref} = V^{ref}$ and $v_{v_q}^{ref} = 0$:

$$v_{f_d}^{ref} = V^{ref} - R_v\,i_{g_d} + X_v\,i_{g_q} \tag{A.37}$$

$$v_{f_q}^{ref} = -X_v\,i_{g_d} - R_v\,i_{g_q} \tag{A.38}$$

In case we apply reactive power control and TVR, (A.37)-(A.38) will have additional terms, resulting in (3.66)-(3.67), as described in Section 3.2.2. Due to the drawbacks discussed in Section 2.3.2, most of our simulations were performed without a virtual impedance, hence with $R_v = X_v = 0$.

Appendix B

Simplified Modeling of IBRs connected to MVDGs

Contents

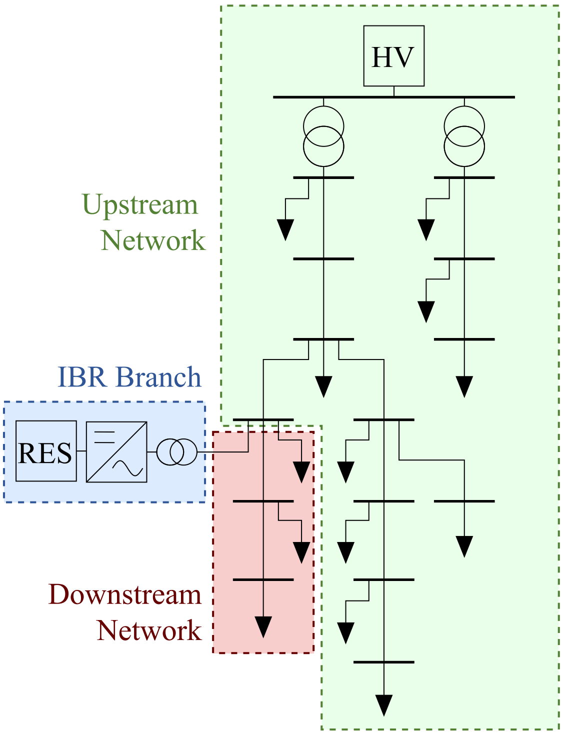

Figure B.1: Simplified representation of an IBR connected to an MVDG

At the beginning of Chapter 3, our third hypothesis for the modeling of IBRs connected to MVDGs claimed that aggregated passive elements can be replaced by RLC circuits in the context of SICDS, where EMT models are applied for the study of primarily slow phenomena. This was mostly intended at justifying the simplified representations of aggregated loads.

Considering also the proposition presented in Hypothesis 2, where loads are assumed to be passive, one may extend the notion of "aggregated load" to larger portions of the network, as illustrated in Figure B.1, encompassing both loads and lines. Once again, this simplification will lead to small-signal discrepancies with respect to the original system, but only in higher frequencies, while on the other hand, the number of states associated with the MVDG representation could be drastically reduced, facilitating the studies and enhancing computation time. Our usage of this approach is nonetheless limited to scenarios involving one or two IBRs.

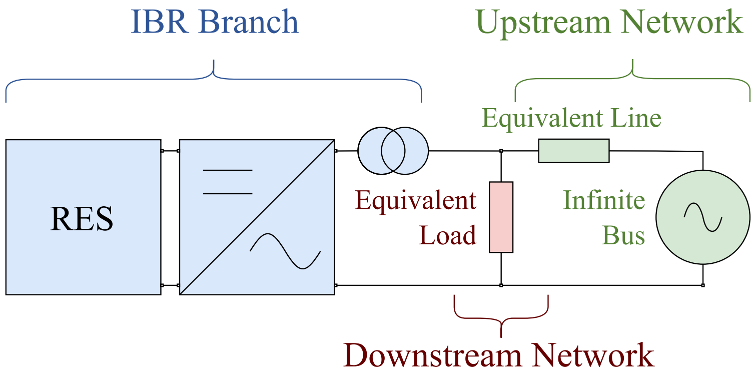

Figure B.2: Equivalent model of an IBR branch connected to an MVDG

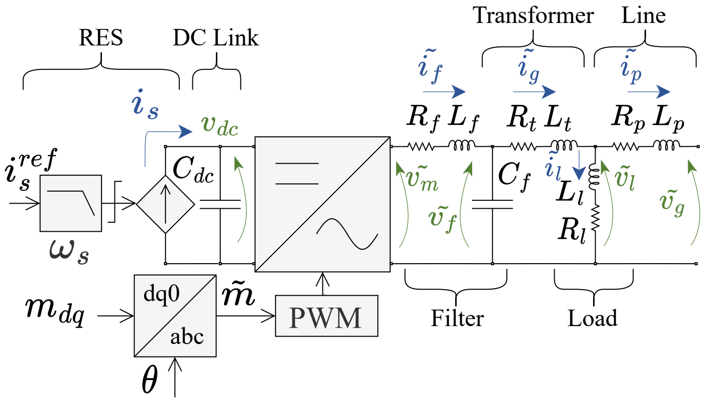

Figure B.3: Physical model of an IBR branch

B.1 "T-line" simplified model

Take the example of a single IBR connected to the benchmark MVDG from Figure 3.1. With the system partitioned into an IBR branch, and both an upstream and a downstream network, as in Figure B.1, leading to Figure B.2, the application of the aforementioned hypotheses results in the model from Figure B.3. This representation is suitable for the aggregated load, which is taken to be a passive constant-impedance load during the time scale of interest, ranging from a few milliseconds up to a few seconds.

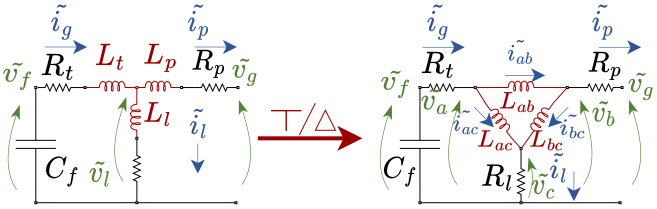

Figure B.4: Y-Δ transformation for “T-line” inductances

An equivalent line connecting the IBR transformer to the point of common coupling (PCC) is also represented as a bundled RL branch, where the capacitance is neglected. These three components forming a “T” will lead to a singularity if all inductor currents are taken as state variables, insofar as their linear combination is equal to zero. In order to avoid this, we may leave $\tilde{i}_p$ aside and take only $\{i_{g_d}, i_{g_q}\}$ and $\{i_{l\,d}, i_{l\,q}\}$ as state variables, obtaining their differential equations by applying a star-delta (Y-Δ) transformation on the inductances, as illustrated in Figure B.4. This leads to the following equations:

$$L_{ab} = \frac{L_\Delta}{L_l} \qquad L_{ac} = \frac{L_\Delta}{L_p} \qquad L_{bc} = \frac{L_\Delta}{L_t} \tag{B.1}$$

$$\frac{L_{ab}}{\omega_b}\,\dot{i}_{ab} = v_a - v_b \qquad \frac{L_{ac}}{\omega_b}\,\dot{i}_{ac} = v_a - v_c \qquad \frac{L_{bc}}{\omega_b}\,\dot{i}_{bc} = v_b - v_c \tag{B.2}$$

$$v_a = v_f - R_t\, i_g \qquad v_b = v_g + R_p\, i_p \qquad v_c = R_l\, i_l \tag{B.3}$$

$$\dot{i}_g = \dot{i}_{ab} + \dot{i}_{ac} \qquad \dot{i}_l = \dot{i}_{ac} + \dot{i}_{bc} \qquad \dot{i}_p = \dot{i}_{ab} - \dot{i}_{bc} \tag{B.4}$$

where

$$L_\Delta = L_t\, L_p + L_t\, L_l + L_p\, L_l \tag{B.5}$$

Taking (B.1)-(B.5) and applying a Park transformation on $\{\tilde{i}_g, \tilde{i}_l\}$, we finally obtain a set of four differential equations to represent the “T” line:

$$\frac{1}{\omega_b}\,\dot{i}_{g_d} = \frac{(L_p + L_l)}{L_\Delta}\,v_{f\,d} - \frac{L_l}{L_\Delta}\,v_{g_d} - \frac{R_{\alpha_g}}{L_\Delta}\,i_{l\,d} - \frac{R_{\beta g}}{L_\Delta}\,i_{g_d} + \omega_{ibr}\,i_{g_q} \tag{B.6}$$

$$\frac{1}{\omega_b}\,\dot{i}_{g_q} = \frac{(L_p + L_l)}{L_\Delta}\,v_{f\,q} - \frac{L_l}{L_\Delta}\,v_{g_q} - \frac{R_{\alpha_g}}{L_\Delta}\,i_{l\,q} - \frac{R_{\beta g}}{L_\Delta}\,i_{g_q} - \omega_{ibr}\,i_{g_d} \tag{B.7}$$

$$\frac{1}{\omega_b}\,\dot{i}_{l\,d} = \frac{L_p}{L_\Delta}\,v_{f\,d} + \frac{L_t}{L_\Delta}\,v_{g_d} - \frac{R_{\alpha l}}{L_\Delta}\,i_{g_d} - \frac{R_{\beta l}}{L_\Delta}\,i_{l\,d} + \omega_{ibr}\,i_{l\,q} \tag{B.8}$$

$$\frac{1}{\omega_b}\,\dot{i}_{l\,q} = \frac{L_p}{L_\Delta}\,v_{f\,q} + \frac{L_t}{L_\Delta}\,v_{g_q} - \frac{R_{\alpha l}}{L_\Delta}\,i_{g_q} - \frac{R_{\beta l}}{L_\Delta}\,i_{l\,q} - \omega_{ibr}\,i_{l\,d} \tag{B.9}$$

with

$$R_{\alpha g} = L_p\,R_l - L_l\,R_p \qquad R_{\alpha l} = L_p\,R_t - L_t\,R_p \tag{B.10}$$

$$R_{\beta g} = L_p\,R_t + L_l\,R_t + L_l\,R_p \qquad R_{\beta l} = L_t\,R_p + L_t\,R_l + L_p\,R_l \tag{B.11}$$

Taking all aforementioned equations into account, namely (B.6)-(B.9), in addition to the differential equations from Section 3.1, i.e., (3.10)-(3.17), it is possible to build a state-space model for the physical components in an IBR *branch*, as shown in Figure B.3, with state vector $\boldsymbol{x}$, input vector $\boldsymbol{u}$, and parameter vector $\boldsymbol{p}$:

$$\boldsymbol{x} = \begin{bmatrix} i_{f_d} & i_{f_q} & v_{dc} & v_{f_d} & v_{f_q} & i_s & i_{g_d} & i_{g_q} & i_{l_d} & i_{l_q} \end{bmatrix}^t \tag{B.12}$$

$$\boldsymbol{u} = \begin{bmatrix} i_s^{ref} & m_d & m_q & \theta_{ibr} & \omega_{ibr} & v_{g_d}^g & v_{g_q}^g & \theta_g \end{bmatrix}^t \tag{B.13}$$

$$\boldsymbol{p} = \begin{bmatrix} \omega_b & R_f & L_f & C_f & R_t & L_t & R_l & L_l & R_p & L_p & C_{dc} & \omega_s \end{bmatrix}^t \tag{B.14}$$

This state-space, in conjunction with the one representing the IBR controller, could provide $\tilde{i_p}$ and $\tilde{v_l}$ as outputs, so that multiple IBR branches get grouped into a single state-space, as in Figure B.5. These variables would have to be rotated onto a global dq frame, with phase θ_g, giving us an output vector $\boldsymbol{y}$ (B.15). If there is no filter capacitor, $i_{f_{dq}}$ must replace $i_{g_{dq}}$. As in Chapter 3, θ_{ibr} is either θ_{pll}, in case of a GFL, or θ_{psl}, in case of a GFM.

$$\boldsymbol{y} = \begin{bmatrix} i_{p_d}^g \\ i_{p_q}^g \\ v_{l_d}^g \\ v_{l_q}^g \end{bmatrix} = \begin{bmatrix} \boldsymbol{R}(\theta_{ibr} - \theta_g) & \boldsymbol{0_2} \\ \boldsymbol{0_2} & \boldsymbol{R}(\theta_{ibr} - \theta_g) \end{bmatrix} \begin{bmatrix} i_{g_d} - i_{l_d} \\ i_{g_q} - i_{l_q} \\ v_{l_d} \\ v_{l_q} \end{bmatrix} \tag{B.15}$$

In order to compute (B.15), we get $v_{l_{dq}}$ by substituting (B.8)-(B.9) in (B.16)-(B.17).

$$v_{l_d} = \frac{L_l}{\omega_b}\,\dot{i}_{l_d} + R_l\,i_{l_d} - \omega_{pll}\,L_l\,i_{l_q} \tag{B.16}$$

$$v_{l_q} = \frac{L_l}{\omega_b}\,\dot{i}_{l_q} + R_l\,i_{l_q} + \omega_{pll}\,L_l\,i_{l_d} \tag{B.17}$$

B.2 SSAT applied to the simplified model

Going back to the state-space association technique presented in Section 3.5, it is possible to assemble multiple IBR branches into a single state-space, as in Figure B.5. Because there is no full representation of the MVDG, this procedure is significantly simpler than the one from Section 3.5.2, although we shall reiterate that they are only statically equivalent if there are at most two IBRs in the system. For more IBRs, we should resort to either the full representation of the MVDG or a different simplified representation, with more nodes. Adopting thus a case study with a generic number of n IBR branches, a step-by-step procedure to obtain the $\boldsymbol{A}$ matrix is described below.

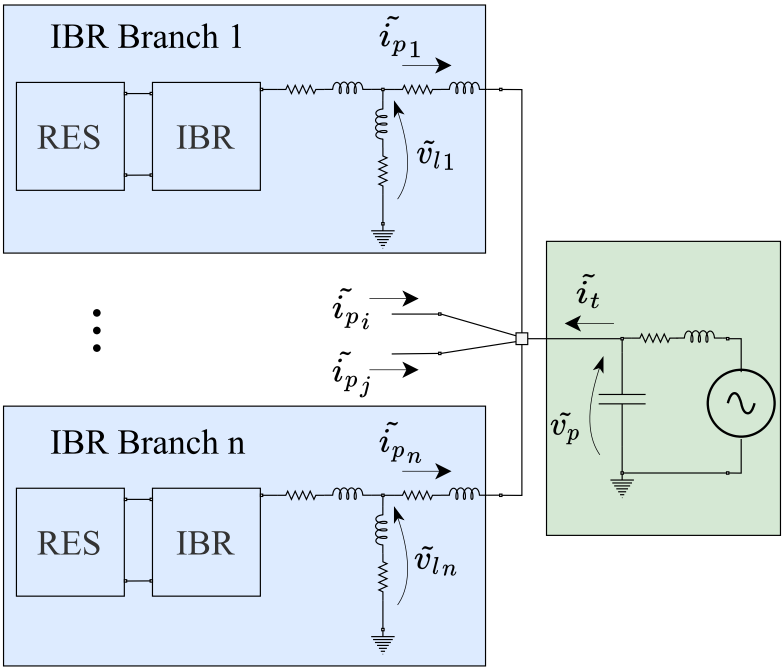

Figure B.5: SSAT applied to simplified IBR branches

In order to build a global state-space for this case study, we consider the n IBR branches connected to a common node, which also includes the upstream network, as in Figure B.5. Here, for each IBR branch k, with $k \in [1, n]$, we have:

$$\boldsymbol{u_k} = \begin{bmatrix} \boldsymbol{u_k}^{\boldsymbol{s}} \\ \boldsymbol{u^g} \end{bmatrix} \qquad \boldsymbol{y_k} = \begin{bmatrix} \boldsymbol{i_k}^{\boldsymbol{g}} \\ \boldsymbol{v_k}^{\boldsymbol{g}} \end{bmatrix} \tag{B.18}$$

where the k^{th} input vector $\boldsymbol{u_k}$ is subdivided into two components: setpoint vector $\boldsymbol{u_k^s}$, unique for each IBR, according to its operation mode (GFL or GFM), and grid input vector $\boldsymbol{u^g}$, same for all IBR branches. For convenience, output vector $\boldsymbol{y_k}$ may also be subdivided into a current vector $\boldsymbol{i_k^g}$ and a voltage vector $\boldsymbol{v_k^g}$. All of these are described below:

$$\boldsymbol{u_k^s} = \begin{bmatrix} i_s^{ref} & v_{dc}{}^{ref} & q^{ref} \end{bmatrix}^t \qquad \text{if GFL} \tag{B.19}$$

$$\boldsymbol{u_k^s} = \begin{bmatrix} i_s^{ref} & p^{ref} & V^{ref} & q^{ref} & v_{dc}{}^{ref} \end{bmatrix}^t \qquad \text{if GFM} \tag{B.20}$$

$$\boldsymbol{u^g} = \begin{bmatrix} v_{g}{}_d^g & v_{g}{}_q^g & \theta_g \end{bmatrix}^t \tag{B.21}$$

$$\boldsymbol{i_k^g} = \begin{bmatrix} i_{p}{}_{dk}^g & i_{p}{}_{qk}^g \end{bmatrix}^t \tag{B.22}$$

$$\boldsymbol{v_k^g} = \begin{bmatrix} v_{l}{}_{dk}^g & v_{l}{}_{qk}^g \end{bmatrix}^t \tag{B.23}$$

A similar representation may be adopted for the upstream network:

$$\boldsymbol{u_{up}} = \begin{bmatrix} \boldsymbol{u_{up}^s} \\ \boldsymbol{u_{up}^g} \end{bmatrix} \qquad\qquad \boldsymbol{y_{up}} = \begin{bmatrix} v_{g}{}_d^g \\ v_{g}{}_q^g \\ \theta_g \end{bmatrix} \tag{B.24}$$

where

$$\boldsymbol{u_{up}^s} = \begin{bmatrix} \omega_g & V_{up} \end{bmatrix}^t \tag{B.25}$$

$$\boldsymbol{u_{up}^g} = \begin{bmatrix} i_{t}{}_d^g & i_{t}{}_q^g \end{bmatrix}^t \tag{B.26}$$

From (B.21) and (B.24) we observe that the grid input vector for each IBR branch is identical to the upstream output vector: $\boldsymbol{u^g} = \boldsymbol{y_{up}}$.

Finally, we can obtain an upstream grid input vector $\boldsymbol{u_{up}^g}$ as a function of IBR output currents $\boldsymbol{i_k^g}$ by applying Kirchhoff's first law to the common node:

$$i_{t}{}_d^g = -\sum_{k=1}^{n} i_{p}{}_{dk}^g \qquad i_{t}{}_q^g = -\sum_{k=1}^{n} i_{p}{}_{qk}^g \tag{B.27}$$

We may thus rewrite $\boldsymbol{u_{up}^g}$ as:

$$\boldsymbol{u_{up}^g} = \begin{bmatrix} i_{t}{}_d^g \\ i_{t}{}_q^g \end{bmatrix} = \begin{bmatrix} \begin{pmatrix} -1 & 0 \\ 0 & -1 \end{pmatrix} & \cdots & \begin{pmatrix} -1 & 0 \\ 0 & -1 \end{pmatrix} \end{bmatrix} \begin{bmatrix} \begin{pmatrix} i_{p}{}_{d1}^g \\ i_{p}{}_{q1}^g \end{pmatrix} \\ \vdots \\ i_n^g \end{bmatrix}$$

or even:

$$\boldsymbol{u^g_{up}} = \begin{bmatrix} \begin{pmatrix} -1 & 0 & 0 & 0 \\ 0 & -1 & 0 & 0 \end{pmatrix} & \cdots & \begin{pmatrix} -1 & 0 & 0 & 0 \\ 0 & -1 & 0 & 0 \end{pmatrix} \end{bmatrix} \begin{bmatrix} \begin{pmatrix} i_{p_{d1}}^{\,g} \\ i_{p_{q1}}^{\,g} \\ v_{l_{d1}}^{\,g} \\ v_{l_{q1}}^{\,g} \end{pmatrix} \\ \vdots \\ \boldsymbol{y_n} \end{bmatrix} \tag{B.28}$$

In short, $\boldsymbol{u^g_{up}}$ is a function of IBR branch outputs $\boldsymbol{y_k}$, defined in (B.15) and (B.18):

$$\boldsymbol{u^g_{up}} = \begin{bmatrix} \begin{pmatrix} -\boldsymbol{I} & \boldsymbol{0} \end{pmatrix} & \cdots & \begin{pmatrix} -\boldsymbol{I} & \boldsymbol{0} \end{pmatrix} \end{bmatrix} \begin{bmatrix} \boldsymbol{y_1} \\ \vdots \\ \boldsymbol{y_n} \end{bmatrix} \tag{B.29}$$

Hence, there is a relation between IBR branch inputs and upstream outputs, namely $\boldsymbol{u^g} = \boldsymbol{y_{up}}$, as well as a relation between IBR branch outputs and upstream inputs, as in (B.29). Adding to these the differential and algebraic equations from each state-space, and linearizing them around an equilibrium point, we may write down an open-loop state-space formulation of the global system according to (3.109)-(3.110):

$$\boldsymbol{\Delta\dot{x}_L} = \boldsymbol{A_L}\,\boldsymbol{\Delta x_L} + \boldsymbol{B_L}\,\boldsymbol{\Delta u_L} \tag{B.30}$$

$$\boldsymbol{\Delta y_L} = \boldsymbol{C_L}\,\boldsymbol{\Delta x_L} + \boldsymbol{D_L}\,\boldsymbol{\Delta u_L} \tag{B.31}$$

where, for subscripts “1” to “n” designating IBR branches and “up” designating the upstream network,

$$\boldsymbol{\Delta x_L} = \begin{bmatrix} \boldsymbol{\Delta x_1} \\ \boldsymbol{\Delta x_2} \\ \vdots \\ \boldsymbol{\Delta x_n} \\ \boldsymbol{\Delta x_{up}} \end{bmatrix} \qquad \boldsymbol{\Delta u_L} = \begin{bmatrix} \boldsymbol{\Delta u_1} \\ \boldsymbol{\Delta u_2} \\ \vdots \\ \boldsymbol{\Delta u_n} \\ \boldsymbol{\Delta u_{up}} \end{bmatrix} \qquad \boldsymbol{\Delta y_L} = \begin{bmatrix} \boldsymbol{\Delta y_1} \\ \boldsymbol{\Delta y_2} \\ \vdots \\ \boldsymbol{\Delta y_n} \\ \boldsymbol{\Delta y_{up}} \end{bmatrix} \tag{B.32}$$

For IBR branch 1, we may express $\boldsymbol{\Delta u_1}$ as:

$$\boldsymbol{\Delta u_1} = \begin{bmatrix} \boldsymbol{\Delta u_1^s} \\ \boldsymbol{\Delta u^g} \end{bmatrix} = \begin{bmatrix} \boldsymbol{\Delta u_1^s} \\ \boldsymbol{0} \end{bmatrix} + \begin{bmatrix} \boldsymbol{0} \\ \boldsymbol{\Delta u^g} \end{bmatrix} = \begin{bmatrix} \boldsymbol{\Delta u_1^s} \\ \boldsymbol{0} \end{bmatrix} + \begin{bmatrix} \boldsymbol{0} \\ \boldsymbol{\Delta y_{up}} \end{bmatrix}$$

leading to:

$$\boldsymbol{\Delta u_1} = \begin{bmatrix} \boldsymbol{I} & \boldsymbol{0} & \dots & \boldsymbol{0} \\ \boldsymbol{0} & \boldsymbol{0} & \dots & \boldsymbol{0} \end{bmatrix} \begin{bmatrix} \boldsymbol{\Delta u_1^s} \\ \boldsymbol{\Delta u_2^s} \\ \vdots \\ \boldsymbol{\Delta u_n^s} \\ \boldsymbol{\Delta u_{up}^s} \end{bmatrix} + \begin{bmatrix} \boldsymbol{0} & \boldsymbol{0} & \dots & \boldsymbol{0} & \boldsymbol{0} \\ \boldsymbol{0} & \boldsymbol{0} & \dots & \boldsymbol{0} & \boldsymbol{I} \end{bmatrix} \begin{bmatrix} \boldsymbol{\Delta y_1} \\ \boldsymbol{\Delta y_2} \\ \vdots \\ \boldsymbol{\Delta y_n} \\ \boldsymbol{\Delta y_{up}} \end{bmatrix} \tag{B.33}$$

Similarly, for the upstream network, we may rewrite $\boldsymbol{\Delta u_{up}}$ as:

$$\boldsymbol{\Delta u_{up}} = \begin{bmatrix} \boldsymbol{\Delta u_{up}^s} \\ \boldsymbol{\Delta u_{up}^g} \end{bmatrix} = \boldsymbol{F_{up}} \begin{bmatrix} \boldsymbol{\Delta u_1^s} \\ \vdots \\ \boldsymbol{\Delta u_n^s} \\ \boldsymbol{\Delta u_{up}^s} \end{bmatrix} + \boldsymbol{G_{up}} \begin{bmatrix} \boldsymbol{\Delta y_1} \\ \vdots \\ \boldsymbol{\Delta y_n} \\ \boldsymbol{\Delta y_{up}} \end{bmatrix} \tag{B.34}$$

where, computing $\boldsymbol{\Delta u_{up}^g}$ from (B.29):

$$\boldsymbol{F_{up}} = \begin{bmatrix} \boldsymbol{0} & \dots & \boldsymbol{0} & \boldsymbol{I} \\ \boldsymbol{0} & \dots & \boldsymbol{0} & \boldsymbol{0} \end{bmatrix} \qquad \boldsymbol{G_{up}} = \begin{bmatrix} \begin{pmatrix} \boldsymbol{0} & \boldsymbol{0} \end{pmatrix} & \dots & \begin{pmatrix} \boldsymbol{0} & \boldsymbol{0} \end{pmatrix} & \begin{pmatrix} \boldsymbol{0} & \boldsymbol{0} \end{pmatrix} \\ \begin{pmatrix} -\boldsymbol{I} & \boldsymbol{0} \end{pmatrix} & \dots & \begin{pmatrix} -\boldsymbol{I} & \boldsymbol{0} \end{pmatrix} & \begin{pmatrix} \boldsymbol{0} & \boldsymbol{0} \end{pmatrix} \end{bmatrix} \tag{B.35}$$

Generalizing (B.33) for n IBRs and grouping it together with (B.34):

$$\begin{bmatrix} \boldsymbol{\Delta u_1} \\ \vdots \\ \boldsymbol{\Delta u_n} \\ \boldsymbol{\Delta u_{up}} \end{bmatrix} = \begin{bmatrix} \boldsymbol{\Delta u_1^s} \\ \boldsymbol{\Delta u_1^g} \\ \vdots \\ \boldsymbol{\Delta u_n^s} \\ \boldsymbol{\Delta u_n^g} \\ \boldsymbol{\Delta u_{up}^s} \\ \boldsymbol{\Delta u_{up}^g} \end{bmatrix} = \boldsymbol{F} \begin{bmatrix} \boldsymbol{\Delta u_1^s} \\ \boldsymbol{\Delta u_2^s} \\ \vdots \\ \boldsymbol{\Delta u_n^s} \\ \boldsymbol{\Delta u_{up}^s} \end{bmatrix} + \boldsymbol{G} \begin{bmatrix} \boldsymbol{\Delta y_1} \\ \vdots \\ \boldsymbol{\Delta y_n} \\ \boldsymbol{\Delta y_{up}} \end{bmatrix} \tag{B.36}$$

where

$$\boldsymbol{F} = \begin{bmatrix} \boldsymbol{I} & \boldsymbol{0} & \dots & \boldsymbol{0} & \boldsymbol{0} \\ \boldsymbol{0} & \boldsymbol{0} & \dots & \boldsymbol{0} & \boldsymbol{0} \\ \vdots & \vdots & \ddots & \vdots & \vdots \\ \boldsymbol{0} & \boldsymbol{0} & \dots & \boldsymbol{I} & \boldsymbol{0} \\ \boldsymbol{0} & \boldsymbol{0} & \dots & \boldsymbol{0} & \boldsymbol{0} \\ \boldsymbol{0} & \boldsymbol{0} & \dots & \boldsymbol{0} & \boldsymbol{I} \\ \boldsymbol{0} & \boldsymbol{0} & \dots & \boldsymbol{0} & \boldsymbol{0} \end{bmatrix} \qquad \boldsymbol{G} = \begin{bmatrix} \boldsymbol{0} & \dots & \boldsymbol{0} & \boldsymbol{0} \\ \boldsymbol{0} & \dots & \boldsymbol{0} & \boldsymbol{I} \\ \vdots & \vdots & \vdots & \vdots \\ \boldsymbol{0} & \dots & \boldsymbol{0} & \boldsymbol{0} \\ \boldsymbol{0} & \dots & \boldsymbol{0} & \boldsymbol{I} \\ \begin{pmatrix} \boldsymbol{0} & \boldsymbol{0} \end{pmatrix} & \dots & \begin{pmatrix} \boldsymbol{0} & \boldsymbol{0} \end{pmatrix} & \begin{pmatrix} \boldsymbol{0} & \boldsymbol{0} \end{pmatrix} \\ \begin{pmatrix} -\boldsymbol{I} & \boldsymbol{0} \end{pmatrix} & \dots & \begin{pmatrix} -\boldsymbol{I} & \boldsymbol{0} \end{pmatrix} & \begin{pmatrix} \boldsymbol{0} & \boldsymbol{0} \end{pmatrix} \end{bmatrix} \tag{B.37}$$

As we can see, (B.36) is in the form $\boldsymbol{\Delta u_L} = \boldsymbol{F}\,\boldsymbol{\Delta u} + \boldsymbol{G}\,\boldsymbol{\Delta y_L}$ (3.114), where closed-loop input vector $\boldsymbol{u}$ assembles all setpoints in the system:

$$\boldsymbol{u} = \begin{bmatrix} \boldsymbol{u_1^s} & \dots & \boldsymbol{u_n^s} & \boldsymbol{u_{up}^s} \end{bmatrix}^t \tag{B.38}$$

Following the same steps from Section 3.5, given that we have $\boldsymbol{F}$ and $\boldsymbol{G}$ from (B.36), we may easily obtain the state-matrix $\boldsymbol{A}$ using (3.121). Since this is the only matrix required for small signal stability, further steps are unnecessary.

Appendix C

Case Study with more IBRs

In order to provide an illustration of the methodology from Section 4.3 applied to a more complex system, we may repeat the same steps using a "multi-IBR" configuration with, for instance, five IBRs connected to the network from Figure 3.1 according to Table C.1. GFLs are connected to relatively weak nodes, while GFMs are connected to strong nodes in close proximity to each other. According to Sections 4.1.1 and 4.2.1, these conditions yield an instability-prone scenario, particularly interesting for our purposes. To avoid an unrealistic generation/load ratio, the total load has been raised to 5 pu, matching the total IBR production, while maintaining the same proportions as in the original benchmark MVDG.

IBR	IBR 1	IBR 2	IBR 3	IBR 4	IBR 5
Type	GFM	GFM	GFL	GFL	GFL
Node	3	4	7	10	11

Table C.1: Scenario with five IBRs

Given that we have already explored GFL-GFL and GFM-GFM interactions in detail, it is unnecessary to explore every single 5-IBR configuration[1]; our analysis is thus restricted to the configuration presented in Table C.1. It is worth noting that, whereas the 2-IBR configuration in Section 4.2 served as a means to investigate the physical origin of IBR interactions *in general*, the goal in this Appendix is more practical: to understand the fundamental interactions *in this specific scenario* and reapply the methodology from Section 4.3 to improve the parameter bounds for SICDS.

Although we have so far considered three key parameters for GFMs, as in (4.26), Section 4.3 showed little effect of $\tau_{v_{dc}}$ compared to the other parameters, hence it is omitted in this appendix, fixed at $\tau_{v_{dc}} = 5\,\text{ms}$. GFMs are represented by m_p and ω_p, exclusively. Using the same initial bounds as in Table 4.5, a set of extreme configurations are given in Table C.2, extracted once again from the worst-case boundary configurations. In this 5-IBR system, each GFM has two parameters while each GFL has three, amounting to four possible ECs

---

[1] In addition to this, we are also assuming that, in practice, DSOs will probably know which among the major IBRs are configured as GFL or GFM, dispensing the need to analyze all possible configurations.

for GFMs and eight for GFLs, since each EC presupposes that every parameter is either at its lower or upper bound. Picking four[2] among these twelve possibilities considerably reduces the complexity of the problem, if every possible combination between ECs is to be studied in detail (as was done in Figure 4.37, for instance).

Par.	GFLA	GFLB	GFLC	Par.	GFMA	GFMB	GFMC
$t_r^{v_{dc}}$	100 ms	220 ms	220 ms	m_p	0.01	0.05	0.05
$t_r^{i_q}$	100 ms	1000 ms	50 ms	ω_p	31.4 rd/s	3.14 rd/s	62.8 rd/s
t_r^{pll}	50 ms	1000 ms	20 ms				

Table C.2: Extreme IBR configurations for five IBRs

Most of the low-damping situations in this system stem from a combination of these ECs, where the worst among them, as indicated in Table C.3 and Figure C.1a, is a configuration with two high-droop GFMs and three slow-acting GFLs (high $t_r^{v_{dc}}$), leading to negative damping ($-4.2\,\%$), i.e., an unstable scenario. This suggests a major role played by both m_p and $t_r^{v_{dc}}$, compelling us to perform multi-parameter sensitivities to investigate their impact, as will be done in Figures C.3a and C.4a. Unlike at the end of Section 4.3, where all combinations between ECs were exposed in the same plot (Figures 4.37 and 4.38), here, in a 5-dimensional problem, we are compelled to pick some of the most illustrative combinations, as in Table C.3.

Combination	Min. ζ	Frequency	IBR 1	IBR 2	IBR 3	IBR 4	IBR 5
1	$-4.2\,\%$	3.14 Hz	GFMB	GFMC	GFLB	GFLC	GFLC
2	$-4.1\,\%$	3.10 Hz	GFMB	GFMC	GFLC	GFLC	GFLC
3	$-1.2\,\%$	3.14 Hz	GFMB	GFMC	GFLB	GFLB	GFLA
4	$0.7\,\%$	3.13 Hz	GFMB	GFMA	GFLB	GFLC	GFLC

Table C.3: Selected combinations between a set of IBR configurations

Going back to the relevance of m_p and $t_r^{v_{dc}}$, we could get to the same conclusion by observing the root cause of the most unstable situation displayed in Figure C.1a. As per the eigenvalue map in Figure C.1b, mode $\lambda_{126,127}$ is responsible for this situation. Examining the participation matrix in Figure C.2, this mode is clearly related to the external P-control loops in all IBRs with the exception of IBR 2. The first IBR is a GFM, for which the states θ and γ_P participate in mode $\lambda_{126,127}$, both of which are associated with m_p and ω_p. It is possible that a fast-acting droop control, i.e., one with low virtual inertia (high ω_p), is keeping IBR 2 out of this mode. IBRs 3 to 5 are GFLs with maximal $t_r^{v_{dc}}$, participating in mode $\lambda_{126,127}$ through states v_{dc} and $\gamma_{v_{dc}}$, evidently related to $t_r^{v_{dc}}$. This confirms our aforementioned assumption, a re-tuning of m_p and $t_r^{v_{dc}}$ could solve this instability.

Note that this GFL/GFM interaction in slow-acting GFLs was already discussed in Sec-

---

[2] Disregarding "GFLA" and "GFMA", which are standard configurations, tuned as in Table 3.5, not ECs.

tion 4.2.3.1, corroborating the interest in studying a 2-IBR system for investigating the interactions between IBRs, and the possibility of extrapolating the conclusions for larger systems. Also, it is interesting to observe how a GFM located on the opposite edge of the MVDG (Bus 3) participates in the same mode as the GFLs. This has an important implication for DSOs, which could resort to a distant GFM to solve GFL-related SICDS issues. An architecture with “key” GFMs integrated into an MVDG for stabilization purposes could be of special interest in networks with high penetration of RES.

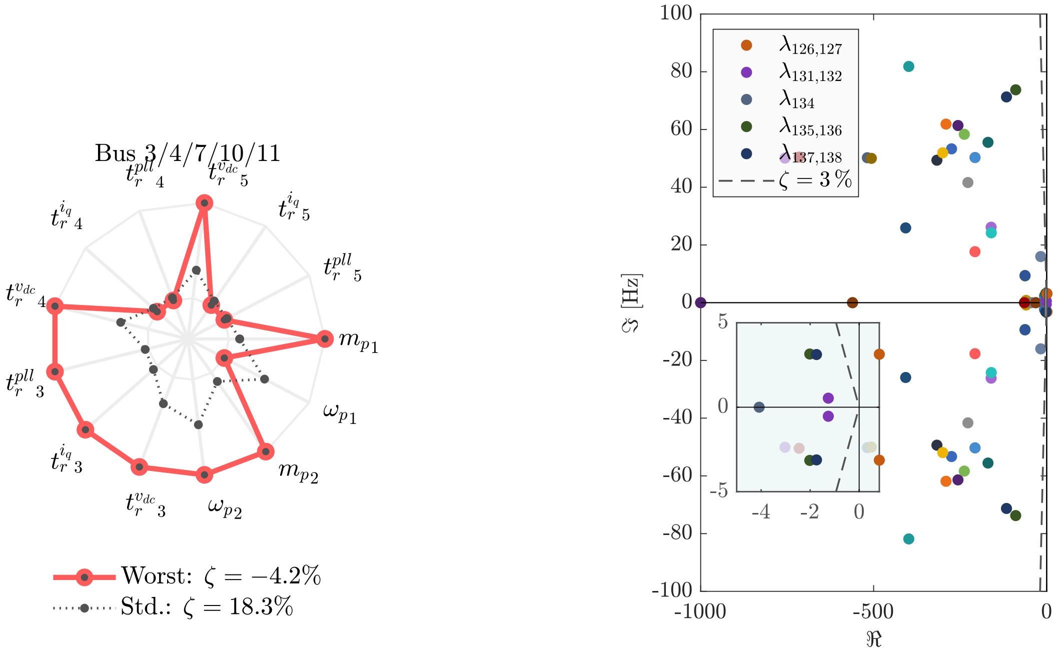

(a) Worst configuration

(b) Eigenvalue map

Figure C.1: Worst combination between bound values for the 5-IBR configuration, leading to a damping of $\zeta = -4.2\,\%$. The bounds are based on their original values.

Let us thus perform the sensitivities. Figure C.3 presents an MPS for m_p in both GFMs, where mode $\lambda_{135,136}$ crosses the $\zeta = 3\,\%$ line when $m_p > 0.037$. Figure C.4 suggests that the same happens for $t_r^{v_{dc}}$ above 205 ms in all GFLs. Hence, we may update the parameter bounds to agree with a maximum droop of $m_p = 0.035$ and a maximum $t_r^{v_{dc}}$ of 200 ms. This leads to the results in Table C.4, which is clearly an improvement with regards to Table C.3. The same EC combinations which were previously unstable now present minimum damping above 12 %, four times more than our acceptability criterion. As depicted in Figure C.5, the worst among all BCs is now perfectly stable, with a minimum damping of $\zeta = 9\,\%$. Figure C.6 illustrates this improvement in a time-domain simulation, where only IBRs 1 to 3 are depicted. As expected, the oscillations are almost imperceptible in IBR 2, which has low participation in this mode, but IBRs 1 and 3 do interact with each other.

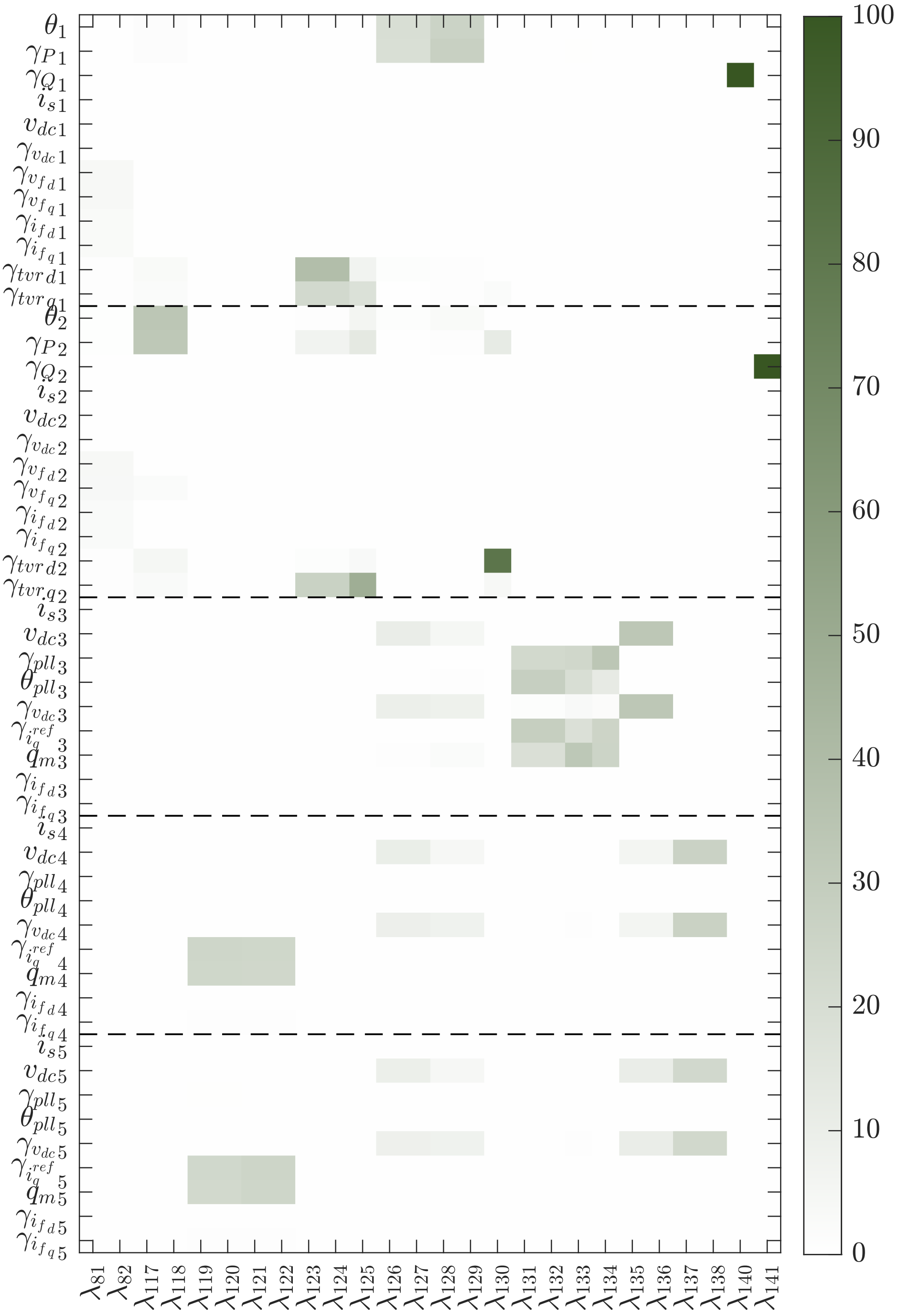

Figure C.2: PFs for the Eigenvalue Map from Figure C.1b

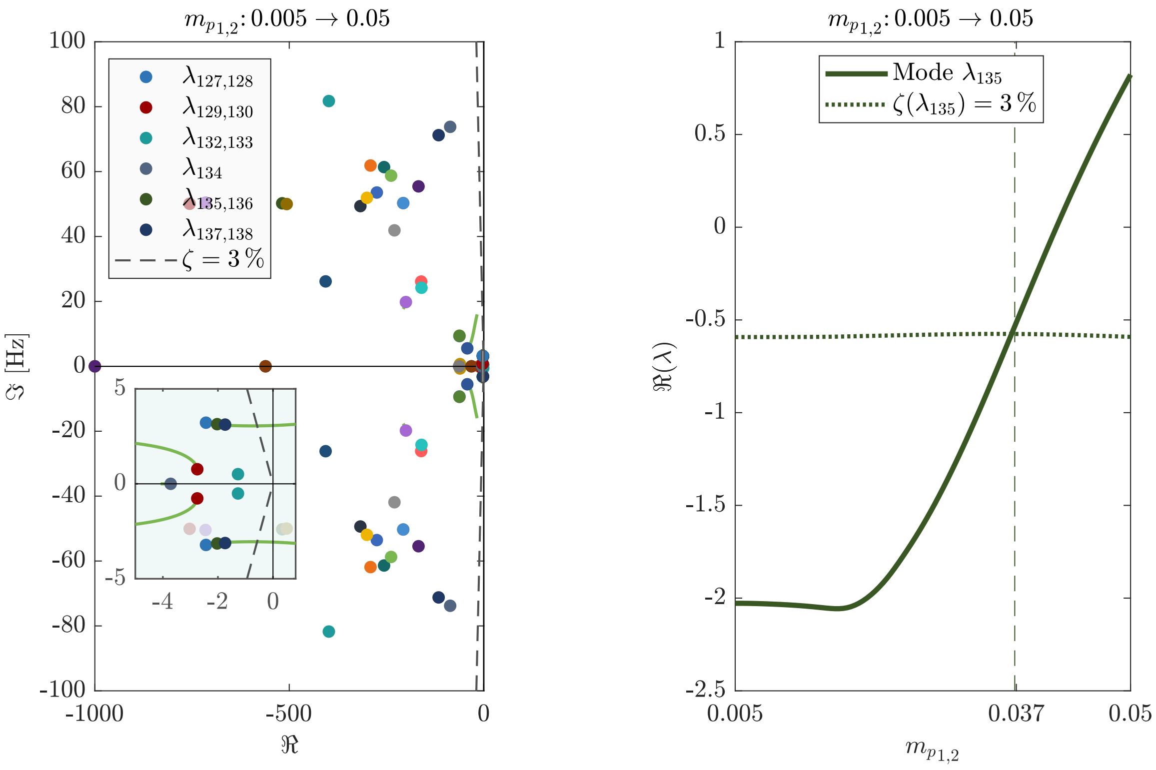

(a) MPS

(b) Eigenvalue trajectory

Figure C.3: MPS for m_p in the 5-IBR configuration

Combination	Min. ζ	Frequency	IBR 1	IBR 2	IBR 3	IBR 4	IBR 5
1	13.8 %	3.27 Hz	GFMB	GFMC	GFLB	GFLC	GFLC
2	12.2 %	3.68 Hz	GFMB	GFMC	GFLC	GFLC	GFLC
3	15.2 %	3.37 Hz	GFMB	GFMC	GFLB	GFLB	GFLA
4	12.5 %	3.27 Hz	GFMB	GFMA	GFLB	GFLC	GFLC

Table C.4: Selected combinations after bound improvement

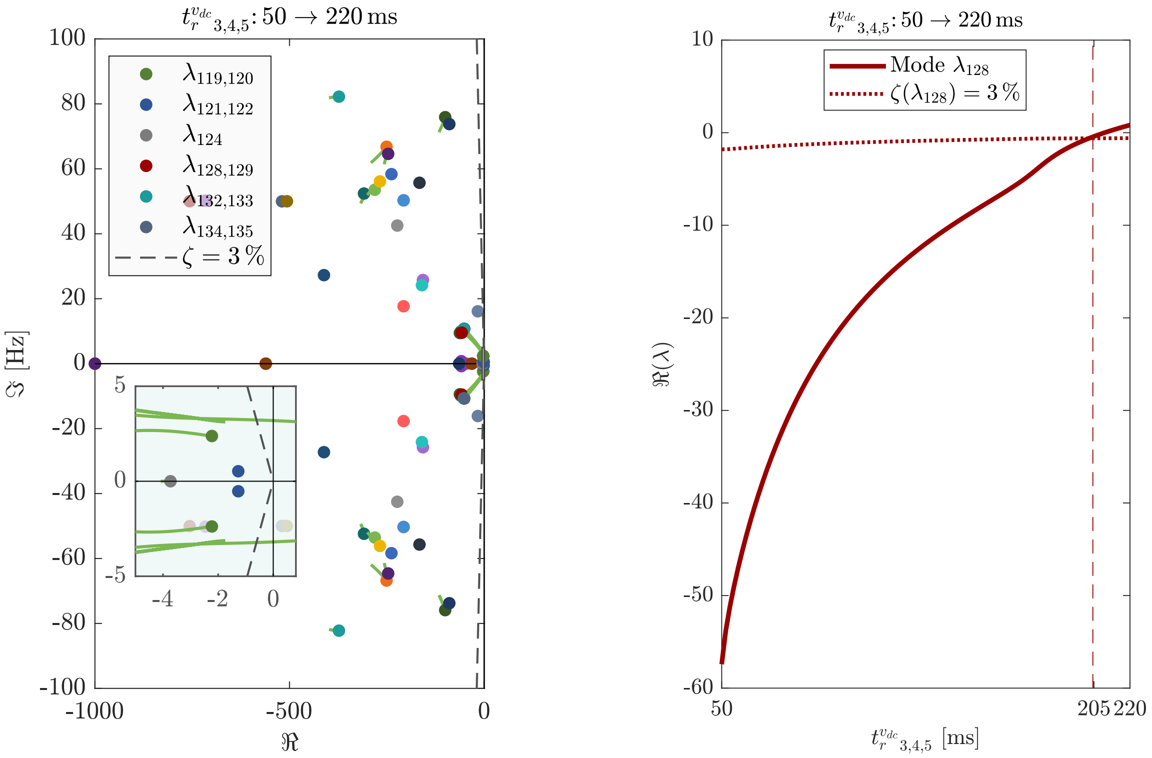

(a) MPS

(b) Eigenvalue trajectory

Figure C.4: MPS for $t_r^{v_{dc}}$ in the 5-IBR configuration

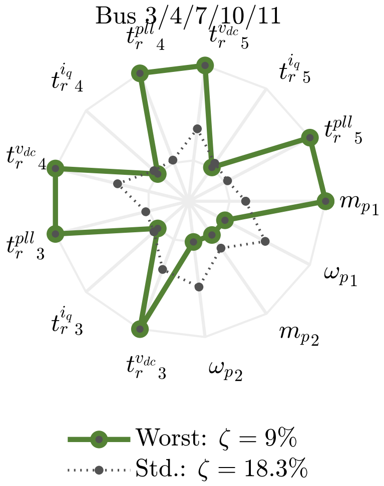

Figure C.5: Worst combination between bound values for the 5-IBR configuration, leading to a damping of $\zeta = 9\,\%$, entirely satisfactory for our purposes. The bounds are based on their *improved* values, with reduced m_p and $t_r^{v_{dc}}$.

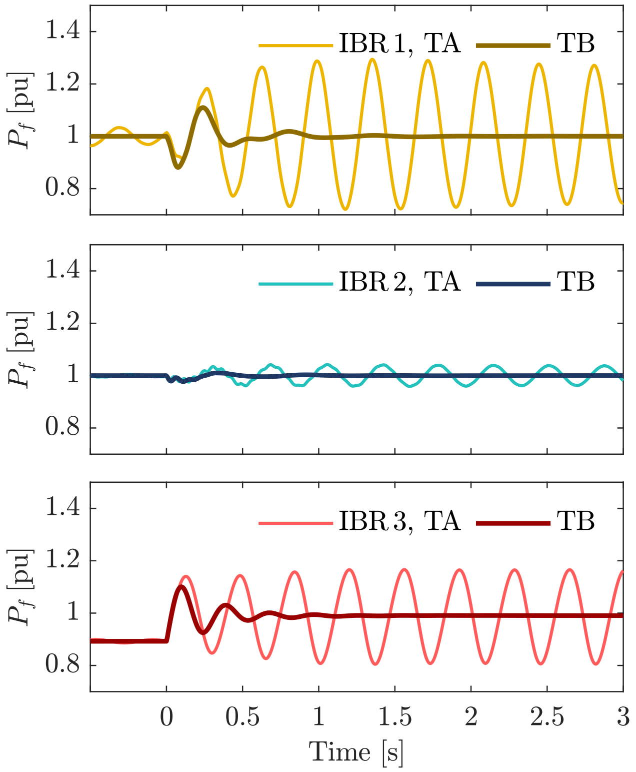

Figure C.6: Time-domain simulation to demonstrate the bound improvement in the 5-IBR configuration. Here we observe the injected power P_f for inverters “IBR 1”, “IBR 2’ and “IBR 3”, following a 0.1 pu step on p^{ref} for IBR 3 (at $t = 0$ s). “TA” is as the worst-case configuration before updating the bounds (high m_p for GFMs and high $t_r^{v_{dc}}$ for GFLs), whereas “TB” presents the same configuration, but with $m_p = 0.035$ and $t_r^{v_{dc}} = 200$ ms.

Résumé Étendu en Français

Contexte

Visant la neutralité carbone en 2050, la France s'est engagée à intégrer davantage d'énergies renouvelables (RES[3]) au réseau électrique. Enedis, le gestionnaire de réseau de distribution (DSO), prévoit jusqu'à dix fois plus d'énergie éolienne et solaire raccordée à son réseau à l'horizon 2050. La puissance cumulée des centrales solaires photovoltaïques (PV) raccordées au réseau HTA pourrait de fait être multipliée par un facteur 15. La plupart de ces RES sont raccordées au réseau par des dispositifs à base de l'électronique de puissance, généralement nommés *ressources interfacées par onduleurs* (IBR), dont le déploiement accru mènera à des changements dans la dynamique du réseau électrique. En effet le comportement des IBR est très éloigné de celui des alternateurs, piliers de la dynamique des réseaux historiques. Cette perspective soulève des inquiétudes quant à la stabilité des futurs réseaux, en particulier en ce qui concerne les interactions entre les onduleurs. Au cours des dernières années, de nombreux épisodes d'instabilités liées à ces convertisseurs ont été observés dans de grands réseaux de transport, en particulier dans des réseaux à forte pénétration de RES. Des questions majeures sont donc soulevées, à savoir : ces événements réels pourraient-ils également se produire dans des réseaux de distribution HTA ? De manière plus générale, quelles sont les circonstances pouvant provoquer des instabilités liées aux convertisseurs ? Quelles sont les mesures que le DSO peut prendre pour les éviter ? Afin d'apporter des éléments de réponse à ces questions, cette thèse propose une étude de la *stabilité liée aux convertisseurs à interactions lentes* au sein des réseaux de distribution HTA, tout en évaluant l'impact des réglages *grid-following* et *grid-forming*. L'objectif est de concevoir une méthodologie destinée aux gestionnaires de réseaux de distribution pour l'analyse et la prévention de ces instabilités.

Contributions

La thèse comprend *dix* contributions majeures, listées ci-dessous (par chapitre).

1. Contexte et études préliminaires

- C-1 Etat de l'art sur la *stabilité liée aux convertisseurs*, une catégorie de stabilité des réseaux électriques récemment définie, accompagné par un aperçu de certains incidents réels marquants. Nous accordons une attention particulière à la *stabilité liée*

---

[3] Tous les acronymes utilisés dans ce résumé renvoient à la terminologie d'origine *en anglais.*

aux convertisseurs à interactions lentes (SICDS), le sujet de la thèse, pour lequel nous comparons les principales méthodes d'évaluation.

C-2 Comparaison entre les onduleurs *grid following* (GFL) et *grid forming* (GFM) dans le cadre des réseaux de distribution moyenne tension (MVDG) interconnectés.

2. Analyse statique des ressources interfacées par onduleurs

C-3 Une étude de l'impact des paramètres statiques du réseau de distribution sur la stabilité des IBRs, notamment le rapport R/X, une propriété particulière des MVDGs.

C-4 Proposition d'une nouvelle méthode de réglage de l'*impédance virtuelle en régime permanent*, un outil permettant d'adapter les onduleurs GFM aux applications MVDG.

3. Modélisation des IBRs raccordées au réseau de distribution

C-5 Proposition de modèles génériques en *transitoires électromagnétiques* (EMT) pour les onduleurs GFL et GFM basés sur les orientations de la littérature scientifique.

4. Analyse de la stabilité petits-signaux des réseaux de distribution comportant des IBRs

C-6 Analyse détaillée des problèmes de stabilité SICDS liés aux régulateurs des onduleurs GFL et GFM, en particulier les interactions entre les onduleurs.

C-7 Identification des paramètres clés qui ont le plus fort impact sur la stabilité SICDS.

C-8 Proposition d'une méthodologie *dédiée au DSO* afin d'assurer la stabilité des « configurations limites »via l'analyse de stabilité petits-signaux (SSSA).

5. Bornes de paramètres-clés pour la stabilité SICDS : une méthode basée sur l'optimisation

C-9 Formulation d'un problème d'optimisation pour concilier les objectifs *locaux* et *globaux* au sein d'un réseau de distribution HTA avec des IBRs.

C-10 Proposition d'une méthode heuristique innovante et efficace en temps de calcul pour déterminer les bornes des paramètres-clés pour la stabilité SICDS.

Résumé des chapitres et conclusions principales

Le **Chapitre 1** comporte une introduction étendue reposant sur l'analyse documentaire, qui sert de base au positionnement de nos travaux, présenté à la Figure 7. Face à la prolifération des IBR, les catégories classiques de stabilité, à savoir la stabilité de l'angle rotorique, de la tension et de la fréquence, ne sont pas suffisantes pour évaluer la stabilité des réseaux de distribution HTA, d'où notre choix de nous concentrer sur une nouvelle catégorie : la stabilité liée aux convertisseurs (CDS). Il s'agit des « problèmes de stabilité, à l'échelle du système, dus aux interactions dynamiques entre les commandes des dispositifs à base d'électronique de puissance et les autres composants du réseau électrique » [17]. Compte tenu de leurs répercussions sur l'ensemble du réseau électrique et du fait qu'elles pourraient découler des interactions entre les IBR, nous avons choisi de nous pencher sur les CDS à *interactions lentes*, i.e. le SICDS, applicable à des phénomènes en dessous de 50 Hz. La plupart des méthodes d'évaluation pour la stabilité SICDS se regroupent en deux catégories : les méthodes basées sur l'impédance (IBM) et l'analyse de la stabilité petits-signaux (SSSA). En raison des outils efficaces qui lui sont associés, tels que les facteurs de participation, la SSSA est mieux adaptée pour expliquer les origines des problèmes de stabilité SICDS *lorsqu'on dispose de modèles détaillés*. Puisque les commandes des IBR agissent sur de nombreuses échelles de temps, il est préférable de modéliser ce système à l'aide de modèles *transitoires électromagnétiques* (EMT) plutôt que de modèles *root-mean-square* (RMS), permettant ainsi une représentation plus exacte. En outre, comme les régulateurs des IBR sont souvent à l'origine des problèmes de stabilité SICDS, il convient de tenir compte des deux principaux modes de fonctionnement des IBR, à savoir le *grid-following* (GFL) et le *grid-forming* (GFM).

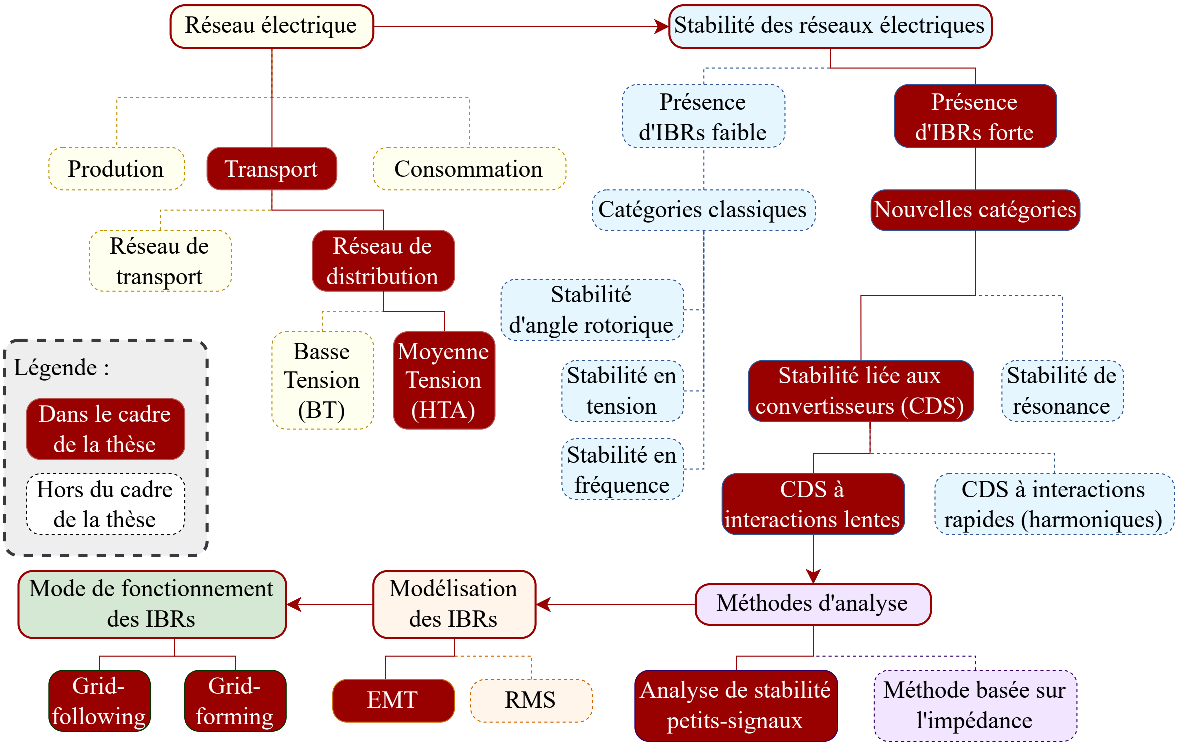

Figure 7: Positionnement des travaux

En principe, les GFLs sont des convertisseurs pilotés en tant que sources de courant, conçus spécifiquement pour des sources intermittentes, et capables d'injecter des puissances de consigne, actives et réactives, tout en se synchronisant sur le réseau par le biais d'une boucle à verrouillage de phase (PLL). Ils ne sont pas en mesure d'imposer une tension précise à leur point de raccordement (POI) et nécessitent une tension externe *soutenue* pour leur synchronisation, ce qui peut engendrer des problèmes de stabilité lorsque le réseau est faible. Les GFM, en revanche, sont des convertisseurs pilotés en tant que sources de tension, capables d'imposer une tension au point de raccordement tout en injectant la puissance active de consigne. Ils sont capables de se synchroniser au réseau sans faire appel à une PLL, ce qui leur permet de fonctionner correctement dans des réseaux faibles. Les GFMs risquent toutefois de provoquer des instabilités dans des réseaux forts et exigent des sources flexibles, avec une marge de production appropriée, en général des batteries. L'étude spécifique des applications GFM pour les réseaux de distribution HTA interconnectés n'en est qu'à ses débuts dans la littérature scientifique, c'est pourquoi nous visons également à évaluer le rôle des GFM dans de tels réseaux, ainsi que les initiatives des DSOs pour mieux les intégrer.

Le **Chapitre 2** présente quelques études préliminaires à la modélisation et à l'analyse de stabilité d'un réseau de distribution HTA comportant des IBR. Ce chapitre examine les propriétés statiques des réseaux HTA, telles que le rapport de court-circuit (SCR) et le rapport R/X, ainsi que leurs répercussions sur la stabilité, l'objectif étant de mettre en évidence des instabilités courantes liées à des paramètres statiques et d'explorer certaines particularités des réseaux HTA ($R/X \approx 1$, par exemple). De cette évaluation, on peut déduire que des situations de réseau faible (SCR inférieur à 3) peuvent se produire dans des réseaux HTA dotés de départs de grande longueur (près de 20 km), de sorte que certaines instabilités observées dans des grands réseaux de transport, notamment l'instabilité de la PLL, pourraient également se produire dans des réseaux de distribution HTA. On en conclut également qu'en cas de SCR faible et de R/X élevé, les GFLs peuvent conduire à des niveaux de tension inadmissibles, qui seraient toutefois réglés en les remplaçant par des GFMs. Des problèmes statiques dus à une sensibilité P-I négative (limitation de transfert de puissance) sont peu probables au sein d'un réseau à R/X élevé. Pour les GFM opérant comme des bus PQ, le couplage en régime permanent entre P et Q, résultant du rapport R/X élevé, pourrait nécessiter une impédance virtuelle (VI) pour la correction de ce rapport. Le bon réglage de cette impédance virtuelle repose sur le couplage P-Q, la tension au point de raccordement et le SCR apparent ; il est possible de réduire le couplage, mais aux dépens d'un maintient précis des niveaux de tension.

Le **Chapitre 3** décrit la modélisation d'un réseau de distribution HTA comportant des IBRs. Il commence par une liste des hypothèses de base, suivie d'une description du réseau choisi (Réseau HTA de référence CIGRÉ) et du modèle physique d'un IBR. Nous proposons des modèles génériques pour les onduleurs GFL et GFM, en détaillant leurs boucles de régulation. Toutes les équations différentielles nécessaires à l'analyse de stabilité petits-signaux y sont exposées, ainsi que des commentaires sur le dimensionnement, le réglage et la paramétrisation des IBRs. Pour finir, nous détaillons le processus de linéarisation et de regroupement des espaces d'état, afin de réunir toutes les informations nécessaires à l'analyse de stabilité.

Nos études sont axées sur de grandes centrales photovoltaïques, bien que les conclusions puissent s'appliquer aux centrales éoliennes de Type 4 (générateurs synchrones à aimants permanents). En examinant les modèles disponibles dans la littérature, on peut conclure que le GFL générique, comme le montre la Figure 8, comprend des boucles de régulation internes et externes (pour P et Q), en plus d'une PLL, où la boucle de régulation de P

pourrait être remplacée par le réglage de la tension DC. Le modèle générique d'un GFM, illustré par la Figure 9, comprend également des boucles de régulation internes et externes, ces dernières comprenant une *boucle de synchronisation par la puissance* (pour P) et un réglage de statisme (*droop*) entre Q et V. Il est tout aussi important de tenir compte des boucles de réglage supplémentaires, telles que l'amortissement actif, l'impédance virtuelle et le réglage de v_{dc}. Malgré les nombreux modèles disponibles dans la littérature, on peut conclure que leur comportement petits-signaux peut toujours être reproduit à l'aide de ces modèles génériques, ce qui constitue un atout pour le DSO.

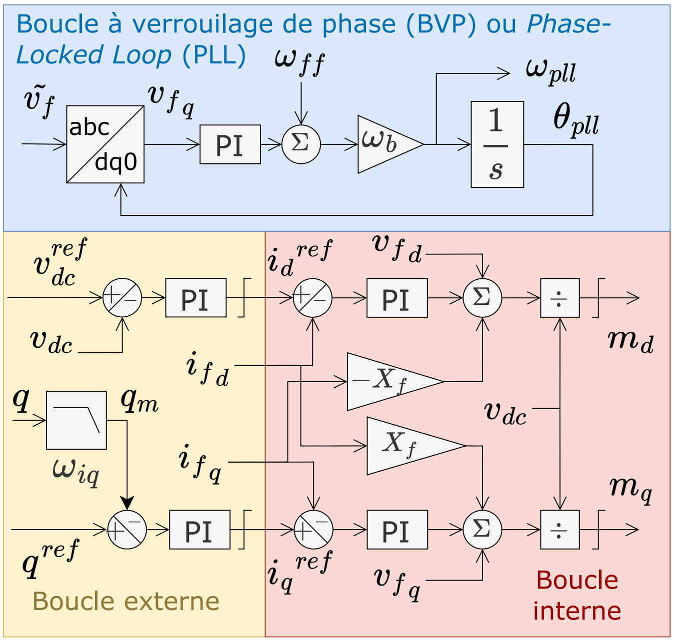

Figure 8: Schéma de réglage pour un onduleur *grid-following*

Une fois les modèles établis, le **Chapitre 4** se consacre à l'analyse de stabilité petits-signaux. Des « cartes modales » permettent d'identifier les modes dominants du système à un onduleur. Nous constatons qu'ils sont liés aux boucles externes de régulation, ainsi qu'à la PLL (pour l'onduleur GFL) et à la boucle de réglage v_{dc} (pour l'onduleur GFM). Grâce à des analyses de sensibilité et des facteurs de participation, il est possible d'identifier les paramètres-clés pour la stabilité SICDS, à savoir $t_r^{v_{dc}}$, $t_r^{i_q}$ et t_r^{pll} chez les GFL, ainsi que m_p, ω_p et $\tau_{v_{dc}}$ chez les GFM. Ces éléments sont essentiels pour que les DSOs puissent prévenir et atténuer les incidents SICDS dans les réseaux HTA. Dans le cas d'un système à un seul GFL, on constate qu'un $t_r^{v_{dc}}$ élevé peut provoquer des instabilités si la capacité du lien DC est réduite, tandis que l'instabilité de la PLL peut se produire lorsque le t_r^{pll} est faible et que l'IBR est raccordé au nœud le plus faible du réseau. Les GFM raccordés à des nœuds forts risquent également de provoquer des instabilités dues à un *droop* élevé. Ce phénomène est expliqué grâce à des analogies avec les machines synchrones, même si cela ne se produit que pour des *droops* trop élevés pour être vraiment réalistes ($m_p = 0,2$, par exemple).

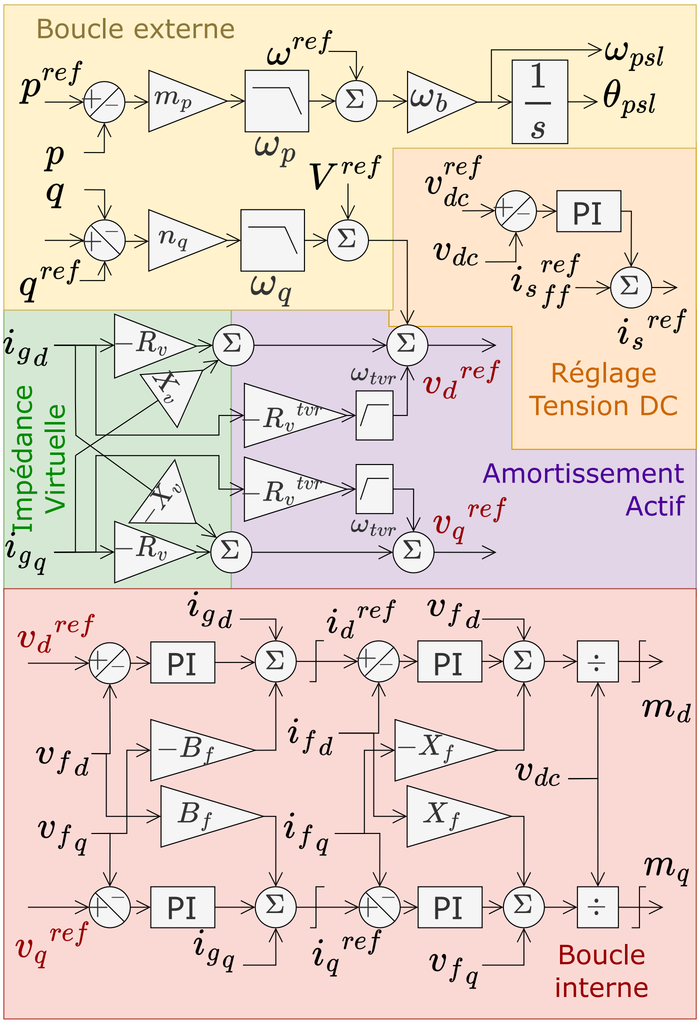

Figure 9: Schéma de réglage pour un onduleur *grid-forming*

Afin d'étudier les *interactions* entre les IBR, nous recourons à des configurations à deux onduleurs, dans lesquelles, outre le SCR au POI, la distance électrique entre les IBRs est elle aussi un paramètre déterminant. Les cartes modales révèlent que les modes dominants découlent de l'interaction entre les boucles externes de régulation *des deux IBRs.* Des sensibilités à un seul paramètre sont employées pour affiner les plages critiques des paramètres clés ; en particulier, un *droop* de $m_p = 0,04$ est désormais suffisant pour provoquer des problèmes de stabilité SICDS lorsque deux GFM sont raccordés à des nœuds avoisinants, ce qui indique une interaction significative entre les GFMs. Bien qu'une configuration mélangeant GFL et GFM semble produire des plages de fonctionnement stables plus importantes que les configurations GFL/GFL ou GFM/GFM, on observe encore quelques interactions négatives : un GFM peut accentuer l'instabilité due à un $t_r^{v_{dc}}$ élevé dans un GFL, par exemple. En revanche, positionner un GFM à proximité d'un GFL permet de régler son instabilité de PLL. Les résultats sont corroborés lorsqu'on étend l'analyse à un système comportant plusieurs IBRs, ce qui atteste la pertinence d'une analyse générique à deux IBRs.

Nous proposons enfin une méthodologie pour améliorer la stabilité des *configurations limites* (BC), à savoir les configurations dans lesquelles chaque paramètre-clé est fixé à sa borne minimale ou maximale. Pour ce faire, on applique des sensibilités multi-paramétriques aux combinaisons les plus défavorables des configurations limites. Les Figures 10 et 11 illustrent cette amélioration : tandis que la première figure, basée sur les bornes originales, présente de nombreux cas d'amortissement insuffisant ($\zeta < 3\,\%$) ou même d'instabilité ($\zeta < 0$), la seconde figure démontre que les bornes améliorées sont capables d'assurer la stabilité de tous ces scénarios.

La conclusion la plus importante est que les DSOs ont un rôle majeur à jouer pour assurer la stabilité SICDS au sein des réseaux HTA. Pour cela, ils pourraient fournir des *plages de régulation* appropriées pour les paramètres-clés. Ainsi, le **Chapitre 5** introduit un problème d'optimisation pour déterminer une surface de paramètres maximale qui assure la stabilité petits-signaux. Cela permet au DSO d'imposer les bornes des paramètres à l'intérieur desquelles tous les producteurs pourront régler leurs IBR selon leurs exigences, sans pour autant aboutir à des configurations insuffisamment amorties, c'est-à-dire un compromis entre la stabilité *globale* du réseau et les objectifs *locaux* des producteurs. Il s'agit d'un problème d'optimisation complexe, dont la fonction de contrainte est en soi un problème d'optimisation. On peut le résoudre à l'aide d'algorithmes méta-heuristiques, tels que les algorithmes génétiques (GA) et l'optimisation par essaims particulaires (PSO), efficaces mais gourmands en temps de calcul. Pour simplifier la procédure, nous proposons une méthode heuristique, dont l'organigramme est présenté à la Figure 12, qui applique un algorithme de type gradient pour trouver une solution approximative au même problème d'optimisation. Les résultats finaux nous permettent de conclure que cette méthode heuristique aboutit à des surfaces similaires à celles des aux autres algorithmes, mais avec des temps de calcul nettement inférieurs ; dans certains scénarios, la méthode heuristique est presque 100 fois plus rapide.

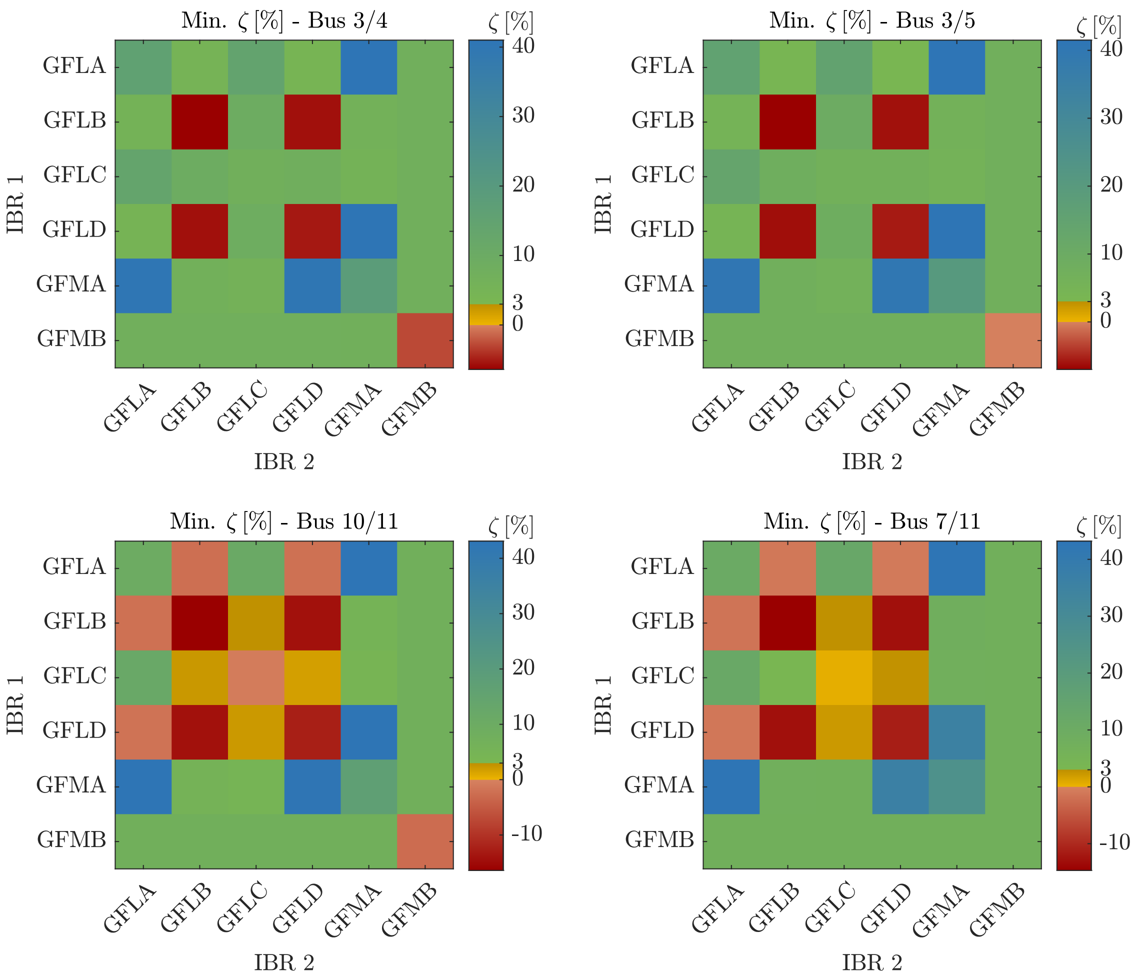

Figure 10: Combinaisons entre des configurations d'IBR, présentées au Tableau 4.6, pour les scénarios S1 à S4 du Tableau 4.4. Chaque point représente le taux d'amortissement minimum parmi toutes les valeurs propres en dessous de 500 Hz pour la combinaison respective entre IBR 1 et IBR 2. Les bornes des paramètres sont celles d'origine (Tableau 4.5), conduisant à de nombreux cas d'instabilité (points rouges) et de faible amortissement (points jaunes).

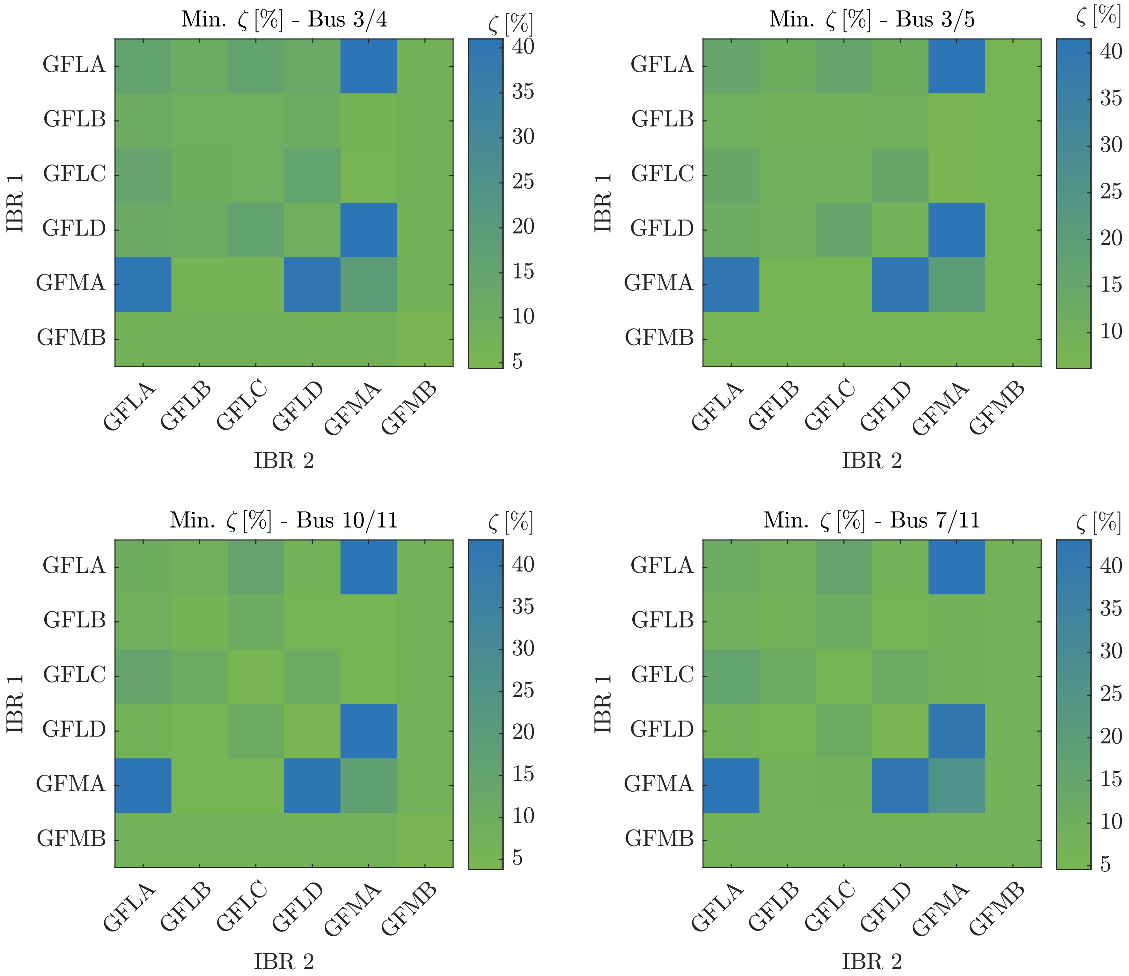

Figure 11: Combinaisons entre des configurations d'IBR, pour les scénarios S1 à S4. Désormais, les bornes des paramètres sont les bornes améliorées (Tableau 4.7), ce qui se traduit par des résultats stables (points verts/bleus) pour toutes les configurations.

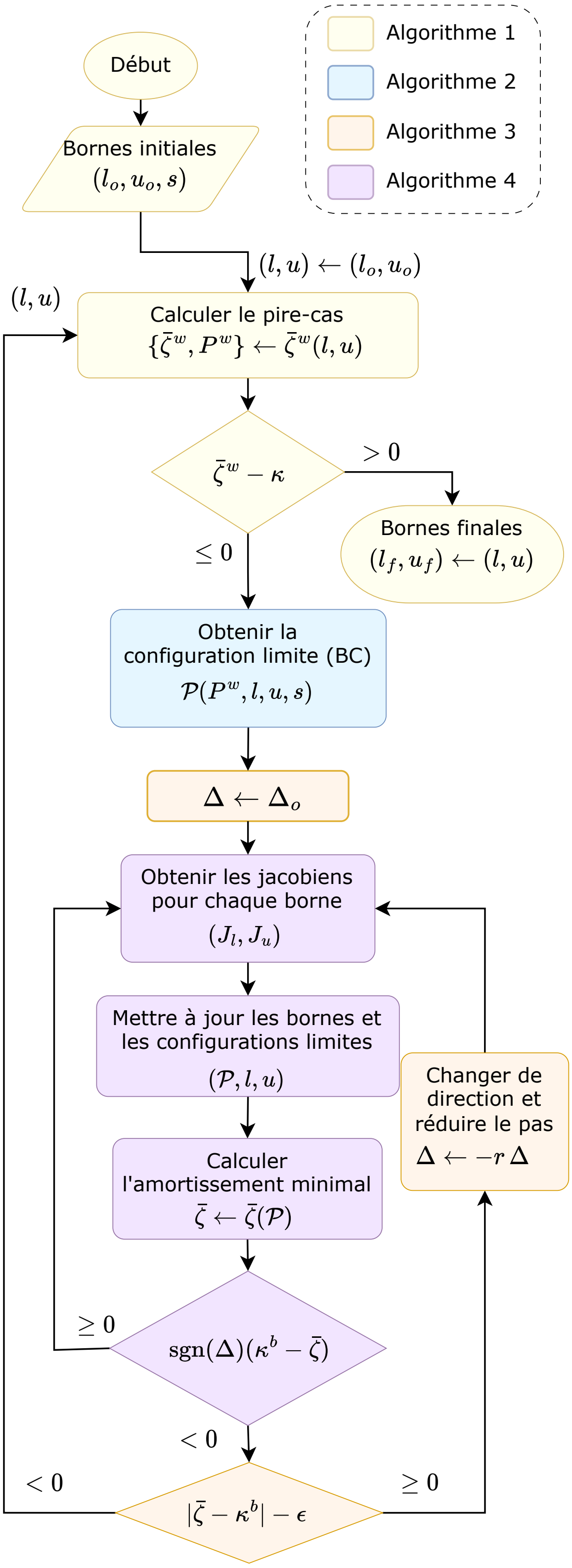

Figure 12: Organigramme de la méthode heuristique